Modular UAV for Military Tasks

Final Design Report

DSE Group 15

Delft University of Technology

TU Delft

Modular UAV for Military Tasks

Final Design Report

by

DSE Group 15

Group members:	4086244	T.C. van Veen
	4192028	Ş. Kılkış
	4277368	U. Avsec
	4289579	B. Herremans
	4293959	R.F.C.Y. Tam
	4348974	K. Nikolakopoulos
	4363221	D. de Leeuw
	4382889	J.G.P. Vermeulen
	4383028	E. de Leeuw
	4394143	D.D.C. De Buysscher

Supervisor: Dr. ir. J.M.J.F. van Campen

Coaches: Y. Liu
J. Khaliq

in cooperation with

M. Goossens K. Knepper J. Willems

Fokker GKN AEROSPACE NLR Koninklijke Luchtmacht

TU Delft Delft University of Technology

Preface

This document is the fourth and final report in the series for the DSE project: I-ACT Modular UAV. The Project Plan initiated the series, followed by the Baseline Report and next the Mid-term report. During the Mid-term review the generated conceptual designs were presented to the stakeholders and they in turn showed their preference towards the quadcopter design. In this report the final design that the team came up with is discussed and will show the innovative aspects, with one of the most important aspects: the modularity of the design.

For the reader, a couple of chapters are thought of as interesting and would be worth to browse if time to read the complete report is limited. First of all, since modularity is the central topic of the project, an interesting chapter would be Chapter 8. Chapter 9 outlines what the Unmanned Aerial Vehicle (UAV) is actually capable of doing in terms of performance. Additionally, Chapter 5 shows the final characteristics of the modular UAV. Lastly, if one is interested in the future developments of the project, Section 20.2 should be read since this displays the future plans of the project in a Gantt chart after finishing the DSE.

Team 15 would like to express their gratitude towards their tutor, Dr.ir. J.M.J.F. van Campen, and our coaches, J. Khaliq PhD and J. Liu PhD, for their support and advice throughout the whole project. Many thanks extended to J. Willems, K. Knepper, M. Goossens, in combination with the University of Technology Delft for creating this interesting but very challenging project that gave us opportunity to see how complex a design process for military purposes is in reality. Lastly, advice and display of expertise by E. van den Bos, E. van der Horst, J. Kober, L. Kram, ir. T. Michelis, Dr.Ir. A.K. Sahai, Dr.ir. M. Voskuijl was very much appreciated.

Summary

In the final report for the Design Synthesis Exercise (DSE), the detailed design phase of the Surveillance Platform for Aerial Reconnaissance and Target Acquisition (SPARTA) Unmanned Aerial Vehicle (UAV) is explained and the result discussed. In this phase, the chosen design from the mid-term report is re-designed and its preliminary design characteristics are presented. Then each subsystem is designed in detail and finally recommendations and improvements are shown.

Based on the needs of the Royal Netherlands Air Force (RNLAF) the design focuses on two main missions: short and long range observation missions where the vehicle has to perform surveillance for at least 2 h.

The detailed design of each subsystem showed the following:

Modulartiy and payload analysis A qualitative trade-off was performed and the following was found: slide snap-fit fasteners are the most optimal choice for this design. The payload analysis was performed to determine the most optimal payload modules. It includes a camera and biochemical sensors or extra batteries. The payload has a mass of 0.75 kg, with 113 mm × 60 mm × 78 mm as general dimensions and a total power consumption of 10 W.

Performance & propulsion analysis The fixed-wing is able to pull a load of 5 g with a corner velocity of 25 m s^{-1}. In addition, it has a turn rate of 1.92 rad s^{-1} and a turn radius of 13 m. For the quadcopter three iterations were performed and an electric propeller with two blades was used with a diameter of 13 in made out of carbon fiber and a mean efficiency of 78 %. The motor used for the quadcopter configuration is the *RimFire .10* type with a mass of 71 g, and a constant power of 325 W. For the fixed-wing, two iterations were performed and an electric propeller with two blades was chosen with a diameter of 10 in, mean efficiency of 85 % and made out of carbon fiber as well. The motor for the fixed-wing is the same as the quadcopter. Both configurations use lithium-ion batteries due to the high specific energy.

Aerodynamics For the quadcopter configuration the most optimal rotor airfoil is the *USNPS4*. For the fixed-wing, special attention was paid to the wing airfoil selection where the *NACA 22112* was found to be most suitable. A simple symmetric airfoil was chosen for the tail, the *R14.0*. Concerning the noise of the UAV, Gutin's and Hubbard's method was used to estimate the Sound Pressure Level (SPL). For the quadcopter configuration the vehicle is inaudible at 70 m, while for the fixed-wing is at 10 m.

Stability and control At first, the tail configuration was found to be a twin-boom A-tail with an anhedral angle of 80 deg. The dynamic stability of the system was also investigated after determining the stability coefficients. The ailerons were sized, with an area of 1.44 × 10^{-2} m^2 and the autopilot software is written in C++ language.

Structural design For the structural analysis, more attention was paid to the numerical weight estimation of the fixed-wing, since this part was deemed the most crucial for the performance. The fuselage and quadcopter were analyzed in *ANSYS*. The chosen material for the wing design is Kevlar fiber due to its low weight and high yield stress, resulting in a wing mass of 1.126 kg when the flight envelope is limited to 7 and −4 load factors. Furthermore, the manufacturing plan for the full program is estimated to take approximately half a year for the structures.

Communication The vehicle will be using one *Superbat 2624* antenna while the ground station uses four *VFM ANT0906* antennas. The system is capable of functioning at minimum bit error rate using any desired encoding system.

As the estimated assembly time is 10 min for both configurations, special care has to be given to the operations and logistics of the Unmanned Aerial System (UAS).

In addition, a risk management strategy was conducted where the risks from every department were identified, assessed and mitigated when necessary. A risk map was created to identify the regions that require close attention. It was found that most risks are associated with avionics and control, as it is the most complicated system of the vehicle. The reliability of the SPARTA UAV was calculated at 81 % and its availability at 90 %.

The final product has an estimated mass of 3.6 kg in quadcopter configuration and 4.43 kg in fixed-wing configuration. This complete system, which includes one fuselage, a quadcopter modules, a fixed-wing module and the ground station comes at a cost of €26 660.

Finally, a post-DSE Gantt chart and project design development show that the product will be ready for delivery mid 2019.

Contents

List of Symbols

Abbreviations

ADCS	Attitude Determination and Control System
Al	Aluminum
AOA	Angle of Attack
BEMT	Blade Element Momentum Theory
BEV	Battery Electric Vehicle
CFD	Computational Fluid Dynamics
COG	Center of gravity
DSE	Design Synthesis Exercise
EASA	European Aviation Safety Agency
FBS	Functional Breakdown Structure
FEM	Finite Element Method
FFD	Functional Flow Diagram
FOR	Field of Regard
FPGA	Field Programmable Gate Array
FPS	Frames Per Second
GPIO	General Purpose Input/Ouput
GPS	Global Positioning System
HPBW	Half Power Band Width
ICEV	Internal Combustion Engine Vehicle
IFOV	Instantaneous Field Of View
LCW	Logistiek Centrum Woensdrecht
LED	Light Emitting Diode
LLT	Lifting Line Theory
MAC	Mean Aerodynamic Chord
MOI	Moment of Inertia
MTBF	Mean Time Between Failure
MTOW	Maximum Take-off Weight
NASA	National Aeronautics and Space Administration
NATO	North Atlantic Treaty Organization
NLR	Netherlands Aerospace Centre

PID	Proportional Integral Derivative
PLA	Polylactic Acid
PMW	Pulse Modulate Wave
RAMS	Reliability, Availability, Maintenance, and Safety
REACH	Registration, Evaluation and Authorization of Chemicals [EU Reg 1907/2006]
RNLAF	Royal Netherlands Air Force
RPM	Revolutions Per Minute
SNR	Signal to Noise Ratio
SPARTA	Surveillance Platform for Aerial Reconnaissance and Target Acquisition
SPL	Sound Pressure Level
TBD	To Be Determined
TRL	Technology Readiness Level
UAS	Unmanned Aerial System
UAV	Unmanned Aerial Vehicle
VLM	Vortex Lattice Method
WFD	Work Flow Diagram
WFOV	Wide Field Of View

Greek symbols

α	Angle of attack	deg
β	Side slip angle	deg
δ_a	Aileron deflection	deg
δ_e	Elevator deflection	deg
δ_r	Rudder deflection	deg
δ_t	Change in throttle	–
$\vec{\eta}$	Drone position vector	–
η_{elec}	Electric system eficiency	–
η_{prop}	Propeller efficiency	–
γ	Flight path angle	deg
λ	Taper ratio	–
μ_g	Airplane mass ratio	–
Ω	Angular velocity	rad s^{-1}
ϕ	Roll angle	deg
$\rho_{0,\mathrm{ceil}}$	Air density at sea level, ceiling	kg/m^3
σ	Direct stress	Pa
τ	Shear stress	Pa

θ	Geometric pitch angle	deg

Latin symbols

A	Aspect ratio	–
b	Wing span	m
$\bar{c}$	Mean Aerodynamic Chord	m
C	Coefficient	–
CG	Climb gradient	–
C_{L_α}	Lift coefficient gradient	rad^{-1}
$C_{L,D,M,Q,T}$	Lift, Drag, Moment, Torque, Thrust coefficient	–
D	Drag force	N
e	Oswald efficiency factor	–
E_{bat}	Battery energy capacity	W h
f	Equivalent parasite drag area	ft^2
$I_{xx,zz,zy}$	Moment of inertia around x, z, origin	m^4
K	Lift-induced drag proportionality factor	–
K_g	Gust alleviation factor	–
L	Lift force	N
M	Mach number	–
p	Roll rate	$\mathrm{deg\,s}^{-1}$
$P_{R,A}$	Required, Average power	W
Q	Torque	N m
q	Pitch rate	$\mathrm{deg\,s}^{-1}$
q	Shear flow	$\mathrm{N\,m}^{-1}$
R	Radius	m
r	Yaw rate	$\mathrm{deg\,s}^{-1}$
RC	Rate of climb	$\mathrm{m\,s}^{-1}$
Re	Reynolds number	–
S	Wing area	m^2
S_h	Horizontal tail area	m^2
S_v	Vertical tail area	m^2
S_{wet}	Wetted wing surface area	ft^2
T	Thrust	N
t	Skin thickness	m
$\hat{u}$	Velocity ratio V/V_0	–
U	Gust velocity	$\mathrm{m\,s}^{-1}$

$V_{\mathrm{EAS,TAS}}$	Equivalent, True air speed	m s^{-1}
$V_{A,C,D}$	Design velocity for maneuvering, cruise, dive	m s^{-1}
v_i	Induced inflow velocity	m s^{-1}
W	Weight force	N
W_{TO}	Maximum Take-Off Weight	kg
X	Force in x direction	N
$\bar{x}, \bar{z}$	x, z centroid	m
Y	Force in y direction	N
Z	Force in z direction	N

1 Introduction

In recent history, modern armies focus more and more on the use of Unmanned Aerial Vehicles (UAVs) for reconnaissance missions. UAVs are safe and cheap systems to use in dangerous situations. Additionally, it is possible to obtain sensitive information without the target noticing that it is being observed.[1] Royal Netherlands Air Force (RNLAF) gave design team 15 the assignment to build a modular UAV capable of obtaining information and identifying targets while having modular subsystems. In the previous reports, the initial design planning was made, thus completing the conceptual design phase. The first phase in this report is the preliminary design, followed by a more detailed analysis. In the preliminary phase, the chosen concept from the conceptual phase is evaluated. After which it is optimized with incremental design changes in the detailed phase. Additionally, every subsystem is analyzed in detail to obtain the final design.

The purpose of this report is to provide the reader with a comprehensive explanation on the detailed design of each subsystem. For decision-making processes, relevant choices will be substantiated, while attention has also been given to systems engineering and project management.

The report is divided into four main parts: system overview, technical analysis, product integration analysis and future development. The first part includes Chapter 2 which gives an overview of the mission and the necessity of the project, together with the functional flow diagram and functional breakdown structure. In Chapter 3 the market is analyzed and the main competitor products are described. Chapter 4 describes the concept possibilities as well as the initial sizing process of the chosen concept. After that, Chapter 5 shows the final design characteristics that were evaluated in the rest of the report. Concluding this part, Chapter 6 shows how well the system complies with the requirements that were set at the start of the project.

The next part includes the technical analysis, which analyzes each subsystem in detail. It starts with Chapter 8 where the modularity of the system is explained. This includes the modules that will be attached to the the fixed-wing, quadcopter or fuselage. Furthermore, the different types of fasteners that could possibly be used are discussed. Then Chapter 7 discusses the payload characteristics while giving recommendation of possible payload modules. This chapter also includes an analysis of the camera and explains the chosen payload bay fastener. All other chapters in this part have the following layout: At first the assumptions are stated, then the approach towards the solution of the problem is elucidated based on theories and articles. The final results are depicted at the end of each section. Furthermore, verification and validation is performed in each chapter and at the end, recommendations are given for future research. In Chapter 9, a performance analysis including sizing of rotors and propellers is done for both configurations. Next, in Chapter 10 the aerodynamic and noise analysis of the vehicle for both configurations is performed. Chapter 11 comprises of a stability and control analysis for both configurations. It includes sizing and configuration of the tail, ailerons and quadcopter motor configuration. In Chapter 12 the structural analysis of the wing is done using the aerodynamic loads and resulting stresses. Additionally, the material choices and manufacturing plans are included. Afterwards, Chapter 13 presents an overview of the communication system following the same layout as the previous chapters. Finally, Chapter 14 sizes the necessary hardware for UAV operations, which includes the choices of hardware components and Chapter 15 describes the inter-subsystem sensitivities and the overall iterative process.

The next part characterizes the final design and expected outcome of the product. Firstly, Chapter 16 narrates the sustainability of the product, stating the advantages of modularity, describing a possible execution of a sustainability plan and recommendations for a less environmentally impacting product. In Chapter 17, the operations and logistics are described, including assembly times of the vehicle. Risk management and RAMS are described in Chapter 18 where the risk overview of the different subsystems is presented. Lastly, the cost, power and mass analysis can be observed in Chapter 19.

The last part of this report recounts the future development of the vehicle, which includes the project design and development logic in Chapter 20, which includes a post DSE project Gantt chart in Section 20.2. The conclusions and recommendations can be found in Chapter 21.

[1] aviationweek.com/bca/what-business-aviation-flight-department-needs-know-about-uas, last accessed: 2017-06-22

I

System Overview

I-2

Functional Analysis

This chapter explains the different functions the Unmanned Aerial Vehicle (UAV) needs to perform. For this, the different mission profiles are needed, which is explained in Section 2.1. Next, the functional flow diagram of the UAV is presented in Section 2.2.

2.1. Mission Profile

In cooperation with customer contacts at the Royal Netherlands Air Force (RNLAF) and Netherlands Aerospace Centre (NLR), two main mission archetypes were found, which were taken as the main function requirements for the Unmanned Aerial System (UAS). These missions are explained and analyzed here. Firstly, the missions are described for a military environment and then an example of a civil application is given.

Long range surveillance During this mission, specially trained infantrymen are close to a distance of 5 km from the point of interest. For a period of 2 h, the UAV should provide surveillance data on the target, without the targets knowing they are being watched, as seen in Figure 2.1a. A possible civil application is the monitoring of traffic flow from the air without imposing noise pollution on civilians. This mission is shown in Figure 2.1a and Figure 2.1b.

Short range surveillance During an active engagement or in possibly suspicious environments, the UAV should be able to navigate slowly and hover in an urban environment. Its function in this mission is to provide real-time tactical data to the troops. Civil applications may include disaster relief teams scouting inside buildings that are possibly unsafe for personnel to enter. A schematic representation of this mission is given in Figure 2.1c and Figure 2.1d.

These two missions were converted to a set of technical, top-level, demands for the system. Firstly, the system should be capable of loitering, undetected, for 2 h. Secondly, the system should be capable of hovering and operating in hostile urban environments, with spaces as small as 2 m $\times$ 2 m $\times$ 2 m. Furthermore, the system must be both man portable as well as man operable for all phases of the mission, including take-off and landing.

2.2. Functional Flow Diagram

This section presents the functional analysis of the product and the adjoining system. Its aim is to depict the physical functionality of the system and how the requirements are achieved while the system performs the specified actions. The following functional analysis was derived using the overall life cycle methods and system interface analysis. The lower level functions have been found using the method of functional decomposition and functionality aggregation. For the purpose of overview, the top life cycle level and first decomposition level are presented in Figure 2.2 and Figure 2.3. The decomposition was carried out by analyzing the top function, its traceability to particular requirements and how the derived function interacts with the environment and the system.

Furthermore the Functional Breakdown Structure (FBS) can be seen in Figure 2.4. It shows the grouping of the functions three levels deep, where the decomposition was done based on Functional Flow Diagram (FFD). The presented FFD and FBS were done based on the preliminary design and are not detailed enough for the detailed design where more sublevels are required. They do however present the general functional flow of the system. The full black circle represents the begin of life while the smaller one represents the end of life. The begin of life represents the start of production in function block 1. The end-of-life can be intentional and unintentional destruction, retire or loss of the system. The system is retired through completing function 7 and lost during mission functional step 6. Finally a mistake can occur during production which would result in the destruction of the product.

The storage functional body represents the long term storage of the system in the military base where scheduled regular maintenance is carried out. Pre-mission operations in functional body 3 represent all activities between storage and actually arriving at the mission start location. While post-mission operations include retrieval of the system and regular post-mission inspection.

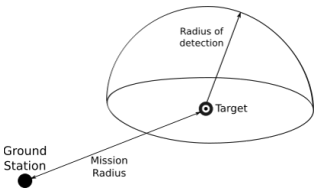

(a) Long range: outside of the detection range

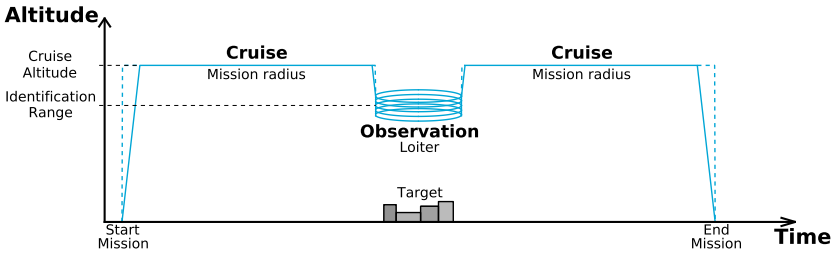

(b) Long range mission profile

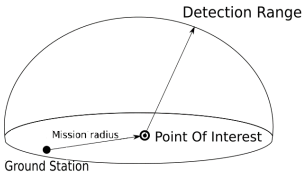

(c) Short range: in detection range

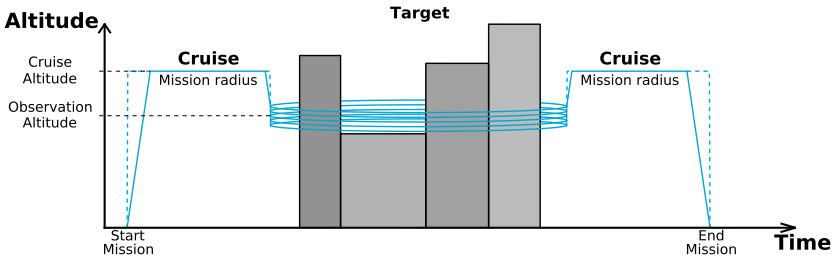

(d) Short range mission profile

Figure 2.1: Mission diagrams

The mission step is functionally most complicated and only the simplified version has been presented here. The possible malfunction of the system may result in failed mission or lost drone. One mission cycle does not conclude with the packing of the UAV, since more batteries can be brought in the field such that the mission may continue with the new cycle.

Finally the maintenance functional body 6 is highly dependent on the entry conditions. If the system has been scheduled for a regular maintenance or upgrade, the activity is pre-planned and executed directly. If the system had a malfunction, firstly the effect of malfunction must be analyzed, damage assessed and a repair plan generated. If the repair is impossible or too expensive, the system must be sent to retire or recycle function. Moreover the conditional structure of FFD is at the moment based on first and second level of functional decomposition. More detail on the conditional nature of the functional flow can be seen in lower levels of the functional design.

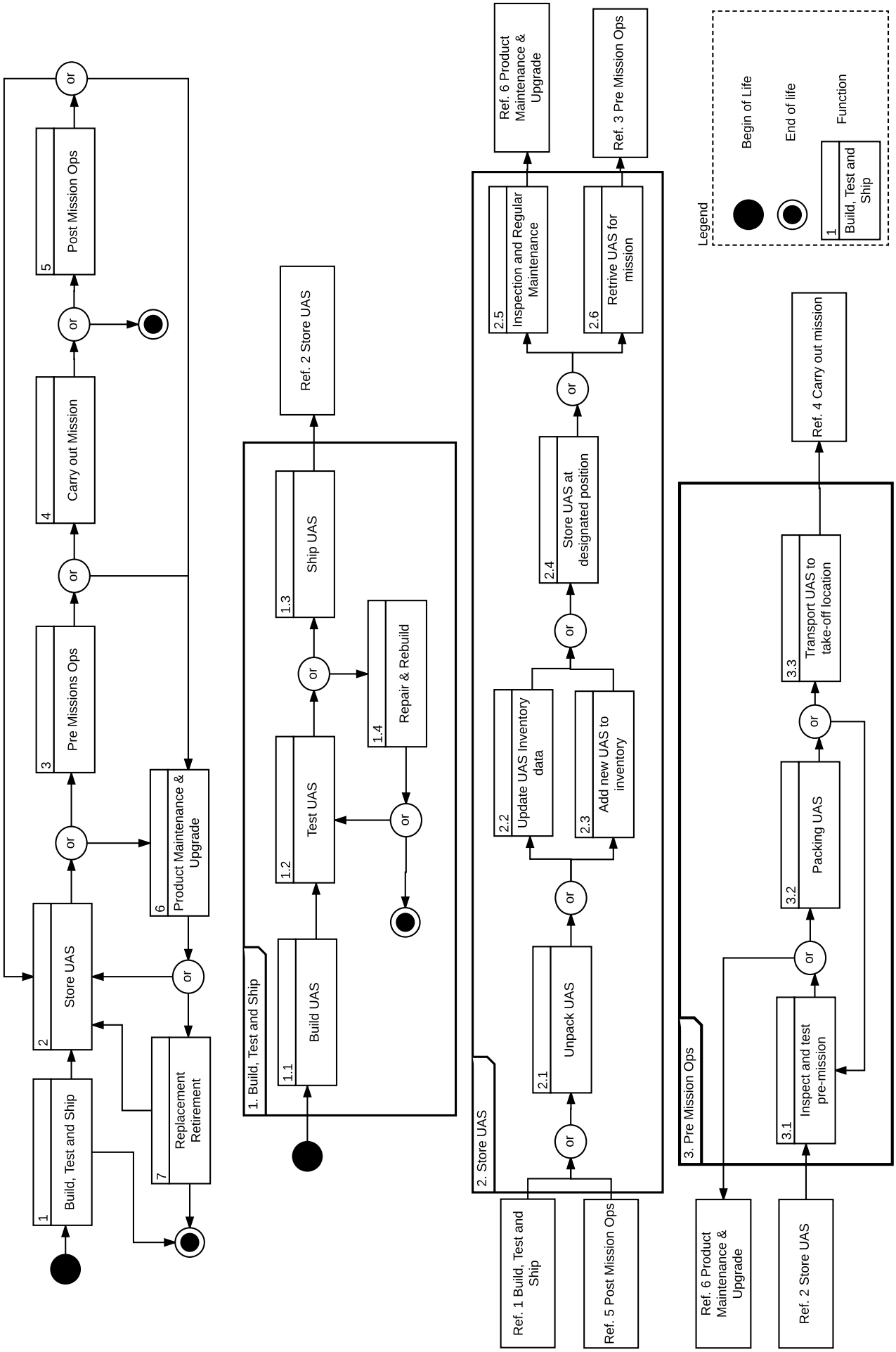

Figure 2.2: Functional flow diagram part 1

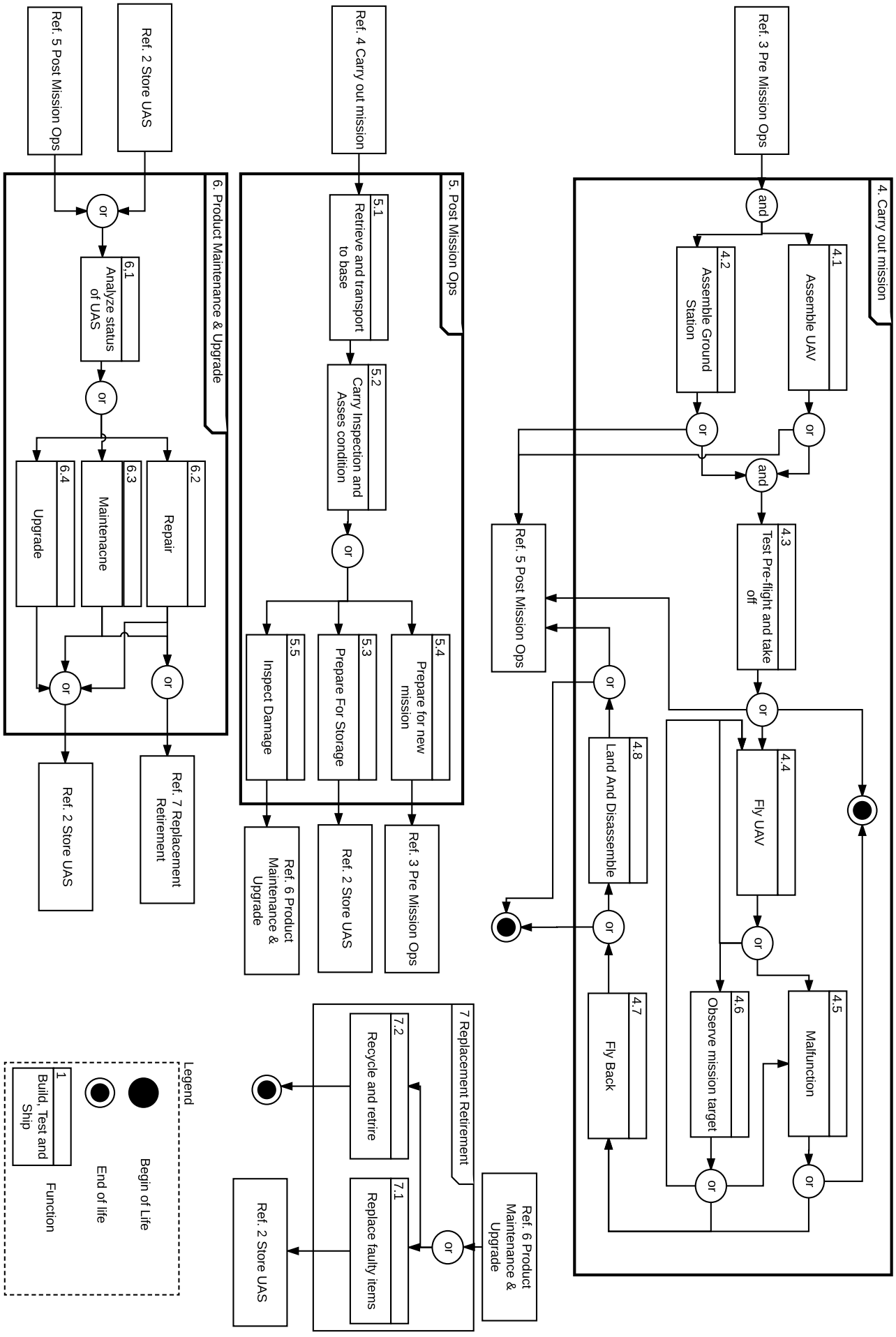

Figure 2.3: Functional flow diagram part 2

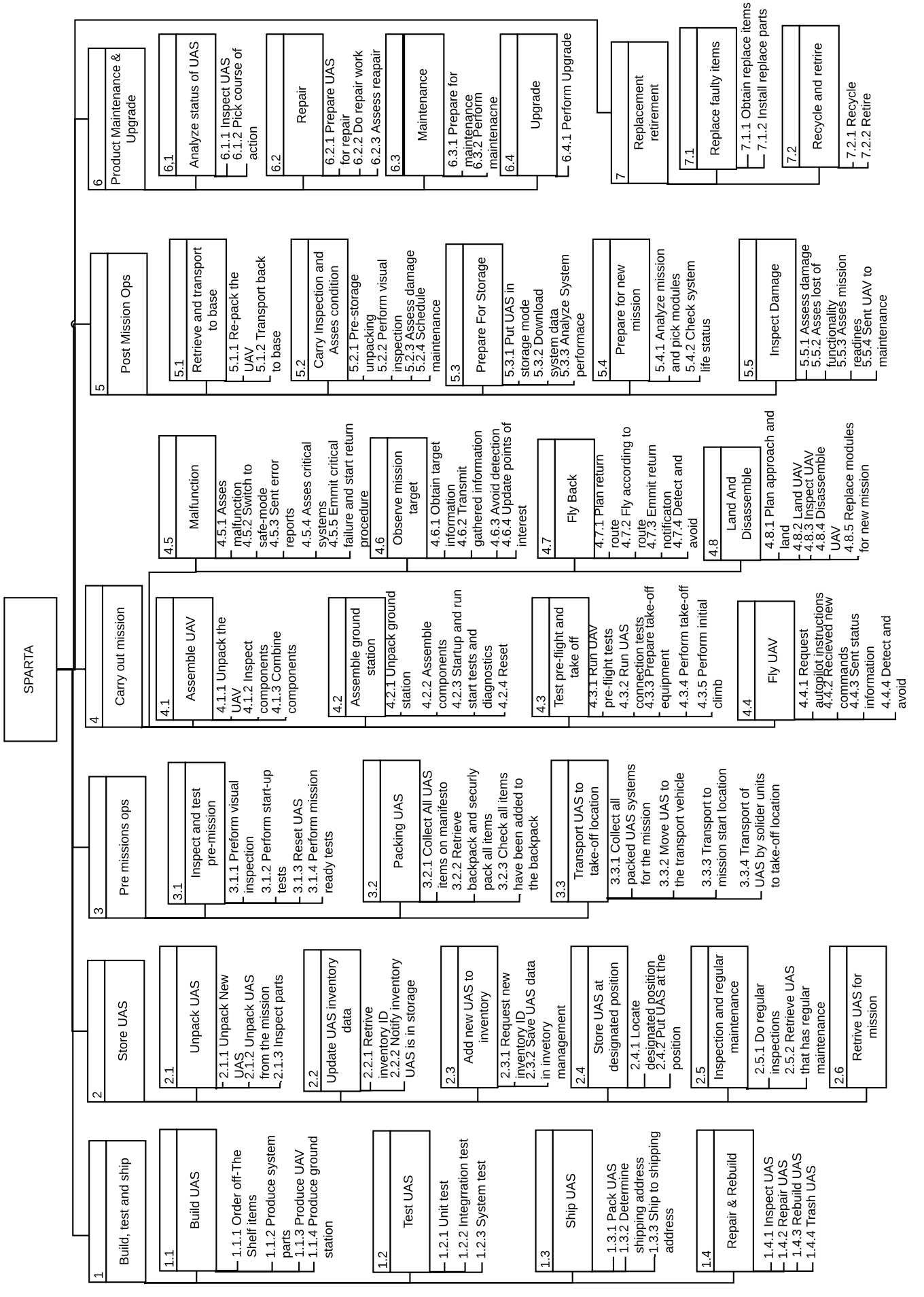

Figure 2.4: Functional breakdown structure

I-3

Market Analysis

This chapter discusses the market analysis for military Unmanned Aerial Vehicles (UAVs) of similar mission profiles. UAVs have a fast expected market growth and are being developed widely, especially for military applications. In Sections 3.1 and 3.2 a general market overview is discussed together with possible customers that includes the most important market regions. Section 3.3 discusses the about competition, companies with similar projects and a brief indication of their market shares. Lastly, Section 3.4 explains the product analysis that has been performed.

3.1. Market Overview

UAV shares are growing fast in the military market. More particularly, their market values for 2016 reach out to $8.5 billion. Estimations show that the market is expected to grow further in 2026 by 4.89 % and their market value will reach $13.7 billion [6].

Projections show that the main customers to dominate in the UAV industry are North America and Europe with total market shares of 32 % and 31 %. Both regions look at further developing their UAV industries due to the fast development of reliable airborne systems. The United States industry, is interested in developing new aerial platforms to perform missions in the safest way, i.e. with minimum losses. Furthermore, a modular payload is essential as the airborne vehicles should both identify and target domestic and international threats. On the other side, Europe wants to develop UAVs for varieties of military missions in order to increase their safety and demonstrate power. The rest of the world possess about 37.5 % of the market.

3.2. Customers

From the overall market trends and the design overview the main focus is on governments and departments of defence. A successful completion of the modular UAV will further push the product to the market due to its tested technology and reliability. North America which possesses 32 % of the market, could be a potential customer. Other military customers could include North Atlantic Treaty Organization (NATO) or other countries from the European Union. Apart from governments, the product can be used by private investors as well. This includes companies for exploring terrains, roads, maps, prisons and emergency or security services in big companies. More information concerning the above mentioned potential customers can be found in [6].

3.3. Competitors

As mentioned earlier, Unmanned Aerial Systems (UASs) are expected to grow rapidly in the following years in the market and therefore not many companies construct small modular UASs for military purposes. Most UAV developers are a form of government funded by their department of defence and very rare from commercial companies. Some of these companies that produce military products are depicted in Table 3.1. The table includes an overview of the country the company is based in, the revenue per year in millions US$ and the niche market in which the UASs are present [6].

Once the main competitors have been identified, the examination of how the product will be positioned in the market and whether it will fulfill the needs of a certain part of the market will be performed. This research is of utmost importance to ensure the financial feasibility of the project.

Table 3.2, the columns represent the multiple possibilities used by military forces in terrestrial reconnaissance missions. Two main tactics can be distinguished (namely, the ground observation of the target and the aerial observation). Both of these tactics were even more divided into manned and unmanned missions.

Once this division was made, the multiple branches were put against some important subjects. Table 3.2 not only describes the status of the tactic in the given subject, but additionally gives an overview of the strengths and weaknesses for each of the tactics. More information about the niche competition can be found in [6].

Table 3.1: Competitors on the global UAS market

Company	Country	Revenue [M$]	Niche
The Boeing Company	United States	94 600	Commercial and military surveillance UAS that can loiter without fuel
AeroVironment	United States	180	Military targeting and reconnaissance UAS with real-time intelligence and electrical propulsion
INSITU	United States	400	Military UASs with high endurance and relatively high service ceiling
Aeryon	United States	46	Easily deployable and modular military UASs for intelligence retrieval with vertical take-off and landing capabilities
Lockheed Martin Corporation	United States	46 100	Military surveillance UASs for the United States army.
Israel Aerospace Institutes	Israel	859	Military unmanned systems

3.4. Product Analysis

In order to get a feeling of the operational capabilities and the general specifications of very small UAVs that are currently in the market. An overview can be found in Table 3.3 of reference UAVs for both civil (black) and military (blue) application. Some of these UAVs are portrayed in Figure 3.1.[1] [2] [3] [4]

- Most of the reference UAVs have a theoretical ceiling of 3000 m, this is the same limit as the one found in requirement **SPARTA-UAV-1**. The ceiling of 152 m of the *AeroVironment* RQ-11B Raven and the *Indago* UAS is the operational ceiling and is limited by the cameras.
- The average Maximum Take-off Weight (MTOW) is equal to 7.2 kg. The maximum is 20.83 kg of *SD-30 Dragon*. For the UAV that is to be designed, **SPARTA-UAV-16** allows for a much larger MTOW, i.e. 50 kg.
- The average endurance without the two outliers of the *FULMAR* fixed-wing micro-UAV and the *Nostromo Yarara*, is equal to 42.9 min. No requirements are present as of yet for the endurance of the UAV, only a loiter time of 2 h in **SPARTA-UAV-3**.
- Most commercial UAVs have a range smaller than the one defined in requirement **SPARTA-UAV-2**, except for the *Skyprowler*. On the other hand, the military applications have an average range of 14 811.11 m, with the *FULMAR* fixed-wing micro UAV having the smallest range of 800 m.
- The operational temperature range found in the specification list of each UAV is −33 °C to 50 °C. The requirement for this UAV in **SPARTA-UAV-4** is bigger than the range that is currently on the market.
- The maximum gust the reference UAVs can withstand is equal to 70 km h^{-1}, which is less than in requirement **SPARTA-UAV-1.3.1**, namely 50 km h^{-1}.

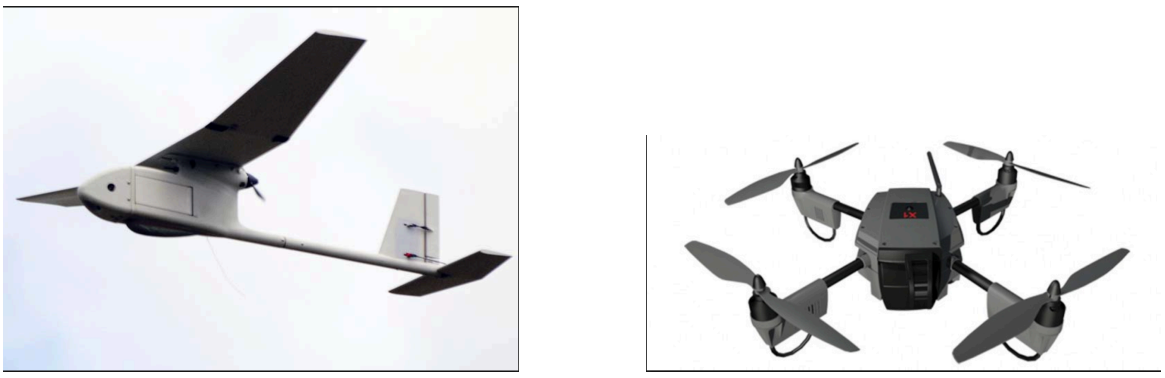

(a) AeroVironment RQ-11B Raven (b) Huggin X1

Figure 3.1: UAV products already in the market

[1] www.abovetopsecret.com/forum/thread981255/pg1, last accessed: 2017-06-22
[2] en.avia.pro/blog/nostromo-yarara-tehnicheskie-harakteristiki-foto, last accessed: 2017-06-22
[3] www.ainonline.com/aviation-news/defense/2016-02-16/iai-unveils-quad-copter-bomb, last accessed: 2017-06-22
[4] www.eurolinksystems.com/product/huginn-x1-mini-vtol/, last accessed: 2017-06-22

Table 3.2: Comparison between different types of reconnaissance units [6]

	Infantry Reconnaissance	**Manned Ground Vehicle Reconnaissance**	**Unmanned Ground Vehicle Reconnaissance**	**Manned Aerial Reconnaissance**	**Unmanned Aerial Reconnaissance**	**Satellite Reconnaissance**
Situational Awareness	Extremely good, can use vision, hearing, touch and smell	Limited, can only use restricted vision from the vehicle, can disembark to increase situational awareness	Bad, signs have to be evaluated by a computer or from a computer screen	Good, can have an overview of a large area in a short time, evaluated by a human	Bad, signs have to be evaluated by a computer or from a distance	Limited, large observable area, but only from above and only vision based
Deployability	Takes time and support from other units to get into position. slow to redeploy	Can deploy and redeploy quickly when open terrain or roads are available	Has to be deployed by other units and needs moderately flat terrain	Can deploy from airfields or carriers within operating range	Has to be deployed by other units or from airfields, generally cannot use carriers	Restricted by the initial orbit but large coverage area.
Positioning	Can get into an overlooking position with difficulty	Can not get to an overlooking position	Can not get into an overlooking position	Can not get into a close observation position	Can get into any kind of position	Can only get into overlooking positions
Resource Dependability	Can remain in position for unlimited time if food and water are available	Uses a large amount of fuel	Uses a small amount of fuel	Uses a very large amount of fuel	Uses a medium amount of fuel	Depends on fly-by moments and time
Range	Short range	Medium range	Medium range	Long range	Medium range	Extremely long range
Speed	Slow speed	Medium speed	Medium speed	High speed	High speed	Very high speed
Detectability	Very good camouflage	Easy to detect	Small, easy to camouflage	Difficult to detect at great range, very easy to detect at close range	Very difficult to detect	Nearly impossible to detect
Replacement Cost/Value	High risk, human lives at stake	High risk, human lives and expensive equipment at stake	Low risk, only relatively cheap equipment at stake	High risk, human lives and very expensive equipment at stake	Low risk, only moderately expensive equipment at stake	Low risk, impossible to attack for all but a handful of nations
On board Equipment	Can only take small and light equipment	Can take the most and heaviest equipment	Can take heavy equipment, easy to make it modular	Can only take light equipment	Can only take light equipment	Can take very expensive and specialized equipment, but has no option for mission dependant modularity
Combat Ability	Can carry light weapons	Can carry heavy weapons	Can carry weapons but cannot engage without human interference	Can carry very heavy weapons	Can carry weapons but cannot engage without human interference	Unable to engage targets
Ethical Decision Making	Can take decisions on its own	Can take decisions on its own	Can only take decisions while a human is in the loop	Can take decisions on its own	Can only take decisions while a human is in the loop	Humans always take the decisions

Table 3.3: Specifications of reference UAVs [6]

Reference UAVs	Cost	Range [m]	Endurance [min]	Wingspan [m]	MTOW [kg]	Ceiling [m]	Max speed [m/s]	Configuration	Payload [kg]
IAI Rotem	> 10 000	1500	30	0.70	5.50	3000	25.72	Quadcopter	1
Huggin X1	50 000		25	0.68	1.40	3000	14.00	Quadcopter	0.18
AeroVironment RQ-11B Raven	173 000	10 000	60	1.37	1.90	152	8.89	Conventional	
Aeryon Skyranger	107 500	3000	50	1.02	2.40	4500		Quadcopter	
DJI Inspire 2	3000	7000	27	0.60	3.29	2500	30.00	Quadcopter	
Indago UAS	25 000	2000	45	0.81	2.20	152	20.00	Quadcopter	0.20
XplusOne	800	1600	22	0.83	1.27	3000	26.82	Hybrid	0.45
Nostromo Yarara		50 000	3600	4.00	35.00	4000	40.00	Conventional	
SD-30 Dragon		2133		2.44	20.83		31.29	Conventional	11.30
FULMAR fixed-wing micro-UAV	1 100 000	800	3600	3.00	20.00	4000	28.00	Conventional	8
DJI Phantom 4	1500	5000	28	0.35	1.38	6000	20.00	Quadcopter	0.50
DJI Phantom 3	500	2000	23	0.59	1.28	6000	16.00	Quadcopter	0.30
RQ-16 T-Hawk	99 500	11 000	40	0.61	8.40	3200	36.11	Ducted fan	
SkyProwler	> 2199	69 000	40	0.90		5000	29.06	Hybrid	0.50
DJI Matrice 100	3300		40	0.65	2.36		22.00	Quadcopter	1
AeroVironment RQ-20 Puma	250 000	15 000	120	2.80	5.90		12.78	Conventional	
AeroVIronment dragon eye UAV		40 000	50	1.10	2.27	3000	18.01	Conventional	0.50

I-4

Preliminary Design Characteristics

During the mid-term review five vastly different potential designs were presented to the stakeholders in order to better understand the type of airframe that they prefer. These designs are presented by Figure 4.1 and covered three main categories of airframes: multicopter, hybrid, and fixed-wing.

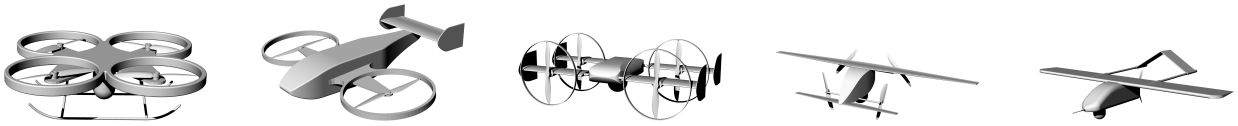

(a) DADIE (b) ARRO (c) THIBA (d) UBKO (e) ERAN

Figure 4.1: Conceptual designs presented at *mid-term review*

The performance parameters of these concepts were presented in a trade-off table during the mid-term review. The result being that rather than trying to optimize for two mission types, discussed in Chapter 2, it was preferable in terms of cost, simplicity, performance, and reliability to perform one mission type well. For reference purposes the final scores of each concept are presented by Table 4.1. The consensus among the stakeholders was that a hybrid airframe would be difficult to design. This by associating it with a high non-recurring engineering costs, since a lot more research and testing would be necessary before flight readiness. Furthermore, the two designs utilizing internal combustion engines (ARRO and ERAN) were discarded on a similar basis as the stakeholders voiced their preference for some form of electric propulsion. In the end the stakeholders requested a quadcopter for the final design, praising its high technology readiness level, simplicity, and performance in an urban setting. They also wanted to see some level of integration with a fixed-wing design in order to meet the 2 h endurance requirement (**SPARTA-UAV-3**).

Table 4.1: Final scores of the conceptual design trade-off [8]

Design	**Score**
DADIE	6.2
ARRO	5.0
THIBA	4.0
UBKO	4.0
ERAN	5.9

Due to this request, along with the desire of the stakeholders to avoid tilt-rotors, new concepts were required before the final design process began. In the integration of a fixed-wing with a quadcopter three possibilities were investigated. First, a concept integrating a fixed-wing with a quadcopter, with the trust axis of each aligned, was investigated. This was dubbed a thrust-axis aligned integration. Next, an offshoot on this concept was a fixed-wing integration with a quadcopter such that the thrust axes of each were perpendicular, dubbed a thrust-axis offset integration. The differences of these two integration methods are depicted in Figure 4.2. Finally, the last concept investigated was to standardize a fuselage that a fixed-wing and quadcopter airframe would both attach to. Examples of these concepts will be given on the next page.

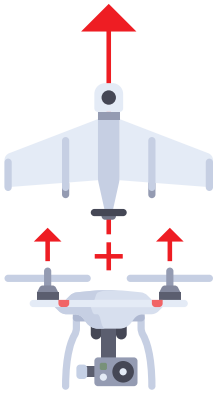

(a) Thrust-axis aligned integration

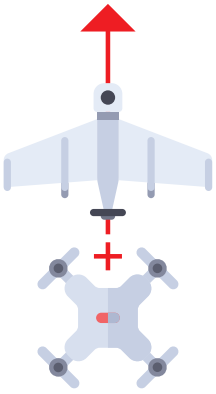

(b) Thrust-axis offset integration

Figure 4.2: Difference between thrust-axis aligned and offset integration[1]

Thrust-axis aligned integration

By aligning the thrust-axis of both the quadcopter and the fixed-wing a smooth transition between hovering flight and horizontal flight can be achieved while utilizing the same motors. Two examples of this concept are the *ATMOS Marlyn* and *VertiKUL* drones shown in Figure 4.3.[2] [3]

(a) ATMOS Marlyn mapping & surveying drone

(b) VertiKUL Automated aerial transport drone

Figure 4.3: Examples of thrust-axis aligned integration

Thrust-axis offset integration

By offsetting the thrust-axis of both the quadcopter and fixed-wing, propellers and motors can be chosen such that they are optimized primarily for their flight-mode. However, this comes at the cost of having to always carry both propulsion systems adding “dead-weight”. Two examples of this concept are the *Krossblade Skyprowler* and *ALTi Transition* drones shown in Figure 4.4.[4][5] The Skyprowler has four retractable propellers that it utilizes for hover as well as two pusher propellers for horizontal flight. The Transition drone has a similar configuration but instead of retractable propellers it chooses instead to fix them to the booms of its twin-boom aircraft configuration.

(a) Krossblade Skyprowler

(b) ALTi Transition

Figure 4.4: Examples of thrust-axis offset integration

[1] www.freepik.com/, last accessed: 2017-06-21
[2] startupjuncture.com/wp-content/uploads/2013/12/ATMOS-Prototype-5-banner.jpg, last accessed: 2017-06-20
[3] nieuws.kuleuven.be/en/content/2014/students-build-drone-for-transporting-packages/image, last accessed: 2017-06-20
[4] regmedia.co.uk/2015/02/26/skyprowler_teaser.jpg?x=648&y=348&crop=1, last accessed: 2017-06-20
[5] i.ytimg.com/vi/mVovWJA3Fmg/maxresdefault.jpg, last accessed: 2017-06-21

Standardized fuselage with modular airframes
The previous two airframe choices sparked the imagination of the design team. In order to optimize for two missions separately, it was envisioned to integrate a quadcopter and fixed-wing module onto a standardized fuselage that has the capacity to sufficiently power both. With this concept, all essential components would be located within the fuselage. Namely, avionics, payload, batteries, and sensors. All components required for flight, such as actuators and propulsive units would be part of their respective modules. From work done for the preliminary design stage, detailed in [8], the power required to loiter with a fixed-wing was significantly less than for a quadcopter of similar size. Thus if the batteries were sized to sufficiently execute a mission with the quadcopter module, a significantly greater endurance would be observed utilizing the fixed-wing module. The penalty for utilizing this design is that it does not have vertical take-off and landing capability with the fixed-wing module. Additionally, it relies on the operator knowing before-hand the type of mission that is to be flown. For clarification purposes Figure 4.5 shows the initial conceptual sketch for this concept.

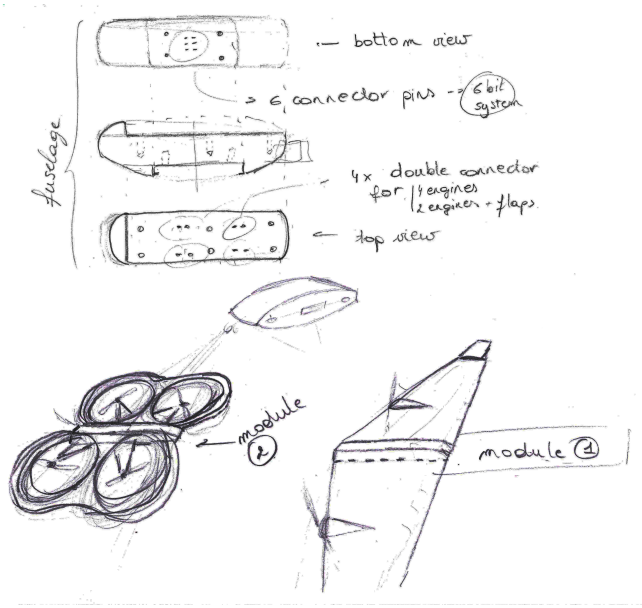

Figure 4.5: Design sketch of the SPARTA modular quadcopter & fixed-wing with standardized fuselage

Concept design option tree and selection
The integration concepts presented previously were put into a design option tree and a discussion was held with the design team. All concepts in the design space were initially deemed feasible for the scope of this project. However, the two integrated design families were rejected since they could not be instantly recognizable as a quadcopter which was the desire of the stakeholders. From a technical standpoint the integrated designs were rejected since the non-detachable lifting surfaces would complicate urban operations by increasing the overall dimensions of the Unmanned Aerial Vehicle (UAV). From literature it is stated that the ideal placement for the camera is at the nose in order to obtain maximum Field of Regard (FOR) [27]. In compliance with this result, with the trust-axis aligned integration, if the camera would be placed placed at the nose, then the FOR would be greatly diminished in hover configuration. This is because the view of the camera would be blocked in nadir direction by the fuselage. On the other hand, if the camera would be placed at the tail the FOR during horizontal flight would be affected as the view of the camera would be blocked in flight path direction by the fuselage. For a surveillance application where targets might be located all around the UAV this type of hindrance is not acceptable. As a result the chosen concept was the standardized fuselage with modular airframes. This concept is new to the market and can be optimized for both missions separately. Also, in quadcopter configuration it complies with the stakeholder requests.

4.1. Initial Sizing

In order to perform the first iteration, it is necessary to determine how to size both the quadcopter and the fixed-wing configuration in such a way that the the two methods are compatible with each other. For the first order iteration, mainly statistical relations are used as well as some simplified technical analysis. This is done for the quadcopter and the fixed-wing module separately. Afterwards, the feasibility of the integration of both designs is checked. Firstly, the quadcopter design is described in Section 4.1.1, after which the methodology as well as the calculations for the fixed-wing design are stated in Section 4.1.2.

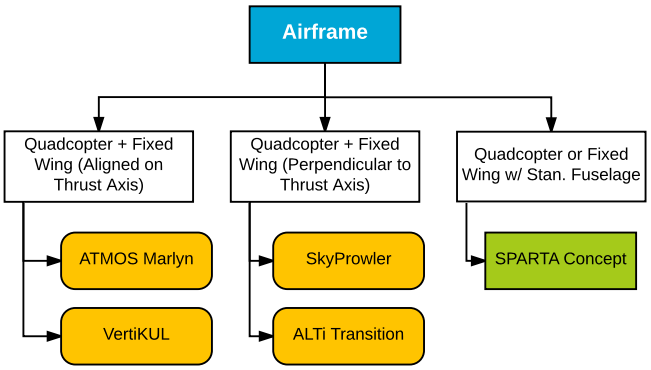

Figure 4.6: Post mid-term airframe design option tree

4.1.1. Quadcopter

First of all, the Maximum Take-off Weight (MTOW) was determined for the quadcopter, based on the statistical relation already determined in [8]. The MTOW was calculated to be 3.6 kg from a known payload of 750 g. Next, an initial selection of a disc loading had to be chosen. A range of 70 N m^{-2} to 165 N m^{-2} was selected, corresponding to propellers with a size of 10 in to 16 in. According to [9, 35], this region is generally used when sizing quadcopters. By writing an optimization program that maximizes the hover power, an initial disc loading of 142.66 N m^{-2} is determined. As the disc loading is known and the MTOW, the disc area is determined to be 0.245 m^2. From this value, it can be calculated that each of the four discs should have a diameter of 11 in Then, the length of the ”arms” of the quadcopter were determined to be 43 cm from statistics, based on the average propeller diameter of 11 in.

Knowing the initial dimensions, the required power is calculated for hovering, forward flight and climbing. Compared to the methodology used in [8], the maximum climb rate and maximum cruise speed were determined from the maximum available power, which is obtained from the selection of an appropriate engine and propeller. The engine is selected from a database consisting of brushless as well as brushed direct current motors. The power for climb, cruise, and descent was determined to be the maximum available power which is equal to 254 W. For hovering a power of 97 W is needed.

This permits the first order calculation of the mass of the quadcopter flying module. Table 4.2 states the resulting initial mass fractions of the quadcopter, which were based on a statistics and the analysis from [8].

The endurance and the range was calculated to be 33.71 min and 20.85 km, respectively. These values need to be optimized as much as possible in the technical analysis. With it, the maximum cruise speed and maximum climb speed were both determined to be 27.0 m s^{-1}. The noise emitted by the quadcopter was estimated from a statistical relation of the *DJI Phantom 3*, during hover this would be 82.43 dBA, and cruise 88.75 dBA at 1 m form the source. From these values, the audible range was calculated to be 41.82 m for hover and cruising it is 86.63 m.

4.1.2. Fixed-wing

The first step to being able to size the fixed-wing is to fix a maximum allowable wing-span such that man-portability would still be feasible. Too big of a wing-span would necessitate having to design a custom backpack to be able to carry the Unmanned Aerial System (UAS) which could potentially increase cost. The inner dimensions of the *Lowe Alpine Saracan* were used. This backpack is the large backpack currently used by the Dutch military and has a height of around 80 cm.[6] To ensure that the design would easily fit in such a space a safety factor of 10 cm was taken on each side to allow for packaging material. Therefore, the maximum allowable span of a wing section would be 60 cm. This corresponds to a wing span, b, equal to 1.8 m for a three-section wing. Furthermore, the choice of a three-section wing was found to be an optimum number since it allows for a center section to be directly attached to the fuselage. An increase in the number of sections would increase overall weight due to an increase in the amount of overlap of material required. Conversely, a decrease to two sections would restrict the portability of the wing as the length per section would increase.

Once this restriction was established, the next step was to utilize the same reference UAVs used in the fixed-wing conceptual design, to construct a statistical relationship between the MTOW and wingspan. Although the R-squared value is not high by any means, it provides a useful initial estimate and starting point for UAVs having an MTOW between 1 kg to 5 kg. As previously stated, from the final iteration value for the quadcopter and fixed-wing sizing, the MTOW was found to be 3.6 kg. Utilizing this relation yields a wingspan of 1.63 m.

[6] `www.outdoorkit.co.uk/product.php?product_id=4618`, last accessed: 2017-06-23

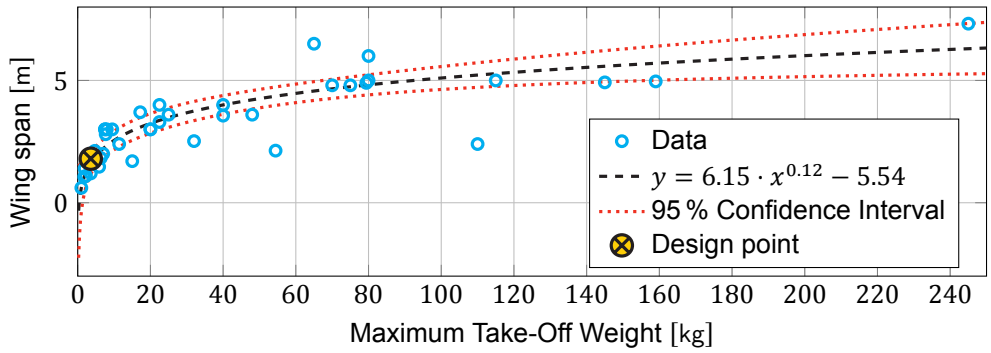

Figure 4.7: Correlation between wing span as a function of MTOW $(R^2 = 0.71)$

Assumptions

Using the derived weight estimate and wingspan as a starting point the following assumptions were then made to progress further in the initial sizing process:

FW-SA-I	The UAV is in a steady-symmetric flight regime $(L = W)$ $(T = D)$, no side-slip $(\beta = 0)$.
FW-SA-II	The wing is rectangular and has no taper.
FW-SA-III	Propeller efficiency is constant and does not vary with airspeed.
FW-SA-IV	Efficiency of the propulsion system is constant.
FW-SA-V	Total energy capacity of the battery is constant and independent of power draw.
FW-SA-VI	The non-propulsive power draw of the UAV is at maximum 25 W.
FW-SA-VII	The max C_L of 1.5, corresponding to a home-built aircraft, is attainable [62, p. 84].
FW-SA-VIII	The maximum negative lift coefficient, $C_{L_{\min}}$, -0.6 is attainable.
FW-SA-IX	The lift coefficient gradient, C_{L_α}, of the wing is equal to that of a symmetric thin airfoil (2π) [3].
FW-SA-X	The Oswald efficiency factor is roughly 0.8 for moderate aspect ratio wing [62, p. 81].

Optimum aspect ratio and wing loading

For the scope of this project the optimum aspect ratio is defined as the point that balances aerodynamic performance with high-lift capability. In essence, an increase in aspect ratio yields a slight increase in parasitic drag but a greater decrease in lift-induced drag. Therefore, increasing aspect ratio can be seen as being analogous to increasing aerodynamic performance expressed by the lift to drag ratio (LD). However, since the UAV is limited in wing-span due to portability constraints an increase in aspect ratio also decreases the surface area of the wing. This increases wing-loading and stall speed. Since it was determined previously that a three-piece wing has a maximum allowable wing-span of 1.8 m, utilizing this dimension to the fullest extend would yield the lowest possible stall-speed while maximizing aerodynamic performance. As a result, iterating through Equations (4.1) to (4.3) resulted in obtaining an optimum aspect ratio $A = 7$. This corresponded to a wing loading, $W/S = 76.27\,\mathrm{N\,m^{-2}}$ and a stall speed V_{stall} of $\approx 9\,\mathrm{m\,s^{-1}}$

$$S = \frac{b^2}{A} \qquad (4.1) \qquad V_{\text{stall}} = \sqrt{\frac{W}{S}\frac{2}{\rho_0}\frac{1}{C_{L_{\max}}}} \qquad (4.2) \qquad K = \frac{1}{\pi A e} \qquad (4.3)$$

Drag estimation

In order to get an approximation for the zero-lift/parasite drag, C_{D_0}, in the early stages of the design statistics can be used. These statistics utilize relations correlating the MTOW to the wetted surface area, S_{wet}, and later utilizing this value to obtain the equivalent parasite drag area, f. These relations are presented by Equations (4.4) and (4.5) [62, p. 83].

$$S_{\text{wet}} = 10^{1.23+0.43\cdot\log_{10}(2.20\cdot W_{TO})} \qquad (4.4) \qquad f = 10^{-2.70+\log_{10} S_{\text{wet}}} \qquad (4.5)$$

Next, after obtaining the equivalent parasite drag area, the calculation of, the zero-lift/parasite drag is relatively straightforward by utilizing Equation (4.6).

$$C_{D_0} = \frac{0.093 \cdot f}{S} \qquad (4.6)$$

Power loading and motor selection

In order to determine the required shaft power the engine of the UAV must generate the critical power-loading constraint is derived from the climb gradient must be utilized. The climb gradient requirement set out in [8] of avoiding a 10 m building at a distance of 17 m was relaxed due to urban missions being handled with the quadcopter mission. Therefore, a new requirement was necessary and the climb gradient of 0.12 was used, corresponding to the requirement set out by CS-23 specifications for low speed airplanes [25, p. B-2]. This constraint has been placed such that the fixed-wing UAV has the ability to be launched from a urban setting. The final power-loading constraint is derived from the the rate of climb requirement of 1.524 m s^{-1} at an altitude of 3000 m **SPARTA-UAV-1.1.2**. Thus these requirements can be translated into power loading, P/W, utilizing Equations (4.7) and (4.8). Equation (4.7) shows the relationship for the rate of climb requirement, with the rate of climb at ceiling altitude as defined in **SPARTA-UAV-1.1.2**. Equation (4.8) is the final critical constraint that needs to be taken into account. The lift coefficient (C_L) is equal to the maximum lift coefficient ($C_{L_{\max}}$) with a margin of 0.2. After the power loading is obtained, the MTOW can be used along with an assumed propeller efficiency η_{prop} of 0.6, to find the power required from the motor.

$$\left(\frac{W}{P}\right)_{CR} = \frac{\eta_{\text{prop}}}{RC + \sqrt{\frac{W}{S}\frac{2}{\rho_{\text{ceil}}}\frac{\sqrt{C_{D_0}}}{1.81(Ae)^{\frac{3}{2}}}}} \tag{4.7}$$

$$\left(\frac{W}{P}\right)_{CG} = \frac{\eta_{\text{prop}}}{\sqrt{\frac{W}{S}}\left(CG + \frac{C_D}{C_L}\right)\sqrt{\frac{2}{\rho_0}\frac{1}{C_L}}} \tag{4.8}$$

Power required depending on airspeed

The next step in the sizing of the fixed-wing is to compute its power required as a function of airspeed. This can be done by first computing the required lift coefficient, C_L as a function of equivalent airspeed, V_{EAS}, Equation (4.9). Following from this, the drag coefficient, C_D, can also be expressed as a function of the equivalent airspeed, Equation (4.10).

$$C_L = \frac{2 \cdot W}{\rho_0 V_{\text{EAS}}^2 S} \tag{4.9}$$

$$C_D = C_{D_0} + K C_L^2 \tag{4.10}$$

Now that the drag coefficient at various equivalent airspeeds is known, the power required, P_{R}, can be computed utilizing Equation (4.11)[62, p.89]. Equation (4.12) converts Equation (4.11) to provide functionality to compute the power required at varying altitudes.

$$P_{\text{R}} = \frac{C_D}{2}\rho_0 V^3 S \tag{4.11}$$

$$P_{\text{R}} = C_D\sqrt{\frac{\rho_0^3}{4 \cdot \rho}} V_{\text{EAS}}^3 S \tag{4.12}$$

Furthermore, the components of drag, namely zero-lift/parasite drag and lift-induced drag, can be used in Equation (4.11) to express their contribution to the power required. In essence, at lower velocities the lift-induced drag comprises most of the power-draw while at higher velocities the zero-lift/parasite drag makes up a significant portion of the total power draw. Finally, multiplying the total power output of the motor by the propeller efficiency and electric system efficiency produces a constant power available line. The result of these computations are provided by Figure 4.8.

Figure 4.8 also yields optimal and maximum airspeeds. The airspeed corresponding to minimum power required results in the largest endurance. In this analysis this value was found to be 33 W at an equivalent airspeed of 11.5 m s^{-1}. However, this is too close to the stall speed that was calculated previously and thus a buffer is required. 5 m s^{-1} is taken for the value of this buffer. This results in a loiter velocity around 15 m s^{-1}. Finally, the maximum velocity is found by intersecting the burst power available line with the power required lines and is equal to 33 m s^{-1}.

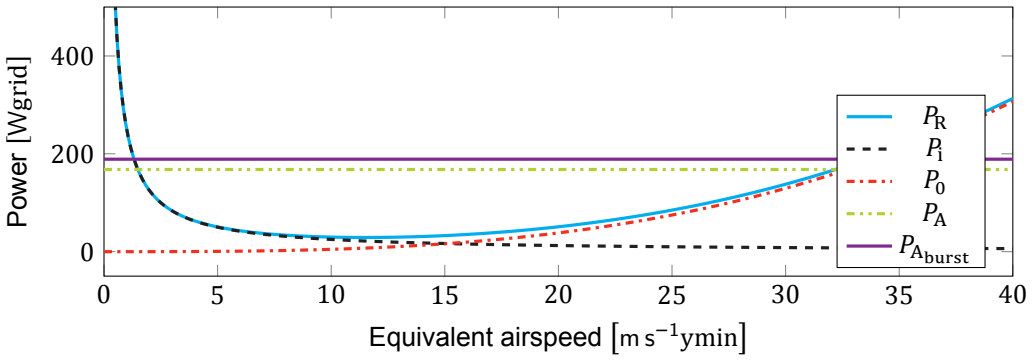

Figure 4.8: Power required and available as a function of equivalent airspeed

Flight envelope

Even though the Surveillance Platform for Aerial Reconnaissance and Target Acquisition (SPARTA) UAV is primarily designed for the Royal Netherlands Air Force, in the future its use might spread to the commercial market. Therefore, to future proof the design and ensure compliance with civil aviation authorities the current state of their regulations must be analyzed. In Europe, the present state of legislation by the European Aviation Safety Agency (EASA) is in the consultation phase [23, p. 1]. The aim of this legislation is to reduce air risk and ground risk that UASs pose and thus is primarily focused on placing operational constraints on UAVs. On the other hand a policy statement published by EASA for the airworthiness certification of UASs aims to classify UAVs under pre-existing CS guidelines based on impact energy [21, p. 13]. Two situations exist for classifying the impact energy: the unpredetermined descent scenario utilizes the stall speed of the aircraft along with the MTOW to assess the impact energy, the loss of control scenario utilizes the maximum speed of the aircraft along with the MTOW to assess the impact energy. To simplify the analysis the critical case, which is the loss of control scenario will be used to classify the SPARTA UAV. This can be done by substituting the previously calculated maximum velocity of 33 m s^{-1} into Equation (4.13) [21, p. 14].

$$\text{Kinetic energy} = \frac{W_{TO}\left[1.4 \cdot (0.51 \cdot V_{\max})\right]^2}{10^9} \tag{4.13}$$

The result of Equation (4.13) shows that the SPARTA UAV has a minuscule impact energy which was to be expected due to its relatively small sized when compared to manned aircraft. However, the microlight category which it would fall under does not contain as detailed legislation as the CS-VLA (Very Light Aeroplane) category when it comes to generation of the maneuver and gust loading diagrams. Therefore, for the purpose of this analysis the legislation for CS-VLA will be used. This legislation dictates that the maximum positive load factor, $n_{\max}$, cannot be less than 3.8 and that the minimum negative load factor, $n_{\min}$, cannot be less than -1.5 [22, p. 1-C-3]. Furthermore, the legislation provides the minimum allowable maneuver (V_A), cruise (V_C), and dive speed (V_D) presented by Equations (4.14) to (4.16).

$$V_A \geq \sqrt{n_{\max}} \tag{4.14}$$

$$V_C \geq 2.4 \times \sqrt{W/S} \tag{4.15}$$

$$V_D \geq 1.4 \times V_C \tag{4.16}$$

After these speeds are determined the maneuvering diagram can be generated utilizing the assumed maximum and minimum lift coefficients. Equation (4.17) presents the relation for creating the curved section of the maneuvering diagram as a function of equivalent airspeed. Legislation also states that the UAV must withstand a vertical gust load of 15.24 m s^{-1} at cruise velocity and of 7.62 m s^{-1} at dive velocity [22, p. 1-C-2]. With these values the gust gust loading diagram can be generated utilizing Equations (4.18) to (4.20). Note that the critical case for gusts occurs at service ceiling where the air density is lowest since the gust alleviation factor, K_g, increase with altitude. Thus, at the service ceiling of 3000 m (**SPARTA-UAV-1.3.1**) gust speed will be maximum.

$$n_{[\max,\min]} = \frac{\rho_0 V_{\text{EAS}}^2 C_{L_{[\max,\min]}} S}{2g \cdot W_{TO}} \tag{4.17}$$

$$\mu_g = \frac{2 \cdot (W_{TO}/S)}{\rho \bar{c} C_{L_\alpha}} \tag{4.18}$$

$$K_g = \frac{0.88 \cdot \mu_g}{5.3 + \mu_g} \tag{4.19}$$

$$n = 1 + \frac{\rho_0 V_{\text{EAS}} C_{L_\alpha} K_g U}{W/S} \tag{4.20}$$

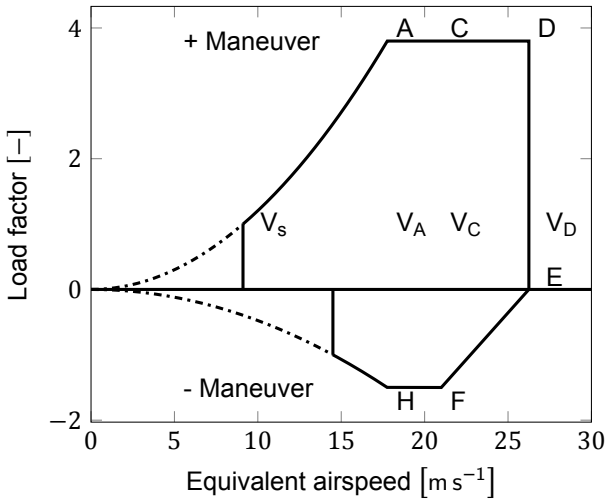

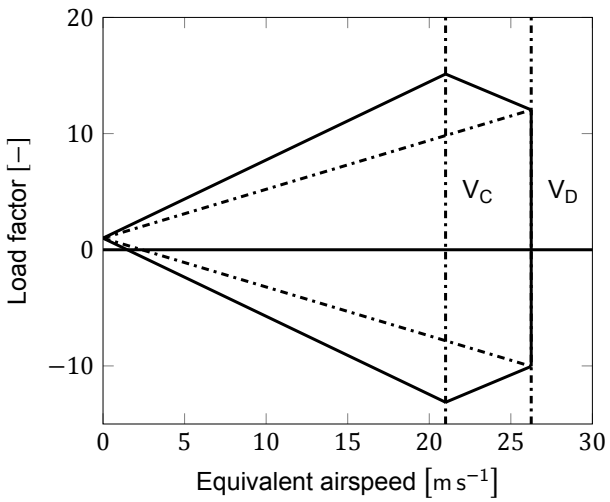

Range and endurance
Finally, after obtaining the required minimum cruise velocity from [22] the endurance and range of the UAV can be calculated, using Equations (4.21) and (4.22) respectively. This endurance is defined as the total flight time achievable at loiter velocity while maintaining a constant flight path. The resulting range and endurance for the fixed-wing design is therefore given by Equation (4.22) and Equation (4.21) respectively. The initial sizing yields an endurance of 2.7 h and a range of 146 km which is comfortably above the 2 h endurance requirement (**SPARTA-UAV-3**)

$$\text{Endurance} = \eta_{\text{prop}}\eta_{\text{elec}}\frac{E_{\text{bat}}}{P_{R_{\text{loiter}}} + P_{PL}} \quad [\text{h}] \quad (4.21) \qquad \text{Range} = 3.6 \cdot \frac{\eta_{\text{prop}}\eta_{\text{elec}}E_{\text{bat}}}{P_{R_{\text{cruise}}} + P_{PL}}V_{\text{cruise}} \quad [\text{km}] \quad (4.22)$$

Preliminary mass breakdown
The final overview of the preliminary design can be seen in Table 4.2. This indicates the different UAV elements and their assigned maximum mass. The first three elements were found using the preliminary sizing method. The weight of the aerodynamic surfaces was found using statistical relationships and literature on their normal mass.

Table 4.2: Preliminary mass breakdown of both configurations

	Parameter	Value	Unit
Overall mass breakdown	MTOW	3.6	kg
	Payload	0.75	kg
	Battery	1.5	kg
Fixed-wing configuration	Aerodynamic surfaces	0.72	kg
	Fuselage and miscellaneous	0.63	kg
Quadcopter configuration	Aerodynamic surfaces	0.5	kg
	Fuselage and miscellaneous	0.65	kg

Verification
The initial sizing code was written in *MATLAB* and its inherent syntax checking capabilities were used to eliminate errors. Also, individual arrays were checked to make sure they have the correct magnitude and follow the expected trend. All calculations were verified by cross-referencing typical values to act as a sanity check. For example, the maximum take-off weight of the *RQ-11 Raven* was used to check the derived empirical relations. The result was an estimation of 1 m while the actual value of the RQ-11 Raven's wing span is 1.4 m. This inaccuracy is due to the presence of larger UAVs which have much higher wing loading values and thus shorter wing-spans when compared to their maximum take-off weight. For rectangular wings, while keeping aspect ratio constant, an increase in span yields a quadratic increase in wing surface area. This coupled with large aircraft having higher stall speeds results in the non-linear distribution seen in Figure Figure 4.7. Eventually, this inaccuracy was avoided by not using the wing-span value given by empirical relations but rather to use the maximum allowable wing-span that can still fit in a backpack.

I-5

Final Design Characteristics

This chapter presents the final characteristics of the Unmanned Aerial System (UAS) Surveillance Platform for Aerial Reconnaissance and Target Acquisition (SPARTA). This section gives a general overview of the detailed treatment of subsystems and components, that was done in the subsystems analysis chapters. The aim of this chapter is to present the current state of the SPARTA design.

5.1. General Configuration

The SPARTA UAS includes both Unmanned Aerial Vehicle (UAV) and the ground station. To fulfill various mission needs the UAV is capable of two default configurations; a fixed-wing one for long missions Figure 5.1a and a quadcopter for closer observation missions Figure 5.1b. Both fixed-wing and quadcopter module are attached to the core using slide and click mechanism on the opening on the top of the core module. The interface of the connection is the same for both configurations. The connection is capable of providing both power and control to modules inside the wing over contact pins.

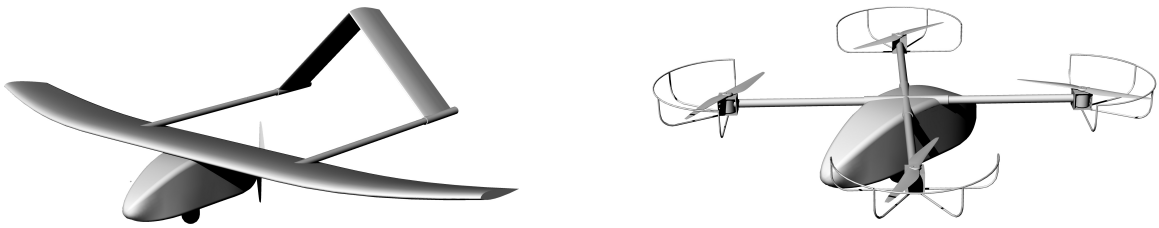

(a) The fixed-wing configuration

(b) The quadcopter configuration

Figure 5.1: The general UAV configurations

Both configuration are based on the same core module seen in Figure 5.2. The module consists of avionics, batteries and the payload and payload bay as seen in the Figure 5.2. Most of internals such as batteries and payload are modular and can thus be taken out and replaced on demand. The general configuration backpack will carry batteries for 5 missions. The replacement of batteries can be achieved similarly to the wing module and payload bay; by click and remove snap-fit. The payload module is hosted inside the payload bay which is rigidly connected to the core module structure. On the other hand the avionics and electronics can be reached through the wing attachment opening. The electronics include *D0 Nano FPGA board* for hardware drivers and control. The control algorithms and autopilot lives on *PixHawk* module that is connected to D0Nano board. The *PixHawk* unit includes 3-axis gyro, a magnetometer compass, and internal accelometer. The *SuperBat2624 di-pole antenna* is placed on the bottom of the core module and can be bended to be oriented along side the body so it does not restrict the take-off and landing.

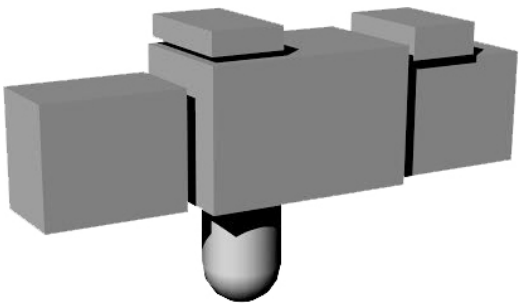

Figure 5.2: Core internals with outer skin removed

The fixed-wing configuration consists of the main-wing two-boom body and an A-tail. The two boom body was chosen so that a nested engine could be used. Furthermore, the choice offers less pitching moment due to engine position relative to center-line. The basic sizing is presented in Figure 5.3. The fixed-wing configuration is ideal for the long endurance mission. With the maximum payload it can achieve more that 2.6 hours of flight. It possesses a detect-and-avoid system with evasive maneuver algorithms to increase the UAV survivability. The takeoff is hand assisted and landing is carried out by skidding on the ground.

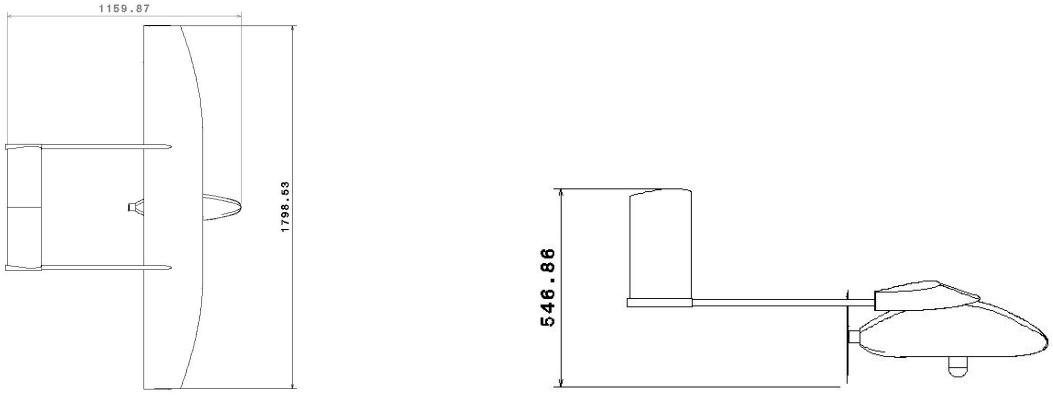

(a) Top view (b) Side view

Figure 5.3: The fixed-wing layout and overall size

The quadcopter configuration is based on a simple square frame hosting the engines and other electronics. The motors have additional protection using the semi-closed fan protection. The basic sizing can be seen in Figure 5.4. This configuration excels at proximity flying in tight spaces where the control must be fast and reliable. The UAV is equipped with 6 sonar modules and two fish-eye cameras to provide a reliable detect-and-avoid system. The maneuvers are achieved using differential thrust and are controlled by the core controller. Both take-off and landing are vertical and require minimal space.

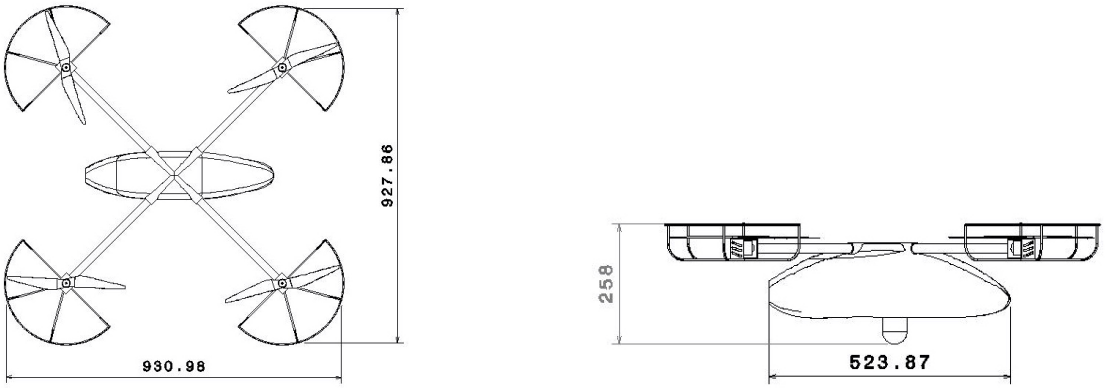

(a) Top view (b) Side view

Figure 5.4: The quadcopter layout and overall size

5.2. General Performance Characteristics

The SPARTA UAV has been optimized for performance in various low-altitude flying conditions. The final design performance characteristics can be seen in Table 5.1. The values were calculated for sea-level conditions with nominal environment and assuming maximum payload. Performance can be further increased by optimizing the payload based on the mission requirements. Such as taking less payload and more batteries if long endurance mission is needed. For the fixed-wing this means 0.52 kg extra and for the quadcopter 0.59 kg. Which means a maximum extra endurance of approximately 30 % for both configurations.

Table 5.1: Final characteristics for both configurations

	Quadcopter		Fixed-wing	
Final characteristics	**Value**	**Units**	**Value**	**Units**
Propulsion				
Blades no.	2	-	2	-
Diameter	13	in	10	in
Pitch	8	in	10	in
Rotor type	RimFire.10	-	RimFire.10	-
Aerodynamic				
Airfoil	USNPS4	-	NACA 22112	-
Inaudibility	70	m	10	m
Performance				
Endurance	1.7	h	2.4	h
Range	24.7	km	99.9	km
Wing loading	-	-	94.5	$N\,m^{-2}$
Power loading	-	-	0.158	$W\,kg^{-1}$
Disc loading	102.4	$N\,m^{-2}$	-	-
Max cruise speed	21.7	$m\,s^{-1}$	30.5	$m\,s^{-1}$
Max climb speed	15.4	$m\,s^{-1}$	6.2	$m\,s^{-1}$
Max L/D	-	-	11.68	-

I-6

Compliance Matrix

The aim of this chapter is to determine whether the final design is able to meet the requirements set during the requirements analysis which were subsequently validated by the customer. Firstly, it is necessary to give an overview of any changes in the requirements, which is done in Section 6.1. Afterwards, the compliance matrix is given in Section 6.2. Lastly in Section 6.3 a feasibility study is performed to determine if the requirements which were not met, will impact the functionality of the Unmanned Aerial Vehicle (UAV) or the customer satisfaction.

6.1. Requirements Update

Firstly, it is necessary to update certain requirements, as a meeting with the client was held to validate certain requirements. During that meeting, some requirements were also added or removed. The following section will state all altered requirements.

SPARTA-UAV-1.1 The requirement for a certain vertical force was not necessary, as the climb rate of the UAV already had to be calculated. Therefore, this requirement, as well as the subrequirements were removed. In its place the requirement **SPARTA-UAV-1.1** was refined to include the climb rate.

SPARTA-UAV-1.2.1, SPARTA-UAV-1.2.2 To still be able to communicate with the ground station, as well as have a constant downlink, a Signal to Noise Ratio (SNR) of 10 dB and a bit rate of 400 $\mathrm{Mbit\,s^{-1}}$ was needed.

SPARTA-UAV-2 Based on the input gathered by the customer, the UAV will be deployed at maximum 6 km away from the point of interest, influencing the minimum range of the UAV. It thus changed to 12 km.

SPARTA-UAV-3 In the same manner, the loiter time of 2 h was reduced to encompass the full endurance of the system.

SPARTA-UAV-4 The requirement for the operational temperature range of −20 deg to 60 deg for operation is altered. This range is based on the degradation of battery performance with temperature, the maximum temperature of the engines and that of the hardware.

SPARTA-UAV-17 From the market research it became apparent that the payload modules would be extremely costly. Due to this, the requirement for the recurring cost per aircraft was changed. The new requirement only takes into account the recurring cost per vehicle, and does not include the payload module.

SPARTA-UAV-19, SPARTA-UAV-20 From the input gathered by the customer, it was decided that there would be 3 extensions of the default UAV configuration, with at least a payload capability of 3 sensors.

6.2. Compliance Matrix

In this section the compliance matrix is found, which determines if the final design is able to meet the requirements. This is based on the requirements set by the customer and the technical analysis of the final design, which can be found in Section 6.3. In some cases it is unclear if a certain requirement was met or not, as the level of detailed of some was too great for the scope and time frame of this project. In that case, To Be Determined (TBD) is put into Table 6.1. If a requirement has been met (✔) was used as symbol, if it is not the (✘) symbol was placed.

For the requirements for which a number determines whether or not they are complied with, the value is shown. For a requirement, for which a numerical value could not disclose whether it complies or not, a qualitative evaluation is given.

SPARTA-UAV-7 During day and night the UAV should be operable and this has been kept in mind while choosing the camera.

SPARTA-UAV-12 The UAV has been designed such that a collision avoidance system is present.

SPARTA-UAV-13 The database of REACH has been consulted and all of the materials that are used in the final product comply.

SPARTA-UAV-17 The total cost of the Unmanned Aerial System (UAS), which includes the fuselage, one quadcopter module, one fixed-wing module and the ground station is equal to €26 500.

SPARTA-UAV-19 This requirement has been met. The UAV is able to carry more than three sensors simultaneously as described in Chapter 14.

6.3. Feasibility Study

The feasibility study is performed to clarify why certain requirements could not be met, or why some are yet to be determined. This is to give the client a better understanding of the significance of certain requirements.

SPARTA-UAV-1 The service ceiling of 3000 m could not be met by the quadcopter. Instead the service ceiling is approximately 1000 m. However, the quadcopter is designed for the short range mission (Figures 2.1c and 2.1d) and is therefore not critical fail of a requirement. This would be critical as long as the fixed-wing reaches the ceiling.

SPARTA-UAV-4 The thermal requirement that states the UAV should be operable between −20 °C to 60 °C could not be evaluated due to it being out of the scope of this project. However, this is an analysis that should be performed in the future.

SPARTA-UAV-5 Critical elements for dusty environments are the connectors and attachment points for the UAV. This is something that is difficult to model and should be tested once the attachments and connectors have been set-up.

SPARTA-UAV-6 For this requirement, the same holds as for **SPARTA-UAV-5**. The easiest way of determining the structure for salt permeability is by testing and can be done once the UAV has been constructed.

SPARTA-UAV-8 A quadcopter is designed to hover so its ability to fly in urban environment is self-evident. However, this is not the case for the fixed-wing configuration as it is designed for the long range loitering mission (Figures 2.1a and 2.1b). As long as the quadcopter satisfies this requirement there is no critical noncompliance of this requirement.

SPARTA-UAV-9 This requirement relates to **SPARTA-UAV-6**, it concerns the controllability of the UAV in tight spaces. And since the fixed-wing configuration is not able to hover in a box of 2x2x2 m, this requirement is not met. However, since the quadcopter is designed for these kind of missions and meets this requirement, it is not critical for the fixed-wing to meet this requirement.

SPARTA-UAV-11 Unfortunately the structural analysis could not be performed in the desired detail. Although impact could be analyzed analytically, constructing a prototype and testing the UAV for its resistance against a 3 m fall is the best way to make sure this requirement is met or not.

SPARTA-UAV-22 This requirement has not been analyzed yet and is to be determined in the future developments phase.

SPARTA-SYS-4 The analysis of the maintenance cost has not been performed yet since there are a lot of types of maintenance. This will be analyzed in the next phase.

SPARTA-SYS-5 The cost of obsolescence upgrades are not yet determined and will be done in the future design.

As can be derived from the explanations given above, the compliance of a lot of requirements have not yet been determined. This is due to the fact that for a lot of requirements further detailed design is necessary. The analyses that have been performed do not have the amount of depth that is required in order to determine whether UAS complies with the requirements comply or not.

Table 6.1: Compliance matrix for the final design

Identifier	Requirement	Compliance	
		Quadcopter Module	Fixed-wing Module
Unmanned Aerial Vehicle			
SPARTA-UAV-1	The UAV shall have a service ceiling of 3000 m above sea level when flying with standard configuration in ISA conditions.	✖ 1353 m, Section 9.3.3	✔7479 m, Section 9.4.3
SPARTA-UAV-2	The UAV shall have a range of at least 12 km.	✔24.7 km, Section 9.3.3	✔99.9 km, Section 9.4.3
SPARTA-UAV-3	The UAV shall have a total endurance time of at least 2 h.	✖ 1.7 h, Section 9.3.3	✔2.4 h, Section 9.4.3
SPARTA-UAV-4	The aircraft shall be fully operational between −20 °C to 60 °C.	TBD	TBD
SPARTA-UAV-5	The UAV shall be operable in dusty environment.	TBD	TBD
SPARTA-UAV-6	The UAV shall be operable in salty environment.	TBD	TBD
SPARTA-UAV-7	The UAV shall be operational during day and during night.	✔	✔
SPARTA-UAV-8	The UAV shall be able to fly in an urban environment.	✔	✘
SPARTA-UAV-9	The UAV shall be operable in a box of 2x2x2 m.	✔	✘
SPARTA-UAV-10	The UAV shall have a noise level of at most 50 dBA at a distance of 300 m.	✔38.6 dBA, Table 10.14	✔23.8 dBA, Table 10.15
SPARTA-UAV-11	The UAV shall be able to withstand a fall of 3 m onto concrete without taking damage.	TBD	TBD
SPARTA-UAV-12	The UAV shall have an integration of a collision avoidance system.	✔	✔
SPARTA-UAV-13	The UAV shall be made up of materials according to the REACH requirements.	✔	✔
SPARTA-UAV-14	The UAV shall be recyclable for 60 % of the weight.	✔	✔
SPARTA-UAV-15	The UAV shall have a volume of at most 120 L.	✔78.1 L, Section 17.4	✔78.1 L, Section 17.4
SPARTA-UAV-16	The UAV shall have an aircraft mass of at most 50 kg.	✔3.57 kg, Section 19.1	✔4.43 kg, Section 19.1
SPARTA-UAV-17	The recurring cost per aircraft shall be less than €25 000 for a series of 100 UAVs.	✔	✔
SPARTA-UAV-18	The UAV shall have a lifetime of 5 years or 5000 flight cycles, whichever comes first.	✔	✔
SPARTA-UAV-19	The UAV's assembly shall be able to carry at least 3 sensors simultaneously.	✔	✔
SPARTA-UAV-20	The UAV shall have at least 3 extensions of the default configuration.	✔	✔
SPARTA-UAV-21	The UAV shall have a visual uplink that is real time.	✔	✔
SPARTA-UAV-22	The UAV shall have an emergency landing capability.	TBD	TBD

Ground Station			
SPARTA-GRO-1	The ground station and aircraft support gear shall have a mass of at most 50 kg.	✔	✔
SPARTA-GRO-2	The ground station and aircraft support gear shall have a volume of at most 120 L.	✔	✔
SPARTA-GRO-3	The recurring cost per ground station shall be less than €100 000 for a series of 100 UAVs.	✔	✔
System			
SPARTA-SYS-1	The non-recurring cost for the full program shall be less than €10 000 000.	TBD	TBD
SPARTA-SYS-2	Half of the sum of the recurring and non-recurring cost shall be attributed to Dutch companies, institutes or universities.	TBD	TBD
SPARTA-SYS-3	The maintenance of the full UAS shall be performed at Logistiek Centrum Woensdrecht.	✔	✔
SPARTA-SYS-4	The maintenance cost shall be lower than 5 % of the aircraft cost.	TBD	TBD
SPARTA-SYS-5	The maintenance cost excludes obsolescence upgrades.	TBD	TBD
SPARTA-SYS-6	The total required assembly time from a backpack shall be less than 10 min.	✔	✔
SPARTA-SYS-7	The system shall comply with the EMACC regulations.	✔	✔
SPARTA-SYS-8	The UAS shall be able to be carried by two infantrymen in two standard army backpacks.	✔	✔
Payload			
SPARTA-PAY-1	The payload exchange shall be able to be carried out by a single operator in field.	✔	✔
SPARTA-PAY-2	The payload exchange shall be able to be carried out in less than 10 min.	✔	✔
SPARTA-PAY-3	The payload exchange shall be able to be carried out with a basic tool set that is portable in a backpack.	✔	✔
SPARTA-PAY-4	The sensor modules shall have a standardized setup.	✔	✔

II

Technical Analysis

II-7

Payload Analysis

The most important part of the Unmanned Aerial Vehicle (UAV) is to fulfill the mission for the military, which is done with the use of payload bays in the UAV. This bay is a specific place in the fuselage where different payload modules can be placed. For the analysis of these payload modules, the final dimensions will first be given in Section 7.1 as it is necessary for the overall design of the bay. They are found using the final values that were used during the conceptual design of the UAV. Then the final camera specifications will be given in Section 7.2. Finally, the overall payload bay will be structurally designed in Section 7.1, such that it will be able to fulfill all the requirements.

7.1. Payload Characteristics

The overall characteristics of the payload are stated in Table 7.1. These include the sizing information from the conceptual phase of the maximum payload mass and power draw. Which were used for their respective final budgets. Furthermore, the final dimensions of the payload bay are also given in the table. This is necessary to fit the payload bay into the fuselage, as the latter will need to be optimized to reduce the fuselage drag.

Table 7.1: Resource allocation of the payload module from the conceptual design analysis [8]

Mass	0.75	[kg]
Dimensions	$113 \times 60 \times 78$	[mm]
Power	12	[W]

There will be two specific modules: one for the fixed-wing option of the UAV and one for the quadcopter configuration. This is done due to the inherently different goals of the long range and the urban mission. The former will need a better camera and can also benefit from having a cellular signal activity monitoring sensor, as it could detect possible rural locations of targets. The latter does not necessarily need a camera with a big observation range, as the quadcopter will mainly fly in urban areas. This leaves space for other payload such as an electromagnetic sensor or a biochemical sensor to prevent most types of attacks when the troops are in enemy locations. On the other hand, additional batteries can be mounted in the case an extended mission is needed.

7.1.1. Final recommended payload modules

Different payload modules can be recommended with the preliminary payload constraints. These depend on the configuration of the UAV. The final recommendation of the fixed-wing design can be found in Table 7.2. This design has to fulfill a relatively long range mission with a high endurance and at an altitude of around 100 m. This means that useful payload configurations have to be chosen conformingly. In this case it would mean a camera, the *SPI M2-D* and a cellular activity monitoring sensor, the *HackRF One*. The former is chosen because it is the only military graded camera found under the allowed mass budget of 0.75 kg. It also ensure operations in both day and night, as it has electro-optical and infra-red imaging systems. The latter because it still fits in the mass and power budget of the payload bay and has a high frequency range of 1 MHz to 6000 MHz.[1] Instead of taking this last sensor, the military can also choose to take an extra set of lithium polymer batteries with them to increase the UAV endurance with 30 %, calculated by adding the extra battery mass and recalculating Equation (4.21).

The final suggestion for the quadcopter configuration and thus the short range urban mission can be found in Table 7.3. The biggest difference between this recommended payload and Table 7.2 is the cellular activity monitoring sensor that is replaced by the biochemical sensor. The latter one is chosen as it would aide the soldiers more in an urban setting, whenever there is a (biochemical) attack. For this, the *Orion Multigas* was chosen as it was again the only sensor that complied to the resource allocation.

[1] greatscottgadgets.com/hackrf/, last accessed: 2017-06-30

Table 7.2: Final recommendation of the payload module for long range mission

	Sensor type	Mass [kg]	Dimensions [mm]	Power [W]
SPI M2-D	Camera	0.16	53 × 53 × 78	10
HackRF One	Cellular activity	0.1	25 × 39 × 53	4.6
OR				
LiPo batteries	Battery	0.52	70 × 60 × 60	-
Total	-	**0.75**	**113 × 60 × 78**	**13.6**

Table 7.3: Final recommendation of the payload module for short range urban mission

	Sensor type	Mass [kg]	Dimensions [mm]	Power [W]
SPI M2-D	Camera	0.16	53 × 53 × 78	10
Orion Multigas	Biochemical	0.45	165 × 91 × 66	-
OR				
LiPo batteries	Battery	0.59	80 × 60 × 60	-
Total	-	**0.75**	**113 × 60 × 78**	**10**

7.2. Camera Specifications

The most important aspect of the mission is targeting, for which a camera is needed. Therefore, the operability of the camera has to be assessed. This is done by first determining what targeting is exactly.

The photographic range is necessary to find the minimum range where the UAV needs to be inaudible during night- and day-time operations. In order to determine this range the different degrees of imaging a target need to be defined. Besides a quantified expression needs to define the usefulness of information. For this, imaging is normally divided in three parts: detection, recognition, and identification. The Johnson's Criteria quantifies the amount of pixels needed for these three, and links the angular size of the target to the amount of pixel bars necessary to still identify the target. The point where there are not enough bars in an image made from further away, is the identification range. The Johnson's Criteria deals with the probability of a human operator successfully completing detection, recognition, and identification tasks for a target of critical dimensions [37]. In case of identification the necessary critical dimensions are the ones that correspond to a image of a human target. This means that the critical target height (h_{target}) and width (w_{target}) are equal to 1.8 m and 0.5 m [37]. With this the critical dimension is equal to 0.95 m by using Equation (7.1).

After this, the Instantaneous Field Of View (IFOV) also needs to be calculated by using Equation (7.2)[2]. The IFOV is the minimum area the camera can still detect in an image, expressed in mrad. In Equation (7.2) the Wide Field Of View (WFOV) is equal to 30 deg and the number of pixels in that direction (N_{pixel}) is 640[3], the second fraction is to convert it to mrad. The outcome of is an IFOV of 0.87 mrad at night and 0.72 mrad during the day.

$$\text{Critical dimension} = \sqrt{h_{\text{target}} w_{\text{target}}} \quad [37] \quad (7.1)$$

$$\text{IFOV} = \frac{WFOV}{N_{\text{pixel}}} \frac{\pi}{180 \cdot 1000} \quad (7.2)$$

The outcome of Equation (7.3) is the number of required pixels per meter in the plane of the target (PPM). It is calculated by taking two times the number of required cycles (N_{cycle}) equal to 6 and dividing it by the critical dimension found in Equation (7.1). N_{cycle} is the amount of pixel bars needed to identify a target correctly with a probability of success of 50 % [37] and is again derived from the Johnson's Criteria. The final outcome is a PPM of 12.6. Finally, by using Equation (7.4) one finds a camera range equal to 110 m during daytime operations and 91 m during night.

$$\text{PPM} = \frac{2 \cdot N_{\text{cycle}}}{\text{Critical dimension}} \quad [37] \quad (7.3)$$

$$\text{Camera range} = \frac{1000}{\text{PPM} \cdot \text{IFOV}} \quad [37] \quad (7.4)$$

[2] www.ircameras.com/support/calculators/ifov-calculator/, last accessed: 2017-06-18

[3] www.x20.org/m2-d-mini-gyro-stabilized-eoir-uav-uas-multicopter-drone-flir-thermal-imaging-camera-turret-ball/, last accessed: 2017-06-15

II-8

Modularity Analysis

To comply to both the assembly requirement of 10 min and the portability requirement of the Unmanned Aerial Vehicle (UAV), a modularity analysis has to be performed. First, the modularity of the design will be discussed in Section 8.1. Next, Section 8.2 includes an analysis on modular fasteners, as these components connect the different parts of the UAV.

8.1. Design Modularity

The design philosophy is to have one common fuselage and two completely different flying modules for the different mission stated in Section 2.1. The fixed-wing configuration is optimized for long range flight with high endurance, and the quadcopter module for short range urban support missions. To comply with the portability requirement the UAV and ground station have to fit into two backpacks. As both modules have bigger dimensions than can fit in the backpack both modules had to be split into multiple parts. As a result the UAV will have to be assembled before operation. All the different parts of the fuselage, the fixed-wing module and the quadcopter module can be found below. For an overview of splitting the components, Figure 17.3 and Figure 17.4.

Fixed-wing
- The wing split in three parts
- Booms attach the empennage to the wing
- The empennage is split into two

Quadcopter
- Rotor protectors
- Four separate trusses, each connected to a rotor
- Quadcopter-fuselage attachment point

Fuselage
- Battery
- Short or long range payload bay module
- Fixed-wing or quadcopter module attachment point

Each of the three modules will have different assembly mechanisms, depending on different criteria for each. Therefore, a trade-off should be made on what kind of attachment point should be used per connection point between parts. Another aspect that should be taken into consideration is that the assembly mechanism should be modular. This means that the assembly and disassembly time should be as low and as simple as possible.

8.2. Modular Fasteners

Most of the different connectors, such as the screws and latches, are separate parts of the structure and have to be assembled to the different parts of the UAV. As such, they can be bought of the shelf and have a Technology Readiness Level (TRL) of 9, but will not be specifically designed for UAV load cases nor are they particularly compatible if the prime material group of the UAV is composites.

Screw type joints

This is a screw that uses clamping, rotation and pressure locks to create repeatedly releasable joints. They are screws that are rotated once and are clamped into the material. They have a functional length of between 15 mm to 50 mm and are lightweight. An example of this type of joint is the *QUICKLOC®* and can be seen in Figure 8.1a.[1] Because it is already available, they have a high TRL and thus a high Reliability, Availability, Maintenance, and Safety (RAMS). They require relatively much assembly time, as the two parts would have to be screwed together and it might be difficult to properly align the holes of the two parts.

[1] www.boellhoff.com/de-en/products-and-services/special-fasteners/quick-release-system-quickloc.php, last accessed: 2017-06-12

(a) *QUICKLOC®*

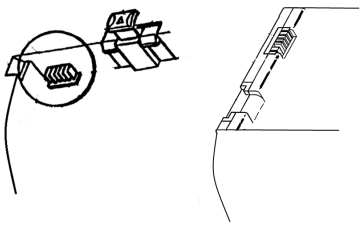

(b) Slide snap-fit

(c) Draw latch

(d) Snap-fit fastener [27]

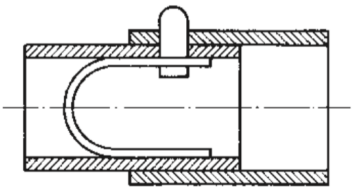

(e) Push button fastener [27]

(f) Ball-locking pin

Figure 8.1: Modular fasteners

Slide snap-fit
A schematic drawing of the fastener can be seen in Figure 8.1b [43]. It is a mechanism that can be found in e.g. the battery of a laptop. It consists of a latching member for the attachment of the two parts, placed near the sides of the wall on the male and female part. On the female part there is a locking member, preventing the latch from being released by contact with the outer latching member. Finally, rails are present in both parts, that assist the assembly by guiding the attaching mechanism. This means that its assemblability is extremely good. These kind of fasteners are quite light as they only consist of three parts. Because it is a mechanism that is integrated in the inner side of the UAV its environmental resistance is also good. Although care should be taken by designing the system with enough tolerance, as dust particles could infiltrate and prevent the mechanism from functioning.

Draw latch
Draw latches clamp two different parts of the UAV together by using a hook, as can be seen in Figure 8.1c.[2] They are weather resistant, but susceptible to corrosion. This is due to the easy mechanism with a relatively high tolerance level. This easy mechanism is also the reason for their relatively low assembly time. One of the drawbacks of this mechanism is that it is quite difficult to properly align the two parts without having a small gap present. It can only be achieved by having a low tolerance, which conflicts with the tolerance necessary for environmental resistance [44].

Snap-fit fastener
Snap-fit fasteners are mainly made of plastics or springy metals, an example of such a fastener can be found in Figure 8.1d.[3] Such a joint needs to be integrated into the structure of the UAV and can therefore be designed for the specific load cases. This reduces assembly time and cost in production and in use [10]. On the other hand, this diminishes the TRL of the fastener, as it has to be designed specifically for each application and will thus have to be tested before the military can use it. Furthermore, this means that its maintainability is very low, as a new part will have to be bought if the snap-fit fastener fails. As a result the snap-fits have a relatively low RAMS [11, 56].

Finally, its environmental resistance is lower than some other fasteners, as it is small and will thus be more impacted if dust particles enter the mechanism. As it is mainly fastened on the inside of the two parts, the weather will however not impact it as much, which in turn increases its performance on this matter [56].

[2] `www.protex.com/270-600SS-junior-prolatch-with-safety-catch-stainless-steel-natural`, last accessed: 2017-06-13
[3] `www.tms-scotland.co.uk/Article/SolidWorks/Two-Must-Answer-Questions-When-Developing-a-New-Product/4211`, last accessed: 2017-06-28

Push button snap joint

An example of a push button snap spring mechanism can be found in Figure 8.1e.[4] They are normally a few centimeters wide. To operate well, the spring needs to be able to compress and decompress within the part it is latched to. It is not weather resistant due to the small tolerance necessary to fit the spring button to the part and because it is located on the outside of the UAV. Furthermore, if the part where the push button spring snap has to fit in is too small, it has too little room to bend inwards and will subsequently not open.

On the contrary, its assemblability and RAMS is relatively high as it consists of only a few parts that are easily replaceable, as they can be bought off-the-shelf [57].

Ball locking pin

The fastener depicted in Figure 8.1f[5] are quick-release alignment pins with a precision ground shank. It is locked until released by pushing the button, which moves the center spindle forward to allow the locking balls to retract. There are also ball locking pins that can clamp the pin to the part, so that there are more. As a result the assemblability of these fasteners is favorable and because they are readily available their RAMS is as well.

Because it is normally made of stainless steel, their weight is more substantial than fasteners made from plastic. Nevertheless, the pins are quite small and will thus still be light. Stainless steel ball locking pins are more environmentally resistant than those made from other metals. Their resistance is also increased if their grip is encased in the two parts it has to fasten.

8.3. Overall Fastener Trade-off

Now that all the different fasteners and their characteristics are known, the next step is to make a preliminary trade-off. This initial trade-off is qualitative, as there are no numbers that can be found at this stage of the design process. Extensive Finite Element Method (FEM) of each fastener during all the different load cases would be needed in order to find for instance the final mass of the fastener.

This preliminary trade-off is performed, because each fastener will have a number of trade-off criteria that are the same, as some features are inherent for the overall design of the UAV. They are given in Section 8.3.1. This means that during each different fastener trade-off, the results of this partial trade-off will be taken into account together with any additional criteria that might occur. One of the most important aspects of these additional criteria is the feasibility of each fastener when trying to integrate it in each different location of the UAV where such a part is needed.

8.3.1. Trade-off criteria

Next to the sizing of the fastening joint with the extreme load cases present during the UAV operations, there are other criteria that need to be taken into account when choosing the final fastening mechanism, found below:

Mass *10 %* The fastener should be as light as possible, because its weight is included in the payload bay and maximizing the mass of the payload itself is a priority.

Assemblability *20 %* The assembly time of the joint needs to be as quick and practical as possible. It is increased when the number of fasteners is increased, or when the fastener mechanism is difficult to operate.

Robustness *20 %* The fastening mechanism must be able to be assembled during all operational conditions. These include dusty and salty environments.

RAMS *10 %* The RAMS of the joint should be as high as possible, due to the consequent decrease in non-recurring costs.

8.3.2. Preliminary trade-off results without feasibility

The preliminary trade-off results can be found in Table 8.1. The best value is rated with an A and the worst is rated with an F. Everything in between is rated within the range of letters, which is then converted to numbers 1 to 10. The values from the table are obtained by combining the information given in Section 8.2 and the trade-off criteria mentioned in the previous paragraph. The results are low, because the feasibility and possible other trade-off criteria still need to be added to obtain the final result for each fastener. As can be seen from Table 8.1, the slide snap-fit is the preferred fastener when looking at these different trade-off criteria. If this type of fastener is not feasible, the next best is the ball-locking pin.

[4] www.grainger.com/category/snap-buttons/pins/fasteners/ecatalog/N-n3p, last accessed: 2017-06-19

[5] www.tracepartsonline.net/(S(lgtmveskesfoxn4euwyqswfn))/PartDetails.aspx?Class=TRACEPARTS&clsid=/TRACEPARTS/TP01/TP01001/TP01001008/&ManID=NORELEM&PartFamilyID=10-30082011-103319&PartID=10-30082011-103319&SrchRsltType=0&SrchRsltId=32, last accessed: 2017-06-16

Table 8.1: Qualitative trade-off of payload bay fastener

	Mass	Assemblability	Robustness	RAMS	Final score
Screw type	B	C	B	A	4.6
Slide snap-fit	A	B	C	B	**5.0**
Draw latch	D	C	B	B	4.0
Snap-fit	A	A	D	D	4.6
Push button spring snap	C	D	C	A	4.2
Ball locking pin	B	B	B	B	4.8

8.3.3. Preliminary fastener feasibility

The next step in making the trade-off is to define the feasibility in each design at each critical location that will need to be assembled for the UAV. These critical locations include the fasteners that are placed between the fuselage-flying module, the boom-wing, the payload-fuselage and the battery-fuselage.

Fuselage-flying module The most critical fastener in terms of stresses as of yet is the flying module attachment to the fuselage. For this attachment it is of importance that it can only be placed at the bottom of the flying module. It is restricted by the aerodynamic design and the material selection and will have to carry the most amount of stresses. As a result, the draw latch becomes unfeasible as it is relatively bulky. The ball-locking pin, the *QUICKLOC®*, and the push button fastener also get a lower grade due to this. With composites as final material selection of the UAV, extra care has to be taken to see if the chosen fastener will not create additional stresses in the structure. Most fasteners except for the slide snap-fit are less feasible and received a worse mark, because they do add relatively more stresses to the UAV.

Booms The structure of the booms for both the quadcopter as the fixed-wing configuration comprises of simple rods. The fasteners for this type of connection point should thus be small enough to fit. This makes the draw latch unfeasible. The aerodynamics could also not be compromised too much by adding relatively bulky fasteners from the outside. As this would increase the drag substantially. This is the reason why a *QUICKLOC®* is not chosen, as it is more bulky than the ball-locking pin. This is also the reason why a ball-locking pin has a *B* in the feasibility category. As such the final selection for fastener mechanism was the ball-locking pin.

Payload There are multiple options that were given in Section 8.2 that are not feasible when fastening the payload bay to the fuselage. This is due to the fact that the payload bay needs to be placed from the bottom or from the side of the fuselage, without adding any additional stresses and needs to withstand mainly tensional and some shear stresses. Another aspect that imposes unfeasible options from the different fasteners is the fact that the body should keep its aerodynamic shape. This means that the outside fasteners such as latches should either be integrated into the aerodynamic shape or they become unfeasible, or at least less feasible as it would increase the drag more compared to other fasteners.
Finally, snap-fit fastener is a less feasible than the slide snap-fit, as it imposes quite some extra stresses on the fuselage, as it deforms the material when the payload bay is inserted in the fuselage.

Batteries For the modular battery packs the same fasteners is chosen as for the payload bay, as it has the same feasibility.

8.3.4. Trade-off results of payload and battery fastener

Now that the extra criterion has been explained, the trade-off can be performed. The final outcome can be found in Table 8.2. The best value in the table is rated with an A and the worst is rated with an F. Everything in between is rated within the range of letters, which is then converted to a numbering scale from 1 to 10. In this table the unfeasible options are indicated with a dashed line, and the outcome is also not given for these kind of fasteners.

8.3.5. Overview of chosen fasteners

gives the qualitative trade-off of the payload bay and by default the batteries. Such a trade-off was conducted for all connector types, using the information from Table 8.1 together with the different feasibility studies per connection point in Section 8.3.3, to obtain the final fastener choice seen in Table 8.3.

Table 8.2: Qualitative trade-off of payload bay fastener

	Feasibility *40 %*	Mass *10 %*	Assemblability *20 %*	Robustness *20 %*	RAMS *10 %*	Outcome
Screw type	-	B	C	B	A	-
Slide snap-fit	B	A	B	C	B	**8.2**
Draw latch	D	D	C	B	B	5.8
Snap-fit	C	A	A	D	B	6.8
Push button	-	B	B	C	C	-
Ball locking pin	B	B	B	B	B	7.2

Table 8.3: Overview of the chosen fasteners

Connection point	Preliminary fastener choice
Fuselage-flying module	Slide snap-fit
Booms	Ball-locking pin
Payload	Slide snap-fit
Batteries	Slide snap-fit

8.4. Tolerance Analysis

To ensure the two parts of the fastener can always be connected to each other a tolerance analysis needs to be performed. There are two main factors that have to be taken into account during this analysis. The first one is the thermal expansion of the joint. Because of the broad temperature range (ΔT) of −20 °C to 55 °C, the joint will have an addition strain (ϵ_{T}) with a value equal to the one calculated in Equation (8.1). In this equation the thermal expansion coefficient (α) is a material property and is most critical for plastics. Kevlar for instance has an α equal to $-1.98 \times 10^{-6}\,\mathrm{K}^{-1}$, and the maximum temperature difference of the UAV is ±75. This makes the δ_{T} equal to $\pm 1.5 \times 10^{-3}$ %.

$$\delta_{\mathrm{T}} = \alpha \Delta T \tag{8.1}$$

The second factor is the tolerance that is added due to machining and due to assembly errors. For a part that is under the 20 mm, the maximum tolerance level is around 0.1 mm. The tolerance is negative for the male part of the fastener as its width is limited by the female part, the female part through the same reasoning has a positive tolerance.

8.5. Recommendations and Future Improvements

Due to the limitations in time and the scope of this project, the structural analysis and the computer aided design of the UAV is fairly preliminary. This means that as of yet the final stresses and loads in the structure, including fasteners, are not known. As a result, it is impossible to correctly size the fasteners or even to make a correct free body diagram at each fastener location. Also, it is partially because they are made of plastic, and less information is available on their sizing and overall characteristics. So a very important further improvement is to have detailed parts in computer aided design software. This allows for in depth FEM and to make a final selection and sizing of the fastener.

A more in depth interaction between the material of the fastener and the different UAV parts is also necessary, as for instance some material combinations react to each other (e.g. galvanic corrosion) [14]. One example of this is Aluminum (Al) and carbon fibre. Also because of the different thermal expansion and other mechanical properties of plastics have to be taken into account.[6] All this is part of the reason why so many snap-fits have been chosen for the preliminary design, as they are made of plastic and are fairly reliable.

It is also true that less information can be found about the design and sizing of plastic fasteners. This is mainly because most fasteners in the industry are made from metals with only recent development in plastic components as the prime material.

[6] `www.fastenercomponents.com/news/plastic-fasteners-vs-metal-fasteners/`, last accessed: 2017-06-23

II-9

Performance and Propulsion Analysis

Because the design has two different configurations, the analysis of the performance was separated in two different parts. This is because they both have a different method for analyzing the performance. This chapter is ordered as follows. Firstly, the assumptions per configuration are stated in Section 9.1. Next an overview is given of the approach used to calculate the performance of each configuration in Section 9.2. Finally, the outcome of the analysis of the quadcopter and fixed-wing configuration is given in Sections 9.3 and 9.4 subsequently.

9.1. Assumptions

Before starting the performance analysis it is important to keep track of all the assumptions that are made during the process, as they are needed for the verification and validation of the analysis.

Quadcopter

QC-PA-I **Steady symmetric flight** The external forces are assumed to be in equilibrium, thus no accelerations were used during calculations. This assumptions can be applied during cruise, but not for other flight operations. As a result an analysis can be made based on free-body diagrams of the quadcopter and momentum theory. The dynamics involved during accelerating flight are beyond the scope of this report.

QC-PA-II **Uniform inflow** This is a requirement to use the momentum theory for quadcopter performance [35]. This means that the rotors have ideally twisted blades, which would be impossible to manufacture. This can however be approached by using high values of linear twist [48].

QC-PA-III **No blade flapping** Blade flapping is caused by the asymmetry in the lift during forward flight and creates a moment at the hub of the rotors. To minimize this moment and the asymmetry, the quadcopter rotors are rigidly attached. As such the flapping effect is minimized and this assumption is justified [9]. As a result, the blade profile drag coefficient is constant[19].

QC-PA-IV **Constant propeller efficiency** Due to the varying Revolutions Per Minute (RPM) the propeller efficiency is not completely constant. The range for the chosen propeller is between 20 % to 80 %. A value of 70 % is assumed.[1] [2] A relatively high value has been chosen, as it is known at what RPM the efficiency is at its best and those will be the values the quadcopter will mainly fly at.

QC-PA-V **Ideal rotor flow** This means that the flow is one-dimensional, quasi-steady, incompressible, inviscid, and behaves as an ideal fluid. Furthermore, the radius of the flow plane is perpendicular to the control volume at the rotor disc, which in turn equals the rotor radius [9].

Fixed-wing

FW-PA-I The Unmanned Aerial Vehicle (UAV) is in a steady-symmetric flight regime (i.e. $L = W,\ T = D,\ beta = 0$).

FW-PA-II Maximum load factor occurs at maximum bank angle and the controllability of the aircraft is sufficient to sustain maximum angle of attack during this coordinated turn.

FW-PA-III Efficiency of the propulsion system is constant.

FW-PA-IV Total energy capacity of the battery is constant and does not decrease with increased power draw.

FW-PA-V The non-propulsive power draw of the UAV is at maximum 23.1 W.

FW-PA-VI The Oswald efficiency factor can be approximated to be roughly 0.9 and is constant in all flight conditions.

[1] `www.electrifly.com/motors/gpmg4505.html`, last accessed: 2017-06-20

[2] `www.rctigermotor.com/html/2013/Professional_0912/52.html`, last accessed: 2017-06-20

9.2. Approach

Before starting the code of the performance analysis, it is very useful to make a flow diagram indicating the approach during the writing. This will help to get an overview of how to write the code and when doing verification of the code.

Quadcopter

Figure 9.1 shows the flow diagram made for the performance analysis. One starts at the blue rectangular boxes. Those are the inputs for the next processes, indicated with white rectangular boxes. There are three decision points in Figure 9.1, depicted by solid blue rhombuses. The first one is a check for stall, when choosing an airfoil and computing the normalized thrust coefficient $\frac{C_T}{\sigma}$ one has to check if stall occurs. If this is the case a new airfoil needs to be chosen from the Aerodynamics department database. The second decision is the convergence of the code when updating all the values. If divergence is present, the new update needs to set an angle of attack such that no stall occurs during the convergence of the code. Finally blade stall needs to be checked as well to obtain the final design.

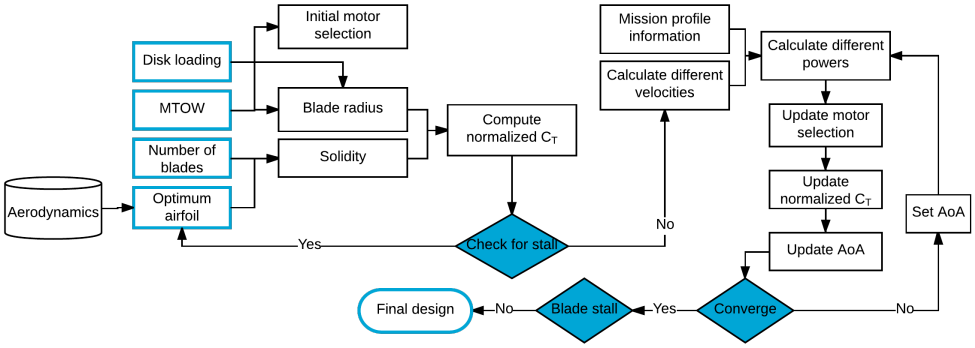

Figure 9.1: Approach for the quadcopter performance analysis

Fixed-wing

For the optimization of the fixed-wing performance, an updated version of the model used during the initial sizing was used. In essence, the same relations were utilized with updated weights, power draws, and efficiency. This method is summarized graphically by Figure 9.2. First of all, there are three main databases where the information of the engines, the propellers and the different fixed-wing parameters are stored. Secondly, the optimization is done by reiterating the efficiency to get an optimal value. This reiteration is represented by the blue rhombus labeled *Improvement*. Finally, the compliance with the requirements is guaranteed by having an extra decision point. When the chosen configuration that optimizes the performance does not comply with the given requirements, it will start the whole process over again, by choosing a new engine.

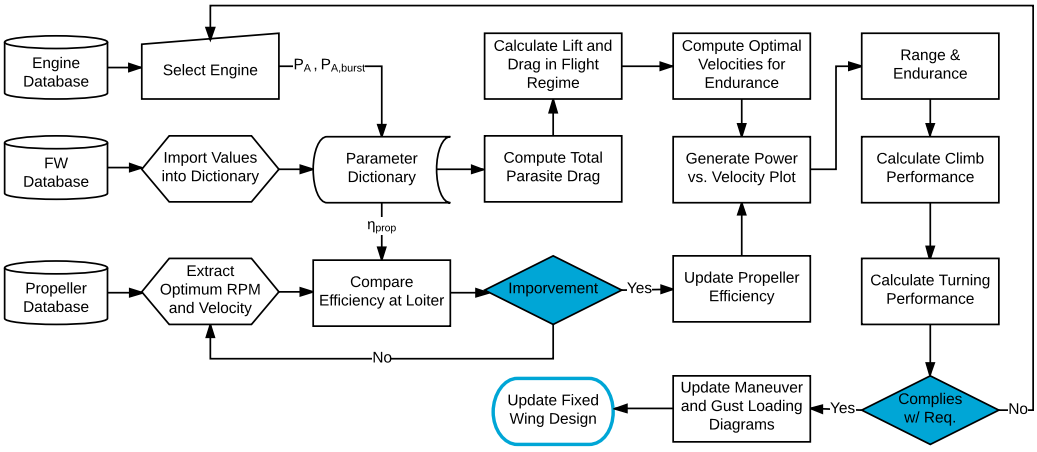

Figure 9.2: Flow diagram of the fixed-wing design and performance estimation

9.3. Quadcopter Configuration

To get an estimation on the performance of the quadcopter the modified momentum theory is used to obtain results on the power required for all mission segments. After this, Chapter 10 will further analyze the propeller characteristics. The outputs from the other departments are then used to iterate further.

The performance of the quadcopter as well as the power required for hovering, horizontal flight and climb was determined by using the flow chart as seen in Section 9.2. Firstly the input parameters will be determined. Then, by optimizing for maximum hover endurance, the output values of the flow chart are determined.

9.3.1. Input parameters

The final input values necessary to calculate and optimize the required power to sustain all mission segments is given in Table 9.1. The values for the first iteration were either already determined during the initial quadcopter sizing, or additional calculations had to be performed which will be discussed below.

Table 9.1: Input parameters

Parameter	Symbol	First Iteration	Second Iteration	Third Iteration	Unit
Maximum Take-off Weight	W	3.57	3.57	3.57	kg
Disc loading	DL	142.66	120.63	102.37	$N\,m^{-2}$
Rotor diamater	D_b	11	12	13	in
Number of blades	N_b	2	2	2	
Blade chord	c_b	0.04	0.04	0.05	m
Blade aspect ratio	A_b	7	7.6	6.6	
Blade twist	ϕ	−7	−7	−7	deg
Mean drag coefficient	C_{d_0}	0.015	0.015	0.015	-
Equivalent flat plate area	f_{e_0}	0.11	0.06	0.06	m^2

Disc loading

First of all, to calculate the rotor dimensions needed to carry the UAV, the disk loading needs to be estimated. It is preferred to have the disk loading as low as possible, as this increases the hover efficiency and decreases the noise during hovering [35]. As already stated in Section 4.1.1 a range of $70\,N\,m^{-2}$ to $165\,N\,m^{-2}$ was used to determine the optimized corresponding blade radius. After iterating, a final value of $102.37\,N\,m^{-2}$ was found.

Number of blades

The choice of the number of blades influences tip velocity as well as the efficiency of horizontal flight or hover. Typically, two bladed propellers are used for smaller rotorcraft, as their operating Reynolds number for a given motor speed increases. This makes them more efficient compared to rotors with three or more blades with the same motor solidity. Additionally, increasing the number of blades also increases the noise. On the other hand, if single bladed propellers with a counterweight are used for the design, the Reynolds number of the blade can be increased even further. However, as this would decrease the solidity, not enough thrust is produced to sustain powered flight.[20, 35] Therefore, two bladed propellers were chosen per engine.

Optimum airfoil

USNPS4 was chosen for the rotor airfoil, as it has a high maximum lift-over-drag ratio of 75 at the operational Reynolds number of 250 000. Additionally, it has a maximum lift coefficient of 1.63 and a stall angle of 20 deg. The airfoil drag coefficient at an angle of attack of 0 deg is equal to 0.015.

Twist needs to be added to allow for an equal thrust distribution over the length of the blade independent of the quadcopter speed. If the quadcopter is nearing its surface ceiling, the propeller needs to be more coarse in pitch to be efficient. Most helicopters use linear twist in the range of −5 deg to −16 deg [35]. However, as the aspect ratio of helicopters is much higher than for quadcopters, the propellers should have relatively low negative values of twist. A linear twist of −7 deg is assumed. By adding this linear twist, the angle of attack experienced by the complete blade is relatively constant, as the distribution of the inflow velocity is relatively constant. [35].

Blade diameter
As the disc loading and the maximum take-off weight have been determined, the diameter of the blades R_b can be calculated. This is done by using Equation (9.1), which divides the maximum take-off weight W by the previously determined disc loading to determine the complete disc area. The diameter of the blades influences the performance and the dynamic behaviour of the quadcopter, the larger it becomes, the higher the static thrust efficiency for a given thrust setting. However, the maximum pitch and roll rates will be slower, making the quadcopter less maneuverable[20]. After the final iteration a blade diameter R_b of 13 in is found.

$$D_b = \sqrt{\frac{W/\mathrm{DL}}{\pi}} \tag{9.1}$$

Solidity
Solidity is the ratio of the effective lifting area of the blades to the complete area of the rotor. The lower the solidity, the more efficient the hovering configuration, as the rotor profile drag is decreased. However, decreasing the solidity also means an increase in angle of attack of the blade sections is needed to obtain the same disc loading values. Due to this, the stall margin of the rotor is reduced [9, 34]. Therefore, the solidity was optimized such that it would be as low as possible, but still within an angle of attack margin. As the solidity also depends on the chord of the blade, an initial value for this has to be assumed. A chord range of 0.03 m to 0.05 m was used for the calculation, as this would allow for a blade aspect ratio of between 5 and 10, which according to [61] is desirable for the efficiency of the quadcopter. A chord length of 0.05 m was found after optimizing. Based on this value and Equation (9.2) a solidity of 0.182 was found. From these values, the program optimized for lowest hover power required with as additional constraint the blade aspect ratio.

$$\sigma = \frac{N_b c_b R_b}{\pi R^2} \tag{9.2}$$

Equivalent flat plate area
The equivalent flat plate area can be calculated by multiplying the zero lift drag coefficient of the body with the wetted fuselage surface area. As it is not possible to obtain this coefficient without performing a windtunnel test, a value has to be assumed. For quadcopters, values between 0.046 m^2 to 0.186 m^2 are generally used [50]. As the quadcopter has a Maximum Take-off Weight (MTOW) of 3.57 kg, it can be classified as a small UAV. Therefore, it is assumed that it will have an equivalent flat plate area of around 0.11 m^2. However, in Section 10.6.3, the fuselage was simulated in ANSYS, resulting in an updated value of 0.06 m^2.

9.3.2. Output calculations
Now that all the inputs for the momentum theory are known, all the relevant outputs can be calculated. The most important output is the power, as it is needed to calculate the endurance and the range. However, it is also necessary to check for the stall characteristics as well as the climb performance.

Velocities
To calculate the power required for the different parts in the mission, it is first necessary to determine the initial velocities. There are three different optimal velocities for each mission segment. The induced velocity in hover, and the axial climb and the cruise velocity, which are obtained from the induced hover velocity.

The induced velocity during hovering is calculated using Equation (9.3). This velocity is easily determined with the input parameters disc loading DL and the density ρ, which is known from the mission profile.

The climb rate induced velocity v_i can be calculated from the induced hover velocity and the climb velocity by using Equation (9.4). In this equation, the symbol $\pm$ denotes the two possible solutions for climb rate: one being the climb, where it is positive and one being the descent, where it is negative. For descent, this formula is not valid for $-2 < \frac{V_c}{v_h} < 0$, due to the interaction between the rotor and its own downwash, a condition known as *vortex ring state*. In this case, one can assume the power needed for controlled descent to be equal to the required power to hover.

The cruise speed can be calculated in a similar manner from cruise speed V and angle of attack α. Here, α is chosen to be 20 deg, as this is a normal range for most rotorcraft [35]. Additionally, in Section 10.6.4 it is mentioned that separation occurs of the flow after 20 deg angle of attack. The induced velocity is given by Equation (9.5). Iterations are required to calculate the cruise speed, in order to optimize for the minimum power.

$$v_h = \sqrt{\frac{\mathrm{DL}}{2\rho}} \tag{9.3}$$

$$\frac{v_i}{v_h} = -\left(\frac{V_c}{2 \cdot v_h}\right) \pm \sqrt{\left(\frac{V_c}{2 \cdot v_h}\right)^2 + 1} \qquad (9.4)$$

$$v_i = \frac{v_h^2}{\sqrt{(V_\infty \cos\alpha)^2 + (V_\infty \sin\alpha + v_i)^2}} \qquad (9.5)$$

Hover performance

As the main ability of the quadcopter is to hover, this operation should be optimized. By using revised momentum theory, the power required for hovering can be estimated using Equation (9.6). The induced power P_i is dependent on the disc loading and the density, while the profile power P_0 is only dependent on the air density.

The induced power for hovering flight is the first term in the Equation (9.6). The hover correction factor κ represents any interactions between the induced velocity of the rotors and the body. For helicopters this value is between 1.12 to 1.25 [35]. For the quadcopter a value of 1.15 was chosen, in line with most small UAVs [61]. It depends further on the maximum take-off weight W, the disc area A, and the density at hover altitude ρ_h

The second term denotes the profile power P_0. By using the data of the motors stated in Table 9.6, such that the angular velocity Ω of each motor is known,and the input data, the profile power can be calculated. From the input data the following parameters are used: the solidity σ, the zero lift drag coefficient C_{d_0}, the blade radius R_b, as well as reusing the density during hover ρ_h and the disc area A from the previous term.

$$P = P_i + P_0 = \frac{\kappa W^{\frac{3}{2}}}{\sqrt{2\rho_h A}} + \rho_h A\,(\Omega R_b)^3 \left(\frac{\sigma C_{\mathrm{d}_0}}{8}\right) \qquad (9.6)$$

Forward flight performance

The power necessary for the quadcopter in steady, symmetric forward flight can be determined by using Equation (9.7). Where the induced power P_i is calculated in the same manner as explained above, with as difference the altitude and thus the density.

As during cruise a forward velocity component needs to be present, the profile power already explained in Equation (9.6), increases with the second term between the square brackets. For K a single average value is used between 4.6 and 4.7. This value represents the increase in surface profile, when flying at an angle.

Additionally, the parasite power P_p is the third term in the equation. The power increases with the cube of the cruise speed. As such, the velocity during cruise should be as low as possible. Also, the fuselage should be optimized in one direction, such that the equivalent flat plate area f_{e_0} is reduced [19].

$$P = P_{\mathrm{i}} + P_0 + P_{\mathrm{p}} = \frac{\kappa W^{\frac{3}{2}}}{\sqrt{2\rho A}} + \rho A\,(\Omega R)^3 \left(\frac{\sigma C_{\mathrm{d}_0}}{8}\right)\left[1 + K\frac{V\cos\alpha}{\Omega R_b}\right] + \frac{1}{2}\rho V_\infty^3 f_{\mathrm{e}_0} \qquad (9.7)$$

Climb performance

Finally, the power necessary for climb P_c has to be calculated as well, using Equation (9.8). This is the power needed to maintain the aircraft level at the chosen angle of attack of the fuselage. The climb speed can be determined from Equation (9.4). It is realistic to assume that that for low rates of climb (or descent) the rotor induced power P_i, the profile power P_0, and the equivalent flat plate area f_{e_0} remain nominally constant [19].

To calculate the maximum climb velocity P_i, P_0, and P_p are subtracted from the available burst power, and divided by the MTOW of the quadcopter. This formula is only valid for vertical climb in equilibrium.

$$P_c = W V_C \qquad (9.8)$$

$$\frac{P_h + P_{\mathrm{excess}}}{P_h} = \frac{V_c}{2v_h} + \sqrt{\left(\frac{V_c}{2v_h}\right)^2 + 1} \qquad (9.9)$$

$$V_{c_{\max}} \frac{P_a - \left(P_i + P_0 + P_p\right)}{W} \qquad (9.10)$$

Stall performance

There are two main stall characteristics for the quadcopter configuration. The first is the rotor airfoil stall. During hover it can be calculated with the normalized thrust coefficient $\frac{C_T}{\sigma}$ and the maximum lift coefficient of the blade $C_{l_{\max}}$. To have no rotor stall the following requirement needs to apply: $6\frac{C_T}{\sigma} < C_{l_{\max}}$ [48].

Because of the application of momentum theory, the flow is considered inviscid. This results in a thrust equal to half the weight per rotor [35]. As it will need to hold for all conditions, the worst one has been chosen, which is minimum RPM at 3000 m. With this $\frac{C_T}{\sigma}$ can be calculated by using Equation (9.11). The other parameters from this equation can be found in Table 9.1 and the density (ρ) at that altitude is computed to be 0.909 kg m^{-3}.

Six times the normalized thrust coefficient is then equal to 0.52, which is lower than $C_{l_{\max}}$ so no rotor stall will occur.

$$\frac{C_T}{\sigma} = \frac{T}{\sigma \rho A \left(\Omega_h R_b\right)} \tag{9.11}$$

The other stall characteristic is retracting blade stall. It occurs during forward flight as the forward blade experiences extra velocity. If the Mach number at the tip of the rotor (M_{tip}) is greater than 0.8 separation starts to occur at the tip of the rotor. The critical RPM (RPM_{crit}) can be calculated by using Equation (9.12), which assumes uniform flow [9]. Again, stall should be prevented during all operational activities. As such, the critical case should be used. This occurs when the operating temperature is minimum and thus equal to 253 K. Using the final input parameters from Table 9.1, one finds a value equal to 13 425 rpm. The theoretical maximum of the motor is equal to 13 875 rpm, this limit will however never be reached during normal operations.[3] [4].

$$RPM_{\text{crit}} = \frac{M_{\text{tip}}\sqrt{\gamma R T} - V_\infty \cos\left(\alpha_T\right)}{R_b} \frac{60}{2\pi} \tag{9.12}$$

Gust performance

The quadcopter configuration is less susceptible to gusts than the fixed-wing configuration. As the quadcopter has brushless electric motors, it is able to counter the gusts with a fast reaction time. Additionally, the power required to sustain a stable hover during gusts was estimated as the power needed when flying horizontally or vertically with a velocity of 50 km h^{-1}, as per the requirement. The power needed to retain the hover capabilities of the drone, would increase with 9.7 %.

9.3.3. Results

Now that all the output parameters have been calculated, there are multiple graphs that can be made. The first can be seen in Figure 9.3, which gives an overview of all the required powers that have been calculated for horizontal flight, as a function of the airspeed. As seen from the figure, the induced power is prominent at low velocities, while the parasite power increases cubically with airspeed. Additionally, the profile power is extremely small, as the fuselage body is optimized for horizontal flight. In this figure, the maximum cruise speed is denoted with a solid black circle, and is equal to 21.7 m s^{-1}.

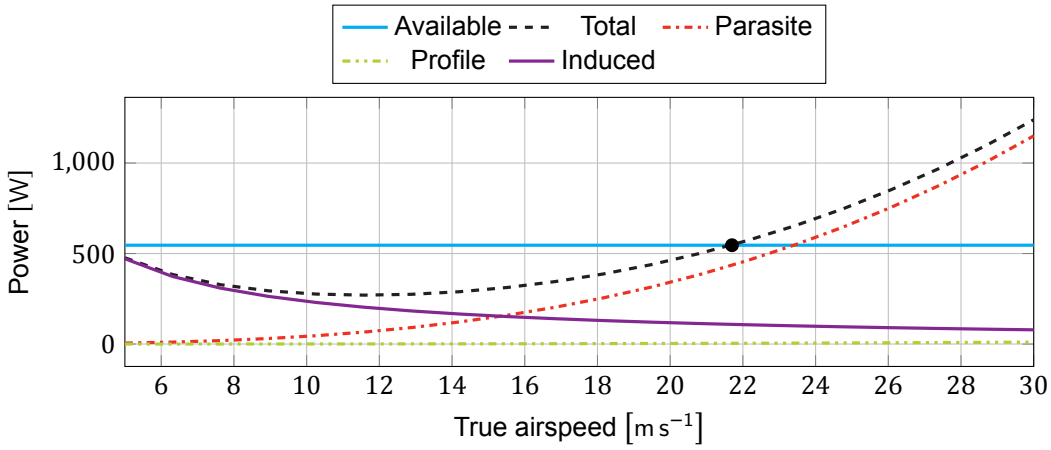

Figure 9.3: Required and available power depending on airspeed

To subsequently get the endurance of the quadcopter configuration, all the different power values per mission segment had to be calculated. This was done using again the different powers that are required to sustain the operations of the quadcopter and are also already calculated in Section 9.3.2. The final outcome can be found in Figure 9.4. As can be derived from this figure, the cruise segment uses less power than the climb. This is expected, as the quadcopter has to overcome its weight during climb. The maximum climb speed is 15.4 m s^{-1} and is indicated in the figure by a solid black square.

[3] www.electrifly.com/motors/gpmg4505.html, last accessed: 2017-06-20

[4] www.rctigermotor.com/html/2013/Professional_0912/52.html, last accessed: 2017-06-20

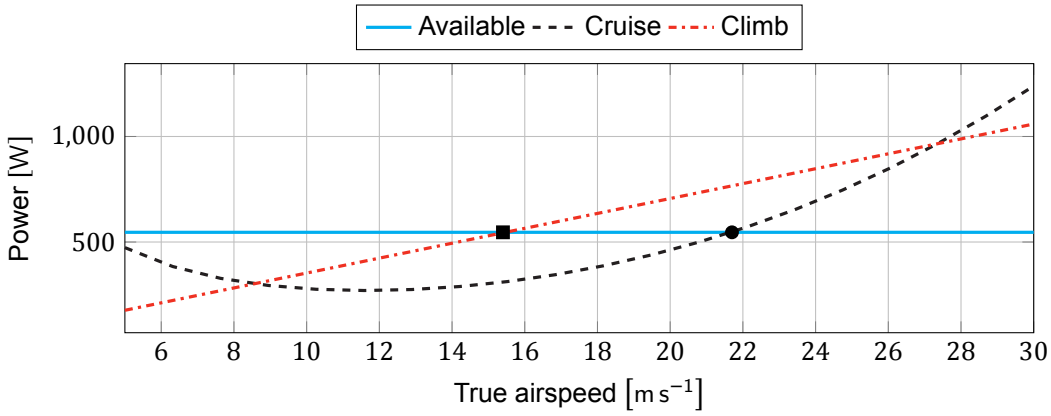

Figure 9.4: Power per mission segment

By using the velocity outputs from Section 9.3.2, as well as Figure 9.4, and the mission profile from Chapter 2 one can find the total mission time of the UAV, as well as the maximum loiter time. Table 9.2 gives an overview of all those values and the final energy needed per mission segment. During the calculations it was assumed that the payload is only functional during hovering and that landing requires the same amount of power as hovering. To calculate the total mission time, first the maximum loiter time is determined by using Equation (9.13). In this equation the total available power from the batteries is known and the energy of each mission phase, except during loiter is subtracted. This value is then divided by the total instantaneous power draw of the UAV during hovering. One then obtains a loiter time equal to 93 min.

Table 9.2: Parameters for the calculation of the energy for the short range mission

	Altitude [m]	Distance [m]	Velocity [m s^{-1}]	Power [W]	Time [s]	Energy [W h]
Take-off and climb	0	70	15.4	546	4.5	0.7
Cruise	70	1000	21.7	546	46.1	7.0
Loiter and hover	70			87.6+$P_{\text{PL}} + P_{\text{avionics}}$		
Cruise	70	1000	21.7	546	46.1	7.0
Descent and landing	0	70	8	87.6	8.8	0.2
Total	-	>2140	-	-	105.5	14.9

$$t_{\text{loiter}} = \frac{E_{\text{sp}} m_{\text{batt}} \eta_{\text{elec}} \eta_{\text{prop}} \text{DOD} - E_{\text{climb}} - 2 \cdot E_{\text{cruise}} - E_{\text{descent}}}{P_{\text{Loiter}} + P_{\text{Avionics}} + P_{\text{PL}}} \tag{9.13}$$

The range of the quadcopter can be calculated by taking the cruise power to first calculate the endurance and multiplying this value by the velocity it is going at. One then finds a range equal to 24.7 km

The endurance, defined as the total time the quadcopter is capable of only hovering, was calculated in the same manner as Equation (4.21), but then using P_{hover} instead of loiter. This means that the only thing the UAV will do with the battery is operate the payload and hover. This results in an endurance equal to 1.7 h.

The final graph for the quadcopter performance can be seen in Figure 9.5. It depicts the climb speed as a function of the altitude. At 3000 m the climb speed is negative. This means that requirement **SPARTA-UAV-1** will not be met for the quadcopter configuration, as it can climb for 300 ft min^{-1} at only an altitude of 1353 m.

9.4. Fixed-wing Configuration

Now that the performance of the quadcopter has been analyzed, the fixed-wing performance can be determined. The process follows the one the quadcopter uses. This means that there will first be an overview of the input parameters and afterwards the output parameters will be calculated.

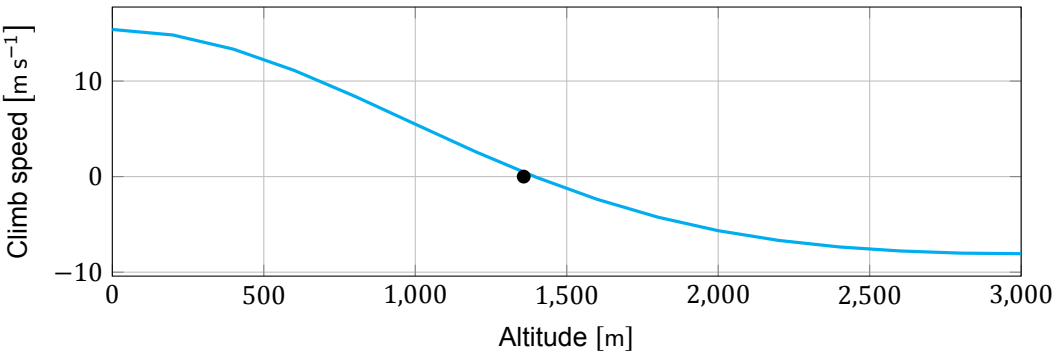

Figure 9.5: Climb performance with varying altitude

9.4.1. Inputs

As mentioned above, the first step in the performance analysis process is having an overview of all the input parameters that are used for calculations. All aerodynamic coefficients, such as the Oswald efficiency factor, zero lift drag, and maximum lift coefficient are all obtained from Chapter 10. The rest of the values are attained from Chapter 4, with some minor revisions on the assumptions. As can be seen in Table 9.3 the input parameters changed per iteration, which subsequently resulted in different output values.

Table 9.3: Input parameters of the fixed-wing configuration for performance analysis

Parameter	Symbol	First iteration	Second iteration	Third iteration	Unit
Wing loading	W/S	76.3	76.6	98.1	$\mathrm{N\,m^{-2}}$
Power loading	W/P	0.187	0.196	0.253	$\mathrm{W\,m^{-2}}$
Wing area	S	0.46	0.46	0.46	$\mathrm{m^2}$
Aspect ratio	AR	7	7	7	-
Wingspan	b	1.8	1.8	1.8	m
Mean Aerodynamic Chord	MAC	0.257	0.262	0.262	m
Zero lift drag	$C_{\mathrm{D_0}}$	0.055	0.034	0.034	-
Maximum lift coefficient	$C_{L_{\max}}$	1.5	1.3	1.3	-
Oswald efficiency factor	e	0.8	0.8	0.9	-
Aerodynamic constant	K	0.065	0.065	0.051	-
Propeller efficiency	η_{pr}	0.7	0.77	0.85	-
Lift-over-drag ratio loitering	LD_{loiter}	7.6	11.7	11.7	-
Loiter speed	V_{loiter}	15.0	13.9	15.8	$\mathrm{m\,s^{-1}}$

9.4.2. Outputs

There are a lot of values of the performance analysis of the fixed-wing that can be calculated, but most of them are not relevant when looking at the long-range mission the UAV has to perform. There are three parameters that are most critical for the performance of the UAV, besides the ones calculated in Section 4.1.2. These are the glide, turn, and pull-up performance together with the drag divergence of the propeller, described in the following sections. This is because the UAV will make gliding circles around the target area and once it is outside of the audible sphere it will quickly pull-up to gain altitude and start the whole process over again. This last one is very important, as during the pull-up there will be a short time frame where the UAV will not observe the target and this will have to be minimized.

Glide performance

One of the most important parameters of the long-range targeting mission is the glide velocity (V_{glide}). The expression for this parameter can be found in Equation (9.14) and it is calculated by assuming that the thrust settings are turned off [4, 39]. The input parameters for this equation can either be found in Table 9.3. Using them one obtains a V_{glide} equal to 17.5 $\mathrm{m\,s^{-1}}$.

$$V_{\mathrm{glide}} = \sqrt{\frac{W}{S}\frac{2}{\rho_\infty}\sqrt{\frac{K}{C_{\mathrm{D_0}}}}} \tag{9.14}$$

To maximize the endurance of the UAV in gliding performance, the sink rate ($\dot{h}$) has to be minimized. This occurs when one maximizes the lift-to-drag value given in Equation (9.15). Using all the values given in Table 9.3 one finds a sink rate equal to $-1.35\,\mathrm{m\,s^{-1}}$. At this sink rate the UAV is going $15\,\mathrm{m\,s^{-1}}$, this means that if the UAV would descend 30 m, it would still travel 333 m.

$$\dot{h} = -\sqrt{\frac{2}{\rho}\frac{W}{S}}\left(\frac{C_\mathrm{D}}{C_\mathrm{L}^{\frac{3}{2}}}\right) \tag{9.15}$$

One of the options the UAV has during night to improve the images it can make is to turn off the engine to become inaudible and glide toward a target, all the while being in camera range. This means that one wants to turn off the engine at propeller audibility range, so that it becomes almost soundless. In this case that is equal to 10 m, calculated in Section 10.7. One then also has to check if the camera can identify its target at that range. This is the case during all operations as the camera has a range of 95 m, calculated in Section 7.2. If the military then wants to make extremely detailed images of the target, at around an altitude of 50 m. This means that the UAV needs to stop its engine at a height of 65 m.

Maneuvering flight

Next to gliding, the fixed-wing configuration should also have a low turn- and pull-up radius, so that its maneuverability increases. The radii should be small during all operational phases. This means that it should be checked at maximum turn speed, in this case equal to the maximum flight velocity. Using those values together with the maximum load factor ($n_{\max}$) found in Section 4.1.2, one obtains a turn radius equal to 12.5 m and a pull-up radius equal to 15 m.

$$R_{\mathrm{turn}} = \frac{V_{\mathrm{turn}}^2}{g\sqrt{n_{\max}^2 - 1}} \tag{9.16}$$

$$R_{\mathrm{pull-up}} = \frac{V_{\mathrm{turn}}^2}{g\,(n_{\max} - 1)} \tag{9.17}$$

Another thing that can be calculated is the maximum sustained turn rate Ψ. It is calculated based on the assumption that the highest load factor is attained at the maximum possible bank angle. Furthermore, at such a bank angle the wing needs to generate a maximum amount of lift. Thus the aircraft will be flying close to its stall Angle of Attack (AOA) and it is valid to assume that $C_L \approx C_{L_{\max}}$. Following from this $C_{L_{\max}}$ is used to create a another power required curve. Finally, the intersection of this line and the power-available curve represents the maximum sustained turn rate since beyond this point the power-plant cannot provide enough thrust to counter the drag generated from higher bank angles and lift. Thus beyond this point it can also be seen as the instantaneous turn-rate. It must also be noted that the the maximum AOA was assumed to be at 10 deg. Due to the increase in weight, the fixed-wing UAV is able to pull 3.4 g_0 at its corner velocity of $20\,\mathrm{m\,s^{-1}}$. This corresponds to a turn rate of $1.6\,\mathrm{rad\,s^{-1}}$ and a turn radius of 12.5 m.

Hand-launch

For practical purposes, the fixed-wing aircraft should ideally be launchable by hand. This ensures that no extra infrastructure or equipment is needed for the aircraft to be operated. The easiest way to calculate the required wing size is to look at the highest speed a human can reliably throw an object of this size and weight. For a 2.5 kg UAV this speed was found to be around $8\,\mathrm{m\,s^{-1}}$ [63]. For a 3.6 kg aircraft, the same W/S would correlate to a 1.8 m wingspan for an aspect ratio of 7.

To expand on this, A further analysis was performed, which included the height at which the aircraft was thrown and also analyzed the effects of wing speed. In order to model this, a simple point mass system with lift, drag, weight and thrust, assuming a constant angle of attack, was set up. A Monte-Carlo analysis was performed on this model for wingspans between 1.0 m to 2.0 m. The random parameters were set to be throwing speed, with a μ of $8\,\mathrm{m\,s^{-1}}$ and σ^2 of $0.8\,\mathrm{m\,s^{-1}}$; and throwing angle, with a μ of 30 deg and a σ^2 of 5 deg. A successful hand-launch was defined as one where the aircraft would not descend closer to the ground than 0.5 m. The results can be seen in Section 9.4.2. Here, we can see that a 95 % succes rate is achieved at 1.69 m wingspan and a 99 % succesrate is achieved at a span of 1.80 m. The influence of even a minor amount of wind on the launch is very apparent. In Section 9.4.2, the take-off is simulated with $5\,\mathrm{km\,h^{-1}}$ of headwind. Now, only 1.5 m of span is required to reach a 99 % successrate. An important factor to consider is the fact that this headwind can also be generated by walking forwards during launch. Thus, including a 10 cm safety margin, a wingspan of at least 1.6 m is considered sufficient to allow hand-launching of the UAV in the expected operating conditions.

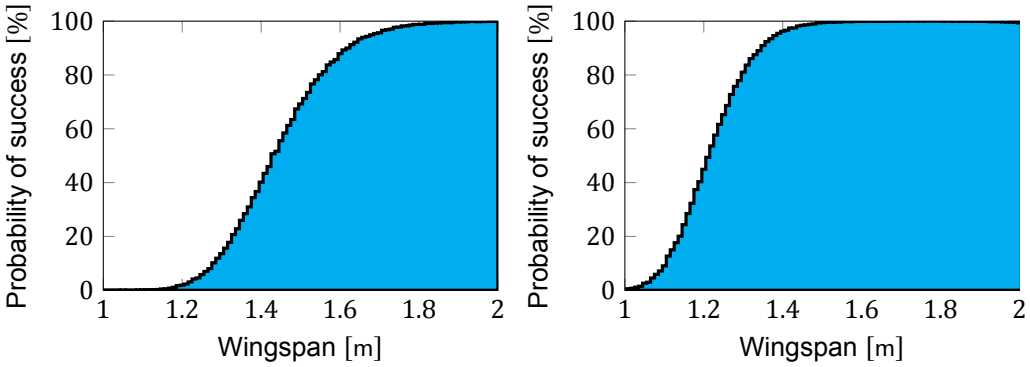

(a) Hand launch without wind (b) Hand launch with 5 km h^{-1} headwind

Figure 9.6: Probability of successful hand launch

9.4.3. Results

Due to the increase in wing-weight calculated by the structures department the performance of the final design was reduced from an endurance of 2.65 h for a 3.6 kg UAV down to an endurance of 2.14 h for a 4.46 kg UAV. Since this is purely straight-line endurance, the compliance with **SPARTA-UAV-3**, would not be guaranteed. Especially, due to the drag values obtained from the aerodynamics department plausibly being underestimations. As a result, upon realizing that the wing-weight might not be reducible, it was of paramount importance to properly select the propeller to increase the efficiency as much as possible. The initial selection for the propeller was based off of the minimum propeller pitch recommendation of the specification sheet of the *RimFire .10* engine which was the APC 10×4. From the propeller data provided from the manufacturer the mean propeller efficiency was computed to be approximately 0.77. The iteration process for propeller selection later revealed that increasing the propeller pitch also increased the efficiency as depicted by Figure 9.7.

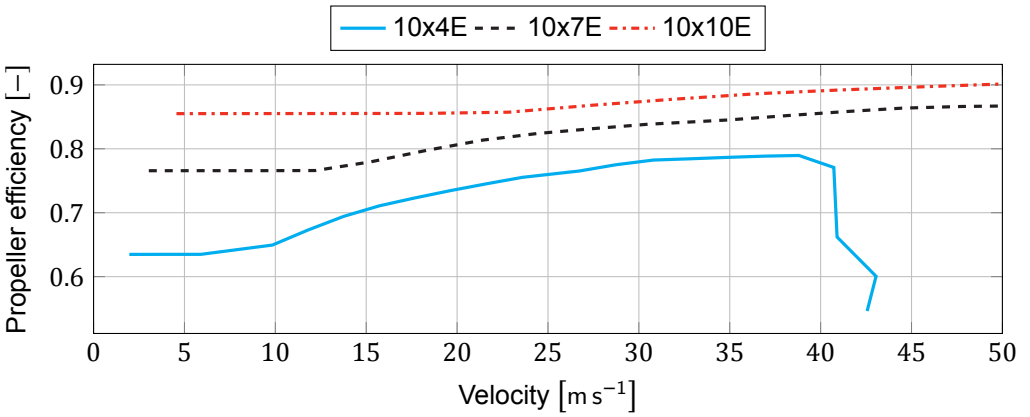

Figure 9.7: Propeller selection based on optimal efficiency at loiter (From low efficiency to high: APC10×4, APC10×7, APC10×10E)

The final design utilizes the APC10×10E propeller which has a mean efficiency of 0.85. This increase the endurance of the fixed-wing airframe to 2.4 h which corresponds to a 12 % as compared to the endurance before the optimized propeller choice.

In the same method utilized for the initial sizing for the fixed-wing, the power required and power available curves were generated using updated values, as the propeller efficiency factor was known. This can be seen in Figure 9.8. From this figure, the maximum velocity during a turn can be determined from the burst power and is equal to 21.8 m s^{-1}. This is denoted in the figure by a solid square. The solid diamond mark indicates the maximum cruise speed equal to 30.5 m s^{-1}.

The flight and gust envelope of the fixed-wing UAV can also be updated using the parameters of the third iteration from Table 9.3, found in Figures 9.9a and 9.9b respectively. One thing that can be observed is that the maximum load factor is equal to 8.2 and the minimum value is equal to −6.2. These values are lower than the ones found in the first iteration equal to 10 for the maximum and −8 for the minimum, because the MTOW of the UAV in the fixed-wing configuration increased to 4.5 kg.

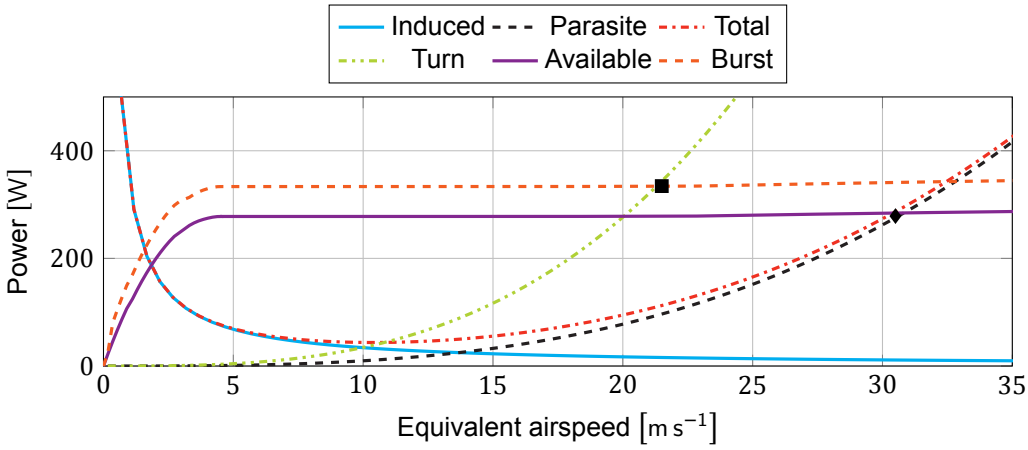

Figure 9.8: Fixed-wing power as a function of equivalent airspeed

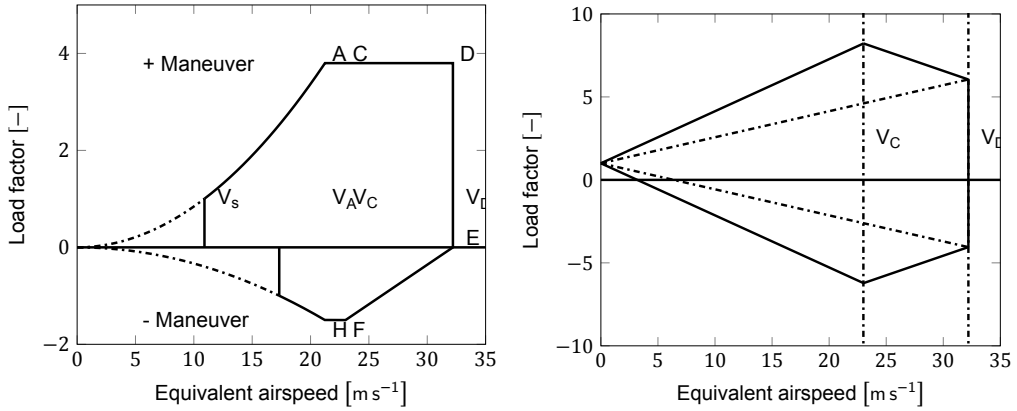

(a) Flight envelope

(b) Gust envelope

Figure 9.9: Updated values for the maximum and minimum load factors of fixed-wing configuration of the UAV

9.5. Verification and Validation

There are several possible processes that can be used to verify code, those are all listed in Section 9.5.1. However, validation is next to impossible if there is no wind-tunnel data available. Actual validation of the performance analysis will thus only be possible if a model is built and tested. As the UAV is not extremely sizable, this will not require the use of a very advanced wind tunnel and is thus less expensive.

9.5.1. Verification

Verification is checking if the code that was made actually models the physics that was used to write it. This means that mainly equations and syntax had to be checked for possible errors.

Quadcopter configuration

The overall code verification was done by checking it with *print* statements after running it. This way any possible errors within for instance lists and arrays could be checked. One example of this was the wrong usage of the *numpy concatenate function* in *Python*, which lead to erroneous values when printing and was fixed by this. Furthermore, the syntax of the code was verified by python itself so no additional measures had to be taken.

If possible, a unit test was made as well for difficult equations. This way one could easily check if there was a problem with the equation if it did not give the right solution. There were two main parts of the performance analysis code of the quadcopter that had to be done. The first was checking if the stall compliance equation was correct by calculating some values manually and see if the code gave the same output. The first time it did not give the same value as

The second was checking all the different velocities and powers. For the latter it was especially critical to check if the code was written correctly, as the induced-, profile- and parasite power all had to be calculated simultaneously.

Fixed-wing configuration
For the verification of the calculations multiple tests were used. Firstly, most equations were checked by hand to see if the values in the printed code were equal to the ones calculated. Secondly, the outputs of all functions were checked for correct shape and magnitude using print and plot statements.

For the code verification of the fixed-wing configuration *PyCharm* was used. For a detailed description of the code verification process one can look at Section 12.5.1.

Results
For both the quadcopter and the fixed-wing configuration, the analytical and numerical model are sufficiently similar. The comparison has shown that there is a good agreement in the majority of cases. There were some discrepancies at higher flight velocities, where the result of the modified momentum theory for the quadcopter diverged from the simple analytical equations. For the fixed-wing the same phenomenon occurred. This however, is to be expected since simulation in increased flight velocities result in a multitude of second order effects, which have been ignored in the simple analytical model. The general comparison results in a successful verification of the method for both the quadcopter and the fixed-wing configuration.

9.6. Propulsion Analysis

In this section the design and analysis of the propulsion unit is described. A propulsion system includes rotors, motors and a power source. The propulsion system determines the main output performances of the quadcopter, such as the hovering time, the flying speed and the range. Firstly, Section 9.6.2 describes in motor detail the designing of the propellers. Afterwards, in Section 9.6.3 the motor choice is analyzed. Finally, Section 9.6.4 states what power source is used and the corresponding electrical model.

9.6.1. Approach

A short flow diagram of the propulsion approach is depicted in Figure 9.10. It is valid for both configurations as they have electric motors and use batteries. The maximum power is needed to choose the appropriate motor, and the total required energy is needed to find the mass of the batteries. The outcome is the final propulsion mass.

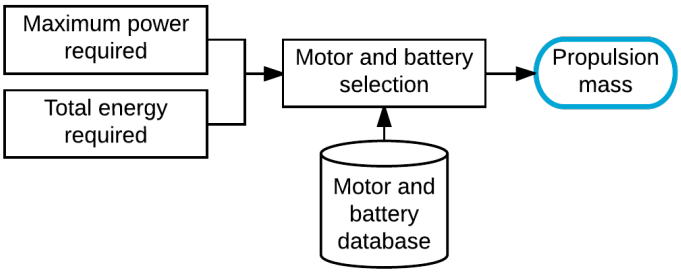

Figure 9.10: Flow diagram for the propulsion analysis

9.6.2. Propeller

For the quadcopter configuration as well as the fixed-wing configuration the propellers of the UAV need to be chosen in such a way that the motor is producing thrust as efficiently as possible. In Chapter 10 and Table 9.1, many parameters of the propeller were already determined. However, an overview can be found in Table 9.4 for the quadcopter and Table 9.5 for the fixed-wing module

Additionally, the material of the propeller needs to be determined. Generally, light weight propellers are made out of carbon fiber, plastic or wood. Wooden propeller are heavier and more expensive than the other two options, so this material is deemed infeasible. Propellers made of carbon fiber cost almost twice as much as those made of plastic. Nevertheless, they produce much less vibration and noise because of their high rigidity. They are also much lighter and stronger as well as more suitable for the motor with high angular velocities. Therefore, all propellers will be made out of carbon fiber.

Conclusively, for the quadcopter as well as the fixed-wing, *APC propellers* were chosen. These are designed to produce a constant lift coefficient across the blade section, making them as efficient as possible. Due to this, it is not possible to determine the exact spanwise chord and twist distribution on the blade. For the fixed-wing configuration a 10×10E propeller was chosen, and the quadcopter will have a 13×8E propeller, as this is optimal for endurance. The first number denotes the diameter of the blade in inches, while the second represents the theoretical forward advance in one revolution of the blade also in inches. A conversion table can be found at the website of *APC propellers*, which determines the pitch angle.

Table 9.4: Electric propeller parameters of the quadcopter

Parameter	Symbol	First iteration	Second iteration	Third iteration	Unit
Diameter	D_b	11	12	13	in
Chord	c	0.04	0.04	0.05	m
Pitch	p	6.5	7	8	m
Number of blades	N_b	2	2	2	-
Mean efficiency	η_{mean}	0.66	0.67	0.78	-
Material	-	Carbon Fibre	Carbon Fibre	Carbon Fibre	-

Table 9.5: Electric propeller parameters of the fixed-wing

Parameter	Symbol	First iteration	Second iteration	Third iteration	Unit
Diameter	D_b	10	10	10	in
Pitch	p	4	7	10	m
Number of blades	N_b	2	2	2	-
Mean efficiency	η_{mean}	0.77	0.81	0.85	-
Material	-	Carbon Fibre	Carbon Fibre	Carbon Fibre	-

9.6.3. Motor

The motor is chosen based on the propeller and the necessary constant power and burst power. Generally, brushless outrunners motors are used, as they are very efficient and have a high power to weight ratio whilst being less noisy when compared to brushed motors. Additionally, they are also simpler and have a longer cycle lifetime. Another advantage is the fact that there is no power loss in the brushes or in reduction gears, which occurs for brushed DC motors.[5]

There are two types of brushless DC motors, out-runner and in-runner. Out-runner motors have magnets woven around the winding array, while in-runner motors spin the magnets inside the circular coil. In-runner motors can be smaller as the body of the motor is static. However, the out-runner configuration can produce more torque. Therefore, brushless direct current in-runner motors are normally used for smaller UAVs under 100 g, while out-runner are chosen for anything heavier.

Not only the efficiency of the motor is important, also the KV constant which specifies how many revolutions per minute the motor will turn when one volt is put into the unloaded system, is of use. Special attention should be paid to the compatibility of the motor and rotor combination. A smaller KV value and the motor has to spin too fast to generate enough thrust. If the KV value is too large, the motor may get overloaded and thus unable to handle the loads at high throttle. Additionally, it is is possible that the motor will spin at a lower efficiency regime [12].

As can be seen from Tables 9.1 and 9.6, the first iteration for the quadcopter was performed with an engine which has a smaller KV constant and with a 11 in diameter propeller. Nevertheless, the next two iterations have an engine with a higher KV value with first a 12 in propeller and then a 13 in propeller. The rotor and motor combination of the third iteration will mean a decrease in motor efficiency of 3 %.[6] However, as the diameter of the propeller increases, the hover efficiency also increases due to a decrease in disc loading.

For the fixed-wing configuration the same engine was chosen as for the quadcopter configuration, which is the *RimFire .10*. This was done, first of all, because this engine meets the requirements regarding the climb performance. Additionally, this would decrease the cost of the maintainability since the same engine is chosen for the quadcopter.

[5] `www.jiaats.com/Journals-Pdf/March-2015/jcme/Jcme-11.pdf`, last accessed: 0021-06-2017

[6] `www.apcprop.com/Articles.asp?ID=262`, last accessed: 2017-06-21

Table 9.6: Electric motor parameters

	Quadcopter		Fixed-wing	
Parameter	**1st iter.**	**2nd & 3rd iter.**	**1st & 2nd iter.**	**Unit**
Motor type	Mk4008	RimFire .10	RimFire .10	-
RPM constant	600	1250	1250	$\mathrm{rpm\,V^{-1}}$
Constant power	290	325	325	W
Burst power	310	390	390	W
Voltage range	11.1 to 22.2	7.4 to 11.1	7.4 to 11.1	V
Propeller range	10 to 16	10 to 14	10 to 14	in
Mass	108	71	71	g
Dimensions	40×8	35×30	35×30	mm

9.6.4. Power source

For long endurance quadcopters the specific energy is of utmost importance, whilst simultaneously taking into account a high enough specific power for the motors. Since the drone can be classified as a small UAV, generally only three options are considered: combustion engines, electric engines and a hybrid version [61].

Small UAVs with a combustion engines are generally not considered feasible for independently driven propellers, as the engine is heavier and much more sensitive to the operating conditions. The latter reduces the reliability of the throttle response for the auto-piloted stability and control. It is also possible to have a hybrid solution where a central engine or generator is used in combination with battery packs for buffer. Nonetheless, both of these solutions would increase the size and the weight of the quadcopter, which in turn means that a variable pitch rotor is needed to ensure enough thrust control in a short reaction period. Therefore, the current simplicity and reliability would be reduced with such a concept.

Fuel cells could be a future alternative due to their constant improvement in recent years. However, at the moment fuel cells are infeasible due to their extremely low specific power. Additionally, they are not compact in size, even though they have a larger specific energy than any batteries. Any fuel cells that do have a larger specific power, are too unreliable to be used as a power source [1].

Nickel–metal hydride batteries could also be used, since they are cheaper and have a longer cycle life. However, they have a low specific energy compared to lithium batteries and are heavier. Nickel-cadmium batteries could be used for small to medium size quadcopters but their meager specific energy, limits the endurance of the quadcopter such that it is not able to perform its mission. This type of battery does have the highest current output and is even cheaper than nickel–metal hydride batteries. Lithium based batteries are preferred due to their high discharge rate and high specific energy. Specifically, lithium polymer batteries are optimal for the design of the UAV as these have the highest specific energy and current ratings, compared to all lithium batteries. The first characteristic is beneficial for the endurance, the latter is needed for the payload [12, 20, 34].

The final battery choice was determined from the engine *RimFire .10*. According to the manufacturer, the *GPMP0623* battery would be the optimal configuration. The total battery weight will be split into two separate parts, both with a 3S3P battery. This is a 11.1 V, 9600 mA h battery.

9.7. Recommendations and Further Improvements

For the overall quadcopter performance and propulsion there are two main points that could be improved. The first is an in-depth maneuvering analysis. As it is of particular importance for military operations. For now it has been assumed that the quadcopter only hovers in the target area to assist the soldiers. In reality, it will need to maneuver around buildings, which will require more power and an analysis of its maneuvering capabilities.

The second recommendation is a heat analysis of for the propulsion performance of the batteries. Due to the broad operating temperature range of the UAV, the performance of lithium polymer and lithium-ion batteries are drastically affected. All batteries have a discharge temperature around 20 deg for maximum service life.[7] As such below and above this temperature the performance and lifetime will change. This will need to be analyzed.

[7] batteryuniversity.com/learn/article/discharging_at_high_and_low_temperatures, last accessed: 2017-06-20

II-10

Aerodynamic Analysis

The performance parameters as mentioned before in Chapter 9 depend highly on the aerodynamic properties of the Unmanned Aerial Vehicle (UAV). In this chapter the design and analysis of the aerodynamics will be explained for the quadcopter and the fixed-wing configuration. Furthermore the acoustics of the UAV will be discussed in Section 10.7.

10.1. Assumptions

To be able to perform the aerodynamic design and analysis for this project with the available knowledge, equipment and within the given timespan, some assumptions had to be made. They are presented below:

Quadcopter configuration

QC-AA-I The flow through the rotor is one-dimensional, quasi-steady, incompressible, inviscid, and behaves as an ideal fluid.

QC-AA-II The radius of a plane perpendicular to the control volume at the rotor disc equals the rotor radius.

QC-AA-III Uniform flow is assumed. This causes the lowest induced power consumption for the quadcopter. This means that the thrust varies only linearly with the blade radius [17].

QC-AA-IV There is not interaction between different blade elements. This means that it will not include any effects the blade elements have on each other, therefore making it an independent two-dimensional problem with an ad hoc solution [30].

QC-AA-V All the forces on each blade element are determined by the aerodynamic coefficients acting on it. Therefore, it can be assumed that the power coefficient is equal to the torque coefficient. This is due to the fact that the total power is determined from the thrust coefficient, making it equal to each other when made dimensionless [17, 18, 30].

Fixed-Wing configuration

FW-AA-I The interaction between the wing and the body is not taken into account in the calculations. Usually the performance of a wing decreases when it has more surface area close to the body. Therefore this assumption is compensated for by linearly grading wing planforms with more area close to the body negatively.

FW-AA-II The influences of the propeller on the aerodynamic properties of the wing and the tail are neglected. In reality the extra airspeen underneath the tail will slightly reduce its effectiveness which will increase the size that the tail needs to have, and the suction over the body towards the propeller will increase the energy of the airflow which will reduce the drag produced by the body.

FW-AA-III The 2D evaluation of the body is assumed to represent the evaluation of the whole 3D body. This assumption is driven by availability of time and equipment. It is a 'best we can do' evaluation. In reality the 3D shape of the body will create a flow in the y-direction of the body as well. Since the body is higher than it is wide, and airflow tends to separate when the curvature of the object changes too fast, it can safely be assumed that the flow in y-direction will be laminar at least as long as it is in the shown simulations. This means that the simulations without flow separation can be trusted as reasonably well, but after flow separation is visible in these simulations, there is no way of telling if how reliable the results are. What we can predict for this assumption is that it will reduce the performance of wings with a lot of area close to the body more, so again this is a reason to punish these types of wing planforms in the trade-off.

FW-AA-IV A steady state simulation was used. This makes the program ignore higher order terms which makes simulating faster and makes convergence easier at the cost of some reliability. This is not deemed too much of a problem since the other assumptions mean the results can only be used as a preliminary estimation anyway.

10.2. Approach

As can be seen in Figure 10.1, the flow diagram of the aerodynamic approach of the quadcopter is fairly simple. However, its complexity stems from its iterative nature.

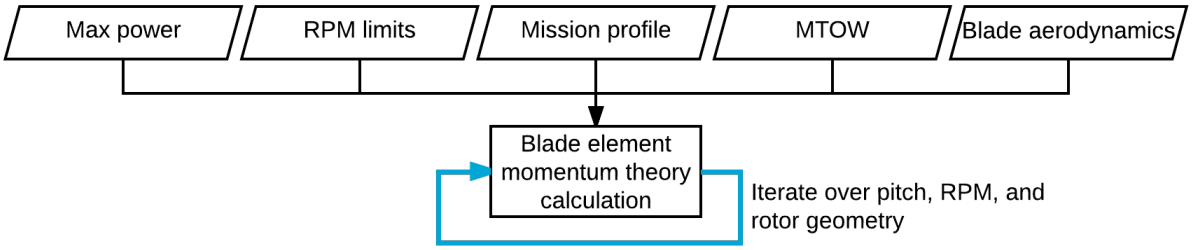

Figure 10.1: Flow diagram of the blade element theory including momentum theory

10.3. Quadcopter Design

In Section 9.3, momentum theory was used to determine the rotor performance. However, as it gives limited level of detail on the analysis, a combination between blade element theory and momentum theory was used to calculate the aerodynamic forces and torques acting on the rotor [9, 17].

10.3.1. Reference model

In Blade Element Momentum Theory (BEMT) the propeller is divided into a finite number of independent blade sections. Each blade section acts as a two dimensional airfoil that produces aerodynamic forces and moments. Force equilibrium is applied in combination with axial and angular momentum theory which produces a set of non-linear equations that can be solved by iterating along each blade section [9].

BEMT does not take into account three-dimensional flow effects such as the change in induced velocity due to the shedding of tip vortices, or an additional angular acceleration from the rotation of the propeller. It is possible to include this by adding empirical correction factors [18].

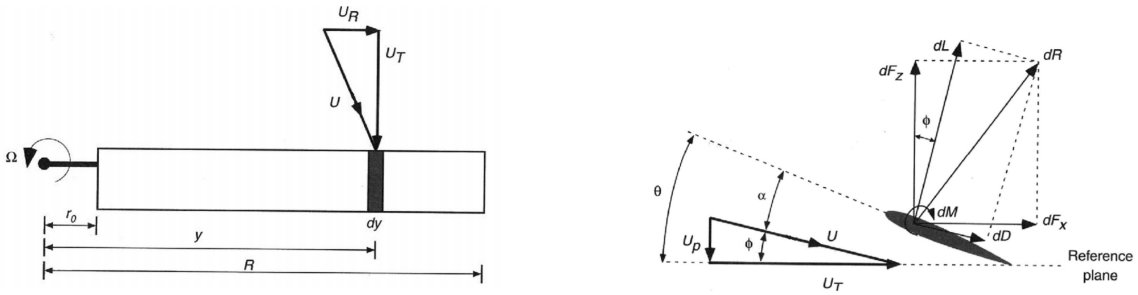

(a) Top view of rectangular blade element

(b) Side view of blade element with force equilibrium

Figure 10.2: Blade element model [35]

The aerodynamic performance of the propeller is calculated by integrating the loads caused by the airflow at each blade element over the whole length of the blade, as found per Figure 10.2a. In Figure 10.2b, the reference frame for the flow velocities experienced by the blade, as well as the aerodynamic forces acting on it can be seen. The blade was sectioned into 16 blade elements, as a number between 5 to 20 had to be chosen and 16 allows for an easy convergence.

10.3.2. Input parameters

In order to use BEMT, first some input values need to be known. First to fall the complete rotor geometry needs to be determined, which is done in Section 10.3.2. Additionally, it is necessary to know the mission profile, which determines the complete flight conditions of the rotor, this was already done in Chapter 2.

Rotor geometry

For the rotor geometry, values such as the number of blades, the radius, the chord distribution or the twist distribution need to be calculated or assumed. In Chapter 9 it was already determined that there would be two propellers per motor, with each a diameter of 11 in for the first iteration and 13 in for the last one.

However, the chord and twist distribution, as well as the blade taper were assumed to be constant, without an optimal value. The assumption of constant chord distribution is still valid as this is true for most quadcopters. An example of such a quadcopter is the Y4-Triangular configuration quadcopter [9]. On such quadcopters, the airfoils need to have more camber to produce a larger thrusts to torque ratio needed. As the local Angle of Attack (AOA) is lower for rectangular blades, making it necessary to produce lift at smaller angles of attack.

The propeller performance increases when the blade has an ideal twist distribution, as calculated from Equation (10.1), where θ_t is the ideal pitch angle, and y the radial distance from the blade hub. However, as it is easier to manufacture linearly twisted blades, and the performance only decreases marginally with around 2 % [34], it was determined that the propellers would have linearly twisted blades. To determine the pitch distribution of the linearly twisted blade Equation (10.2) is used, where θ_0 is the collective pitch angle θ_{tw} is the angle of twist between the hub of the motor and the tip.

$$\theta(y) = \frac{\theta_t}{y} \tag{10.1}$$

$$\theta(y) = \theta_0 + y\theta_{\text{tw}} \tag{10.2}$$

Lift and drag curve

For the selection of the airfoil, the two most important parameters are the maximum lift coefficient and the lift over drag ratio. It is preferred to have both as large as possible, as this will increase the maximum thrust produced by the airfoil, and decrease the power necessary, which will increase the proficiency of the propeller.

By using the criteria stated above and the list of the considered airfoils, the most optimal airfoil for the rotor is the *USNPS4*. As can be seen from Figure 10.3, the maximum lift coefficient of this airfoil is 1.69 It also has a maximum lift over drag ratio of 70 at an AOA of 5 deg.

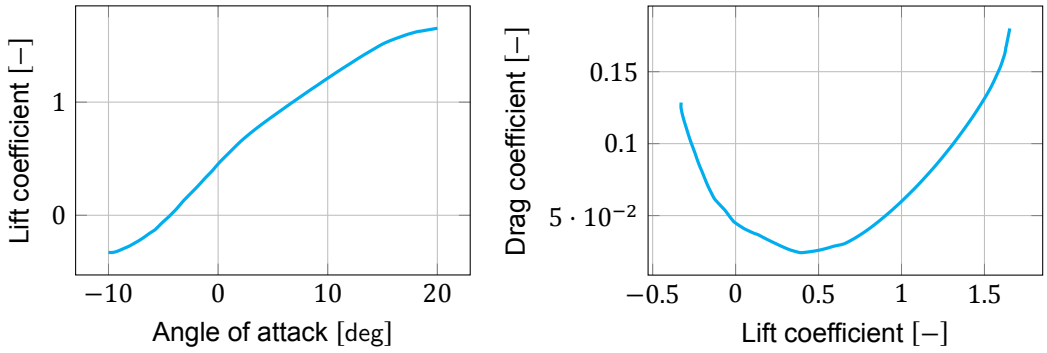

(a) Lift coefficient as a function of angle of attack

(b) Drag polar

Figure 10.3: Data of chosen quadcopter rotor airfoil

10.3.3. Output calculations

As BEMT uses an iterative approach, in the following subsection the calculations necessary for determining this solution will be given. Firstly, it is necessary to determine the flow characteristics, such as the velocities and the angles.

Velocities

First of all, it is necessary to determine the velocity components at any radial distance y from the rotational axis of each blade element. The out-of-plane velocity component perpendicular to the rotor can be calculated by adding the climb velocity V_C to the induced velocity v_i, both calculated in Chapter 9. The in-plane component, which is taken tangent to the rotor is determined from angular velocity of the motor and the distance from the motor.

$$U_p = V_C + v_i \tag{10.3}$$

$$U_T = \Omega y \tag{10.4}$$

$$U = \sqrt{U_T^2 + U_P^2} \tag{10.5}$$

As the propeller blade has a fixed pitch angle, the local velocity vector will create a local inflow angle on the section, which can be determined by the empirical relation Equation (10.6) [35]. This equation is dependent on the polar lift slope C_{L_α}, the number of blades N_b, the dimensionless chord $\frac{c}{R}$. From here, the local AOA can be calculated If θ is the pitch angle at a blade element then the AOA can be calculated by Equation (10.7).

$$\frac{v_i}{\Omega y} = \frac{C_{L_\alpha} N_b \frac{c}{R}}{16\pi y}\left[-1 + \sqrt{1 + \frac{32\pi\theta y}{C_{L_\alpha} N_b \frac{c}{R}}}\right] \tag{10.6}$$

$$\alpha = \theta - \frac{v_i}{\Omega y} \tag{10.7}$$

Aerodynamic coefficients
After having established the inflow characteristics, it is possible to calculate the aerodynamic forces and moments. The lift and drag coefficients of each blade section can be determined by using standard two-dimensional airfoil properties. From these, the thrust and torque of the complete propeller can be determined by summing over each single element, as stated by Equations (10.8) and (10.9). The final thrust coefficient is a funtion of the solidity σ, the lift coefficient C_l and the distance y, while the power coefficient also depends on the drag coefficient C_d, and the flight path angle ϕ. It must be noted that the power coefficient is equal to the torque coefficient, as steady, symmetrical flight is assumed.

$$\begin{aligned} \mathrm{d}C_T &= \frac{\mathrm{d}T}{\rho A \left(\Omega R\right)^2} \\ &= \frac{1}{2}\sigma c_l y^2 \,\mathrm{d}y \end{aligned} \tag{10.8}$$

$$\begin{aligned} \mathrm{d}C_Q = \mathrm{d}C_P &= \frac{\mathrm{d}Q}{\rho A \left(\Omega R\right)^2 R} \\ &= \frac{1}{2}\sigma \left(\phi c_l + c_d\right) y^3 \,\mathrm{d}y \end{aligned} \tag{10.9}$$

The propulsive efficiency is generally of the utmost importance when comparing different propeller geometric and different operating conditions. It is the ratio of the power transferred to the air moving through the disc to the power required to rotate the propeller. To calculate the efficiency of the complete propeller system, an additional electric efficiency term is added. The value of which determines what percentage of the electrical power available of the battery is delivered to the mechanical power produced by the motor, and can be calculated using Equation (10.11). As it was determined that no electronic speed controller was needed, V denotes the battery voltage, and I, the current supplied to the motor.

$$\eta_{\text{prop}} = \frac{TV_\infty}{2\pi\Omega Q} = \frac{1}{2\pi}\frac{C_T}{C_Q}J \tag{10.10}$$

$$\eta_{\text{elec}} = \frac{2\pi\Omega Q}{VI} \tag{10.11}$$

Empirical corrections
As already mentioned in Section 10.1 the BEMT model is a two-dimensional estimation of the aerodynamic characteristics, thus blade elements are independent. However, for blades with a finite aspect ratio the inflow characteristics change, depending on the span, affecting the efficiency of the propeller. In order to take these spanwise dependencies into account, empirical corrections are implemented in the calculations, which are the tip loss factor and the Mach effects.

Tip loss factor The lift produced by the rotor goes to zero when increasing the radial distance from the hub. This is due to the formation of trailed vortices. To include this effect, the effective blade radius becomes smaller with a factor B, thus decreasing the rotor area. It can be estimated using Equation (10.12), which according to [34, 35] was determined form empirical data to be applicable over a range of different geometries.

$$\begin{cases} B = 1 - \frac{0.006}{N_b} & \text{for } C_T < 0.006 \\ B = 1 - \frac{\sqrt{2.27 C_T - 0.01}}{N_b} & \text{for } C_T > 0.006 \end{cases} \tag{10.12}$$

Mach effects As the Mach number of the blade tips might be larger than 0.725, compressiblity effects need to be taken into account for the calculation of the lift coefficient. This is done by using the Prandtl-Glauert correction factor. Compressibility effects become more important in horizontal flight and vertical climb, as a higher engine setting is needed, making the advancing blade tip Mach number approach transoinic conditiions.

10.3.4. Results

To find the optimum rotor diameter and pitch of the quadcopter, the hover power needs to be minimized. The first thing that is noticeable is the fact that in Figure 10.4b the optimum diameter will always be 13 in, independent of the propeller chord. To subsequently choose the right propeller chord, one has to also look at the cruise power draw, which increases when decreasing the chord. This means that a higher propeller chord increases the cruise performance. As such a chord equal to 0.5 m was chosen, as a chord of 0.6 m would have decreased the efficiency of the quadcopter due to the low aspect ratio of the blade. Finally, the propeller pitch with these values is 8.4 deg when looking at Figure 10.4a.

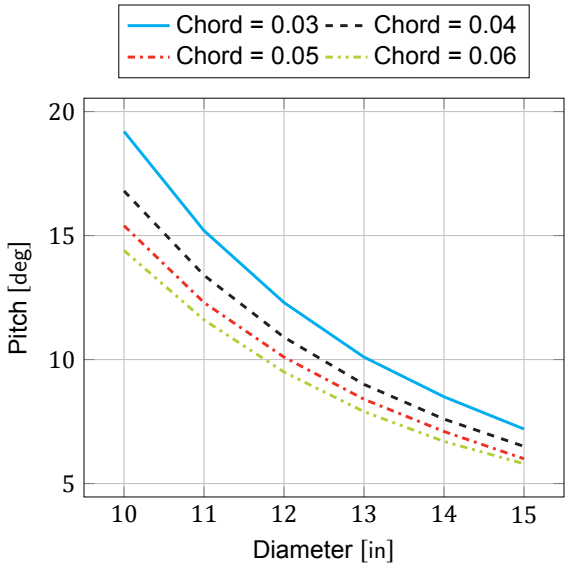

(a) Optimum propeller pitch when known blade chord and diameter

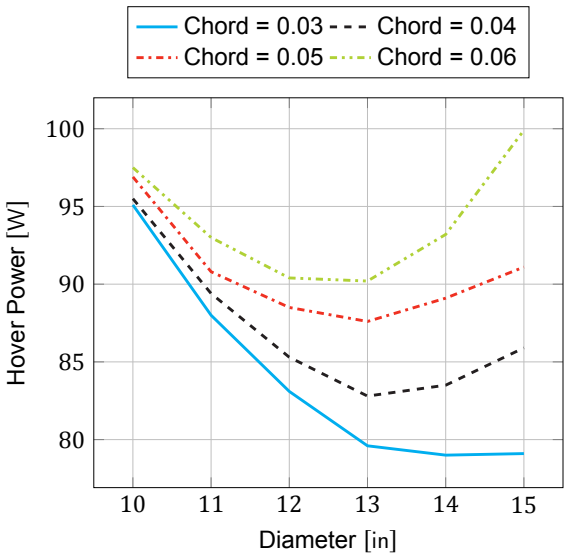

(b) Hover power over rotor diameter diagram

Figure 10.4: Quadcopter aerodynamics results for varying chord length

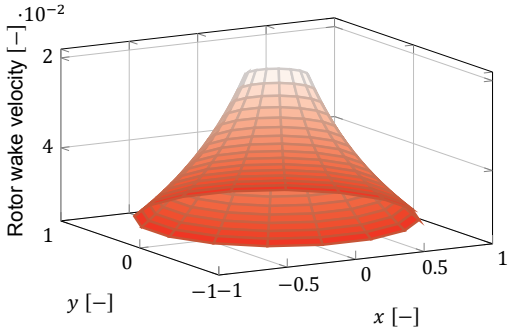

(a) Velocity out of rotor blade in the hover condition

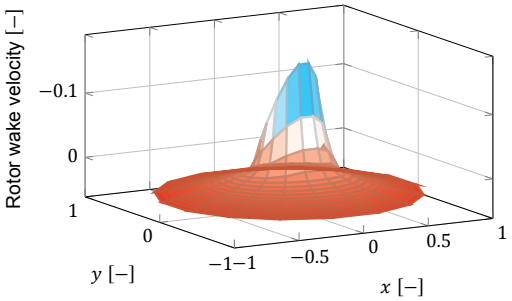

(b) Velocity out of rotor blades during cruise

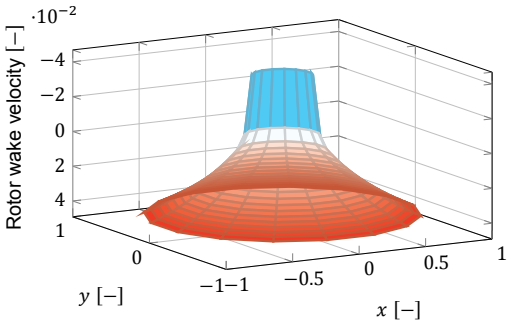

(c) Velocity out of rotor blades during climb

Figure 10.5: Blade element theory wake calculations

Another important thing to note is the propeller behaviour during cruise. A measure of the velocity of the wake just outside the propeller blades for a square propeller is given in Figure 10.5. Note that negative values indicate a velocity opposed to the normal direction. This is an indicator of the limitations of the propeller. In Figure 10.5a, the air velocity profile for the hover condition is shown. Clearly, the velocity increases towards the edge of the rotor. Thus, the tip will be loaded the heaviest. In Figure 10.5b, the profile is shown for the cruise condition. Here the beginning retreating blade stall (where the inside part of the blade moving against the quadcopters velocity stalls due to velocity difference) is clearly visible as the spike in the center. This indicates that increasing velocity of the quadcopter further might make it unstable due to half the rotor being negatively loaded, creating a rolling moment. Lastly, Figure 10.5c shows the wake during climb. The effect of the increased inflow velocity is clearly shown. Here, the inflow causes the inner part of the radius of the blades to have a negative AOA, generating downforce. Thus, increasing the velocity further is unwanted.

10.3.5. Verification and validation

It is possible to verify the code of the model by performing unit and system tests. However, in order to validate the BEMT model, it is necessary to perform either a wind-tunnel test or a propulsion test. It must be stated that, according to [35], BEMT overestimates the theoretical efficiency of the propellers by 5 % to 10 %.

For the verification of the code, mainly equations and syntax had to be checked for possible errors. This was done by using `print` statements after running the code. This way any possible errors within for example dictionaries or lists could be determined. Furthermore, the syntax of the code was verified by python itself so no additional measures had to be taken.

A unit test was performed to check if each equation separately produced to correct results. Simultaneously, system testing of the full model were performed by inserting a simplified model into the iterative program. In this case a blade element with constant chord and pitch, and a linear lift slope with zero-lift AOA airfoil was implemented in the code. As [35] had some examples with these kind of blades, it was possible to check the code.

It should be noted that convergence of the BEMT model, with a nonlinear set of equations is not guaranteed. Usually, some convergence enhancing techniques need o be used, such as under-relaxation to get a result when linear airfoil section properties are used.

10.3.6. Recommendations

For the time frame and scope of this project, it was assumed that the quadcopter was in steady, horizontal and symmetric flight. Thus, for the model only linear approximations were used. However, during the mission the quadcopter will experience a variety of mission profiles as it tailors to the needs of the soldiers during close range operations. It is possible to use BEMT for forward flight and climbing, however this would make the problem significantly more non-linear. According to [35] when non-linear properties are used, such as stall effects in horizontal flight, then obtaining convergence will be significantly more difficult. Therefore, as already stated in Chapter 9, it is more feasible to determine the aerodynamic coefficients from testing.

10.4. Fixed-wing Design

In this section the evaluated design parameters specific for the aerodynamics of the fixed-wing configuration will be introduced. They will be presented with their respective performance characteristics and the best option for the UAV will be chosen. How these values are calculated will be explained in Section 10.5.

10.4.1. Wing airfoil selection

After the an initial size, layout, and flight condition of the fixed-wing configuration was calculated in Chapter 4 an airfoil had to be chosen for the wing.

To make the initial selection of the airfoils that are used in the trade-off, all low Reynolds number airfoils without flap mentioned in [53] were evaluated based on the given wind tunnel acquired lift- and drag-polars at a Reynolds number of 200 000. This is the tested condition closest to the value of our initial estimation of the Reynolds number, which was equal to 250 000. This estimation is based on a desired loiter velocity of 15 m s^{-1} and a mean aerodynamic chord length of 0.26 m. This speed and planform layout come from the preliminary design characteristics as mentioned in Chapter 4.

From the 60 airfoils mentioned in this paper the best 11 were chosen to be included in the trade-off for this project. Since take-off should be hand-launchable, a low stall speed and thus a high $C_{L_{\max}}$ is required. All airfoils with a $C_{L_{\max}}$ value above 1.5 are determined feasible for this project except the *S1223* airfoil because it has an obvious disadvantage in drag over the other airfoils. Other airfoils that do not reach this $C_{L_{\max}}$ value but are much better in drag performance and still have a $C_{L_{\max}}$ of at least 1.25 were also included in the trade-off.

This list of airfoils is extended with the airfoils used by the different concepts shown in [8]. That is because these airfoils are currently used on a lot of other small scale aircraft.

This results in the following list of airfoils that are evaluated for this project,

- Chuch Hollinger *CH 10-48-13*
- Cody Robertson *CR 001*
- Eppler *E423*
- Wortmann *FX63137*
- NACA *22112*
- NACA *632615*
- Selig *S1210*
- Selig *S4083*
- Selig Ashok Gopalarathnam *SA7036*
- Selig Donovan *SD7062*
- Selig Giguere *SG6043*
- Jacobs *USNPS4*

These airfoils are evaluated in the simulation tool *XFLR5* on the wing planform determined in the initial sizing. The details of this analysis, and the reason why the output values were chosen, are explained in Section 10.5. The weights given to these values can be seen in Table 10.1.

Table 10.1: Wing airfoil trade-off weights

Group		Subgroup		Parameter		Target
Aerodynamics	60 %	Take-off	24 %	$C_{L_{\max}}$	24 %	max
		Cruise	6 %	$c_L/c_{D_{\text{cruise}}}$	3.6 %	max
				$C_{D_{\text{cruise}}}$	2.4 %	min
		Loiter	36 %	$C_{L_{\text{loiter}}}$	9 %	max
				$C_{D_{\text{loiter}}}$	16.2 %	min
				$C_{M_{\text{loiter}}}$	10.8 %	min
Structures	25 %			Max bending moment	5 %	min
				Airfoil thickness	10 %	max
				Average/max thickness	10 %	max
Stability	15 %			Stall behaviour	1.5 %	max
				$C_{M_{\max}} - C_{M_{\text{loiter}}}$ (ΔC_M)	9 %	max
				$\alpha_{\text{stall}} - \alpha_{\text{loiter}}$ $(\Delta\alpha)$	4.5 %	max

The take-off parameters are weighted at 24 % of the total because it determines whether or not it is possible to perform a hand-launch. A high maximum C_L is preferred for hand-launchability. Cruise parameters are rated relatively low because it takes up only a small part of the mission. In cruise a high speed and a low drag are preferred. So $c_L/c_{D_{\text{cruise}}}$ is preferred as high as possible and C_D is preferred as low as possible. Loiter is rated the highest from all subgroups of aerodynamics because the largest amount of time will be spent in this flight mode. A high C_L in the optimum loiter condition is desired because it allows for a low speed and a more accurate view of the target area. A low drag is optimal to increase the endurance and a low moment coefficient is favored to keep the tail smaller and therefore the weight down.

For structures, the bending moment around the root chord is preferred as small as possible so that the wing structure can be lighter. For structures a thick airfoil is preferred, this gives a higher moment of inertia and makes the structure stronger. Also the average thickness should be as high as possible, so that there are fewer thin pieces on the airfoil which would break more easily when there is an impact.

In the trade-off, all values are evaluated compared to the worst and the best value in that category. The best value is rated with a one and the worst is rated with a zero. Everything in between is rated linearly with their value. The trade-off values and grades are shown in Table 10.2. From this trade-off it is obvious that the best airfoil for this aircraft is either the *NACA22112* or the *SD7062* airfoil which both get a high grade that is less than 0.1 % apart from each other. The *SD7062* performs slightly better aerodynamically but the *NACA22112* performs clearly better for structural rigidity. Since there is only a small amount of weight assigned to the wings in the initial sizing, the *NACA22112* airfoil is chosen for the wing of this UAV. This airfoil will now be used to produce a new iteration of the planform design.

10.4.2. Wing planform selection

Now that the airfoil is chosen, a new optimized wing planform can be elected. From the initial sizing, a planform was determined where the wing can be taken apart in three pieces that each fit in the backpack. This means that the maximum length of one piece is 0.6 m and the whole wing can have a span of 1.8 m. The aspect ratio chosen in the initial sizing is 7 to balance the take off speed with the loiter efficiency. For a straight wing that means the wing area will be 0.46 m^2. This planform does not say anything about a taper ratio yet. Therefore in this second version of the wing planform design a trade-off will be made between different taper ratios.

Since a lot of low Reynolds number aircraft have small or no taper, taper ratios between one and 0.5 are evaluated in small steps. Apart from that, some smaller taper ratios up to a triangular wing (taper ratio 0) are added in bigger steps because they are not expected to win the trade-off. Elliptical wings are added as well because they give a lift distribution closest to the elliptical wing distribution, which is best for reducing induced drag. Usually these wings are not used in aircraft because they are difficult to produce and have bad stall characteristics.

Table 10.2: Wing airfoil trade-off

		Weight	CH10		CR-001		E423		FX 63137		NACA22112		NACA632615	
		[%]	Value	Score	Value	Score	Value	Score	Value	Score	Value	Score	Value	Score
$C_{L_{\max}}$	[-]	24.0	1.90	0.99	1.31	0.22	1.91	1.00	1.62	0.62	**1.29**	0.19	1.14	0.00
$^{C_L}/_{C_D}$cruise	[-]	3.6	14.7	0	24.9	0.87	15.6	0.08	20.6	0.50	**22.1**	0.63	21.0	0.53
$C_{D_{\text{cruise}}}$	[-]	2.4	0.067	0.00	0.019	0.91	0.056	0.21	0.029	0.72	**0.020**	0.91	0.023	0.84
$C_{L_{\text{loiter}}}$	[-]	9.0	0.860	0.28	0.503	0.99	0.724	0.55	0.503	0.99	**0.501**	1.0	0.501	1.0
$C_{D_{\text{loiter}}}$	[-]	16.2	0.061	0.00	0.020	0.98	0.050	0.26	0.025	0.87	**0.023**	0.91	0.024	0.89
$C_{M_{\text{loiter}}}$	[-]	10.8	-0.51	0.00	-0.27	0.70	-0.44	0.19	-0.35	0.47	**-0.16**	1.00	-0.27	0.72
$M_{\max}$	[N m]	5.0	24.3	0.02	16.8	0.80	24.4	0.00	20.9	0.37	**16.5**	0.83	14.9	1.00
$t_{\max}$	[%c]	10.0	12.8	0.72	7.3	0.00	12.5	0.68	13.7	0.83	**12.0**	0.61	15.0	1.00
$^{t_{\text{avg}}}/_{t_{\max}}$	[-]	10.0	0.65	0.56	0.65	0.60	0.65	0.60	0.60	0.32	**0.68**	0.72	0.62	0.42
Stall char.	[-]	1.5	2	0.50	3	1.00	3	1.00	3	1.00	**2**	0.50	3	1.00
ΔC_M	[-]	9.0	0.26	0.61	0.18	0.29	0.29	0.72	0.26	0.62	**0.18**	0.29	0.11	0.00
$\Delta\alpha$	[deg]	4.5	14.8	0.38	12.8	0.02	16.6	0.71	18.2	1.00	**14.9**	0.24	15.9	0.58
Weighed sum		**100 %**	**45.2 %**		**71.2 %**		**55.8 %**		**71.7 %**		**78.6 %**		**72.4 %**	

		Weight	S1210		S4083		SA7036		SD7062		SG6043		USNPS4	
		[%]	Value	Score	Value	Score	Value	Score	Value	Score	Value	Score	Value	Score
$C_{L_{\max}}$	[-]	24.0	1.87	0.95	1.25	0.14	1.23	0.11	1.54	0.51	1.57	0.56	1.63	0.63
$^{C_L}/_{C_D}$cruise	[-]	3.6	19.1	0.37	25.7	0.94	26.5	1.00	23.0	0.70	20.7	0.51	21.5	0.58
$C_{D_{\text{cruise}}}$	[-]	2.4	0.038	0.57	0.016	0.98	0.015	1.00	0.021	0.88	0.033	0.66	0.030	0.70
$C_{L_{\text{loiter}}}$	[-]	9.0	0.524	0.95	0.498	1.00	0.497	0.99	0.499	1.00	0.500	1.00	0.504	0.99
$C_{D_{\text{loiter}}}$	[-]	16.2	0.033	0.68	0.020	0.98	0.019	1.00	0.022	0.95	0.027	0.82	0.026	0.84
$C_{M_{\text{loiter}}}$	[-]	10.8	-0.37	0.40	-0.23	0.79	-0.22	0.84	-0.23	0.81	-0.32	0.55	-0.27	0.68
$M_{\max}$	[N m]	5.0	24.1	0.04	16.1	0.88	15.8	0.91	19.8	0.49	20.3	0.44	20.9	0.37
$t_{\max}$	[%c]	10.0	12.0	0.61	8.0	0.09	9.2	0.24	14.0	0.87	10.0	0.35	11.9	0.60
$^{t_{\text{avg}}}/_{t_{\max}}$	[-]	10.0	0.54	0.00	0.61	0.35	0.65	0.56	0.62	0.44	0.68	0.71	0.73	1.00
Stall char.	[-]	1.5	1	0.00	2	0.50	3	1.00	1	0.00	1	0.00	1	0.00
ΔC_M	[-]	9.0	0.36	1.00	0.17	0.27	0.18	0.27	0.26	0.61	0.23	0.48	0.25	0.58
$\Delta\alpha$	[deg]	4.5	17.7	0.91	12.8	0.02	12.7	0.00	16.8	0.75	17.2	0.82	16.5	0.69
Weighed sum		**100 %**	**64.1 %**		**70.0 %**		**75.4 %**		**78.5 %**		**68.7 %**		**77.5 %**	

In the scale of this UAV, it would be possible to make the wings out of foam with a Computer Numerical Control (CNC) machine though, so this planform shape is included into the trade-off to assess the possible gains of this more difficult shape.[1] The taper ratio that is normally used in large scale aircraft to mimic this elliptical lift distribution while still being relatively easy to produce is a taper ratio of $3/5$. This ratio is included in this study as well. Concluding, the following wing planforms are evaluated with the tips aligned in the front, middle, and rear as shown in Figure 10.6:

- Taper ratio $5/5$
- Taper ratio $5/6$
- Taper ratio $5/7$
- Taper ratio $5/8$
- Taper ratio $2/3$
- Taper ratio $5/9$
- Taper ratio $5/10$
- Taper ratio $5/12.5$
- Taper ratio $5/15$
- Taper ratio 0
- Elliptical wing

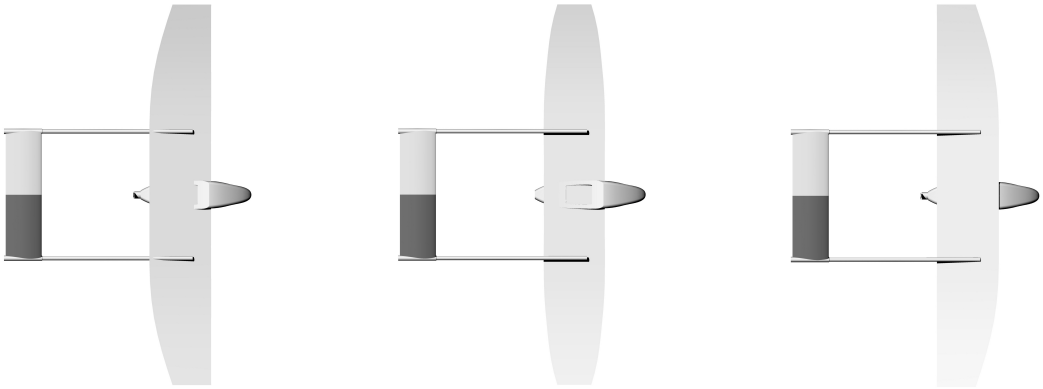

(a) Aligned to the front (b) Aligned to the center (c) Aligned to the rear

Figure 10.6: Alignment of taper in top-view

The trade-off criteria and their weights used in the trade-off are shown in Table 10.3. They are quite similar to the ones used in the airfoil selection with the following differences, the influence of the body on the wing performance (summarized as interaction in the table) is taken into account now. The 3D wing performance is decreased by the disturbance caused by the body, so a wing with a higher percentage of area away from the body is aerodynamically speaking desired. In the trade-off this means that a wing with a smaller root chord is preferred for aerodynamics. This criterion is graded as semi important.

For structures there are fewer parameters that will change per design choice since the same airfoil is used in all planforms and thus the cross section will always be the same for each design option. However, a new parameter is added as well, this is called the number of panels. It is the number of sections needed to make the 3D model of the wing. It is used in the trade-off to represent the difficulty of producing the wing in real life. Because of the reduction in parameters the overall grade for structures is reduced a little. Both parameters in structures are graded equally important.

In stability, an extra parameter controllability is added where the ease to include ailerons and winglets on the wing is evaluated. For efficient winglets a swept back wing is preferred and for ailerons a straight edge at the rear of the wing is preferred. How values for these parameters are found is explained in Section 10.5. The values are summarized in Table 10.4 and their trade-off is found in Table 10.5

As seen in Table 10.5 a tip aligned to the rear will always win this trade-off irrespective of taper ratio. Furthermore, the planform that wins this trade-off is the one with the taper ratio of $5/8$. This is mainly caused by its good aerodynamic performance during loiter and the fact that the only field in which it performs bad is the performance during cruise which is the part of the mission that is least important of all parameters.

10.4.3. Tail airfoil selection

The airfoil selection done for the tail is done in the same way as for the main wing with the difference that the tail planform is already determined by the stability department so there is no iteration on the planform that follows up the airfoil selection.

The airfoils selected for the final trade-off are also taken from the same windtunnel research paper [53]. This time the airfoils are selected on their performance in drag and $C_{L-\alpha}$ at angles of attack between 0 deg and 5 deg. The following list of airfoils was selected where the last five are symmetric airfoils:

[1] `www.rcgroups.com/forums/showthread.php?184049-CNC-Foam-Cutting-Machine`, last accessed: 2017-06-16

Table 10.3: Wing planform trade-off weights

Group		Subgroup		Parameter		Target
Aerodynamics	60 %	Take-off	18 %	$C_{L_{\max}}$	18 %	max
		Cruise	6 %	$c_L/c_{D_{\text{cruise}}}$	3.6 %	max
				$C_{D_{\text{cruise}}}$	2.4 %	min
		Loiter	24 %	$C_{L_{\text{loiter}}}$	6 %	max
				$C_{D_{\text{loiter}}}$	7.2 %	min
				$C_{Di_{\text{loiter}}}$	3.6 %	min
				$C_{M_{\text{loiter}}}$	7.2 %	min
		Interaction	12 %	c_{root}	12 %	min
Structures	20 %			Max bending moment	10 %	min
				Number of panels	10 %	min
Stability	20 %			Stall behaviour	3 %	max
				$C_{M_{\max}} - C_{M_{\text{loiter}}}$ (ΔC_M)	5 %	max
				$\alpha_{\text{stall}} - \alpha_{\text{loiter}}$ ($\Delta\alpha$)	5 %	max
				Controllability	7 %	max

- Eppler *E387*
- Gilbert Morris *GM15*
- Selig *S4083*
- Selig *S7055*
- Selig Donovan *SD7032*
- Dale House *DH4009*
- *NACA 0005*
- *NACA 0009*
- Quickee 500 *R14.0*
- Selig *S8025*

These airfoils are graded on the parameters as shown in Table 10.6 with their respective weights.

How the values for these variables are obtained are explained in Section 10.5. The trade-off is presented in Table 10.7

It is clearly visible from this trade-off that the *R14.0* airfoil is predicted to perform best on the tail. Therefore this airfoil will be used.

10.5. Fixed-wing Analysis

The analysis of the aerodynamics and stability of the design choices for the airfoil, wing planform, and tail were evaluated utilizing *XFLR5* in conjunction with data analysis performed in *MATLAB* [64]. The goal was to design a wing and tail combination that could achieve high lift capability at stall velocity, while still retaining a high level of aerodynamic performance during loiter. To re-iterate this is directly due to key design requirements of having a 2 h endurance and being able to fit in a standard infantry backpack. In order to tackle this problem, a wide set of airfoils and plan-forms were considered, As shown previously by the trade-off tables in this section. The first step in this process was the airfoil selection of the main wing. After, an optimal wing planform for the fixed-wing mission was selected. Followed, finally by tail airfoil selection and optimization.

10.5.1. Wing airfoil selection

In the selection process of the airfoil it is important to assess the performance of these airfoils at various Reynolds numbers in order to ensure that they can perform well on an actual wing planform. The reasoning behind this stems from a difference in Reynolds numbers along the wing sections due to taper. The tip section of the wing experiences a lower Reynolds numbers than the root section due to it's smaller chord length. This can be seen in Equation (10.13) as a smaller chord length, c, decreases the Reynolds number, Re. Therefore, to measure the sensitivity in performance of an airfoil to the Reynolds number, a standardized wing planform was defined for which the geometry is given by Table 10.8. In the same equation V represents the free stream velocity, ρ the density and μ is the dynamic viscosity of the air.

$$Re = \frac{\rho V c}{\mu} \tag{10.13}$$

Table 10.4: Wing planform trade-off values

		taper 5/6			Taper 5/7			Taper 5/8			Taper 2/3			Taper 5/9		
		Front	**Mid**	**Rear**	**Front**	**Mid**	**Rear**	**Front**	**Mid**	**Rear**	**Front**	**Mid**	**Rear**	**Front**	**Mid**	**Rear**
$C_{L_{\max}}$	[-]	1.26	1.26	1.26	1.27	1.27	1.27	1.28	1.28	**1.28**	1.29	1.29	1.29	1.29	1.29	1.29
c_L/c_Dcruise	[-]	22.02	22.02	22.02	22.03	22.03	22.03	22.11	22.11	**22.11**	22.13	22.13	22.13	22.17	22.17	22.17
$C_{D_{\text{cruise}}}$	10^{-2}[-]	1.908	1.908	1.908	1.964	1.964	1.964	1.963	1.963	**1.963**	1.959	1.959	1.959	1.956	1.956	1.956
$C_{L_{\text{loiter}}}$	[-]	0.682	0.682	0.682	0.689	0.689	0.689	0.657	0.657	**0.657**	0.664	0.664	0.664	0.673	0.673	0.673
$C_{D_{\text{loiter}}}$	10^{-2}[-]	3.60	3.60	3.60	3.62	3.62	3.62	3.34	3.34	**3.34**	3.39	3.39	3.39	3.45	3.45	3.45
$C_{Di_{\text{loiter}}}$	10^{-2}[-]	2.20	2.20	2.20	2.21	2.21	2.21	1.99	1.99	**1.99**	2.03	2.03	2.03	2.08	2.08	2.08
$C_{M_{\text{loiter}}}$	[-]	-0.177	-0.194	-0.211	-0.179	-0.208	-0.236	-0.173	-0.210	**-0.245**	-0.175	-0.213	-0.250	-0.177	-0.220	-0.264
c_{root}	[mm]	272	272	272	284	284	284	293	293	**293**	296	296	296	301	301	301
$M_{\max}$	[N m]	16.49	16.49	16.49	16.35	16.35	16.35	16.13	16.13	**16.13**	16.09	16.09	16.09	16.00	16.00	16.00
n_{panels}	[-]	3	3	3	3	3	3	3	3	**3**	3	3	3	3	3	3
Stall char.	[-]	2	2	2	2	2	2	1	1	**1**	1	1	1	1	1	1
ΔC_M	[-]	0.102	0.117	0.132	0.102	0.127	0.152	0.111	0.145	**0.179**	0.111	0.146	0.180	0.109	0.148	0.186
$\Delta\alpha$	[deg]	13.8	13.8	13.8	13.7	13.7	13.7	13.6	13.6	**13.6**	13.5	13.5	13.5	13.8	13.8	13.8
Controllability	[-]	1	2	3	1	2	3	1	2	**3**	1	2	3	1	2	3

		taper 5/10			Taper 5/12.5			Taper 5/15			Elliptical			Other	
		Front	**Mid**	**Rear**	**Front**	**Mid**	**Rear**	**Front**	**Mid**	**Rear**	**Front**	**Mid**	**Rear**	**Straight**	**Triangular**
$C_{L_{\max}}$	[-]	1.29	1.29	1.29	1.28	1.28	1.28	1.26	1.26	1.26	1.32	1.32	1.32	1.23	1.29
c_L/c_Dcruise	[-]	22.19	22.19	22.19	22.27	22.27	22.27	22.31	22.31	22.31	22.36	22.36	22.36	21.94	21.54
$C_{D_{\text{cruise}}}$	10^{-2}[-]	1.949	1.949	1.949	1.930	1.930	1.930	1.869	1.869	1.869	1.934	1.934	1.934	1.894	1.649
$C_{L_{\text{loiter}}}$	[-]	0.675	0.675	0.675	0.692	0.692	0.692	0.701	0.701	0.701	0.663	0.663	0.663	0.668	0.620
$C_{D_{\text{loiter}}}$	10^{-2}[-]	3.46	3.46	3.46	3.58	3.58	3.58	3.65	3.65	3.65	3.34	3.34	3.34	3.54	3.33
$C_{Di_{\text{loiter}}}$	10^{-2}[-]	2.09	2.09	2.09	2.18	2.18	2.18	2.24	2.24	2.24	2.00	2.00	2.00	2.16	1.99
$C_{M_{\text{loiter}}}$	[-]	-0.177	-0.226	-0.275	-0.181	-0.240	-0.299	-0.182	-0.247	-0.312	-0.174	-0.207	-0.240	-0.172	-0.299
c_{root}	[mm]	308	308	308	321	321	321	330	330	330	300	300	300	257	385
$M_{\max}$	[N m]	15.76	15.76	15.76	14.86	14.86	14.86	14.14	14.14	14.14	16.23	16.23	16.23	16.52	12.25
n_{panels}	[-]	3	3	3	3	3	3	3	3	3	22	22	22	3	3
Stall char.	[-]	1	1	1	1	1	1	1	1	1	1	1	1	2	1
ΔC_M	[-]	0.109	0.151	0.194	0.111	0.153	0.195	0.114	0.153	0.192	0.119	0.148	0.176	0.100	0.225
$\Delta\alpha$	[deg]	13.0	13.0	13.0	14.1	14.1	14.1	15.0	15.0	15.0	14.5	14.5	14.5	13.5	16.0
Controllability	[-]	1	2	3	1	2	3	1	2	3	1	2	3	2	2

Table 10.5: Wing planform trade-off grades

		Weight	taper 5/6			Taper 5/7			Taper 5/8			Taper 2/3			Taper 5/9		
		[%]	Front	Mid	Rear	Front	Mid	Rear	Front	Mid	Rear	Front	Mid	Rear	Front	Mid	Rear
$C_{L_{\max}}$	[0-1]	18.0	0.35	0.35	0.35	0.48	0.48	0.48	0.61	0.61	**0.61**	0.65	0.65	0.65	0.71	0.71	0.71
c_L/c_D cruise	[0-1]	3.6	0.24	0.24	0.24	0.25	0.25	0.25	0.29	0.29	**0.29**	0.30	0.30	0.30	0.32	0.32	0.32
$C_{D_{\text{cruise}}}$	[0-1]	2.4	0.18	0.18	0.18	0.00	0.00	0.00	0.00	0.00	**0.00**	0.02	0.02	0.02	0.03	0.03	0.03
$C_{L_{\text{loiter}}}$	[0-1]	6.0	0.65	0.65	0.65	0.71	0.71	0.71	0.39	0.39	**0.39**	0.46	0.46	0.46	0.55	0.55	0.55
$C_{D_{\text{loiter}}}$	[0-1]	7.2	0.14	0.14	0.14	0.10	0.10	0.10	0.99	0.99	**0.99**	0.84	0.84	0.84	0.64	0.64	0.64
$C_{Di_{\text{loiter}}}$	[0-1]	3.6	0.13	0.13	0.13	0.09	0.09	0.09	0.98	0.98	**0.98**	0.82	0.82	0.82	0.63	0.63	0.63
$C_{M_{\text{loiter}}}$	[0-1]	7.2	0.97	0.85	0.73	0.95	0.74	0.54	0.99	**0.73**	0.48	0.98	0.71	0.45	0.97	0.66	0.35
c_{root}	[0-1]	12.0	0.88	0.88	0.88	0.79	0.79	0.79	0.72	0.72	**0.72**	0.70	0.70	0.70	0.66	0.66	0.66
$M_{\max}$	[0-1]	10.0	0.36	0.36	0.36	0.38	0.38	0.38	0.41	0.41	**0.41**	0.42	0.42	0.42	0.43	0.43	0.43
n_{panels}	[0-1]	10.0	1.00	1.00	1.00	1.00	1.00	1.00	1.00	1.00	**1.00**	1.00	1.00	1.00	1.00	1.00	1.00
Stall char.	[0-1]	3.0	1.00	1.00	1.00	1.00	1.00	1.00	0.00	0.00	**0.00**	0.00	0.00	0.00	0.00	0.00	0.00
ΔC_M	[0-1]	5.0	0.01	0.13	0.25	0.01	0.22	0.41	0.08	0.36	**0.63**	0.09	0.37	0.64	0.07	0.38	0.69
$\Delta\alpha$	[0-1]	5.0	0.29	0.29	0.29	0.26	0.26	0.26	0.23	0.23	**0.23**	0.19	0.19	0.19	0.29	0.29	0.29
Controllability	[0-1]	7.0	0.00	0.50	1.00	0.00	0.50	1.00	0.00	0.50	**1.00**	0.00	0.50	1.00	0.00	0.50	1.00
Weighted sum	[%]	100 %	48.6 %	51.8 %	55.0 %	49.4 %	52.4 %	55.5 %	56.5 %	59.5 %	**62.5 %**	55.5 %	58.5 %	61.4 %	55.3 %	58.1 %	60.9 %

		Weight	taper 5/10			Taper 5/12.5			Taper 5/15			Elliptical			Other	
		[%]	Front	Mid	Rear	Front	Mid	Rear	Front	Mid	Rear	Front	Mid	Rear	Straight	Triangular
$C_{L_{\max}}$	[0-1]	18.0	0.64	0.64	0.64	0.55	0.55	0.55	0.36	0.36	0.36	1.00	1.00	1.00	0.00	1.63
c_L/c_D cruise	[0-1]	3.6	0.33	0.33	0.33	0.37	0.37	0.37	0.40	0.40	0.40	0.42	0.42	0.42	0.21	0.00
$C_{D_{\text{cruise}}}$	[0-1]	2.4	0.05	0.05	0.05	0.11	0.11	0.11	0.30	0.30	0.30	0.10	0.10	0.10	0.22	1.00
$C_{L_{\text{loiter}}}$	[0-1]	6.0	0.58	0.58	0.58	0.75	0.75	0.75	0.84	0.84	0.84	0.45	0.45	0.45	0.50	0.00
$C_{D_{\text{loiter}}}$	[0-1]	7.2	0.61	0.61	0.61	0.21	0.21	0.21	0.00	0.00	0.00	0.99	0.99	0.99	0.33	1.00
$C_{Di_{\text{loiter}}}$	[0-1]	3.6	0.60	0.60	0.60	0.21	0.21	0.21	0.00	0.00	0.00	0.96	0.96	0.96	0.33	1.00
$C_{M_{\text{loiter}}}$	[0-1]	7.2	0.96	0.62	0.27	0.94	0.52	0.10	0.93	0.47	0.00	0.99	0.75	0.52	1.00	0.10
c_{root}	[0-1]	12.0	0.60	0.60	0.60	0.50	0.50	0.50	0.43	0.43	0.43	0.66	0.66	0.66	1.00	0.00
$M_{\max}$	[0-1]	10.0	0.47	0.47	0.47	0.61	0.61	0.61	0.71	0.71	0.71	0.40	0.40	0.40	0.35	1.00
n_{panels}	[0-1]	10.0	1.00	1.00	1.00	1.00	1.00	1.00	1.00	1.00	1.00	0.00	0.00	0.00	1.00	1.00
Stall char.	[0-1]	3.0	0.00	0.00	0.00	0.00	0.00	0.00	0.00	0.00	0.00	0.00	0.00	0.00	1.00	0.00
ΔC_M	[0-1]	5.0	0.07	0.41	0.75	0.09	0.43	0.76	0.11	0.42	0.74	0.15	0.38	0.61	0.00	1.00
$\Delta\alpha$	[0-1]	5.0	0.03	0.03	0.03	0.39	0.39	0.39	0.68	0.68	0.68	0.52	0.52	0.52	0.19	1.00
Controllability	[0-1]	7.0	0.00	0.50	1.00	0.00	0.50	1.00	0.00	0.50	1.00	0.00	0.50	1.00	0.50	0.50
Weighted sum	[%]	100 %	52.2 %	54.9 %	57.6 %	49.5 %	51.7 %	53.8 %	46.7 %	48.4 %	50.1 %	55.4 %	58.4 %	61.4 %	48.0 %	58.8 %

Table 10.6: Tail airfoil trade-off weights

Group		Parameter		Target
Aerodynamics	40 %	$C_{L_{\text{trim}}}$	10 %	max
		$C_{D_{\text{trim}}}$	20 %	min
		$c_L/c_{D_{\text{trim}}}$	10 %	max
Stability	40 %	C_{m_α}	20 %	min
		C_{m_0}	20 %	min
Operability	20 %	α_{trim}	20 %	min

The flow diagram presented by Figure 10.7 details the process that was used in the *XFLR5* winning airfoil analysis. In summary, first a 2D *X-foil* analysis was performed for a large range of Reynolds numbers. From these results, a lifting line theory evaluation was performed to create a 3D result. This is done for all different airfoils after which a trade-off is performed and the airfoil is chosen. This process produced data outputs that were then used in the airfoil trade-off presented in the previous section. The result of this trade-off was the selection of the NACA22112 airfoil which is shown in Figure 10.8. Furthermore, the results of the simulation for this airfoil are presented by Figure 10.9. Important values that can be seen in these plots are summarized in bold face in Table 10.2

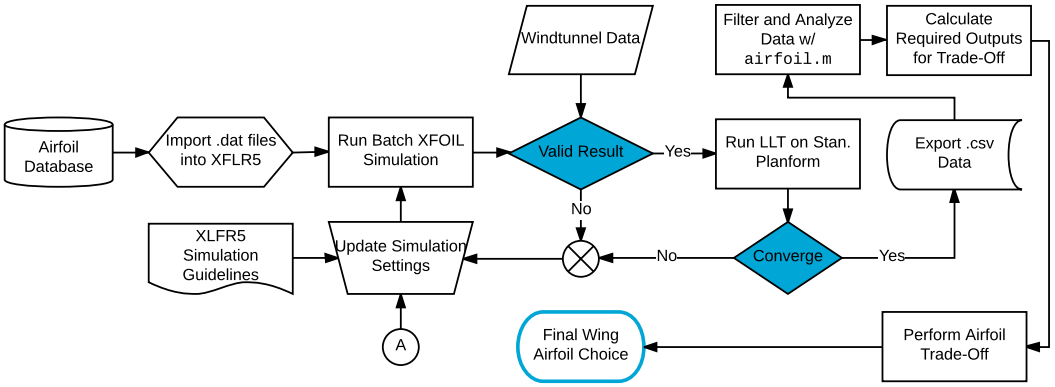

Figure 10.7: Wing arfoil analysis flow diagram

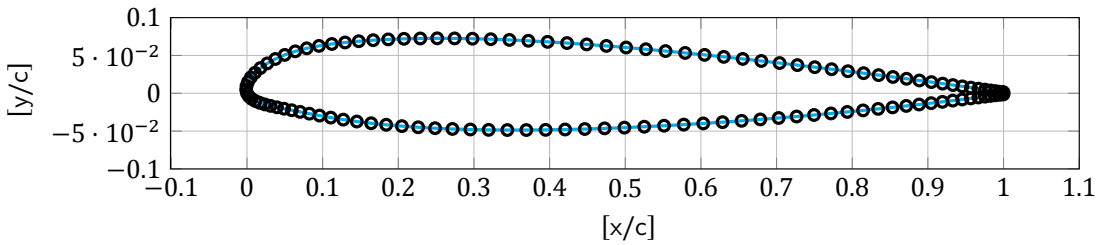

Figure 10.8: NACA22112 Airfoil (121 points)

10.5.2. Wing planform selection

The same method and process, used previously to simulate airfoils on the standard platform, was adapted to be able to deal with a large range of taper ratios. Also, a *MATLAB* script was created to export a *XFLR5* wing coordinate file to be able to properly construct an elliptical wing. The flow diagram showing this process in more detail is provided by Figure 10.10. During this analysis a great deal of simulations would not converge due to the large range of taper ratios and thus Reynolds numbers. As a result, the first step of running batch *XFOIL* simulations on airfoils had to be repeated. This was done in order to ensure that the Reynolds numbers used for the airfoil simulation covered a sufficient range such that *XLFR5* could interpolate the data. The results of this analysis were then exported and a trade-off was performed. The geometry for the resulting optimal wing planform is provided by Table 10.9. Furthermore, the simulation results for the final wing planform are provided by Figure 10.11. The important values shown in these figures are also shown in bold face in Table 10.4.

Table 10.7: Tail airfoil trade-off

		Weight	DH4009		E387		GM15		NACA 0005		NACA 0009	
		[%]	Value	Score	Value	Score	Value	Score	Value	Score	Value	Score
$C_{L_{\text{trim}}}$	[-]	10 %	0.63	0.50	0.61	0.32	0.69	1.00	0.62	0.43	0.62	0.43
$C_{D_{\text{trim}}}$	[-]∗100	20 %	3.46	0.72	3.89	0.36	4.33	0.00	3.28	0.87	3.37	0.79
$c_L/c_{D_{\text{trim}}}$	[-]	10 %	18.2	0.75	15.7	0.00	15.8	0.04	19.37	1.00	18.5	0.84
C_{m_α}	[-]∗100	20 %	-1.89	0.23	-2.03	0.87	-2.06	1.00	-1.88	0.17	-1.88	0.19
C_{m_0}	[-]∗100	20 %	1.61	0.53	1.26	0.64	3.31	0.00	1.24	0.65	1.32	0.63
α_{trim}	[-]	20 %	0.8	0.53	0.6	0.67	1.6	0.00	0.7	0.60	0.7	0.60
Weighed sum		**100 %**	**52.7 %**		**54.0 %**		**30.4 %**		**60.2 %**		**56.9 %**	

		Weight	R14.0		S4083		S7055		S8025		SD7032	
		[%]	Value	Score	Value	Score	Value	Score	Value	Score	Value	Score
$C_{L_{\text{trim}}}$	[-]	10 %	**0.58**	0.00	0.65	0.69	0.60	0.24	0.65	0.63	0.64	0.60
$C_{D_{\text{trim}}}$	[-]∗100	20 %	**3.12**	1.00	3.57	0.62	3.50	0.69	3.44	0.73	3.83	0.41
$c_L/c_{D_{\text{trim}}}$	[-]	10 %	**18.5**	0.83	18.2	0.76	17.2	0.46	18.7	0.91	16.7	0.31
C_{m_α}	[-]∗100	20 %	**-1.86**	0.08	-1.93	0.43	-1.90	0.29	-1.84	0.00	-2.00	0.71
C_{m_0}	[-]∗100	20 %	**1.18**	1.00	2.20	0.35	1.15	0.68	2.27	0.33	1.92	0.40
α_{trim}	[-]	20 %	**0.1**	1.00	1.1	0.33	0.5	0.73	1.0	0.40	1.0	0.40
Weighed sum		**100 %**	**70.0 %**		**49.2 %**		**54.7 %**		**44.6 %**		**48.3 %**	

Table 10.8: Standardized wing planform for airfoil selection $A = 7.01$ $\lambda = 0.7$

Station distance from root [m]	Chord length [m]	Offset [m]	Dihedral [deg]	Twist [deg]
0.000	0.285	0.0	0.0	0.0
0.300	0.285	0.0	0.0	0.0
0.900	0.200	0.042	0.0	0.0

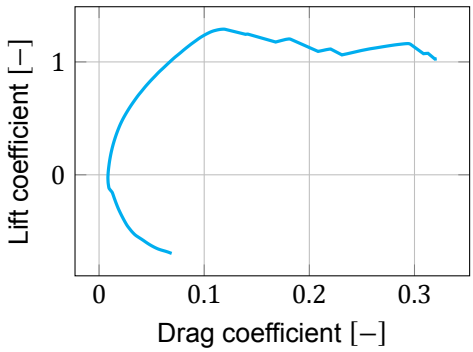

(a) Drag polar

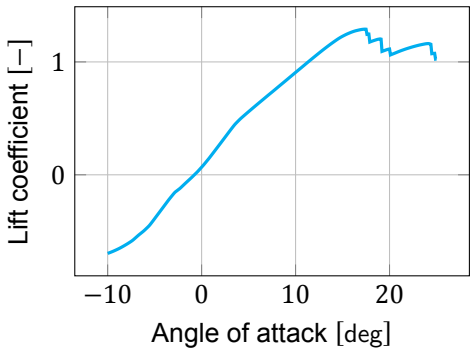

(b) Lift curve

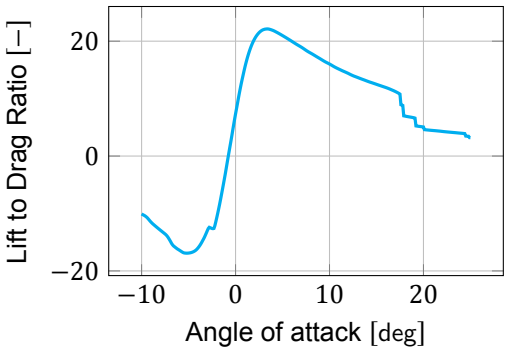

(c) Aerodynamic efficiency

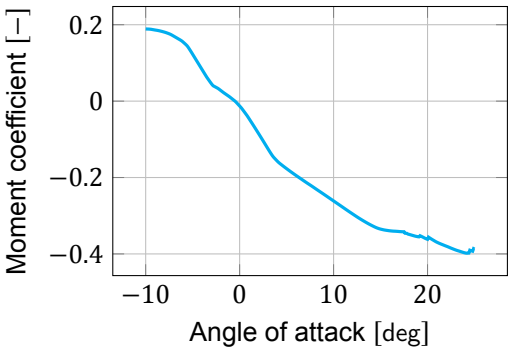

(d) Moment curve

Figure 10.9: NACA22112 LLT simulation results from standardized planform in XFLR5 ($Re_{\text{tip}} = 200\,000, Re_{\text{root}} = 284\,000$)

Table 10.9: Standardized wing planform for airfoil selection $A = 7.01$ $\lambda = 0.7$

Station distance from root [m]	Chord length [m]	Offset [m]	Dihedral [deg]	Twist [deg]
0.000	0.293	0.0	0.0	0.0
0.300	0.293	0.0	0.0	0.0
0.900	0.183	0.110	0.0	0.0

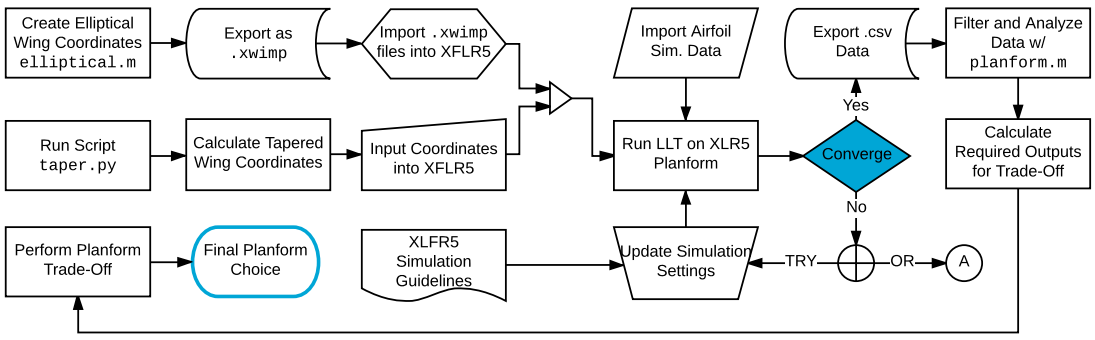

Figure 10.10: Wing planform analysis flow diagram

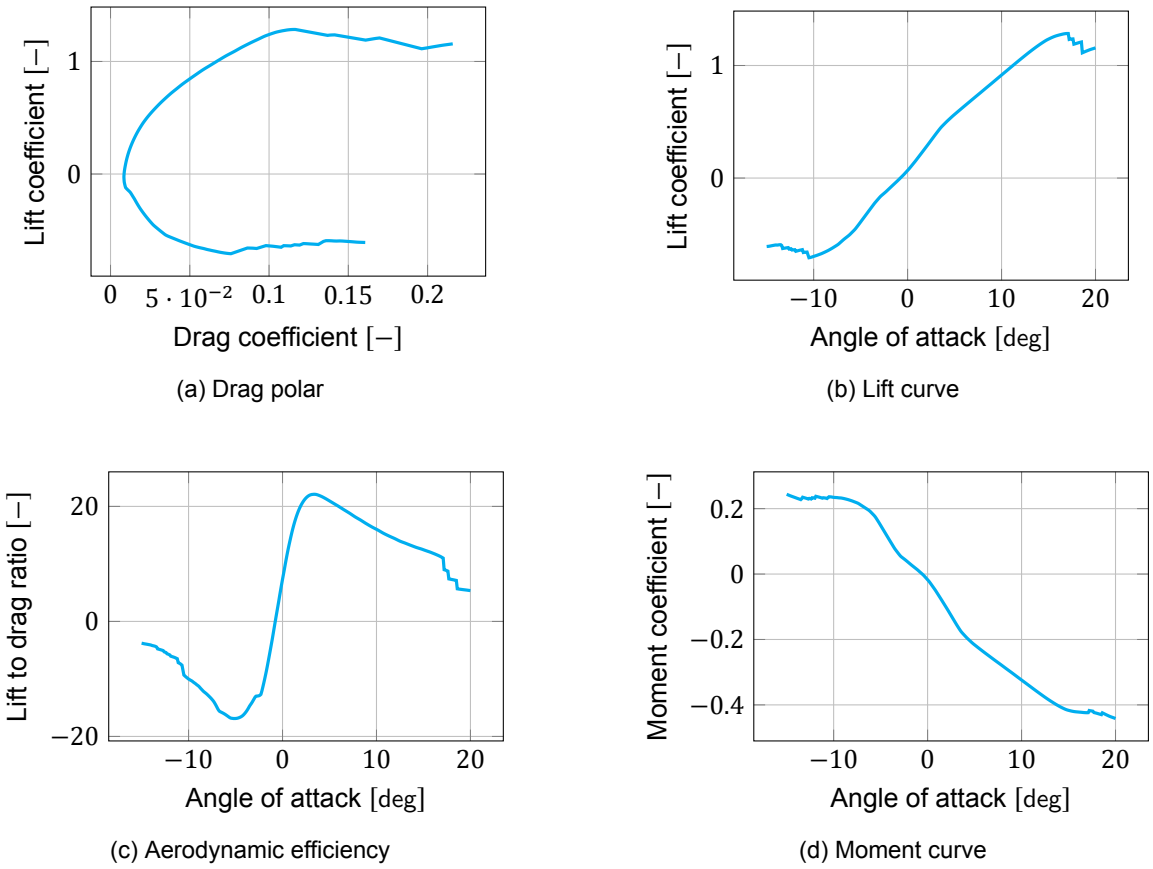

(a) Drag polar

(b) Lift curve

(c) Aerodynamic efficiency

(d) Moment curve

Figure 10.11: NACA22112 LLT simulation results on final planform in XFLR5 (Re_{tip} = 114 000, Re_{root} = 292 000)

10.5.3. Tail airfoil selection

The final step in the aerodynamic analysis of the fixed-wing was to select a tail airfoil as well as find it's optimal incidence angle to ensure stability as well as minimum drag at loiter conditions. Since tail sizing involves a great deal of parameters, the required tail volume found by the stability and control department was used to create a standard planform. This standardized planform was used to iterate the airfoil on. After this, the final choice for both the airfoil and planform were made for this iteration of the whole design. As mentioned in Section 10.4 there were both symmetric and asymmetric airfoils in the range of tested models. The idea was to check if it was more efficient to create the lift by using a lifting airfoil at 0 deg or a symmetric airfoil at an angle. On the planform that was dictated by the stability department, a couple of iterations was used to find the lowest AOA for the tail at which it is still stable. The results of these simulations are used in the trade-off mentioned before. It is important to note however that for the simulations with the wing in combination with the tail it was no longer possible to use the lifting line theory because that only works on a single surface. Therefore in this case the Vortex Lattice Method (VLM) simulation method was used. The results of the configuration that wins the trade-off are summarized in Figure 10.14b and Figure 10.13. As can be seen in Figure 10.14b, while the aircraft without the tail does not meet the stability requirements ($C_{M_0} > 0$ and $C_{M_\alpha} < 0$), the tail does make the aircraft stable.

Table 10.10: Aerodynamic performance of the aircraft with all winning parameters combined

Parameter	Value	Unit	Parameter	Value	Unit
C_{L_α}	0.0846	[deg^{-1}]	α_{trim}	1.0	[deg]
C_{m_α}	-0.0180	[deg^{-1}]	$C_{D_{\text{trim}}}$	0.0364	[-]
C_{D_0}	0.0139	[-]	$C_{L_{\text{trim}}}$	0.6478	[-]
$C_{L_{\text{trim}}}$	1.317	[-]	$C_L/C_{D_{\text{trim}}}$	17.82	[-]
α_0	-6.4	[deg]	x_{ac}	0.2263	[%MAC]
α_{stall}	11.5	[deg]			

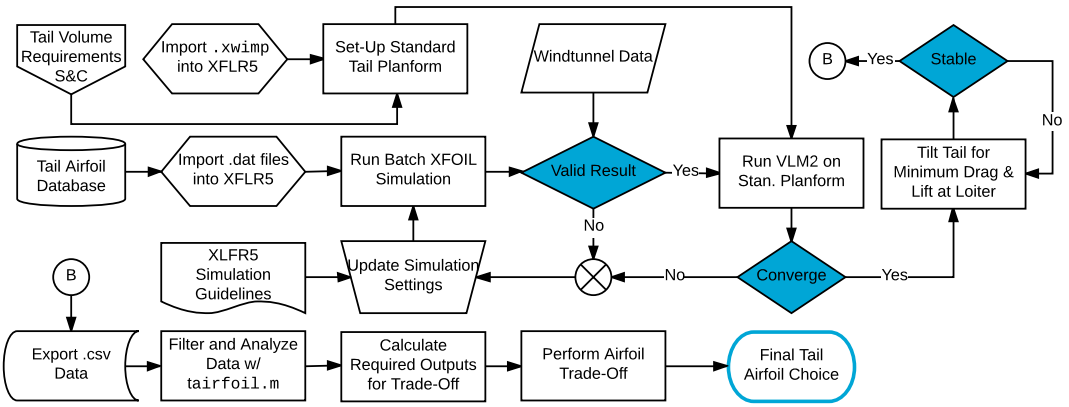

Figure 10.12: Tail airfoil analysis and optimization flow diagram

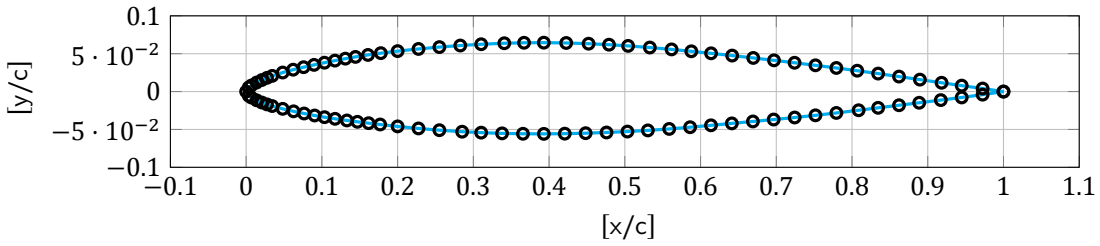

Figure 10.13: R140 Airfoil (121 points)

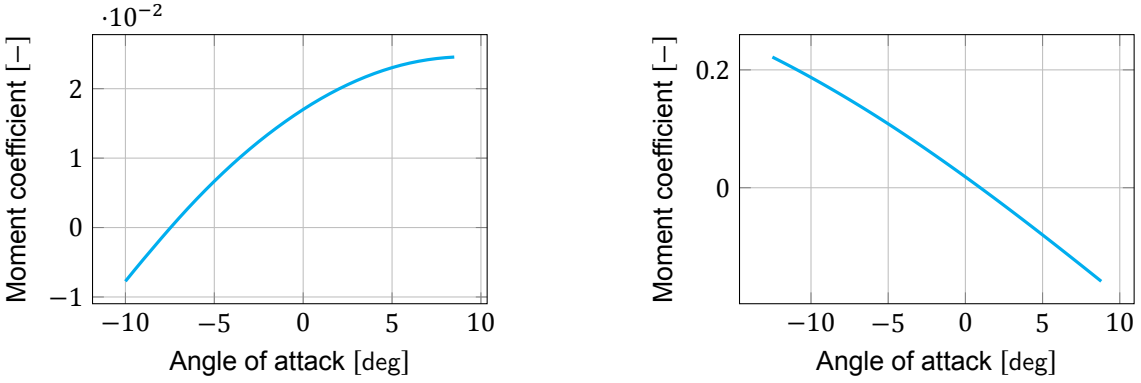

(a) Tailless wing

(b) Wing and tail

Figure 10.14: Stability curves of the aircraft with and without tail

10.5.4. Verification and validation

As demonstrated by the flow diagrams the results out of *XFLR5* were verified by checking convergence of the log files generated from the simulation. Furthermore, the guidelines for *XFLR5* were followed fully to ensure the right settings were used as well as the right simulation model for the various stages of the design analysis. For example, the reason for utilizing Lifting Line Theory (LLT) for the airfoil selection stems directly from its ability to compute non-linear lift-curve slopes, which is useful for analyzing wings near and beyond stall AOA. However, it is important to note that LLT is only applicable in the following conditions: [64]

- The wing must have no sweep or negligible sweep (<10 deg).
- No dihedral or negligible dihedral.
- The wing must have at least moderate aspect ratios (>5)
- The flow is incompressible
- The airfoils have linear lift-curve slopes and are not stalled.

The results that is desired out of the *XFLR5* simulation is to always have a Oswald span efficiency factor, $e < 1$. For reference purposes the definition of this factor is presented by Equation (10.14).

$$e = \frac{C_L^2}{\pi A C_{D_i}} \tag{10.14}$$

However, due to inaccuracies in the VLM simulation with respect to properly modelling the viscous and induced drag, the LLT model is the preferred method. As [64] states, “The LLT method should always be preferred if the wing’s geometry is consistent with the limitations of the theory (as) LLT provides better insight into the viscous drag, gives a better estimation of the behavior around stall conditions at high angles of attack, and is better supported by theoretical published work.” Therefore, utilizing the LLT method with the following parameters, presented by Table 10.11, can be used to increase the convergence of the model and thus yield a better estimation of the Oswald efficiency factor. Even with these improvements to the model, the Oswald efficiency factor computed from *XFLR5* was 0.985. Seeing as the high performance wings of gliders typically reach values of 0.95, for the Surveillance Platform for Aerial Reconnaissance and Target Acquisition (SPARTA) UAV are more conservative value of 0.9 will be used.

In terms of validation, as shown by the airfoil selection flow diagram, the airfoil simulations were referenced with wind tunnel data. Except for drag forces, the *XFOIL* simulation yielded results that were in-line with wind-tunnel data. However, to fully validate the planform a wind-tunnel test would need to be performed. Alternatively, due to the small size of the UAV it could potentially be more cost effective to make a scale model out of foam and use it to measure power consumption during flight, and indirectly measure the drag value from such data.

Table 10.11: Updated parameters for LLT convergence [64, p. 43]

Parameter	Symbol	Value
Number of stations	N_{station}	40
Relaxation factor	Υ	40
Convergence criterion	Ξ	0.001
Max number of iterations	$i_{\max}$	300

10.6. Fuselage Design and Analysis

In this section the design and the analysis of the body are shown. First, the body is designed around the internals of the body which will be explained. Next, the aerodynamics analysis of the body is explained.

10.6.1. Fuselage design

For an aircraft to be stable and controllable, the center of gravity position is very important. Moving the center of gravity too far forward makes an aircraft uncontrollable and moving it too far backward makes it unstable. Especially for this design, where the payload weight is highly variable, the payload must be centered in such a way that the center of gravity stays in roughly the same location independent of payload. For this reason it is chosen to put the payload bay in the center of the UAV.

With this in mind, the design is balanced as much as possible by moving other parts of equal weights to symmetric positions around the payload bay. The other parts that have to be in the body are the batteries, the motor for the flying wing configuration, the sensors, electronics, and cables required for controlled flight. The weights of these are shown in Chapter 5. The heaviest of these modules is by far the battery. If that is located as a whole on one side of the payload bay as close as it can possibly get, the combined center of gravity of all other parts in the fuselage need to have an arm of 1.15 m to balance that. Apart from the fact that that gives an unnecessarily big fuselage for the size of the UAV, it would mean that the body has to be taken apart before it can fit into the backpack. For structural rigidity and on site assembly time, it is preferred to make the body out of one piece. The most obvious solution to solve this problem is to make two smaller batteries that are placed on both sides of the payload bay. The electronics are then located as much as possible above the payload bay so that they are easily reachable through a cutout that is covered by either the fixed-wing or the quadcopter module. A small part of the electronics can also be located in the nose of the UAV to balance the weight of the fixed-wing propeller motor. The distance between every part inside the body is kept at least at 10 mm to leave space for attachment methods.

These parts are modelled in *CATIA*, then cross-sections are drawn around the internals of the body. Here an offset of 20 mm is used because at the time of designing the wing no material was proposed yet and space had to be saved for a possible sandwich material, stringers or other structural reinforcements. Then a rounded shape is added in front and a pointy shape in the end to increase the drag performance of the body, because in low Mach numbers the best shape for a low drag is a droplet shape. In flight direction, the body is modified to mimic an airfoil shape to produce a lifting body. This is done by keeping the lower part of the body as flat as possible by aligning the payload bay and batteries on the bottom and keeping the nose of the body low.

The last thing that has to be added to the body before it can be used it to choose a point where the fixed-wing and quadcopter modules are attached. For the quadcopter it is preferable to have all the rotors at an equal distance from the center of gravity to be able to have much easier control systems. For the fixed-wing, the center of gravity has to be in the range from 0.25 % to 0.54 % MAC as specified by Figure 11.2. Since attaching the wing to the body will shift the center of gravity backwards, the wing is attached with the 0.25 % MAC over the center of the body to be sure that the center of gravity is within the range where the UAV is both controllable and stable. For the quadcopter module this is a very nice place to have the attachment as well. The center of gravity is directly underneath the attachment point so the rods can connect to it in a symmetric way while keeping the rotors all at the same distance of the center of gravity. Figure 10.15 shows how the internal and external layout look. For the internal layout, the two small blocks on top are spaces reserved for the electronics, the big blocks on the side are the batteries and the large middle block is the payload bay. Smaller sensors that are just attached to the body rather than taking up large amounts of space are not modelled here but will be shown in Chapter 14.

(a) Internal layout (side view) (b) Side view of the body (c) 3D view of the body

Figure 10.15: Alignment of taper in top-view

10.6.2. Fuselage analysis method

Now that there is a fuselage shape, it is important to get lift and drag estimations on it. Preferably, this is done by either a wind tunnel test or a 3D Computational Fluid Dynamics (CFD) simulation. However the time and resources available in this project did not allow for any of these methods to be used reliably. It was however possible to do a 2D aerodynamic analysis on the body in order to estimate the aerodynamic body in the best available way. The method and results will be explained in this section.

The model of the body was evaluated in *ANSYS* fluent running on a student license. This means that the maximum number of cells is limited to 512 000 and therefore only a 2D simulation can be run reliably. Normal convention [3] of the simulated windtunnel has at least three times the evaluated body length of empty space on the sides, top, bottom and front of the model and ten times the body length of empty space on the back of the model. This is to ensure that the program can also calculate the aerodynamic forces on the the wake without interference from the wall. In this case a model with a length of slightly above 0.5 meter was used in a windtunnel with 4 m in front of and above the model, 5 m below the model and 13 m behind the model was used. This makes the model a bit more reliable and in 2D the extra number of cells used is not a very big influence on the calculation time.

After the model is put in the windtunnel, the fluid body has to be meshed. A mesh with a minimum mesh size of 5 mm and a maximum mesh size of 0.25 m with a growth rate of 1.01 was used. This results in a mesh of roughly 120 000 cells. In this mesh *ANSYS* does the mesh refinement by itself where the finest mesh is close to the body and the mesh gets coarser as the distance from the body increases.

The mesh is then imported into *Fluent* which calculates the aerodynamic flow and forces. To calculate these a standard $k-\epsilon$ viscous turbulence model is used at a couple of different flight conditions. The straight airflow at 15 m s^{-1} to simulate the loiter condition for the fixed-wing, and the body at angles of −30 deg, −20 deg, and −10 deg at an airspeed of 20 m s^{-1} to find roughly in which range of angles the quad copter is able to fly efficiently. Apart from that, also a −90 deg and 90 deg simulation were done to investigate the drag values during the climb and descent of the quadcopter. These simulations are used to plot a velocity field in order to determine if and where flow separation and turbulence occur. Furthermore the C_L and C_D values are calculated. This is done by calculating the average over the last couple of iterations. *ANSYS* or any other CFD software calculates the flow around a body in iterations until the residuals, which are the differences in velocity, pressure, density and other air properties between cells, are within 0.01 %. This is because the turbulence around a body will never be exactly the same at each given time. For this project, the simulations converge in around 800 simulations so the average of the last 50 iterations is used to calculate the C_L and C_D values. This because here the simulations have already converged reasonably well to the values are oscillating around the average value that will be noticed by the body.

10.6.3. Fuselage analysis result

In this section, the results of the *ANSYS* analysis on the body is shown. The velocity fields are shown in Figure 10.16 and the lift and drag values in Table 10.12. Here the lift values are always taken to the top of the body and the drag values are positive to the rear of the body. So for the 90 deg and −90 deg simulation that means that the lift is the resistance to go up or down and the lift is an extra force that has the tendency to push the body forward when it is trying to climb or descend. Also note that there are some values that have a *larger/smaller than* sign, since the simulations with the most turbulence did not converge properly and therefore the values can not be considered reliable beyond the order of magnitude and direction of the forces.

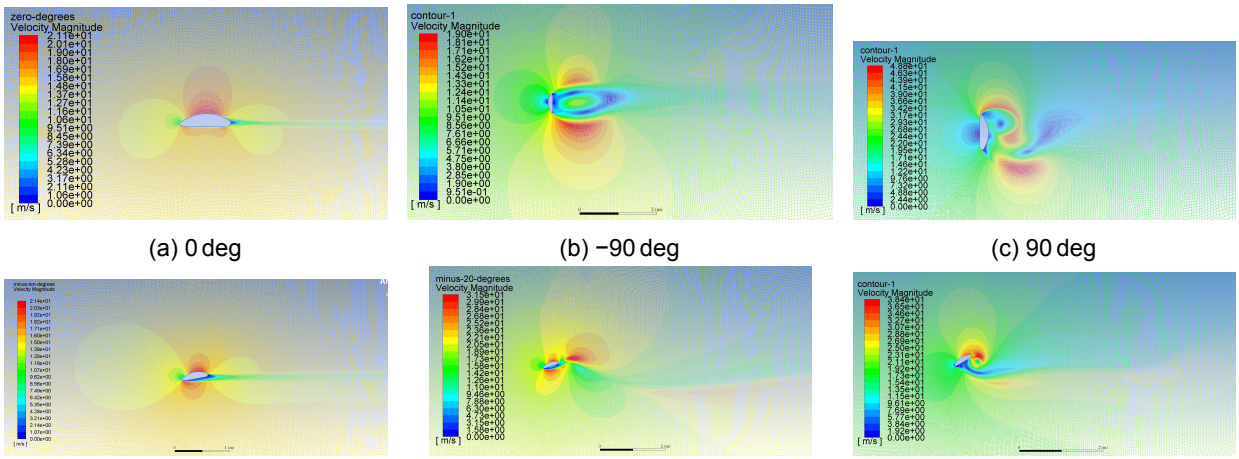

(a) 0 deg (b) −90 deg (c) 90 deg

(d) −10 deg (e) −20 deg (f) −30 deg

Figure 10.16: CFD velocity fields

Table 10.12: Body lift and drag values

α [deg]	C_L [-]	C_D [-]
0	2.63	0.21
-10	-0.16	1.15
-20	-4.36	4.55
-30	-5.89	>1.81
-90	-8.70	-0.43
+90	>8.70	<-0.43

10.6.4. Conclusion

These results have some important implications on the rest of the design. First of all it clearly shows that the body works well as a lifting body and that mounting the body in line with the velocity is aerodynamically the best solution. For the fixed-wing this means that the wing will be mounted onto the body in such a way that the body is straight when the wings are in the angles required for optimum loiter. Which means the main wing will be attached at an angle of 6.3 deg and the tail is mounted at an angle of 2.1 deg.

Also it shows a limit of where it is preferable to fly in the quadcopter configuration. Even though for the rotor efficiency it is best to fly between −30 deg and −35 deg, it is concluded that due to the massive loss in aerodynamic performance, cruise flight with the quadcopter will be performed at −20 deg. The option to mount the body at an angle compared to the rotors to improve the cruise performance is discarded for the reason that it would either require another mounting position for the fixed-wing and quadcopter configuration or it would compromise the steady center of gravity location that is achieved by the current mounting. Both these options are deemed more compromising to the design than an inefficient cruise condition, because cruise is only a small part of the quadcopter mission profile anyway.

10.6.5. Verification and validation

Validation of any aerodynamic analysis is done with a windtunnel test or a flight test, this is however not within the scope of this project. Therefore the validity of the results must be tested with tests done by someone else on bodies that are not exactly similar to the one being tested here. In this case since the *ANSYS* analysis was done in 2D, with the same settings as the ones with which the body has been simulated, a simulation has also been done with the *NACA22112* airfoil on which professional data is available on *airfoiltools* [2]. A chord length of 227.92 mm is used to make sure that a Reynolds number of 200 000 is created in a simulation of 15 m s^{-1} The results are shown in Table 10.13.

Table 10.13: Verification data

α **[deg]**	$C_{L_{\textbf{Wind tunnel}}}$ **[-]**	v$C_{L_{\text{ANSYS}}}$ [-]	**[error %]**	$C_{D_{\textbf{Wind tunnel}}}$ **[-]**	$C_{D_{\text{ANSYS}}}$ **[-]**	**[error %]**
0	0.10	0.286	186	0.0125	0.0021	68
6	0.60	0.61	1.6	0.0175	-0.023	95

This shows that the *ANSYS* evaluation has not been reliable at all, which probably means that too many assumptions have been made. Therefore a more in depth analysis is needed to give a precise evaluation of the aerodynamic properities of the UAV and the results from this chapter can only be used for the initial sizing and performance predictions.

10.6.6. Recommendations

Due to the large amount of assumptions on interaction required for this analysis, and the low reliability of the achieved data for the body, it is recommended that the first step in continuing with this design will be a more in depth aerodynamic analysis of the whole system. This can be done by building a model and testing it in a windtunnel or even just immediately testing its flight performance outside. Another but probably more expensive solution would be to run some 3D CFD simulations wich can be done if a full CFD license and preferably also a computer cluster is available. Apart from that, the shape of the body can still use some iterations. By varying the height of the nose and the rear of the fuselage, the body probably still improve the performance of the UAV a lot.

10.7. Noise Analysis

One of the requirements was that the platform has to be inaudible with a maximum of 50 dBA at a distance of 300 m (**SPARTA-UAV-10**). This can be done in detail through a CFD analysis where computational aeroacoustics are performed. However, the CFD analysis is outside of the scope of the project due its main objectives and complexity. Literature and experts in the field suggest that the noise of the fuselage can be neglected, and the main source of noise is the propulsion system [32, 38]. The estimated noise will include noise from propellers and the tip vortexes. The noise estimation will be examined for both configurations; fixed-wing and quadcopter.

10.7.1. Procedure

The noise is estimated through the Sound Pressure Level (SPL) which is the ratio of a sound pressure (P_m) and a reference pressure level (p_{ref}) which is taken to be the lowest hearing limit of a human and is 20 µPa. It is measured in dB and it is equal to Equation (10.15). It is important to understand the nature of this equation. If the power output is equal or less than the reference power then the SPL will be zero or negative which indicates that it is unheard by humans.

$$SPL = 10 \cdot \log\left(\frac{P_m^2}{p_{\text{ref}}^2}\right) \tag{10.15}$$

Gutin's method

In order to be able to calculate the noise multiple empirical methods are used to calculate the SPL. The first method comes from [38] and is the theoretical work of Gutin. Since both the fixed-wing and quadcopter module use propellers, the propeller noise is analyzed. As explained earlier, noise can be deducted from the rotor, the propellers and their vortexes. This method estimates the overall propeller noise with Equation (10.16). The equation, takes into account the number of blades (B), radius of propellers (R), disc area (A), thrust (T), shaft power (P_h), the tip Mach number (M_t) and the angle between the forward propeller axis to observer (θ). The Bessel function is also part of the calculation which takes as an argument $J_{mB}(x) = 0.8 \cdot M_{\text{tip}} mB \sin\theta$.

[2] airfoiltools.com/airfoil/details?airfoil=naca22112-jf, last accessed: 2017-06-25

$$P_m = \frac{169.3 \cdot m\mathrm{BRM}_t}{SA}\left[\frac{0.76 \cdot P_h}{M_t^2} - T\cos\theta\right]J_{mB}(x) \tag{10.16}$$

From Equation (10.16), the angle θ is not known and had to be determined. In order to do that, an algorithm was written which iterated Equation (10.16) a few times to see at which angles it obtained the highest values. These values were at 1.62 rad (≈90 deg) and 4.65 rad (≈270 deg)

Once θ is determined, the pressure levels are identified for different orders of harmonics $m = 1, 2, 3, 4$. At first their individual result is squared, then summed up and finally the square root of the overall result is taken. This result is then plugged in into Equation (10.15).

Vortex noise

Also from [38], the vortex noise can also be estimated. It is an approximation developed by Hubbard which depends on the constant of proportionality (k) with a value of $6.1e-27$, propeller blade area (A) and the velocity at 0.7 of the radius ($V_{0.7}$) and it is described by Equation (10.17). These values are obtained from the propulsion and aerodynamic departments for the blade, propeller and rotor design.

$$SPL_{\mathrm{vortex}} = 10 \cdot \log\left(\frac{kA_bV_{0.7}^6}{10^{-16}}\right) \tag{10.17}$$

From Equation (10.17) several conclusions can be drawn on how to minimize noise. It can be observed that by doubling the velocity SPL increases the sound level by almost 18 dB when, if the blade area is doubled, only a small increase of 3 dB is noticed [38]. For the most optimum design the blade area is increased to maximum capabilities while sustaining its efficiency and structural integrity the overall noise is minimized [38]. Results show that noise levels due to the vortex noise are approximately 33.1 dB and can be neglected as it is equal to a quiet bedroom at night.[3]

Hubbard's method

A more detailed method which takes into account more parameters is also used to estimate and compare the propeller noise. It is developed by Hubbard, takes more variables into consideration and thus makes the estimation a bit more accurate [29]. All the values are similar with Gutin expression. In Equation (10.18), (y) represents the distance to the observer, (M_r) represents the Mach number of the source to the observer, (M_x) the flight Mach number, (z_{eff}) the effective radius with a value of 0.8, and finally ψ is the non compactness factor.

$$SPL = 20 \cdot \log_{10}\left[\frac{538673 \cdot mBM_t \sin\theta}{yD(1 - M_x\cos\theta)}\left(\frac{T\cos\theta}{1 - M_x\cos\theta} - \frac{550 \cdot P_h}{z_{\mathrm{eff}}^2 M_t^2 c_0}\right)\Psi_L J_{\mathrm{mB}}\right] \tag{10.18}$$

In Equation (10.18) the Bessel function takes as an argument $J_{mB}(x) = \frac{mBz_{\mathrm{eff}}M_t \sin\theta}{1 - M_x\cos\theta}$. In addition, the non compactness factor is equal to Equation (10.19) with the argument shown in Equation (10.20).

$$\Psi_L = \frac{\sin X}{X} \tag{10.19}$$

$$X = \frac{mBM_TB_D}{M_r(1 - M_x\cos\theta)} \tag{10.20}$$

Both methods will measure the SPL at a distance of 1 m and a correction factor will be used to calculate the distance at 300 m with Equation (10.21). In that equation, SPL_1 portrays the SPL at a distance of 1 m.

$$SPL = SPL_{1\mathrm{m}} - 20 \cdot \log S \tag{10.21}$$

The methods derived above calculate the overall sound pressure level which has integrated all frequencies. However, since humans are more sensitive to some frequencies than others and therefore the SPL should be modified according to A-weighted spectra. Since the model is not built and these calculations are only estimations, a literature study was conducted to determine the worst case scenario of the A-weighted spectra frequency. This is found to be at 2.5 kHz where the resulted SPL needs an addition of 1.3 dB.[4]

Two graphs were created, depicted in Figures 10.18 and 10.19, that show the prediction of the noise level and its variation with distance. From the graph the inaudibility of the system could be determined by looking at the value at which the vehicle is at 50 dBA.

Work flow diagram

The process explained above can be summed up in the work flow diagram, portrayed in Figure 10.17. In that figure, the processes explained above are summarized in the required steps, so that the procedure can be repeated.

[3] www.noisemonitoringservices.com/decibels-explained/, last accessed: 2017-10-06

[4] www.sengpielaudio.com/calculator-octave.htm, last accessed: 2017-06-20

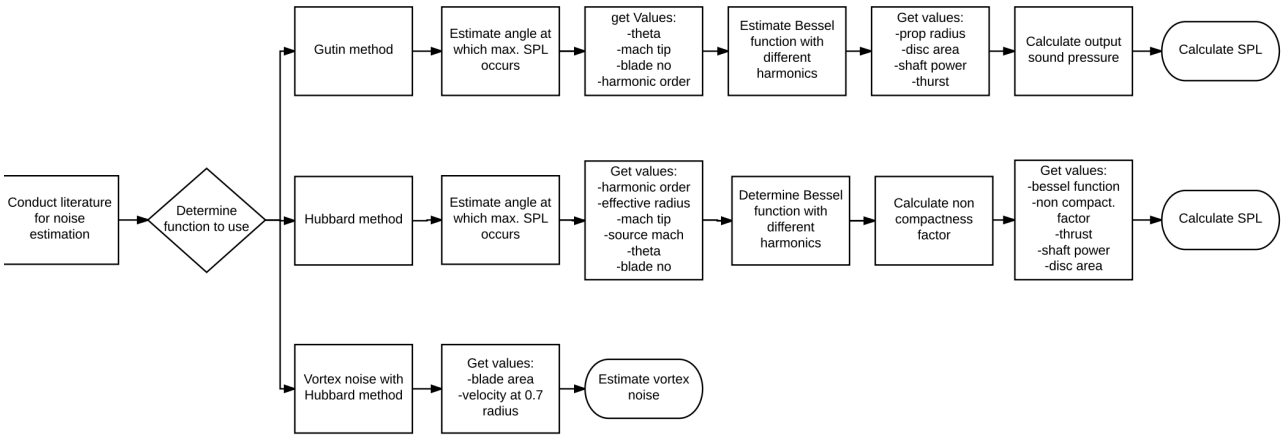

Figure 10.17: Flow diagram of noise estimation

10.7.2. Quadcopter noise estimation

For the quadcopter the following results were obtained from the calculations and Figure 10.18.

- Using Gutin's method the drone becomes inaudible at 47 m
- Using Hubbard's method the drone becomes inaudible at 70 m

Furthermore Table 10.14 was created which depicts the dB change over distance for the quadcopter. The values are taken every 100 m, and both scales dB and dBA are shown.

Table 10.14: Results of noise estimation for the quadcopter configuration

	Gutin method		**Hubbard method**	
Distance [m]	**[dB]**	**[dBA]**	**[dB]**	**[dBA]**
1	79.8	81.1	83.7	85
100	43.5	44.8	46.8	48.1
200	37.8	39.1	40.6	41.9
300	33.9	35.2	37.3	38.6

The graph is depicted in Figure 10.18 and shows the variation of SPL with distance. The sound decay decreases logarithmically with increasing distance and thus the graph has this specific shape which is expected.

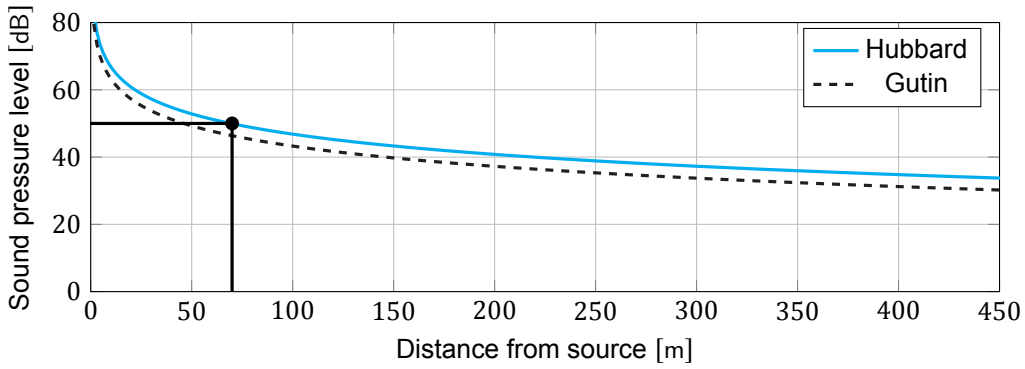

Figure 10.18: SPL variation with distance for the quadcopter configuration

Results suggest that the 50 dBA requirement is met for the quad copter configuration.

10.7.3. Fixed-wing noise estimation

For the fixed-wing the following results were obtained at loiter condition since the performance of the mission will occur at such conditions.

- Using Gutin's method the drone becomes inaudible at 7 m.
- Using Hubbard's method the drone becomes inaudbile at 15 m.

Similarly with the quad copter noise estimation, Table 10.15 was created which depicts the dB change over distance. The values are taken every 100 m, and both scales dB and dBA are shown.

Table 10.15: Results of noise estimation for the fixed-wing configuration

	Gutin method		Hubbard method	
Distance [m]	**[dB]**	**[dBA]**	**[dB]**	**[dBA]**
1	64.9	65.2	69.6	70.9
100	26.7	28	31.5	32.8
200	22	23.3	25.3	26.6
300	18	19.3	22.5	23.8

The graph is depicted in Figure 10.19 and shows the variation of SPL with distance. Similarly with the quadcopter it is logical that it produces less noise, due to the lower requirement of thrust, horsepower and a smaller blade radius.

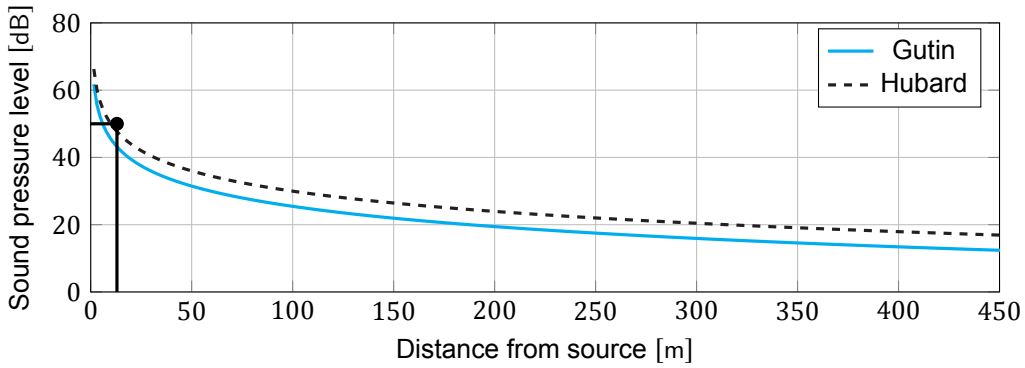

Figure 10.19: SPL variation with distance for the fixed-wing configuration

The results show that the 50 dBA requirement is met for the fixed-wing configuration as well. Similarly with Figure 10.18, the sound decay decreases logarithmically with increasing distance which matches with theory.[5]

10.7.4. Verification and validation

Concerning verification and validation there is not much that can be done without creating a prototype model or using advanced CFD. At first for verification, the code was checked with print statements and discussed in detail to see whether or not results made sense. Furthermore, the final results were consulted by experts in the field such as Ms. K. Knepper and Dr. Ir. Abhishek K. Sahai to see whether or not they are logical so that they could be verified based on their experience and knowledge on topic.

Concerning validation, due to the limited time and constraint of resources it is very difficult to create a prototype model and test it. For this reason it was decided that the two methods explained in Section 10.7 will be compared with each other and with UAVs of similar characteristics at different altitudes and an error margin will be presented to show the reliability of the results. Table 10.16 depicts the validation of noise for the UAV.

Concerning the validation of the fixed-wing, it was based on results from two reports of a small scaled fixed-wing UAVs [13, 40]. The ideal scenario would be to obtain acoustic information from the *Raven*, *ScanEagle*, *Hermes 900*. However that wasn't possible as their noise characteristics were classified. The validated results for the fixed-wing are presented in Table 10.17.

From Table 10.16 and Table 10.17 several conclusions can be drawn about the accuracy of the methods. The methods for both configurations are accurate. A possible reason for having 8 dB difference between the fixed-wing configuration and the validated results, might be the fact that loiter configuration was taken into account and not at full power.

[5] `www.sengpielaudio.com/calculator-distance.htm`, last accessed: 2017-07-03
[5] `www.wetalkuav.com/dji-drone-noise-test/`, last accessed: 2017-06-19

Table 10.16: Validated noise results for the quadcopter configuration[6]

Reference	$SPL_{1\,\mathrm{m}}$ [dB]	Hubbard method [dB]	Gutin method [dB]
Phantom 2	75.8	83.7	79.8
Phantom 3 Pro	76.3	83.7	79.8
Phantom 4 Pro	76.9	83.7	79.8
Inspire 2	79.8	83.7	79.8
Average	77.2	83.7	79.8

Table 10.17: Validated noise results for the fixed-wing configuration

Reference	$SPL_{1\,\mathrm{m}}$ [dB]	Hubbard method [dB]	Gutin method [dB]
1	72	69.6	64.9
2	73	69.6	64.9
Average	72.5	69.6	64.9

It seems that Hubbard's method has higher results than Gutin's and this is because it takes into account more information about the engine and the Bessel function has more arguments. The noise model, can be improved and be made more accurate if an extensive CFD analysis is performed. For very accurate validation results, a model needs to be built, tested and compared with the estimated methods.

10.7.5. Noise reduction techniques

Even though the UAV has an estimated SPL of 83 dB for the quadcopter and 69.6 dB for the fixed-wing configuration, noise can be further reduced so that the vehicle is inaudible at even lower altitudes. As this is outside of the project scope, several methods to reduce noise are described and not analyzed in detail. From extensive literature and by looking at the nature of the equations it is clear that noise depends on the following factors [38, 52, 59]:

Tip speed This factor is mostly found in the equation of the vortex noise. As seen in the equation and explained above, a lower tip speed reduces the vortex noise as it creates lower shock wave formation and it decreases the frequency noise.

Number of blades This factor can be found in the overall propeller noise estimation. Even though it seems that by increasing the number of blades the SPL will increase, that is not true. The reason behind this is because more blades will decrease the required thrust as they produce more and other factors in both Equations (10.16) and (10.18). Sometimes increasing the number of blades is not optimal in terms of structural integrity and Reynolds number. The main reason why the increasing number of blades decrease the overall noise is due to the fact that they create destructive interference between the acoustic signals.

Chord and twist Chord and twist can reduce the overall SPL in a best case scenario by 3 dB. In case the chord thickness is decreased the thickness noise also decreases by having a lower blade volume. A smaller twist, creates a lower loading distribution which decreases the loading noise as well.

Sweep This factor works well when flying at high Mach numbers. At small or almost zero Mach numbers the effect can be considered marginal. By having a different blade sweep angle the acoustic signals are de-phased from the difference of the radial blades.

Blade thickness Reducing the blade thickness will further reduce thickness noise however it will also affect its structural integrity as they are more fragile. At relative low speeds the effect shouldn't be the same.

Blade spacing Unequal blade spacing has an effect on diminishing the different harmonic blade tones and reducing their frequency while introducing tones of other harmonics. Literature suggest that it doesn't necessarily lower the overall noise but it lowers by a big factor the dBA.

Split tip This was derived by Hanson, who found out that splitting blade tips reduces the compactness of blade noise while affecting the Reynolds number and structural integrity of the blades less.

By adjusting the above mentioned changes, several values which were used to calculate the noise level will either decrease or increase, causing a change in the calculations and will reduce the overall noise.

Finally another way of reducing noise while adding safety to the propellers and increasing efficiency is the design of ducts. This comes at a cost of extra weight. Well designed ducts can reduce the required hovering power by almost 60 % which is equal as doubling thrust according to [47]. When coming to duct propeller design a research was conducted by Jason L. Pereira who came up with an optimal configuration and its portrayed in Figure 10.20[47].

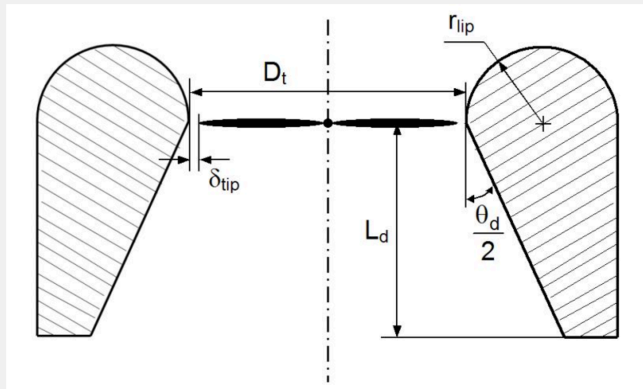

Figure 10.20: Optimal duct propeller configuration

The same paper also suggests that the most optimal configuration includes the following where D_t is the propeller diameter:

- $\delta_{\text{tip}} = 0.1 \cdot D_t$
- $r_{\text{lip}} = 0.13 \cdot D_t$
- $\theta_d \approx 10\,\text{deg}$ (diffuser included angle)
- L_d should be iterated for the most optimum value, varriying from 50 % to 72 % of D_t.

Concerning the materials for the duct there are several possibilities. Literature suggests that the ideal material to use for the carbon fiber with a thickness of 0.5 mm. However, this is not always feasible and another possible material to be used is reinforced fiberglass foam. The material is curved into the desired shape and in case of further rigidity layers of fiber glass can be added on the surface [47].

Due to time constrains the ducted fans are not sized for the UAV as that would cause an increase in weight. This will impact the performance causing a snowball effect. These changes can be done in a future development and in more detail.

II-11

Stability and Control Analysis

This chapter includes the control and stability for both fixed-wing and quadcopter configuration, which includes the sizing and configuration of the tail, ailerons and quadcopter motor configuration. The chapter is split into three major parts. First, in Section 11.1 the coordinate systems that were used for both fixed-wing and quadcopter are discussed. Secondly, the stability is explored of all respective subsystems, which can be found in Section 11.2. Lastly, Section 11.3 researches the control of the Unmanned Aerial Vehicle (UAV), where the designs are checked for controllability and the control software is described in detail.

11.1. Reference Frames

To investigate the stability and control characteristics of the system, the reference frames must be defined. Two main reference frames were used in the analysis, the inertial reference frame and the body reference frame. Additionally, certain assumptions have been made in the construction of these frames:

SA-I It has been assumed that earth is an inertial frame of reference. Furthermore, it has been assumed that the Earth is flat and does not move through space, nor does it accelerate or rotate around its axis.

SA-II The body reference frame has been assumed to be attached to the Center of gravity (COG) of the UAV. The orientation of the frame of reference is the classical body fixed frame as seen in Figure 11.1.

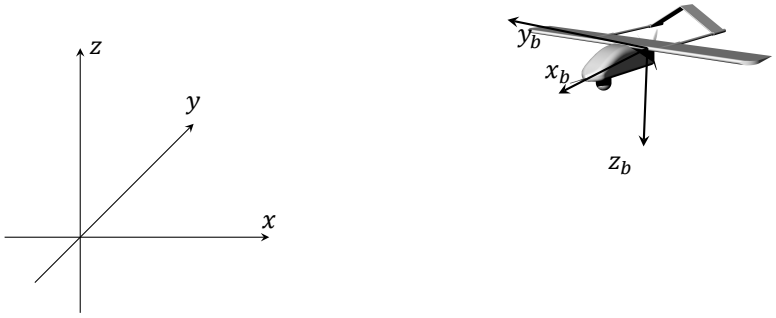

Figure 11.1: Inertial and body reference systems

The body axis system on the other hand always points in the same orientation as the UAV. The transformation from one system to another is achieved by a set of three axis rotations and later translation of the axis system to the new origin, as can be seen in Figure 11.1. The position vector of COG is defined as $\vec{\eta} = [x, y, z]^T$ and the rotation vector of Euler angles is $\vec{\theta} = [\phi, \theta, \psi]^T$. The rotation can be carried out using following rotation matrix, where c represents the cosine and s represents the sine functions.

$$R = \begin{pmatrix} c_\phi c_\psi - c_\theta s_\phi s_\psi & -c_\psi s_\phi - c_\phi c_\theta s_\psi & s_\theta s_\psi \\ c_\theta c_\psi s_\phi + c_\phi s_\psi & c_\phi c_\theta c_\psi - s_\phi s_\psi & -c_\psi s\theta \\ s_\phi s_\theta & c_\phi s_\theta & c_\theta \end{pmatrix} \tag{11.1}$$

11.2. Stability

This section looks closely into the stability of the fixed-wing and the quadcopter. More emphasis is given to the passive stability of the system, while active stability is elaborated further in the control analysis section Section 11.3.

11.2.1. Static stability and controllability

Firstly, the aircraft's static stability and controllability have been analyzed. These are generally a function of the aircraft configuration, aerodynamic characteristics and COG position. The methodology used to determine the dynamic stability follows from [42]. In order to simplify the analysis, several assumptions have been made:

- **SA-I** To simplify the problem, the equations of motion have been linearized. This introduces a significant error that increases with increasing timescales. However, for small time scales it is assumed to be valid.
- **SA-II** In the Taylor expansion, terms of 2^{nd} order and higher were neglected. This introduces another linearization error.
- **SA-III** To eliminate aeroelastic effects as well as bending due to other causes, the vehicle is assumed to be a rigid body. Because of the low loads the UAV is subjected to, this assumption will not generate a large error
- **SA-IV** The flight path angle γ is assumed to be small, such that the small angle approximation (i.e. $\sin(\gamma) \approx \gamma$ and $\cos(\gamma) \approx 1$) holds. This assumption does not hold during steep climbs or descents.
- **SA-V** The angle of attack is assumed to be small, such that the lift coefficient C_L i approximately equal to the normal coefficient C_N. This simplifies the determination of the stability derivative coefficients. Similar to the rectilinear flight assumption, this has significant impact if the angle becomes large (e.g. approaching stall).
- **SA-VI** The aircraft is assumed to be symmetric about the xz-plane. This eliminates negligibly small secondary moments.
- **SA-VII** The loads applied to the aircraft are assumed to be point forces. As bending displacements are neglected, this should be a reasonable assumption, provided the place of application of the force is known.

To visualize the relationship between the COG, and the control and stability of the aircraft, a scissor diagram was constructed for both a canard and a conventional configuration. This is shown in Figure 11.2. The stability lines indicate the furthest rearward possible COG position and the controllability lines indicate the maximum forward position. The design point is indicated by a circle.

As can be clearly seen, the conventional configuration has a large feasible range of COG values and tail sizes. On the contrary, the canard configuration does not show any points that are both stable and controllable in all circumstances and will therefore not be considered.

The quadcopter configuration is inherently unstable since there is no aerodynamic restoring force, contrarily to the fixed-wing aircraft. Given a small disturbance, the quadcopter will not return to a stable position if no action is taken. Nevertheless, the stability of the quadcopter can be ensured by the use of a fly-by-wire system consisting of an extensive control module using Proportional Integral Derivative (PID) controllers

11.2.2. Tail configuration

For the selection of a tail configuration, four options were considered. The first option is the conventional tail configuration, because of its good control characteristics and common use. Secondly, the twin-boom A-tail (or inverted V) was considered, being a version of the simple V-tail with better controllability. The third option is the H-tail, which is known for its small 2-D cross-section, thus fitting easily in the backpack. Lastly, the Y-tail was proven to be a feasible choice, because of its ability to keep the horizontal stabilizers out of the main wing wake, reducing the total drag.

To determine the appropriate tail design, a qualitative trade-off was performed using several categories. The results of the trade-off can be seen in Table 11.1. The selected categories are as follows:

Mass *20 %* The structure needs to be as light as possible.
Wetted area *20 %* Included for its direct correspondence with drag and thus endurance.
Complexity *15 %* Directly corresponds to cost and reliability.
Control actuation *25 %* The dynamic function of the aircraft empennage.
Stall behavior *20 %* A tail should statically reduce stall for stability.

The trade-off was performed through indicating the score of individual components on a qualitative scale ranging from 0 to 10, with intervals of two because of the imprecision of such a scale. The final score is calculated as the average of the score from each category with its corresponding weight [8, 28, 51, 61].

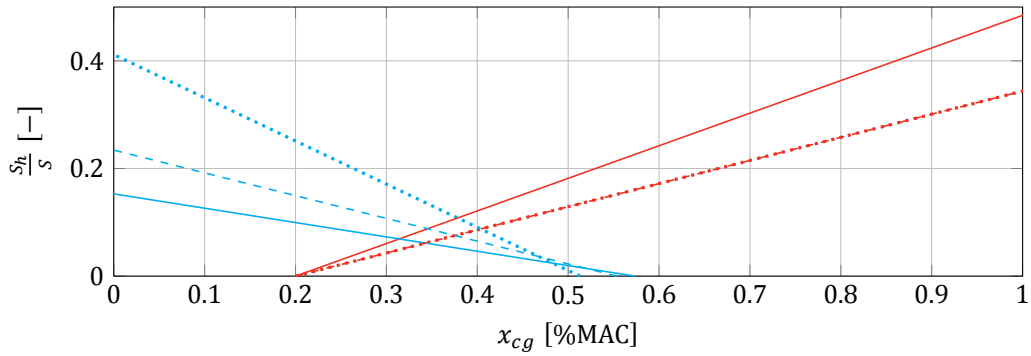

(a) Conventional configuration

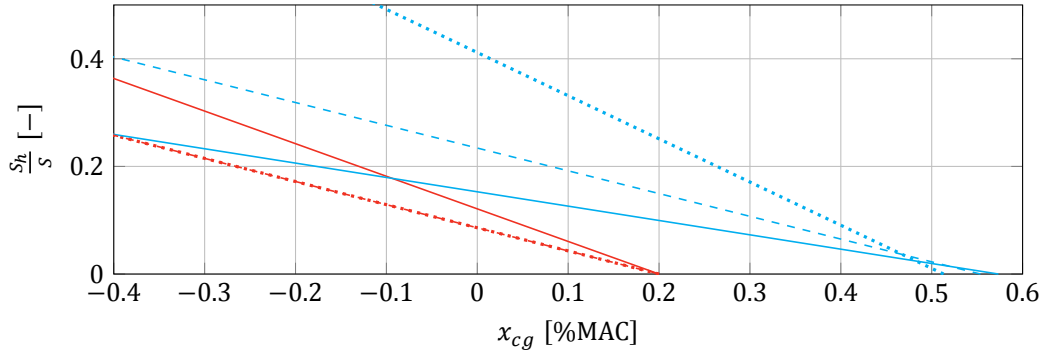

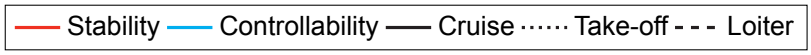

(b) Canard configuration

Figure 11.2: Stability and controllability plots

Table 11.1: Trade-off tail configurations

Tailplane	Mass	Area	Complexity	Actuation	Stall	Final score
Conventional	8	6	8	10	10	8.5
Twin-boom A-tail	10	10	10	6	8	8.6
H-tail	6	4	6	10	10	7.4
Y-tail	6	6	6	8	8	6.9

11.2.3. Empennage design

From the above-mentioned criteria, a twin-boom A-tail empennage was selected. The distance from the main wing and the anhedral angle were both determined from statistics, the latter being determined from vertical tail volume coefficient statistics [51]. This yielded values of 60 cm for the tail arm and 80 deg for the top anhedral angle. The tail surface itself features a chord of 9.6 cm, a horizontal projected span of 48 cm and a vertical projected span of 27 cm. The full empennage design is shown in Figure 11.3 with the anhedral angle being indicated in Figure 11.3b.

11.2.4. Dynamic stability

For the analysis of the dynamic stability, a linearized system of equations was set up for both the longitudinal as well as the lateral dynamics. The longitudinal system uses angle of attack α, dimensionless airspeed u, geometric pitch angle θ and dimenionsionless pitch rate $\frac{q\bar{c}}{V}$ as state variables. The lateral system comprises sideslip angle β, bank angle ϕ, dimensionless roll rate $\frac{pb}{2V}$,and yaw rate $\frac{rb}{2V}$. The stability derivative coefficients for the longitudinal direction were derived from simple two dimensional motion [42]. The used coefficients can be found in Table 11.2 and the model is stated in Equation (11.2). Simulating the system under a step input on the elevator gave the response as shown in Figure 11.4.

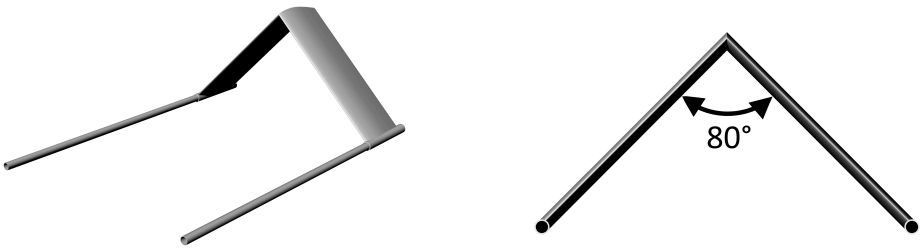

(a) Assembly including booms (b) Rear view including anhedral angle

Figure 11.3: Empennage design

$$\begin{bmatrix} \dot{\hat{u}} \\ \dot{\alpha} \\ \dot{\theta} \\ \frac{\dot{q}\bar{c}}{V} \end{bmatrix} = \begin{bmatrix} \frac{V}{\bar{c}}\frac{C_{x_u}}{2\mu_c} & \frac{V}{\bar{c}}\frac{C_{x_\alpha}}{2\mu_c} & \frac{V}{\bar{c}}\frac{C_{x_0}}{2\mu_c} & 0 \\ \frac{V}{\bar{u}}\frac{C_{z_u}}{2\mu_c - C_{Z_{\dot{\alpha}}}} & \frac{V}{\bar{u}}\frac{C_{z_\alpha}}{2\mu_c - C_{Z_{\dot{\alpha}}}} & -\frac{V}{\bar{u}}\frac{C_{z_0}}{2\mu_c - C_{Z_{\dot{\alpha}}}} & \frac{V}{\bar{u}}\frac{2\mu_c + C_{z_w}}{2\mu_c - C_{Z_{\dot{\alpha}}}} \\ 0 & 0 & 0 & \frac{V}{\bar{c}} \\ \frac{V}{\bar{c}}\frac{C_{m_u} + C_{Z_u}\frac{C_{m_{\dot{\alpha}}}}{2\mu_c - C_{Z_{\dot{\alpha}}}}}{2\mu_c K_Y^2} & \frac{V}{\bar{c}}\frac{C_{m_\alpha} + C_{Z_u}\frac{C_{m_{\dot{\alpha}}}}{2\mu_c - C_{Z_{\dot{\alpha}}}}}{2\mu_c K_Y^2} & -\frac{V}{\bar{c}}\frac{C_{X_0}\frac{C_{m_{\dot{\alpha}}}}{2\mu_c - C_{Z_{\dot{\alpha}}}}}{2\mu_c K_Y^2} & \frac{V}{\bar{c}}\frac{C_{m_q} + C_{m_{\dot{\alpha}}}\frac{2\mu_c + C_{Z_q}}{2\mu_c - C_{Z_{\dot{\alpha}}}}}{2\mu_c K_Y^2} \end{bmatrix} \cdot \begin{bmatrix} \hat{u} \\ \alpha \\ \theta \\ \frac{q\bar{c}}{V} \end{bmatrix} + \begin{bmatrix} \frac{V}{\bar{c}}\frac{C_{X_{\delta_e}}}{2\mu_c} & \frac{V}{\bar{c}}\frac{C_{X_{\delta_t}}}{2\mu_c} \\ \frac{V}{\bar{c}}\frac{C_{X_{\delta_e}}}{2\mu_c - C_{Z_{\dot{\alpha}}}} & \frac{V}{\bar{c}}\frac{C_{X_{\delta_t}}}{2\mu_c - C_{Z_{\dot{\alpha}}}} \\ 0 & 0 \\ \frac{V}{\bar{c}}\frac{C_{m_{\delta_e}} + C_{Z_{\delta_e}}\frac{C_{m_{\dot{\alpha}}}}{2\mu_c - C_{Z_{\dot{\alpha}}}}}{2\mu_c K_Y^2} & \frac{V}{\bar{c}}\frac{C_{m_{\delta_t}} + C_{Z_{\delta_t}}\frac{C_{m_{\dot{\alpha}}}}{2\mu_c - C_{Z_{\dot{\alpha}}}}}{2\mu_c K_Y^2} \end{bmatrix} \cdot \begin{bmatrix} \delta_e \\ \delta_t \end{bmatrix} \quad (11.2)$$

Table 11.2: Longtidinal stability coefficients

Coefficient	Value	Coefficient	Value	Coefficient	Value
C_{X0}	-0.013	C_{Z0}	-0.915	C_{Mu}	0
C_{Xu}	-0.202	C_{Zu}	-1.83	$C_{M\dot{\alpha}}$	-1.075
C_{Xa}	0.883	C_{Za}	-0.384	C_{Mq}	-2.662
$C_{X\dot{\alpha}}$	0	$C_{Z\dot{\alpha}}$	-0.358		
C_{Xq}	0	C_{Zq}	-1.613		
$C_{X\delta e}$	-0.037	$C_{Z\delta e}$	-0.696		

Two oscillatory eigenmodes exist: the heavily damped short period, featuring a rapid change in angle of attack at nearly constant airspeed, and the slower phugoid, a seesawing motion exchanging potential energy for kinetic energy and vice versa. As can be seen, the system is stable under moderate angle of attack variations and control inputs. In the lateral case, the estimation of the stability derivatives is a lot more complex and generally requires a lot of small- and full-scale wind-tunnel testing. As this is outside of the capabilities and resources of the team, these results will have to be checked at a later design stage. In a lot of cases, empirical or simplified theory methods exist for the estimation of the coefficients. Where possible, the coefficients have been estimated using the same method as in [60]. This led to a set of coefficients shown in Table 11.3. The used linear model is shown in Equation (11.3).

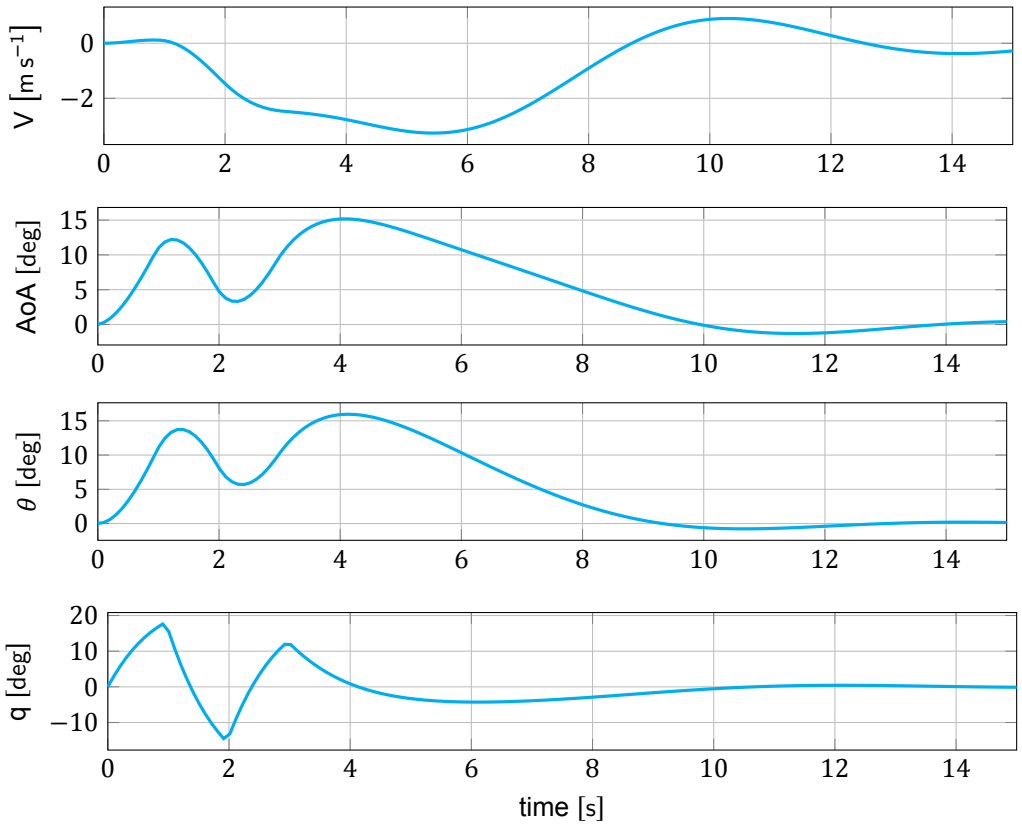

Figure 11.4: Response to a longitudinal disturbance.

$$\begin{bmatrix} \frac{V}{b}\frac{C_{y_b}}{2\mu_b} & \frac{V}{b}\frac{C_L}{2\mu_b} & \frac{V}{b}\frac{C_{Y_p}}{2\mu_b} & \frac{V}{b}\frac{C_{Y_r}-4\mu_b}{2\mu_b} \\ 0 & 0 & 2\frac{V}{b} & 0 \\ \frac{V}{b}\frac{C_{l_b}K_Z^2+C_{n_\beta}K_{XZ}}{4\mu_b(K_X^2K_Z^2-K_{XZ}^2)} & 0 & \frac{V}{b}\frac{C_{l_p}K_Z^2+C_{n_p}K_{XZ}}{4\mu_b(K_X^2K_Z^2-K_{XZ}^2)} & \frac{V}{b}\frac{C_{l_r}K_Z^2+C_{n_r}K_{XZ}}{4\mu_b(K_X^2K_Z^2-K_{XZ}^2)} \\ \frac{V}{b}\frac{C_{l_\beta}K_{XZ}+C_{n_\beta}K_X^2}{4\mu_b(K_X^2K_Z^2-K_{XZ}^2)} & 0 & \frac{V}{b}\frac{C_{l_p}K_{XZ}+C_{n_p}K_X^2}{4\mu_b(K_X^2K_Z^2-K_{XZ}^2)} & \frac{V}{b}\frac{C_{l_r}K_{XZ}+C_{n_r}K_X^2}{4\mu_b(K_X^2K_Z^2-K_{XZ}^2)} \end{bmatrix} \cdot \begin{bmatrix} \beta \\ \phi \\ \frac{pb}{2V} \\ \frac{rb}{2V} \end{bmatrix} + \\ + \begin{bmatrix} 0 & \frac{V}{b}\frac{C_{y_{\delta_a}}}{2\mu_b} \\ 0 & 0 \\ \frac{V}{b}\frac{C_{l_{\delta_a}}K_Z^2+C_{n_{\delta_a}}K_{XZ}}{4\mu_b(K_X^2K_Z^2-K_{XZ}^2)} & \frac{V}{b}\frac{C_{l_{\delta_r}}K_Z^2+C_{n_{\delta_r}}K_{XZ}}{4\mu_b(K_X^2K_Z^2-K_{XZ}^2)} \\ \frac{V}{b}\frac{C_{l_{\delta_a}}K_{XZ}+C_{n_{\delta_a}}K_X^2}{4\mu_b(K_X^2K_Z^2-K_{XZ}^2)} & \frac{V}{b}\frac{C_{l_{\delta_r}}K_{XZ}+C_{n_{\delta_r}}K_X^2}{4\mu_b(K_X^2K_Z^2-K_{XZ}^2)} \end{bmatrix} \cdot \begin{bmatrix} \delta_a \\ \delta_r \end{bmatrix} \quad (11.3)$$

The disturbance response of the system can be found in Figure 11.5. It can be seen that the oscillatory Dutch roll mode is damped, and the spiral motion is divergent. These facts become apparent in the response to a change in sideslip. Up until 5 s, the stable Dutch roll can be seen, apparent in the decrease in the roll rate. It is stable because of the large vertical tail surface and zero wing sweep. The Dutch roll is immediately followed by the unstable spiral, seen from 5 s onward. The small roll angle left from the Dutch roll, quickly diverges due to the unstable spiral. The spiral is unstable because of the low dihedral angle.

This implies that an active stability system will be required to prevent the spiral from diverging. Implementing this should not be a problem as the time to double amplitude of the spiral is roughly 4 s. The implementation of this system will be further discussed in the control section.

Table 11.3: Lateral stability coefficients

Coefficient	Value	Coefficient	Value	Coefficient	Value
C_{Yb}	−0.75	C_{Lb}	−0.009	C_{Nb}	0.135
$C_{Y\dot{b}}$	0	C_{Lp}	−0.458	$C_{N\dot{b}}$	0
C_{Yp}	−0.03	C_{Lr}	0.1	C_{Np}	−0.06
C_{Yr}	0.85	$C_{L\delta a}$	−0.231	C_{Nr}	−0.206
$C_{Y\delta a}$	−0.04	$C_{L\delta r}$	0.034	$C_{N\delta a}$	−0.012
$C_{Y\delta r}$	0.23			$C_{N\delta r}$	−0.094

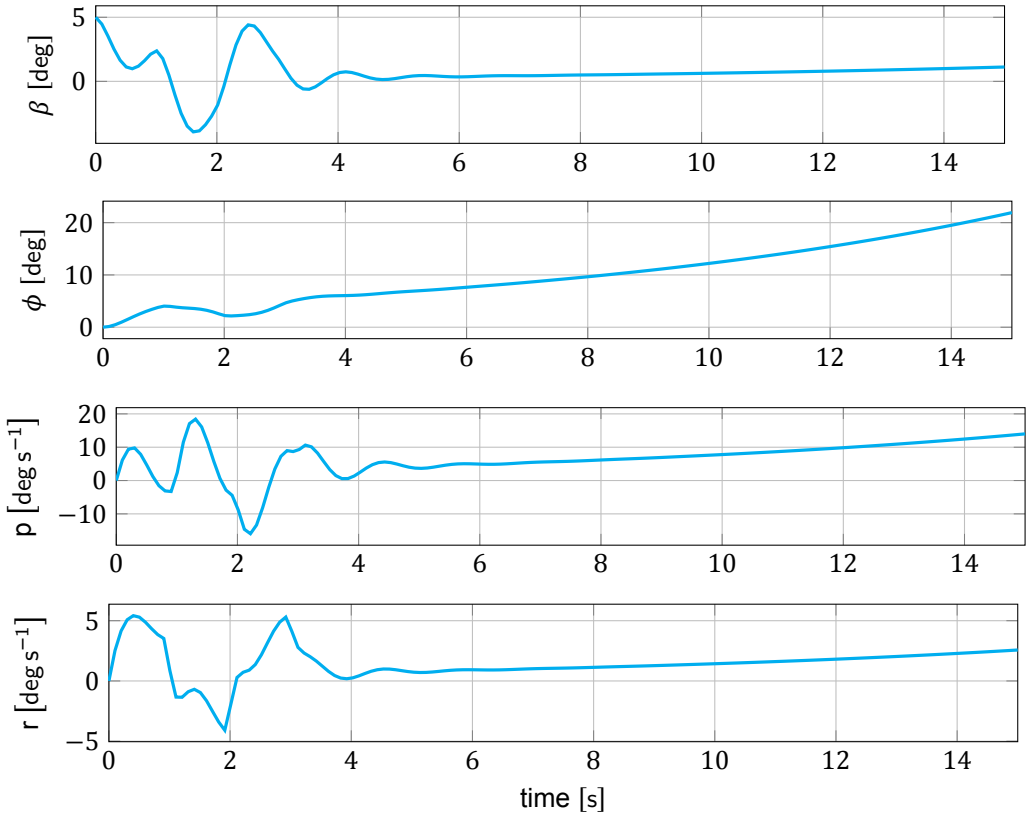

Figure 11.5: Response to a lateral disturbance.

The last eigenmode, not perceived up until this point is the aperiodic roll. In Figure 11.6, it can be seen on the far left. It is heavily damped and aperiodic, as expected [42]. This diagram also shows the stability of the other eigenmodes and the slight instability of the spiral. The eigenvalues are shown numerically in Table 11.4.

11.2.5. Verification and validation

The various methods used for the stability analysis were verified and validated through a set of basic analyses. The static stability and controllability software was verified using hand calculation of several output points, including the zero values. The verification of the aerodynamic coefficients is discussed in Chapter 10. The formulas used in the calculations stem from literature, where they have been verified [24]. The dynamic response calculations used a model previous verified and validated using flight test data from a Cessna Citation II aircraft. However, apart from some ballpark analysis (i.e. checking whether or not the values are *roughly* what they need to be), the coefficients could not be validated without an actual model of the design. Despite this fact, the variables were shown to be changeable up to at least 25 % without changing any eigenmode from stable to unstable or from non-oscillatory to oscillatory.

Table 11.4: Dynamic eigenvalues and eigenmodes

Eigenmode	Eigenvalue
Short Period	−0.548±0.408i
Phugoid	−0.192±0.832i
Aperiodic Roll	−8.610
Spiral	0.116
Dutch Roll	−1.212±4.965i

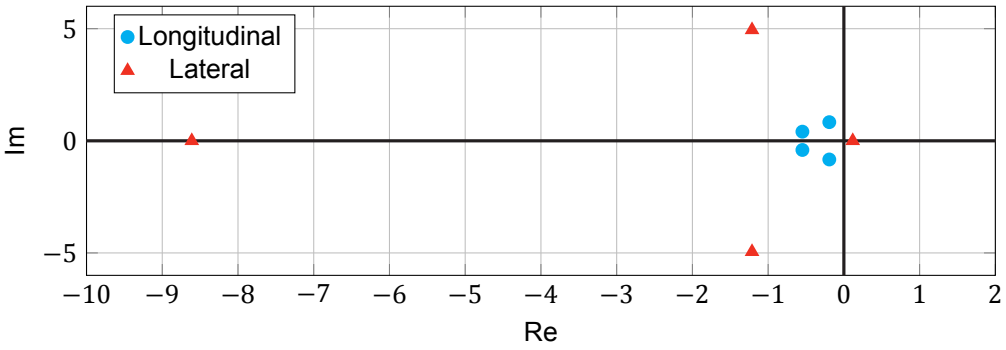

Figure 11.6: Dynamic eigenvalues of the fixed-wing aircraft

11.3. Control

In this section the control of the Unmanned Aerial System (UAS) is explained and characterized based on response times and sensitivity. Both the fixed-wing and quadcopter are analyzed and simulated. The control offers semi-autonomous flying where the operator picks the objectives the UAS should fulfill. The system optimizes the route and comes up with the flying plan which is displayed to controller for review. The control officer is able to influence the plan for custom commands. The UAV tries to follow the flight plan unless unexpected action occurs that forces the system into evasive action or malfunction. The control subsystem is split into two main parts: hardware and software elements. Hardware is further split into actuators such as ailerons and tail, and into electronics which is further elaborated in Chapter 14. Similarly the software is split into two components. Firstly the plane controller is used to fly the UAV in fixed-wing configuration and copter controller to fly the UAV while being in quadcopter configuration.

11.3.1. Design

This sections presents the initial sizing of control surfaces and the design of the control software module. General tail configuration and sizing has already been covered in Section 11.2.2 and this section will further elaborate on it. Lastly the control software has been designed around the open source autopilot package *ArduPilot*.[1]

Ailerons design

The ailerons are sized based on the estimated roll rate. The roll rate is calculated by first calculating the roll damping coefficient C_{l_p} and roll authority $C_{l_{\delta_a}}$ as seen in Figure 11.7. Assuming straight tapered wing with taper ratio λ, span b, and platform area S, the parameters can be found with the following equations:

$$C_{l_p} = -\frac{(c_{l_\alpha} + c_{do})C_R b}{24S}[1 + 3\lambda] \tag{11.4}$$

$$C_{l_{\delta_\alpha}} = \frac{c_{l_{\delta_a}} C_R}{Sb}[(b_2^2 - b_1^2) + \frac{4(\lambda - 1)}{3b} * (b_2^3 - b_1^3)] \tag{11.5}$$

where C_{l_α} is the lift polar slope, C_{d_0} is the skin drag. The design of the aileron was optimized for large maneuvers thus the value for helix angle at roll was picked in the range of military combat aircraft of $\frac{pb}{2V} \approx 0.9$ The aileron design obtained can be seen in Table 11.5.

[1] `ardupilot.org/`, last accessed: 2017-06-22

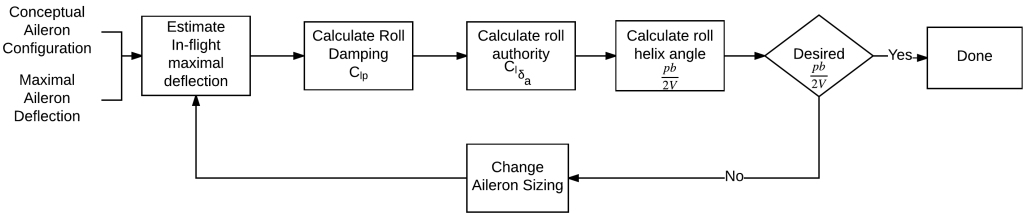

Figure 11.7: Design flow for aileron sizing

Table 11.5: Final sizing of the aileron

Aileron area [m^2]	Aileron start [m]	Aileron span end [m]	Aileron root chord [m]	Aileron tip chord [m]
1.44×10^{-2}	0.384	0.800	4.02×10^{-2}	2.87×10^{-2}

Control software design

This section presents the software architecture of the internals of the UAS and the data flow diagram that is used. The software consists of three components. The autopilot software based on open source *ArduPilot* software written in C++ language. The autopilot is tasked with calculation of optimal routing and controlling all the systems so that mission objectives can be achieved. This includes the active control in the quadcopter mode since the quadcopter is passively unstable. Besides the autopilot the hardware drivers written in the hardware description language, having the main tasks of acting as an interface between the autopilot and the hardware systems. It receives commands from autopilot and translate to hardware control for motors, servos and emitters. On the other hand, the ground station includes its own software component, which includes the mission planner software, targeting software and graphical interface. The aim of the software packages of the UAV is assuring reliability and stability, while the main aim of the ground station software is to provide a good user-friendly experience. The soldier who controls the UAV must be capable of making split decisions. The life status information of the system must be provided to the flight controller in the clear and direct manner. The general software block diagram can be seen below in Figure 11.8.

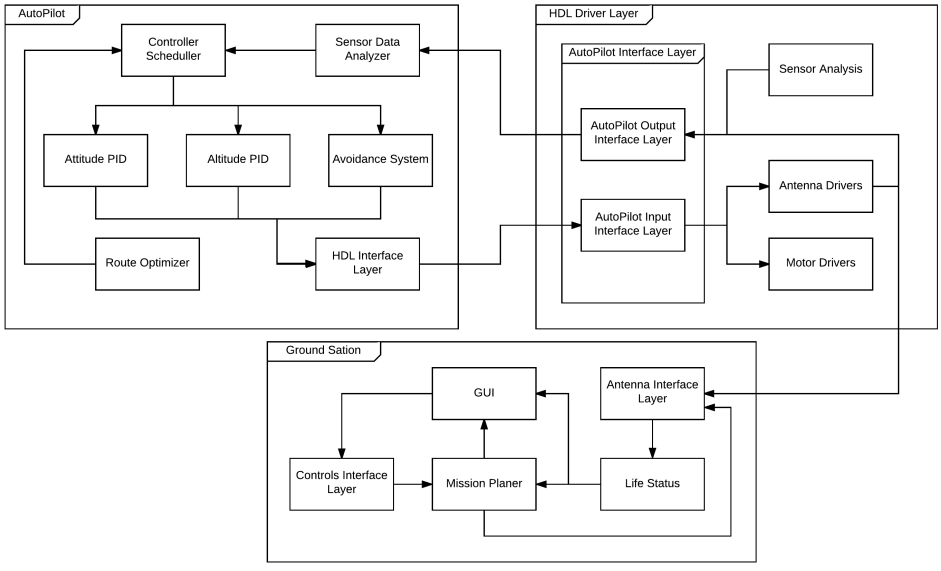

Figure 11.8: General software block diagram

The data flow for the UAS is presented in Figure 11.9. The processes that can be seen are grouped together based on the part of the system in which they occur. The process is any component, system or function which has at least one input and one output and mutates or uses data in some form. The arrows represent the flow and the type of data. The data store is a representation of a short term or a long term data storage component. Finally, the external entities are any systems outside of system boundary which are sources or sinks of data and information.

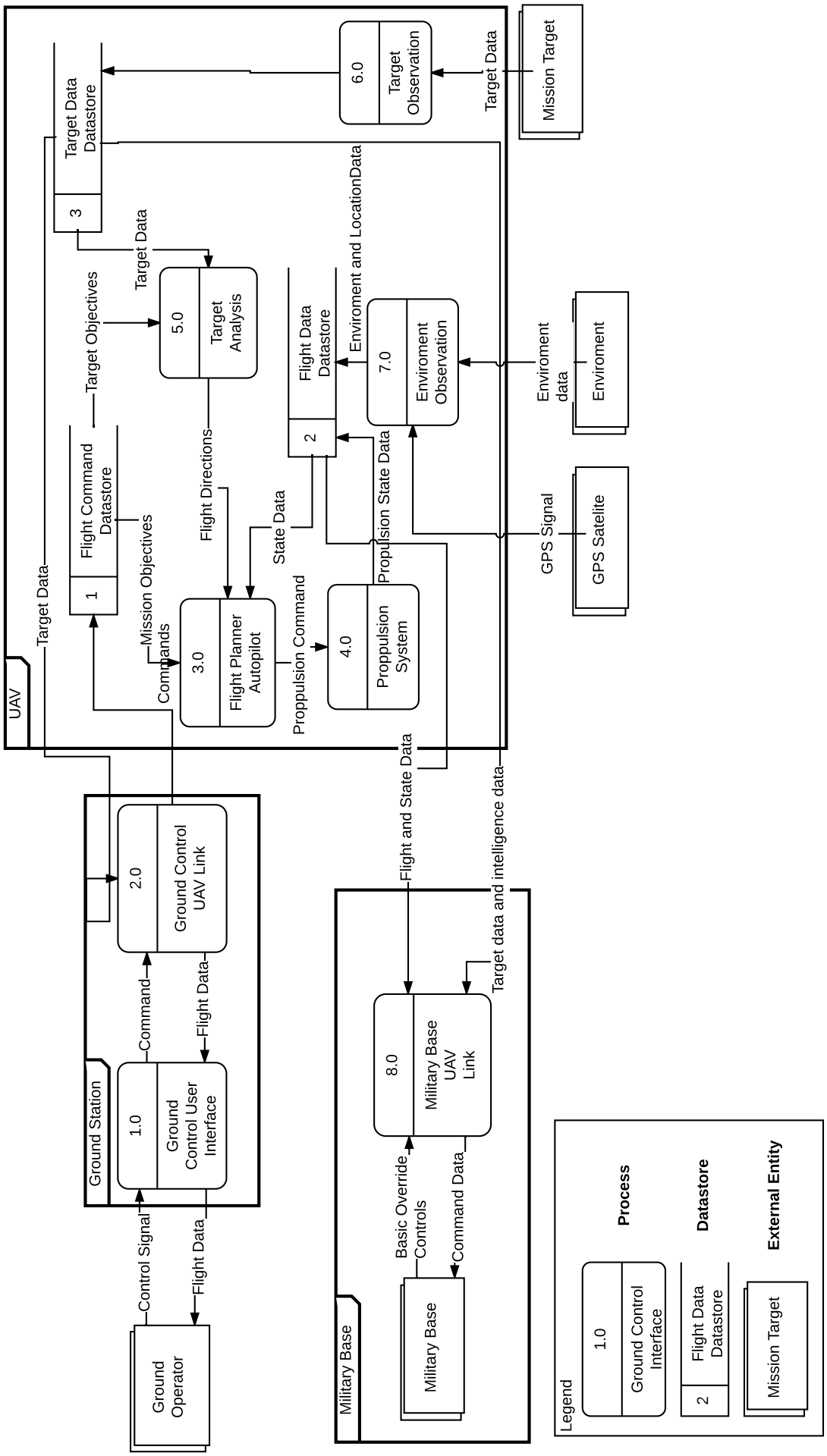

Figure 11.9: Data flow diagram for UAS in Gane and Sarson notation

11.3.2. Verification and validation

The verification of the control of the fixed-wing and the quadcopter was carried out using simplified equations, where the numerical solutions and analytically results was compared. It was found that the behaviour of the model agrees with the conceptual calculations. The response of software in the loop simulation could not be verified due to the lack of hardware. However, the ArduPilot software is an open source software, which is peer-reviewed. This has proven to be accurate in numerous applications[2]. The validation in turn could not be carried out due to the lack of real life data. To perform validation, a prototype should be constructed and the control system should be checked in real life flight mode. The validation of software should further be carried out using extensive unit, integration and acceptance testing based on real data.

11.3.3. Recommendations and suggestions

Firstly it needs to be pointed out that the control module has be designed on a very conceptual level. The module does not have a profound impact on the general layout of the UAV, yet the control characteristics are highly dependent on it. Moreover the control software needs to be configured specifically for each configuration, which would mean a lot of prototype flight hours. Thus, a more detailed analysis would need to be done. Additionally, the sizing of control surfaces needs to be checked for loads caused by vibrations and extreme loading situations. The joint loads need to be checked with Finite Element Method (FEM) simulation. Also, the response on control inputs needs to be analyzed in further detail. The software would need to have been written so that it could be unit tested, simulated and later tested in a prototype flight. Not having actual final software made validation and verification impossible, therefore verification and validation is to be performed when the software has been generated.

[2] `ardupilot.org/casestudies`, last accessed: 2017-06-22

II-12

Structural Design and Manufacturing

Following the wing airfoil design from the aerodynamics group, a first weight estimation of the wing can be performed. This will be done by evaluating the aerodynamic loads and the resulting stresses, using a numerical analysis on a straight wing.

12.1. Wing Structural Analysis

The coordinate system of the wing is chosen to be a body-fixed reference system with the origin located on the wing's leading edge in the spanwise middle of the wing. Because of symmetry only half a wing will be evaluated in the following analysis. The coordinate system with the to-be-evaluated wing section is shown in Figure 12.4.

Since the Unmanned Aerial Vehicle (UAV) will be very lightweight, conventional wing constructions (of large planes) are not applicable here. This is because metal structures consisting of stiffener reinforced skins would be too complex (manufacturing wise) and weight inefficient for low-load and lightweight wings. As a result the use of stiffeners will not be taken into consideration during the wing analysis, and a skin with varying thickness will be modelled [33, p. 65].

A solid core wing, e.g. filled with foam, has been considered as an alternative to a skin shell structure. However, there were some objections and limitations which had to be taken into account. First of all, the skin shell stresses do not come near the yield stress of the composite material considered. This means that there is no need to fill up the core, since it would only add weight. Secondly, foam filled wing design are being replaced by composite shell structures [54]. Finally the group does not have the necessary resources and skill to accurately model a solid core wing. On one hand there is no reliable way to validate a newly constructed numerical model, on the other hand third-party software is not reliable if the user has no proficiency in the use of the software. Figure 12.1 shows the process flow used in this section. Section 12.1.9 will go into more detail regarding the iterative process.

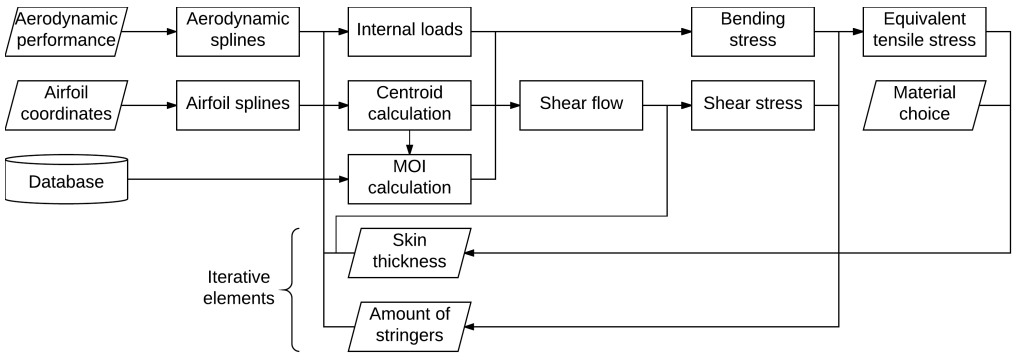

Figure 12.1: Wing structural analysis flow chart

12.1.1. Assumptions during analysis

The following assumptions have been taken during the structural analysis of the wing. The effect of these assumptions on the result can be found after the description.

WA-I A mesh of the wing will be created of which the distance between two adjacent points is assumed to be linear. By increasing the number of points n_x the error will decrease. With $n_x = 100$, the difference in arc lengths is 0.05 %.

WA-II The contribution of the tail weight to the bending and torque stresses are not taken into account in this preliminary design, since the tail will be sized in the detailed design. The weight of the tail would result in bending relieve, as well as a positive shear flow. At the connection location a frame is added which is assumed to be strong enough to support the loads coming from the tail.

WA-III The lift and drag force are assumed to act through the shear center, which coincides with the center of pressure. This point is assumed to always be on the chord. The torque caused by these forces is added using the aerodynamic moment distribution obtained from the aerodynamics group.

WA-IV The cross section is assumed to not deform due to internal forces during the analysis.

WA-V The initial skin thickness is 0.80 mm, which are four layers of woven Kevlar fabric with epoxy resin[1] $\pm 45, 0/90, 0/90, \pm 45$ and are assumed to be the minimum required.

WA-VI During the analysis the lift force is multiplied with preliminary load factors of ±5 from the flight and gust envelope (Section 4.1.2). Furthermore the lift, drag, and aerodynamic moment are multiplied with a safety factor of 1.5 [45, p. 18].

WA-VII For the buckling analysis the top half of the airfoil is approximated by a curved plate. The bottom half is approximated by a double curved plate.

12.1.2. Aerodynamic input processing

The aerodynamics provided airfoil data points of the *FX63137* airfoil to be analyzed. Firstly the top and bottom half of the airfoil coordinates from Chapter 10 are approximated by a one-dimensional interpolating spline. The result of this approximation can be seen in Figure 12.2.

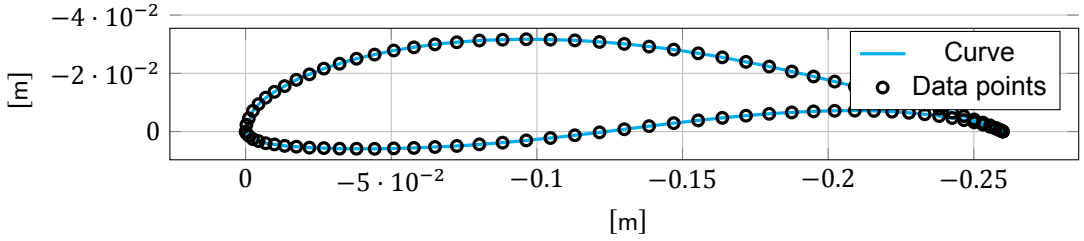

Figure 12.2: Airfoil curve fitting through the provided datapoints

The aerodynamic data exported by *XFLR5* has to be multiplied by the dynamic pressure at the measurement and the Mean Aerodynamic Chord (MAC), also indicated as $\bar{c}$, of the airfoil. The lift and drag distributions are approximated using the same method as the airfoil, resulting in an smooth distribution between the imported data points. The distribution data points and corresponding splines are shown in Figure 12.3.

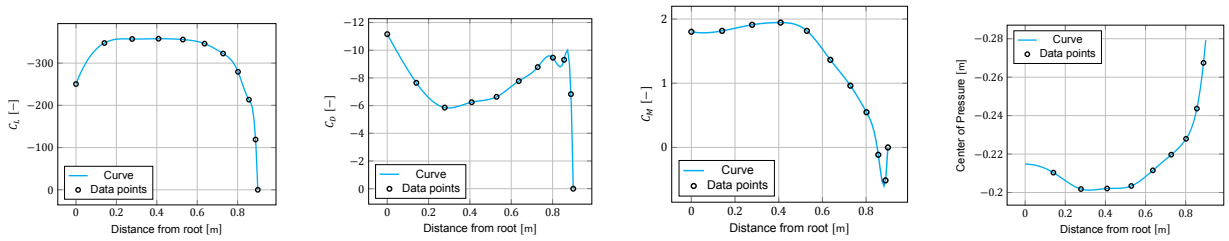

(a) C_L distribution (b) C_D distribution (c) C_M distribution (d) CP location

Figure 12.3: Aerodynamic properties along the wing

These distributions resulted into internal force, moment and torque distributions which are required to do structural analysis of the wing. The internal force (and torque) and moment formulas are given in Equation (12.1) and are calculated using the dynamic pressure q_∞ and the relevant aerodynamic coefficients $C_{[L,D,M]}$. During the calculation of the internal bending moments the sign convention displayed in [41] is applied. Note how the weight is included in the moment calculation, this will be elaborated upon in Section 12.1.9.

$$[-L, -D, T]_i = \bar{c} q \int_{y_i}^{y_{i+1}} C_{[L,D,M]}(y)\, \mathrm{d}y \qquad \left[M_x, M_y\right]_i = \sum_{j=i}^{j|y_{j+1}=b/2} [L_j + W_j, D_j] \frac{y_{j+1} + y_j}{2}\, \mathrm{d}y \tag{12.1}$$

12.1.3. Wing mesh construction and properties

In order to perform analysis over the wing, the wing skin was transformed into a mesh having an accuracy of n_y points over the wing span (y direction) and an accuracy of n_x points over one side of the airfoil (equally spaced over the x oriented MAC), discretizing the wing into a $n_y \times 2 \cdot n_x$ mesh. Increasing the mesh accuracy will decrease linearization errors and increase the accuracy of the result.

[1] www.performance-composites.com/carbonfibre/mechanicalproperties_2.asp, last accessed: 2017-06-09

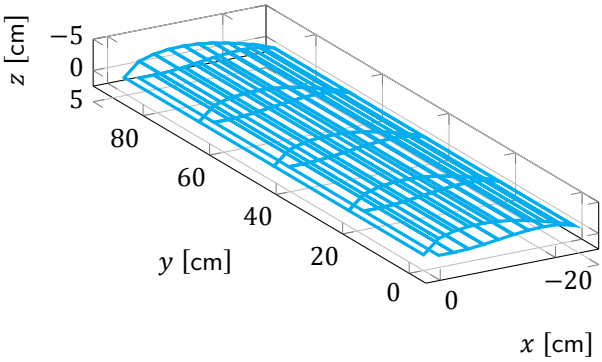

Figure 12.4: Wing mesh with $n_y = 5$ and $n_x = 10$

Initially a uniform skin thickness was assumed, in order to allow the generation of the first loads and resulting stresses. However, because of the construction of the mesh it is possible to implement changing skin thicknesses. Therefore in the following analysis the skin thickness will be a property of a mesh point. The skin thickness in a point $[i, j]$ in a $[n_y, 2 \cdot n_x]$ mesh applies to the patch $[i : i+1, j-1 : j]$.

12.1.4. Airfoil geometry

With the wing mesh set up, the airfoil geometry properties can be calculated. These properties will be required to calculate stresses caused by loading of the geometry.

Calculation of centroid

The centroid is calculated for each xz cross section. As can be seen in Figure 12.2 this cross section has the shape of the airfoil, with a possibly variable skin thickness t_i. The centroid is calculated using Equation (12.2), with Δs_i the linear distance from the previous point (according to **WA-I**).

$$[\bar{x}, \bar{z}] = \frac{\sum_{i=0}^{2 \cdot n_x} [x_i, z_i] t_i \Delta s_i}{\sum_{i=0}^{2 \cdot n_x} t_i \Delta s_i} \tag{12.2}$$

Calculation of MOI

Like the centroid, the Moment of Inertia (MOI) is calculated for each airfoil cross section. It is calculated using the discretised method, using Equation (12.3). This method approximates a skin element as a rectangle, with center at $z_{\text{avg}}, x_{\text{avg}}$. Since no stringers are used, the boom classical boom theory is not applied.

$$[I_{xx}, I_{zz}] = \sum_{i=0}^{2 \cdot n_x} t_i \Delta s_i \left(\frac{\Delta [z_i, x_i]^2}{12} + \left([z_{\text{avg}}, x_{\text{avg}}] - [\bar{z}, \bar{x}] \right)^2 \right) \tag{12.3}$$

$$I_{xz} = \sum_{i=0}^{2 \cdot n_x} t_i \Delta s_i \left(\frac{\Delta x_i \Delta z_i}{12} + \left(x_{\text{avg}} - \bar{x} \right) \left(z_{\text{avg}} - \bar{z} \right) \right) \tag{12.4}$$

12.1.5. Free body diagram, force and moment distributions

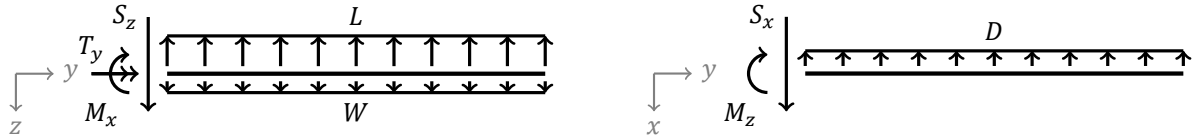

(a) yz view (b) xy view

Figure 12.5: Free body diagrams of the wing modelled as a cantilevered beam

Free body diagram
One half of the wing is modelled as a cantilevered beam, clamped in the middle where the wing will be attached to the fuselage. There are three loads acting on the wing. Firstly the lift and weight changing along the span in the z direction, and the drag in the x direction. For the sake of simplicity the shear center is assumed to be at the center of pressure, causing no internal torque. To compensate this the aerodynamic moment T_y obtained from the aerodynamics group is taken into account for the shear calculation. (**WA-III**)

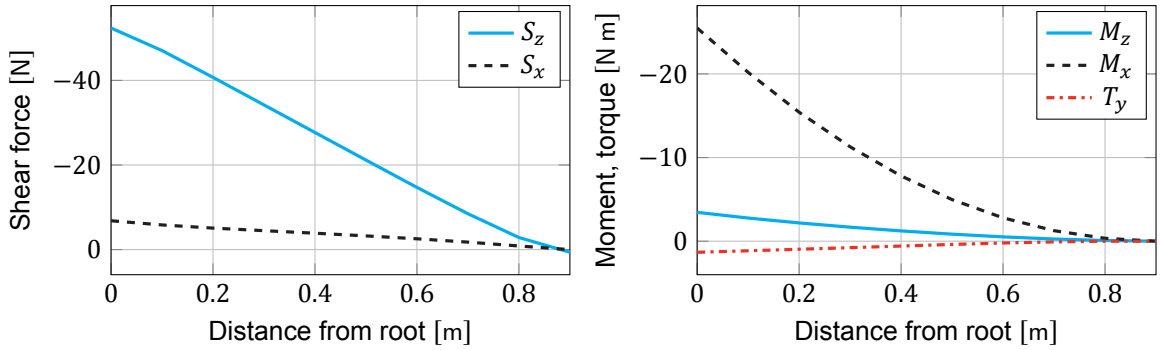

(a) Internal shear force

(b) Internal moment and torque

Figure 12.6: Internal loads along the wing span ($n_y = 10$)

Force and moment distribution
From the free body diagram the internal loads can be calculated. Since there are only reaction forces at the wing root, the diagrams have the shape as expected resulting from a distributed load. The internal load distribution along the wing span can be seen in Figure 12.6.

The vertical shear becomes increasingly negative towards the wing root, because of the lift force being bigger in magnitude than the wing weight. The horizontal shear also increases due to the drag force. The internal bending moments have an exponential increase in magnitude, due to the loads on the wing being distributed along the span. Furthermore the torque is increasingly negative towards the root, because of the aerodynamic moment that causes the wing's pitch up tendency.

12.1.6. Normal stress due to bending

Beam bending theory is used to calculate the resulting stresses in each point in the mesh grid defined above. Since the cross section is not symmetric, the formula for asymmetric bending around the centroid is used, which is given by Equation (12.5) (with i the span wise index, j the airfoil coordinate index) [41, p. 437].

$$\sigma_{y_{i,j}} = \frac{I_{xx_i} M_{z_i} - I_{xz_i} M_{x_i}}{I_{xx_i} I_{zz_i} - I_{xz_i}^2} \left(x_j - \bar{x}_i\right) + \frac{I_{zz_i} M_{x_i} - I_{xz_i} M_{z_i}}{I_{xx_i} I_{zz_i} - I_{xz_i}^2} \left(z_j - \bar{z}_i\right) \tag{12.5}$$

Combining this with the moment distribution from Figure 12.6b it is found that the bending stresses are the biggest in magnitude at the wing root, which can be seen in Figures 12.9a and 12.10a. As expected the top skin is under compression while the bottom skin is in tension at positive ultimate load, with maximum magnitudes of 43.0 MPa and 35.7 MPa respectively. At negative ultimate load the maximum stresses are 37.4 MPa and 44.5 MPa.

Plate buckling
Since the top and bottom skins of the wings can be seen as thin plates, they are prone to buckling. However, they are not straight thin plates in isolation, but irregularly shaped and interconnected. The top skin can be modelled as a curved plate, while the bottom one as a double curved plate. (**WA-VII**) The approximating circle arcs need to have the same boundary points and MOI as the original skin. The bottom skin has to be split up into two arcs for the analysis, treating it as two semi-clamped curved plates [26].

The buckling of a thin plate is given by Equation (12.7). The critical buckling stress depends on the Young's modulus E, the Poisson's ratio v and thickness-to-width ratio t/b. The radius of curvature is calculated by approximating the skin as an arc through the airfoil edge points, with the center at 50 % MAC and the curve having the same I_{xx} as the airfoil [26, p. 55] [41, p. 296].

The factor K_p is dependent on the boundary conditions of the analyzed plate. In [26] this factor is derived from flat thin plate buckling k values by assuming the boundary conditions to be between simply supported and clamped. This is also applicable to the wing skin, since both the top and bottom skin are unable to displace, but can not be considered fully clamped. Figure 12.8 shows K_p in function of Z_b, which is given by Equation (12.6).

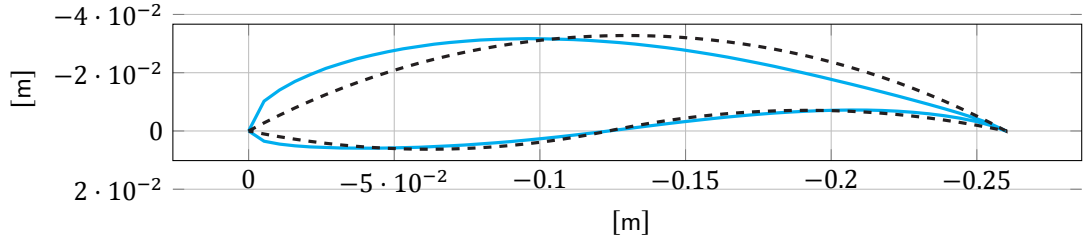

Figure 12.7: Curve approximation used in buckling analysis

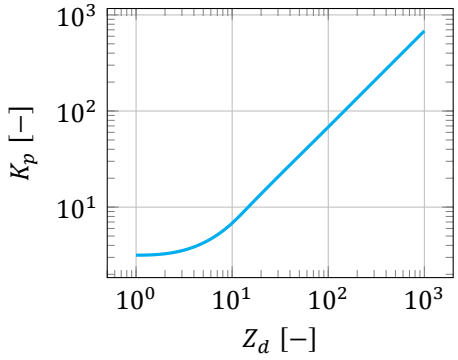

Figure 12.8: Buckling factor for a thin curved plate

$$Z_d = \frac{b^2}{rt}\sqrt{1-v^2} \tag{12.6}$$

$$\sigma_{cr} = \frac{k_p \pi^2 E}{12 \cdot (1-v^2)} \left(\frac{t}{d}\right)^2 \tag{12.7}$$

12.1.7. Shear stress

The shear stress is caused by shear flow through the skin. The shear flow originates from three sources: the vertical shear force (lift and weight), the horizontal shear force (drag), and the internal torque caused by the aerodynamic moment.

Shear flow due to forces

The shear flow caused by the lift, weight, and drag is calculated using the closed section beam method. This method first moves the shear forces towards an arbitrary point and adds an extra torque to compensate for the displacement. At this point the closed section is *cut*, and the total shear flow is split up in a open section shear flow q_b and a constant balancing shear flow q_{s_0} [41, p. 489].

$$q_s = q_b + q_{s_0} \tag{12.8}$$

Equation (12.9) shows the formula for calculating the q_b in every point along the skin. This open shear flow is 0 at the cut, since this is where the shear forces are moved to and acting through.

$$q_b = -\left(\frac{S_z I_{zz} - S_x I_{xz}}{I_{xx} I_{zz} - I_{xz}^2}\right) \int_0^s tz \, \mathrm{d}s - \left(\frac{S_x I_{xx} - S_z I_{xz}}{I_{xx} I_{zz} - I_{xz}^2}\right) \int_0^s tx \, \mathrm{d}s \qquad [41] \tag{12.9}$$

However the above equation needs to be discretized in order to be applicable to mesh calculations. The integral in Equation (12.9) is split up along the skin segments of the mesh, allowing the summation of the shear flow in the previous point and the one in the current segment, which is shown in Equation (12.10) (with i the span wise index, j the airfoil coordinate index).

$$q_{b_{i,j}} = q_{b_{j-1}} - \left(\frac{S_{z_i} I_{zz_i} - S_{x_i} I_{xz_i}}{I_{xx_i} I_{zz_i} - I_{xz_i}^2}\right) t_j \frac{\Delta z_{j,j-1}}{\Delta s_{j,j-1}} \frac{s_j^2 - s_{j-1}^2}{2} - \left(\frac{S_{x_i} I_{xx_i} - S_{z_i} I_{xz_i}}{I_{xx_i} I_{zz_i} - I_{xz_i}^2}\right) t_j \frac{\Delta x_{j,j-1}}{\Delta s_{j,j-1}} \frac{s_j^2 - s_{j-1}^2}{2} \tag{12.10}$$

The torque resulting from the displacement of the shear force and the moments of the shear flows around the cut have to be in equilibrium. Therefore a correctional shear flow q_{s_0} is added, shown in Equation (12.11). Only the vertical shear is taken into account for this torque, since the drag is assumed to act on the chord. (**WA-III**)

$$q_{s_0} = \frac{(L-W) x_{\mathrm{CoP}} - \oint p q_b \, \mathrm{d}s}{2 \cdot A} \tag{12.11}$$

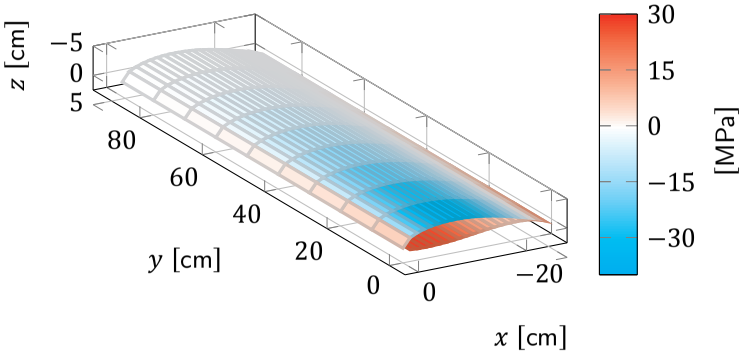

(a) Direct stress due to bending

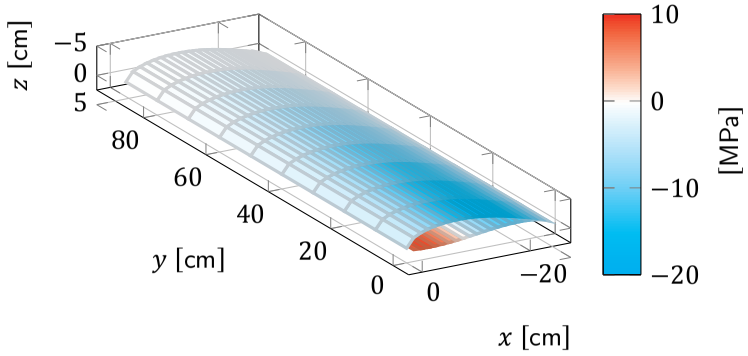

(b) Shear stress due to force

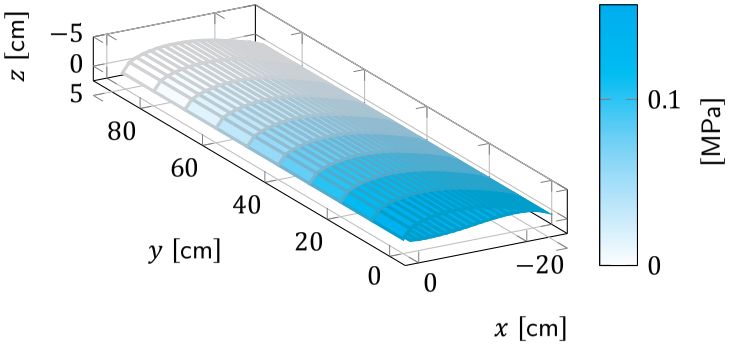

(c) Shear stress due to the aerodynamic moment

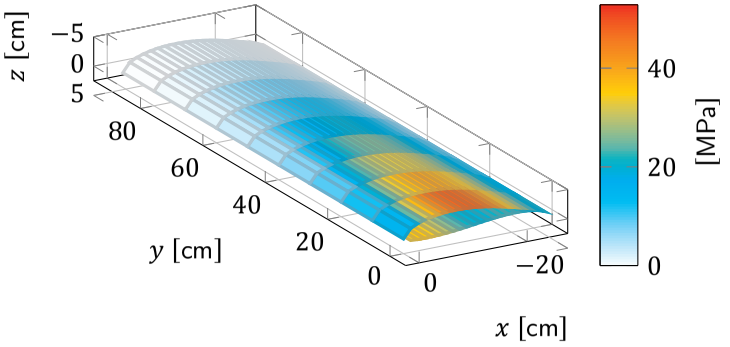

(d) Von Mises stress

Figure 12.9: FX63137 stress distributions at $n_{\text{ult}} = 5$ $n_y = 10$, $n_x = 20$

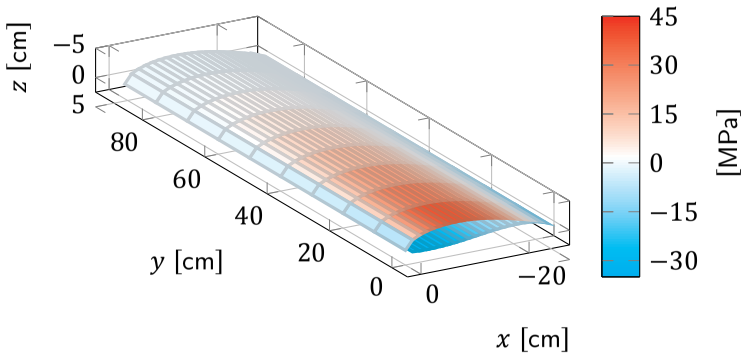

(a) Direct stress due to bending

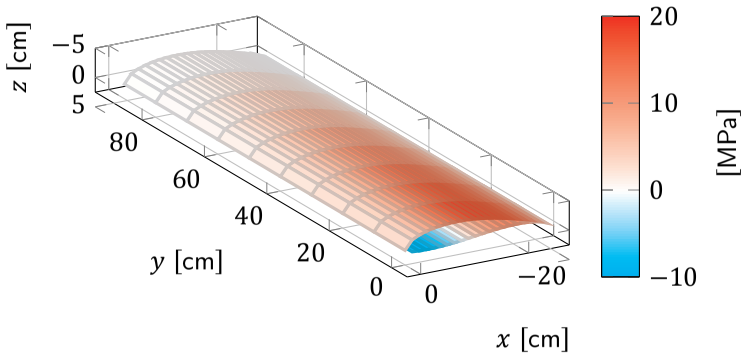

(b) Shear stress due to force

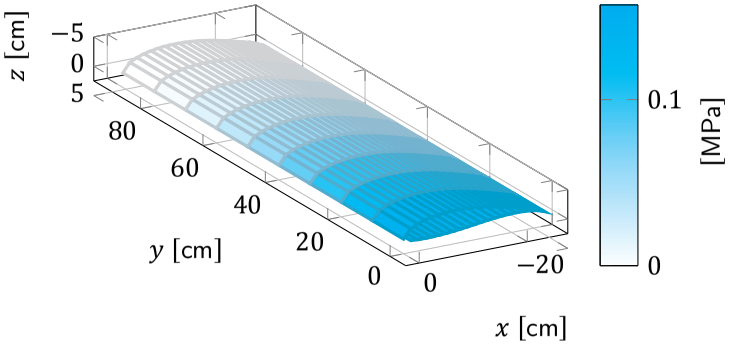

(c) Shear stress due to the aerodynamic moment

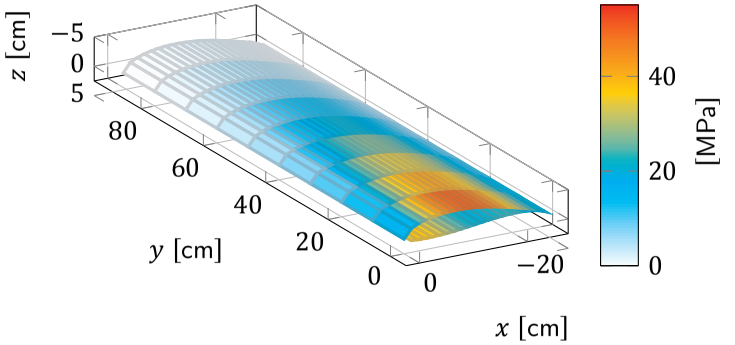

(d) Von Mises stress

Figure 12.10: FX63137 stress distributions at $n_{\text{ult}} = -5$ ($n_y = 10$, $n_x = 20$)

Shear flow due to aerodynamic moment
The aerodynamic moment acting on the wing causes an internal torque, resulting in an internal shear flow through the skin. The shear flow is calculated using Equation (12.12). Since the total aerodynamic moment increases towards the root, so will the internal shear flow [41, p. 504].

$$T_y = \oint p q_T \, \mathrm{d}s = 2 \cdot Aq \quad \Leftrightarrow \quad q_T = \frac{T_y}{2 \cdot A} \tag{12.12}$$

Shear stress from shear flow
The shear stress in a skin segment can be calculated using Equation (12.13).

$$\tau_y = \frac{q_s + q_T}{t_{\text{skin}}} \tag{12.13}$$

The resulting shear stress distributions can be seen in Figures 12.9b and 12.10b due to shear forces, and in Figures 12.9c and 12.10c due to the aerodynamic moment. The corresponding maximum shear stresses due to shear forces are 20.8 MPa and 22.1 MPa at positive and negative ultimate load respectively, while those due to the aerodynamic moment are both 0.16 MPa. (**WA-VI**)

In these figures the sign of the shear stress is only an indication of the direction of the shear stress in the skin segment. The mesh calculations are performed in the right hand ($+y \odot \circlearrowleft$) orientation, indicating also the positive shear stress direction.

12.1.8. Equivalent tensile (von Mises) stress

In order to see the total stress that is experienced by the carrying material at a point in the cross section, the equivalent tensile stress has to be calculated, given by Equation (12.14). This stress has to be compared to the yield stress of the material, with the material failing when the former stress is bigger.

$$\sigma_v = \sqrt{\frac{\left(\sigma_{xx} - \sigma_{yy}\right)^2 + \left(\sigma_{yy} - \sigma_{zz}\right)^2 + \left(\sigma_{zz} - \sigma_{xx}\right)^2 + 6 \cdot \left(\sigma_{xy}^2 + \sigma_{yz}^2 + \sigma_{zx}^2\right)}{2}} \tag{12.14}$$

In this structural analysis only three stresses are calculated: σ_{yy} due to bending, and $\tau_{yx} = \sigma_{xy}$ and $\tau_{yz} = \sigma_{yz}$ due to shear and the aerodynamic moment. However, in Section 12.1.7 only the shear force τ_y in the xz-plane along the orientation of the skin segment is calculated, which can be written (using Pythagoras's theorem) $\tau_y^2 = \tau_{yx}^2 + \tau_{yz}^2 = \sigma_{xy}^2 + \sigma_{yz}^2$, resulting in Equation (12.15).

$$\sigma_{v_{i,j}} = \sqrt{\sigma_{y_{i,j}}^2 + 3 \cdot \tau_{y_{i,j}}^2} \tag{12.15}$$

The equivalent tensile stress distribution can be seen in Figures 12.9d and 12.10d. The highest stress concentrations can be found at the wing root, more precisely in the segments furthest from the centroid. This is because of the big contribution due to the bending moment, which has around twice the magnitude of the shear stress.

12.1.9. Weight estimation and iteration

After completing the calculation process for the first time with the assumed skin thickness of 0.8 mm (**WA-V**) the structure can be optimized. Since the maximum von Mises stress (90.6 MPa) is nowhere near the yield stress of Kevlar (30 GPa, >300 %), they are not deemed critical for the design. This means that the wing should be optimized to resist buckling under loads.

The optimization process is shown in Figure 12.1 as the feedback towards the skin thickness and stiffeners. Although the addition of stiffeners in general is not advantageous for weight reduction, the option was included in the iteration since the wing has no spar and thus carries all loads in the shell (skin).

Buckling calculations showed that no stiffeners were needed when the load factors of the UAV stay between −8 to 14. This results in the wing having an estimated weight of 1.143 kg, with a skin thickness of 0.8 mm.

12.1.10. Updated airfoil calculations

The aerodynamics group found an airfoil which was deemed more favorable, and therefore required new structural analysis for an updated weight estimation. Because of the generic construction of the software, implementing this new airfoil was easily done. The newly generated airfoil curves are shown in Figure 12.11.

The stress calculations of the NACA22112 airfoil resulted in are similar to those obtained with the FX63137 airfoil. The maximum compression and tension stress are 37.8 MPa and 36.6 MPa respectively. The maximum shear stress is 32.4 MPa, with the maximum equivalent tensile stress being 66.6 MPa.

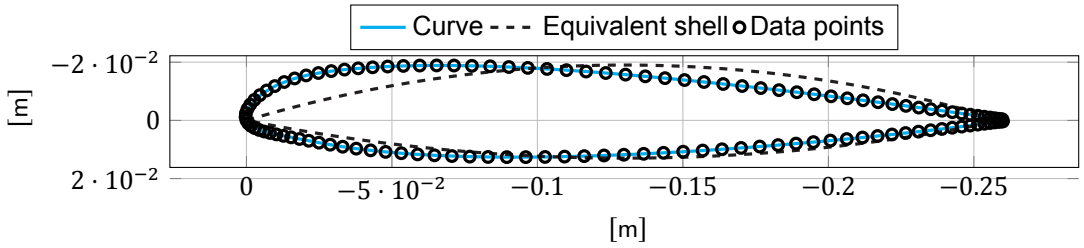

Figure 12.11: Data points and resulting curves of NACA22112 airfoil

Like for the previous airfoil's results, the von Mises stress is not deemed to be the critical stress, therefore the optimization is done in function of buckling. Without any stiffeners, the airfoil is found to buckle under loads greater than 7 and −4. Table 12.1 gives the airfoil mass in function of the required load envelope. This mass is based on the weight of a stiffener, which is modelled as an L-beam 10 mm × 10 mm × 0.5 mm made out of Kevlar.

Table 12.1: Estimated wing mass with different load requirements

Positive load [-]	Negative load [-]	Stiffeners [-]	Estimated mass [kg]
<7	>−4	0	1.126
<7	<−4	1	1.151
>7	>−4	1	1.151
>7	<−4	2	1.178

This means that the new airfoil has a weight reduction of 17 g (1.5 %) if the flight envelope is restricted to load factors 7 to −4. In case the envelope should be extended, this can be done by adding a 25 g stringer on either side (top skin to increase positive load, and vice versa).

12.2. Further Analysis with FEM

In this section, the structural analysis that is performed using the Finite Element Method (FEM)-software *ANSYS* is discussed. For the parts other than the wing of the UAV, the analysis has not been performed analytically like discussed in the previous sections. Instead, analysis using *ANSYS* has been conducted. Unfortunately, the lack of experience using *ANSYS* had a consequence; the results that were generated could not be used quantitatively. However, these results could be interpreted qualitatively. At first, a *CATIA*-model was imported as a geometry out of which a mesh was created. Then the forces and moments were modelled onto the geometry and the analysis generated results which then in turn could be interpreted. This process has been executed for the wing, body and the quadcopter rods and will be discussed below.

12.2.1. Wing analysis

Just like in the previous analytical approach, all the forces and moments were modeled on the wing model that was imported from *CATIA*. The result is shown in Figure 12.13. The moment and forces that the wing is subjected to cause the stresses shown in Figure 12.13a. Also, Figure 12.13b shows the displacement of the wing under the applied forces.

Unfortunately this method did not prove to be as reliable as expected, compared to the results that were determined analytically. The calculated value for the von Mises stress was in the order of 10 MPa, whereas the value determined by *ANSYS* gave a value in the order of 1 MPa. The reason for this could be the way the *CATIA*-model was imported, as *ANSYS* interprets the geometry as a solid instead of a volume with a small thickness. This error is one that could have been prevented or fixed if there was more experience in utilizing the program. Unfortunately the problem could not be solved and the numerical results were not useful to the design process. However, the result that has been produced in Figure 12.13 is not necessarily useless. It can be used qualitatively since it shows the regions where the highest stresses are. Here it can be seen that the largest stresses will occur at the root of the wing, due to the bending moment the lift generates, and at the location where the rod that connects the tail wing to the main wing will be attached. The attachment should be seen as a critical point and the material for the wing should be chosen accordingly. The result can be compared to the one that has been determined analytically in Figure 12.9d and it can be seen that both plots are very similar.

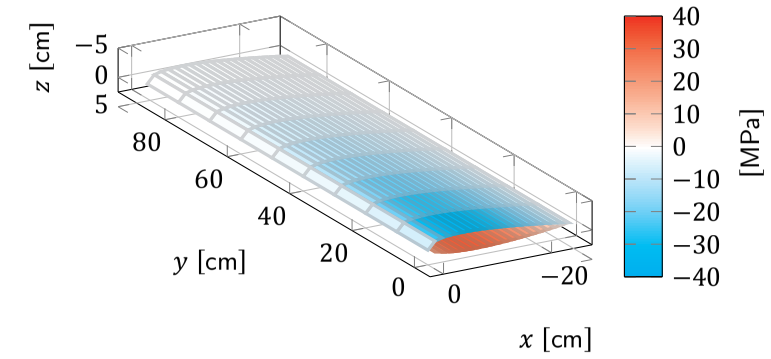

(a) Direct stress due to bending

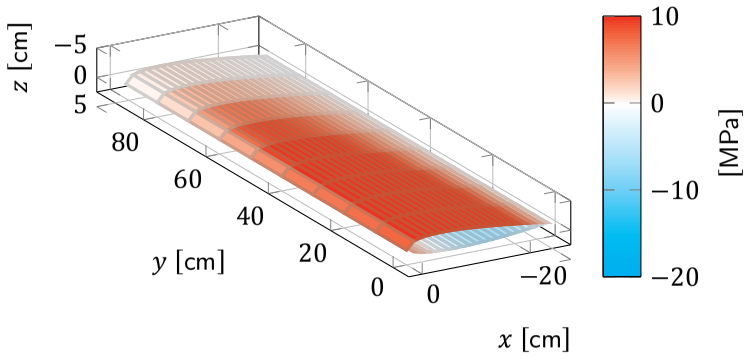

(b) Shear stress due to force

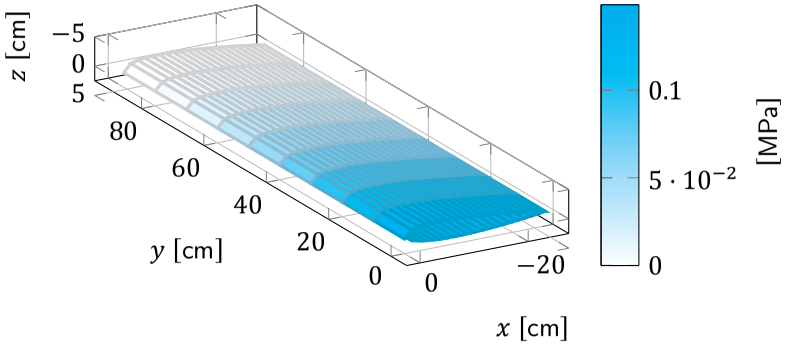

(c) Shear stress due to the aerodynamic moment

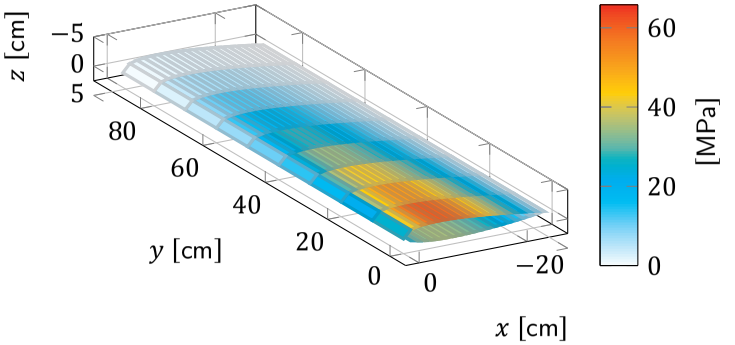

(d) Von Mises stress

Figure 12.12: NACA22112 stress distributions at $n_{\text{ult}} = 5$ ($n_y = 10$, $n_x = 20$)

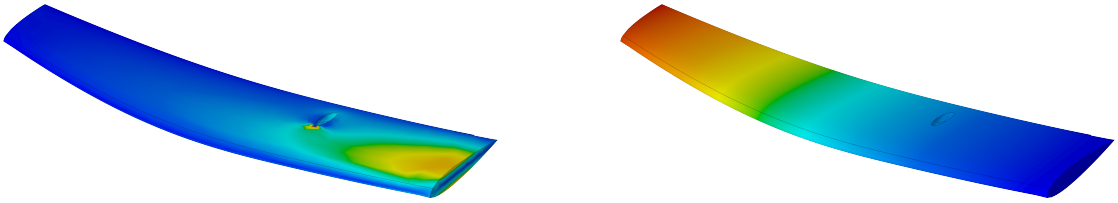

(a) Wing stress (b) Wing displacement

Figure 12.13: Wing simulation

12.2.2. Body analysis

As discussed earlier, the same analysis that was performed for the wing could not be used for all the remaining elements. This includes the fuselage of the UAV as well. Using *ANSYS* is another way to analyze the body. For the fuselage, a simplified model was imported due to the complex curves the design contained. These curves made it difficult to analyze the body using *ANSYS*. Importing a simplified model made it possible to generate solutions to the simulation. Although this is indeed a simplified model (Figure 12.14) compared to the actual design, the main shape of the body is still intact, apart from the curved edges. Since the wing induces higher loads onto the fuselage compared to the quadcopter configuration, the loads of the wing were simulated onto the fuselage. The fuselage was constrained at the sides and the aerodynamic moment, lift, drag, thrust and weight were simulated on the fuselage such that it produced the results displayed in Figure 12.14. Again, both the stress in the fuselage (Figure 12.14a) and the displacement in the fuselage (Figure 12.14b) are shown.

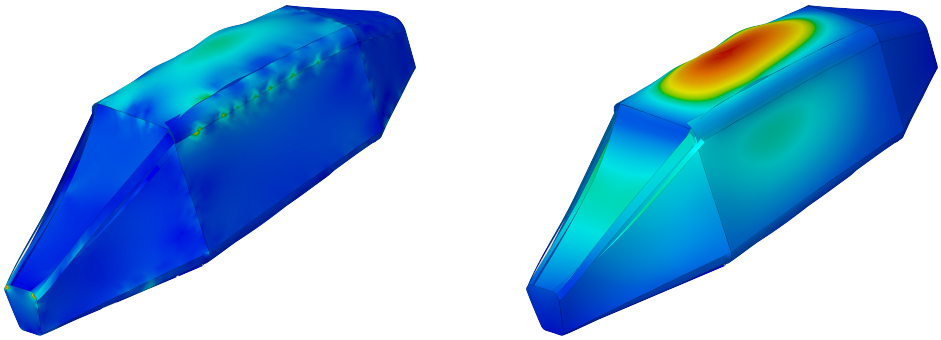

(a) Fuselage stress (b) Fuselage displacement

Figure 12.14: Fuselage simulation

Figure 12.14 shows that the fuselage has the largest von Mises stress at the top of the body where the wing will be connected. Also, the corners and edges at the top and front of the body seem to induce large stresses. For further detailed design this should be considered when modeling the body since the curved edges will lead to different stress distributions compared to this simplified simulation. The displacements of all the faces that are shown in Figure 12.14 are not scaled. It seems like the displacements of the surfaces of the body are very large, however it was determined that the largest deflection the body makes is around 1 mm in this simulation, which is on top of the body.

12.2.3. Quadcopter frame analysis

For the quadcopter, the rods that hold the propellers and are connected to the top assembly were analyzed with *ANSYS*, in addition to the analysis that is performed later this section. As one would suspect, the thrust the propeller generates will induce large bending stresses at the root of the rod where the rod connects to the top section. The thrust was modeled and produced the results shown in Figure 12.15.

Figure 12.15a shows that in this simulation the von Mises stresses are highest at the location where the rod will be connected. This is because of the thrust the propeller creates, which causes the clamped rod to be under pure bending, which will be largest furthest away from the acting force. This bending force also leads to a displacement of the rod as seen in Figure 12.15 The critical stresses are therefore at the connection point and the rod was designed such that it is able to withstand these stresses.

The structural mass of the arm was estimated based on the loads placed on it by the engine at maximum thrust. The free body diagram of the quadcopter, as seen in Figure 12.16, shows a rough estimation of the forces experienced by the drone. The maximum thrust was already found from Chapter 9. Based on this, it was determined that the arms would be circular hollow rods made out of carbon fiber. The rods were chosen to be 1 cm radius with a thickness of 0.5 mm. This gave them a weight of 13 g per boom.

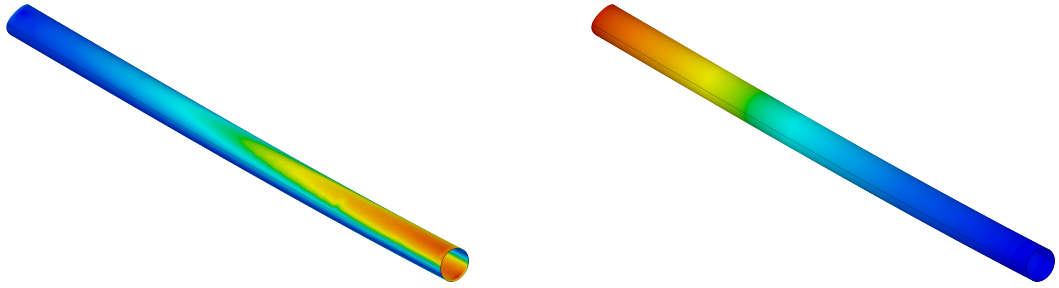

(a) Rod stress (b) Rod displacement

Figure 12.15: Rod simulation

The quadcopter module consists of four motors and propellers attached to the quadcopter rods, a set of rotor guards and the structure connecting the engines to the fuselage. The supports are attached to the fuselage using a socket secured with a pin as stated in Chapter 8. The rotor protectors (which can be seen in the bottom left of Figure 12.18, if added, were determined to weigh a total of 67 g, being constructed out of expanded polystyrene. This material is a preliminary choice, as an impact simulation on these guards are needed to make a final material selection.

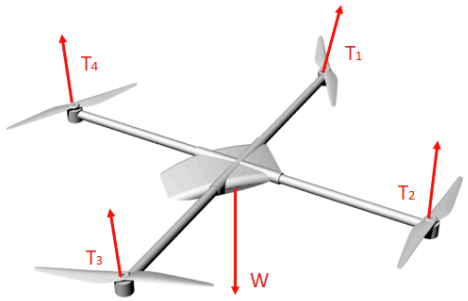

Figure 12.16: Free-body diagram of the quadcopter

An overview of the weights of the base quadcopter attachments can be found in Table 12.2.

Table 12.2: Masses of different quadcopter module components

Item	Mass [g]	Item	Mass [g]
Motor	284	Prop	72
Arm	44	Attachment motor	12
Wire	48	Attachment body	16
		Total	**476**

12.3. Material Selection

In order to familiarize with the types of materials, a material classification of materials that are used in general aviation and smaller scale UAV is given in Section 12.3.1. After that, the multiple failure modes are given that were considered in the design process.

12.3.1. Material classification

The most important aspects to keep in mind while performing the material selection is that apart from that it should be able to carry the loads, it should also be recyclability and comply with the Registration, Evaluation and Authorization of Chemicals [EU Reg 1907/2006] (REACH) requirements.

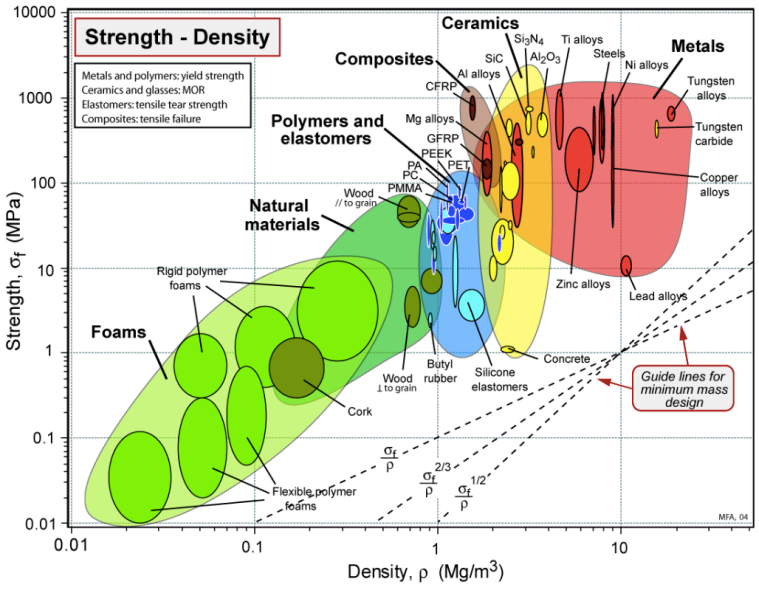

Figure 12.17: Relation between material strength and density

Metals

In aircraft structures, metals are frequently used because they can normally bear high loads due to their strength (Figure 12.17)[2]. Also, according to [14, p. 822], many metals can be recycled which contributes to **SPARTA-UAV-14**. However, it is expected that the loads on the UAV are relatively small. As can be seen in Figure 12.17, the strength of metals comes with a larger density compared to other materials, such as composites and polymers. Therefore, the use of metals will not be extensive for the structure of this UAV.

Composites

Nowadays, composites are used more often in the aviation industry because of various benefits that come with them. Firstly, they can be used to make complex shapes, which means that less parts are needed for a larger structure and the overall structural weight decreases. Also, due to the smaller amount of parts, fewer connectors are needed which leads to less critical failure points. Furthermore, composites have a high specific strength, i.e. they are strong for their weight compared to other material groups such as metals. Composites are made out of more than one material, usually one matrix material and a fiber material. Therefore many possible combinations are possible. In general, composites are quite difficult to recycle as two materials mixed together are intricate to separate. Although this is the case, there are ways to recycle composites as stated in [14, p. 826].

Polymers

Another material type to consider are polymers, in particular plastics and foams. Although both plastics and foams are not known for their strength, they could be suitable to use for this relatively small UAV Figure 12.17. They can be made into complex shapes, suitable for the curved elements in the design. This lead to the same advantages as discussed for composites. Additionally, certain plastics are recyclable. If chosen properly, plastics could be used that comply with the recyclability requirement. Plastics are thus still a suitable material to manufacture the UAV of.

Sandwich structures

Sandwich structures are composed of two thin sheets of one material and a lightweight core of another material. Just like with composites, there are many possible combinations. There are three types that are conventionally used for the core of the sandwich: a honeycomb core, foam core, and a balsa wood core.

Table 12.3 [3][4] [14] shows the materials that have been considered. There are two composites present: carbon fiber epoxy and Kevlar epoxy. The former is considered as it is widely used in the aviation industry and in small aircraft as well. The latter is there due to its lower density and ablility to withstand high impact loads (e.g. it is used in bulletproof clothing). Apart from these composites, the plastic Polylactic Acid (PLA) was considered. They are lightweight with relatively low strength, but could still be suitable for this design. Finally, the core sandwich materials analyzed, are foam polystyrene and balsa wood.

[2] www.grantadesign.com/download/pdf/teaching_resource_books/2-Materials-Charts-2010.pdf, last accessed: 2017-06-06
[3] www.auszac.com/factsheets.html, last accessed: 2017-06-09
[4] www.performance-composites.com/carbonfibre/mechanicalproperties_2.asp, last accessed: 2017-06-09

Table 12.3: Material properties

Material	Yield stress	Density	E-mod
Unit	MPa	$kg\,m^{-3}$	GPa
Carbon Fiber, Epoxy	600	1600	70
Kevlar, Epoxy	480	1400	30
Polylactic Acid	50	1300	3.5
Polystyrene	25	1050	2.28
Balsa wood	30	150	1.38

12.3.2. Failure modes

The dimensions for the structure of the wing can be found by designed it such that it can withstand all the applied loads. All failure modes discussed below should not occur during the operation of the UAV.

Breaking When a structure is loaded in tension by a force that exceeds the maximum tensile strength of the material, it causes the material to fail. This causes the structure to lose its structural integrity.

Buckling If part of a structure is loaded in compression, the surface can buckle. This is an additional failure mode of a structure.

Impact An obvious failure mode to consider is failure due to impact by a projectile or a drop (**SPARTA-UAV-11.1**). It can also cause the material to fail.

Fatigue A structure may fail due to fatigue, which is a repeated load large enough to weaken the structure. If this happens frequently the material can prematurely fail.

Core failure There is an additional failure mode that should be taken into account for sandwich panels. Not only the face of the sandwich can fail, but the core material as well. The latter will mainly be loaded in shear. If it exceeds the shear yield stress, the complete structure fails.

Adhesive bond failure For sandwich structures an adhesive is used to connect the faces to the core. This could fail due to the induced loads and the faces could disconnect from the core.

12.3.3. Material choice

For the wing, the material that is favoured is Kevlar fiber with epoxy resin. It is strong enough to withstand the loads and has a high specific strength. Concerning all the other elements, Kevlar was used as well because of its impact resistance, useful for the more detailed design during the impact modeling **SPARTA-UAV-11.1**. Furthermore, as stated before, Kevlar is recyclable. If the structureis made out of Kevlar, the Unmanned Aerial System (UAS) is more likely to comply with **SPARTA-UAV-14**. The only structural element of the UAV that has a different material other than Kevlar is the quadcopter rods. As explained in Section 12.2.3, the rods will be made of carbon fiber.

12.4. Manufacturing Plan

This section assesses the production plan for the UAS. The UAV is subdivided into three parts. The wing configuration, quadcopter configuration and the body to which the two configurations will be attached.

12.4.1. Production

For the UAS resources it is efficient to use off-the-shelf products. However, some elements of the design have to be manufactured and will be discussed below. As was made clear by a visit to the Logistiek Centrum Woensdrecht, there are a lot of possibilities concerning manufacturing techniques and performing maintenance on site. The two common production types for composite materials are lay-up and resin transfer moulding, explained in the following part of the section. During the whole manufacturing process lean manufacturing should be kept in mind. Simply said, lean manufacturing is a way of thinking that focuses on eliminating waste and therefore increasing profit [55, p. 172]. Figure 12.18 displays all the parts of the UAV structure.

Wing configuration

The wing and tail have a complex frame due to the airfoil shape. As has been discussed in the material trade-off for the wing, Kevlar fabric with epoxy resin will be used. Kevlar fiber is a composite material and it can be manufactured using (manual) lay-up or resin transfer moulding. Lay-up is the process of creating a desired shape using a mould that has been predefined on which the lay-up can be performed. These moulds in combination with the flexibility of fibers before layup are the reason why curved, complex shapes can be generated easily. For the tail, the same procedure can be used with as only difference the mould of the wing.

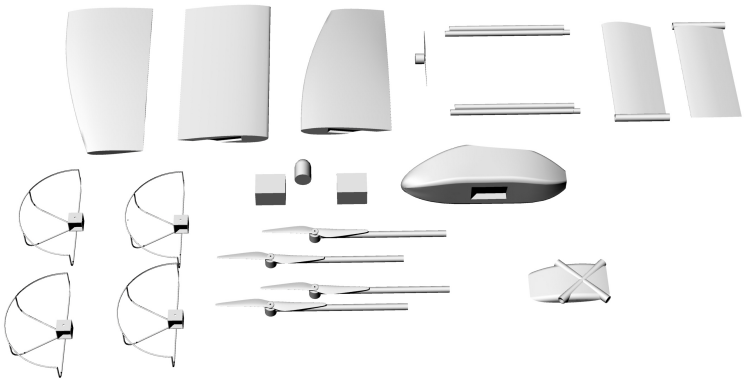

Figure 12.18: All parts of UAV

Resin transfer moulding is another way of producing composite parts. It is less favourable than the lay-up procedure as it produces more waste. In order to comply with **SPARTA-UAV-15.1**, the wing is divided into three sections and the tail into two sections. Two booms consisting of two parts each connect the tail wing to the main wing. These have a simple shape and are commonly produced. However, rods of Kevlar are not very common off-the-shelf products, so they should also be produced using the layup technique.

Quadcopter configuration
The main part of this configuration is the top part connecting the flying module to the fuselage. The rods with rotors and ducts will be attached to this top part assembly. The rods and rotors are off-the-shelf products. However, the top assembly has a more complex shape which leads to a complex lay-up process.

Body
The fuselage has a unique shape and can not be obtained off-the-shelf. It can be produced in the same manner as the wing. Due to the belly-skid landing, the body should be impact resistant and will thus be made of Kevlar.

Lay-up
Manual lay-up is performed to produce the parts. Since this type of production is used for small product series (100) (**SPARTA-UAV-17**) [55, p. 96]. The whole process is relatively time consuming due to the complexity. To create closed sections with composites, split moulds should be created. This consists of multiple parts so that it is disassemblable.

Producing all the parts is time consuming. First, a pattern of the part should be made, which is a copy of the part that should be produced. This should be performed with care, since this will be the end result of the part. This first process could already take 10 h to 15 h, including the dry-time of the pattern. However, it also depends on the complexity of the shape. For instance, the boom of the wing configuration will be a less time consuming process than the wing. After the pattern has been created, it is used to lay a mould upon. The mould should be split into separate sections to create the desired closed shape. The split mould can either be made out of another composite or a metal, since it should be able to withstand pressure as well as high temperature (50 °C to 150 °C) for the curing process [36, p. 19]. The process of creating a mould can take multiple days (20 h to 30 h, as it is a lay-up process for multiple sections and curing of the mould also takes time.

Up until now, the process that has been described is all preparatory work and after completion, the lay-up process of the actual product can commence. Each of the separate split moulds can be laid up. Next, the split moulds are combined firmly using fasteners and connected to create the complete part. The connection between the separate parts is established by the lay over of the separate layers of the split moulds. The next step is to put the setup into a vacuum bag such that the composite layers are compressed onto the mould and will perfectly form to it. The lay-up process of the actual part is roughly estimated to be around 8 h to 10 h, since multiple layers require more curing time. After this, part curing process which will be done in a special oven, which takes several hours (2 h to 4 h) depending on the size of the part and temperature of the oven. Finally, the split moulds are taken apart, and the surfaces and the flash lines of the part are smoothed.

Although the complete process takes time, the first few steps in the process only have to be performed once, since the mould can be reused. However, to improve efficiency multiple moulds could be made increasing the availability of the moulds.

12.4.2. Time

In the section about lay-up, the time it takes to complete a part was estimated. aThe result is shown in Table 12.4. These estimates are based on general curing times in the industry and based on lay-up times from [58]. However, in that configuration, the lay-up that was performed is of a simple sheet, whereas the parts of the UAV are different in terms of complexity and specifically in size so this will not result in the same lay-up time. Therefore, the lay-up time of the parts for this UAV have been increased significantly.

Table 12.4: Manufacturing time [h]

Part			**UAV**				
	Complex	Simple		No.	Complex	No.	Simple
Pattern	10-15	5-10	Pattern	[1]	10-15	[1]	5-10
Mould	15-20	10-15	Mould	[5]	15-20	[3]	10-15
Lay-up	10-12	6-8	Lay-up	[100]	10-12	[100]	6-8
Curing	2-4	2-4	Curing	[100]	2-4	[100]	2-4
Total	37-51	23-37	Total		1285-1715		835-1255

In Table 12.4, the parts that are to be produced are subdivided into complex parts (i.e. the wing parts, tail parts, body and top part of the quadcopter) and more simple shapes (i.e. booms, quadcopter rods). It shows the manufacturing time of one single component. The process initiates with creating a pattern that only has to be built once, so that it can be reused. Multiple moulds should be produced so that the production process is not halted due to the availability of moulds. Furthermore, the time estimation for the lay-up is not exact since the lay-up performed in [58] is used for a relative estimate. Lastly, curing is a process that can take several hours.

For the estimation of the total time the production cycle will cost, it was assumed that five moulds were made for the complex parts and that this amount would suffice. Furthermore, for the simple parts three moulds were made, since this is the time ratio between simple and complex parts. Then the time of the complete manufacturing process can be determined by multiplying the amount of times each cycle has to be performed.

Table 12.4 is a rough estimation of the manufacturing time that implies no concurrent work, e.g. when an element is curing no other work would be done. Therefore this is the maximum amount of hours that it would take to finish the production of all the structural elements. During the curing process new parts could already be laid up. If this feature is neglected an estimate of the maximum prodution time in hours can be computed. There are seven complex parts in the design and eight simple parts. To produce all the structural parts, the manufacturing process would take 22 045 h. Considering a working day of 8 h this would lead to approximately 2756 days. With a manufacturing team of 20 employees, this would lead to 138 days per worker. That would be about half a year of work for the production of the structural components. However, this calculation uses the maximum amount it takes to produce a component, while also neglecting the fact that multiple actions can be done simultaneously. Therefore the time it will take to produce the structures of the complete series will most definitely be less than half a year.

Apart from the production of the structures, there are UAV components that are bought off the shelf and have to be placed into the structure. If all the parts are available, assembly can take place. This process takes time since there are a number of elements that have to be assembled together before it can be integrated into the structure. For instance the avionics, power source and payload bay.

12.4.3. Cost

If the time needed to produce these parts has been determined, an estimation of cost can be performed, based on the amount of labor hours. In the Netherlands, the manual labor cost per hour for a production/manufacturing worker will be approximately around €20 h^{-1}.[5] [6] In Chapter 19 the cost breakdown is discussed and will show an elaborate cost estimation. In order to come up with a full estimation of the cost (Chapter 19), the materials cost have to be found. The raw cost of Kevlar fabric is around €40 kg^{-1}.[7]

12.5. Verification and Validation

The method used has to be verified and validated to ensure the results are a feasible approximation of reality. The script used in this structural analysis was written in *Python*, building on and making use of previously verified and validated software.

[5] gemiddeldgezien.nl/gemiddeld-uurloon, last accessed: 2017-06-10

[6] www.loonwijzer.nl/home/salaris/salarischeck?job-id=8183010000000, last accessed: 2017-06-10

[7] www.alibaba.com/product-detail/EN-388-cut-5-safety-clothing_60375235966.html, last accessed: 2017-06-20

12.5.1. Verification

For verification of the complete methodology, two parts can be defined, software verification and verification of the calculations. The verification process is therefore split up in software and calculation incorporation.

Software verification

The software is written in *PyCharm*, which is an integrated development environment developed by *JetBrains*. This interface provides real-time code analysis, checking the code for syntax errors and incorrect inputs.

However since *PyCharm* cannot detect non-syntax related typos, e.g. wrong indices, the software was cross checked by another team member, who had knowledge of the work flow and calculations used. This led to the discovery of incorrect indices, variable calls, and formula discretization. After correcting these errors and verifying again no more errors were found and the code was deemed verified. However every addition or edit to the software required to be verified before being applied.

Calculation verification

The calculations were verified by different tests. Firstly the outputs of all functions were checked for correct shape and magnitude using print and plot statements, visualizing the outputs. Furthermore each process was calculated by hand with a wide range of values for each variable to verify the correct output.

The bending and shear stress calculations, which are quite big and numerically complex calculations, were verified by making use of plots to see if the locations of the maximum results made sense as well as cross checking with the software written for the third year Simulation, Verification & Validation course. In this course the same mesh model was developed, verified and validated, although for a fuselage instead of an airfoil. Nonetheless the modus operandi is the same disregarding the shape.

Finally the model was once more verified by inserting a different airfoil into the model, which was easily done because of the software's generic structure. With the new airfoil the results had the same order of magnitude, where the location of highest stresses moved corresponding to what was expected with the new airfoil shape.

12.5.2. Validation

Validation is the process of comparing the calculation data with real life test data. The model used was built upon software developed during a course from the 3rd year Aerospace Engineering bachelor at TU Delft: Simulation, Verification & Validation. In this course a numerical model to analyze the stresses in a fuselage was developed. The fuselage was modelled in a mesh containing points along the radius, floor, and length. This model had to be adapted to allow the airfoil shape to be integrated. Because of the generic way the mesh was constructed, the airfoil was easily incorporated without having to change the core structure of the software.

The results of the fuselage stress calculation were validated by comparing them with real life test data. The model was proven to be accurate in the magnitude of the equivalent tensile (von Mises) stress, however the distribution was not found to be corresponding to reality. These errors are expected due to the linear nature of the model, while von Mises stress distribution have a non-linear character.

Comparing the stress distribution of the numerical calculation (Figure 12.12d) with the one resulting from FEM (Figure 12.13a), a similar distribution can be seen. Even though the stress magnitudes in the FEM were not reliable (nor comparable to the numerical results), both methods output the same distribution shape. The software used in this analysis is deemed validated, because the maximum equivalent tensile stresses are of much higher interest than their location (for determination of the top and bottom skin thicknesses), the stress distributions are comparable, and the easy non-intrusive integration of the airfoil into the model.

In the end it is still important that additional and thorough testing is required in the following development phases. One possibility is to build a prototype wing and perform a stress test under different ultimate loads. This way the structure can be tested for displacement (which was not analyzed in this report), material yield and skin buckling. Making a prototype for destructive testing may seem expensive, however it is an essential part for continuing the development.

12.6. Recommendations

During the structural design of the UAV, unfortunately, the analysis did not reach the detail that was expected due to the lack of experience of FEM programs, such as *Abaqus* and *ANSYS*, and the limited time frame. It would be very useful in future developments if the use of *ANSYS* would improve by for example a tutorial, such that meaningful results could be produced and therefore could be used numerically instead of qualitatively. Complete and correct structural analyses could then lead to an outcome of the FEM-software to support design choices. In general, the plan was to generate an analytical model for the complete UAV, however, only the wing and the quadcopter rods were analyzed. A complete model of the UAV is desired, including all the structural components so that each element can be analyzed separately and designed accordingly.

Apart from the approach of the analysis of the design, there were some designs that could not be analyzed due to the lack of knowledge about each specific design. They were thought of as interesting, unconventional ideas. Nevertheless, they could not be analyzed since this was found to be too intricate.

One of the ideas was a wing that was made out of a foam, such that it would be lightweight, with a coating to protect it. To provide strength to this design, a spar like a carbon rod could be inserted. However, the available knowledge about this type of design was eventually too limited to analyze it. To model this kind of design, more time and expertise would be necessary. Nonetheless, this is the recommended design since this would most certainly result in a lower wing weight, while still being able to carry the loads.

Another idea is the concept of inflatable wings, though not actively used in the UAV industry, it could be useful for this project since the system has a volume constraint equal to the backpack casing size. Deflating and inflating the wing will result in lower storage volume. However, since this is only an academically proven concept, this could not be further evaluated in this project.

Lastly, there is the possibility of using different materials throughout each section. For now, the whole UAV is made out of Kevlar, whereas some parts might be under lower loads and do not require the strength or impact resistance that Kevlar comes with. Also, one part could be made out of multiple types of composites so that materials with different mechanical properties can be used to create a structure that would be tailor made for the loads it is subjected to. This would decrease the overall mass of the structure. However, analyzing these structures is beyond the scope of this project.

II-13

Communication Analysis

One of the most essential aspects of this Unmanned Aerial System (UAS) to successfully fulfill the different mission profiles, is the communication with the infantry unit. In this chapter, a broad overview is given of the communication system. First starting by stating the assumptions, followed by a brief look at the theory behind the mathematical approach. Finally the sizing of the UAV communication system as well as the ground station will be discussed.

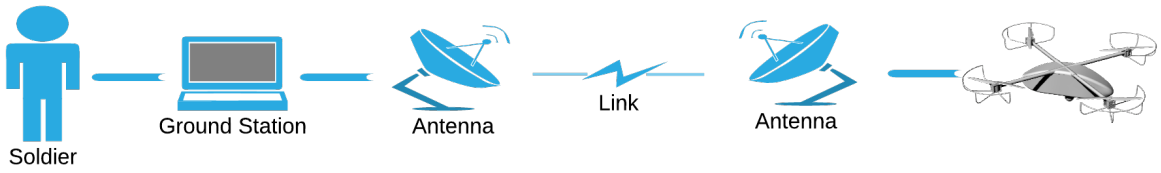

Figure 13.1: Communication diagram

13.1. Assumptions

The assumptions mentioned below might at first glance be difficult to understand. However, these will become clearer after reading Section 13.2.

LB-I The required Signal to Noise Ratio (SNR) should be at least 13 dB
LB-II The data rate for directional commands will be of the order of 1 Mbit s^{-1}
LB-III The frequency used for communication will be between 900 MHz to 930 MHz
LB-IV The system used is not perfect and will induce a certain level of noise in the sent or received signal.
LB-V The signal loses power while traveling in free space.
LB-VI The signal is not reflected by the upper layers of the atmosphere
LB-VII The environment, such as buildings, trees, etc. are not absorbing the signal, but form an obstacle.
LB-VIII No power loss occurs in the cables of the system
LB-IX Pointing loss is neglected
LB-X The signal is an electromagnetic wave travelling at the speed of light (3×10^8 m s^{-1})
LB-XI The input signal is noise free and prefectly modulated.

13.2. Mathematical Approach

The quality of a link between the transmitter and the receiver is evaluated by means of a link budget. The budget is a combination of gains and losses of all the systems between these two parties. In fact, the link budget results in a SNR, which represents the power of the signal compared to the noise power and can be found in Equation (13.1).

$$
\begin{aligned}
SNR &= \frac{P_{\text{signal}}}{P_{\text{noise}}} \\
SNR_{dB} &= P_{\text{trans [dB]}} + L_{\text{transm [dB]}} + G_{\text{transm [dB]}} + L_{\text{trans path [dB]}} + G_{\text{receiv [dB]}} \\
&\quad + L_{\text{space [dB]}} + L_{\text{pointing [dB]}} + L_{\text{receiv [dB]}} + \left(\frac{1}{k}\right)_{dB} - R_{dB} - T_{sys,dB}
\end{aligned}
\tag{13.1}
$$

All the decibel components from Equation (13.1) are related to an icon in Figure 13.1.

13.2.1. Transmitter power

The transmitter power, is the power in the signal delivered by the electronic circuit. It is taken as perfect, or noise free Item **LB-XI**. In the calculations of the link budgets, this was the output of the program. As a matter of fact, this power was used for the power budgets of the ground station and the avionics on the Unmanned Aerial Vehicle (UAV).

13.2.2. Antenna patterns

The most important part in the communication diagram are the antennas. The properties of both the transmitter and receiver antennas will define a multitude of factors that affect the link budget.

To start with, every antenna has a power distribution. These distributions are based on electric field and the magnetic field sent out by the antenna. However rather than going into detail about how these fields affect each other, and how they are positioned, a simplified method was used for the current analysis to stay within the time frame of this report. With these considerations, the power distribution was then found using Equation (13.2).

$$P(\theta) = AF(\theta) \cdot EP(\theta) \tag{13.2}$$

The element pattern represents basic form of the pattern, which is then later multiplied by the array factor. The former is a factor that scales the basic form to the final pattern. To be able to stay within the time frame given for this report, the element pattern was chosen to be constant and independent of the antenna type.

$$\mathrm{EP} = |\sin(\theta)| \tag{13.3}$$

$$\mathrm{AF} = \left| \frac{\frac{1}{N}\sin\left(N\frac{\pi}{2}\right)\cos(\theta)}{\sin\left(\frac{\pi}{2}\right)\cos(\theta)} \right| \tag{13.4}$$

In the case of the array factor, the only variable was N, which represents the number of lobes the pattern has between −90 deg to 90 deg, including the two main lobes. For example, in the case of an omnidirectional antenna, the number of lobes is low (between one and three) and for a directional antenna the number of lobes increases (from four onwards). The more lobes are present, the narrower the main lobe is.

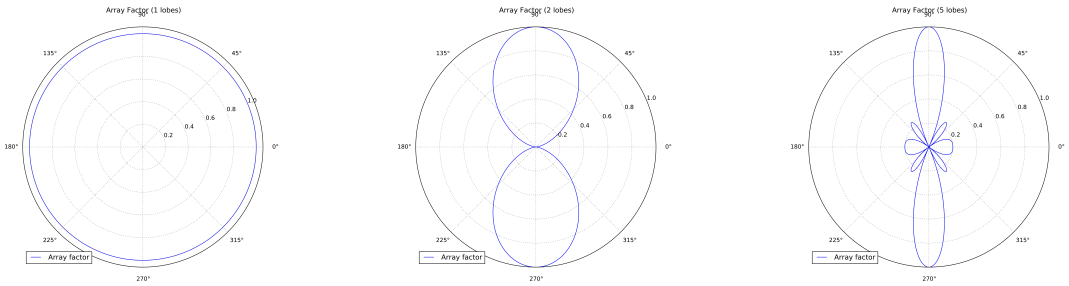

(a) Array factor with N = 1 (b) Array factor with N = 2 (c) Array factor with N = 5

Figure 13.2: Array factors with N lobes

All the array factors represented in Figure 13.2 are for omnidirectional antennas. In case of a unidirectional antenna would be plotted only the angles from 0 deg to 180 deg would be drawn.

13.2.3. Losses

During the the process of communications, many losses occur. These being of technical or physical nature, elaborated in Sections 13.2.3 and 13.2.3 respectively

Technical losses

Technical losses are related to for instance cable properties, antenna imperfections and connector efficiencies. Cable losses were assumed (Item **LB-VIII**) to be negligible. The reason for this is because the cable length between the antenna and the signal source is very small (in the order of centimeters).

Next to cable losses, there are losses in the antenna as well. Normally, the production of the model is not the source of the loss. The losses mainly occur due to the imperfect nature of the antenna concept. For example, a parabolic dish antenna will have an efficiency around 0.5 and so does a horn antenna, while the omnidirectional dipoles are closer to 1 (in the order of 0.7).

To conclude the technical losses, the losses due to connector inefficiencies is neglected, as this analysis would be too detailed for this phase of the design.

Physical losses

In contrast to the technical losses, the physical ones play a smaller role in the link budget. First of all, the transmission path loss is examined.

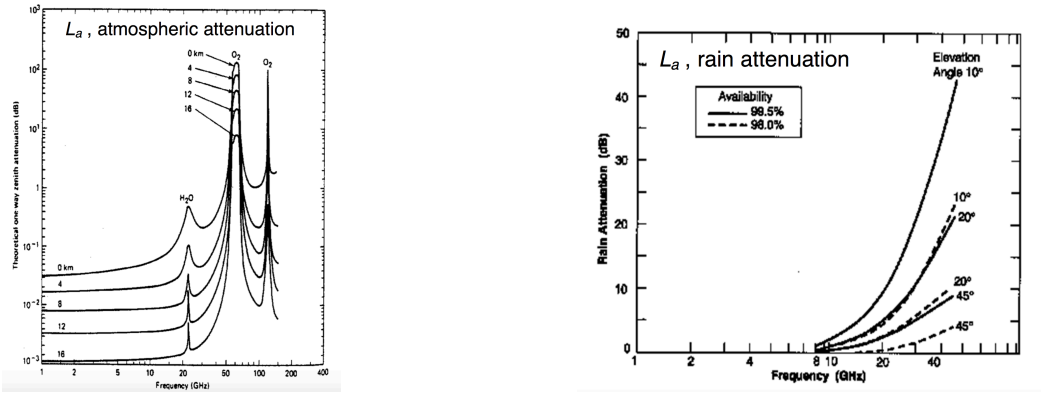

(a) Atmospheric attenuation (b) Rain attenuation

Figure 13.3: Atmospheric interference with the signal

In Figure 13.3 above, one can observe that the most atmospheric attenuation occurs between 20 GHz to 200 GHz. However, the UAS presented in this report will communicate with its ground station at a frequency range between 900 MHz to 930 MHz. When looking at Figure 13.3a it is clear that the lower the frequency, the lower the attenuation. On top of this, the signal will not travel through the ionosphere, which distort the used frequency range the most. Similarly, the attenuation of the signal due to rain as shown in Figure 13.3b is negligible when the signal is below 8 GHz.

The second and most important physical loss is described as the antenna pointing loss. Although this loss is more applicable for space applications, it is worth considering as it is never negligible. The pointing loss is related to the alignment of the antennas of the transmitter and receiver. If these are in perfect concordance, the signal and thus the data throughput is maximal. Although theoretically possible, having such a configuration is either very expensive or not possible.

The pointing loss cannot be accurately calculated, but can be estimated from statistics, based on the the antenna model used.

$$L_{pr} = -12\left(\frac{e_t}{\alpha_{1/2}}\right)^2 \tag{13.5}$$

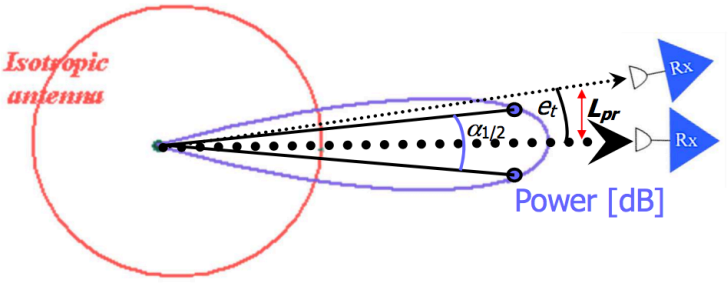

Figure 13.4: Pointing offset angle e_t

From Equation (13.5) it can be observed that the pointing loss depends on the pointing offset angle (e_t) and the Half Power Band Width (HPBW)-angle ($\alpha_{1/2}$). The former is dependent on the mission and the relation between the transmitter and the receiver.The latter is dependent on the antenna type. Since application of the mission profiles in the communication scheme will be discussed in Section 13.3, the pointing offset angle will not be discussed further in this section.

On the other hand, the HPBW-angle is shortly explained. As shown in Figure 13.4, $\alpha_{1/2}$ is the angle between the lines connecting the origin with the points at which the power is 3 dB smaller than the maximum power. This variable changes depending on the power distribution of the antenna, which is directly related to the antenna type.

Since little information was found on statistical estimations, an algorithm was made to determine this angle. It approximates it by drawing the power distribution of the antenna and numerically finding where the HPBW-point was.

System temperature
The last physical loss that is considered, is the system noise (T_{sys}). This is the loss of the mechanical system. For example how much noise is added to the signal by the digital to analog conversion of the signal. In contrast to other losses where the power of the signal was diminished, the system distorts the signal. Typical values are given in Table 13.1.

Table 13.1: System temperature

Link	System noise temperature
Downlink	221 K
Crosslink	682 K
Uplink	614 K

13.2.4. Antenna gain

Besides the losses, the gain of the antennas is to be taken into account. It is this feature that mainly defines the link budget of the communication flow of the UAS.

The gain of antennas depends on the type of antenna used. In the case of a parabolic dish antenna and a horn antenna, approximations can be found using Equation (13.6).

$$G_{\text{parabola}} = G_{\text{horn}} = \frac{\pi^2 D^2}{\lambda^2}\eta \tag{13.6}$$

On the other hand, no approximation could be found for omnidirectional antennas, and more specifically for dipole antennas. To still have an appropriate approximation, a range was acquired by looking at what is currently on the market.

Table 13.2: Currently available omnidirectional antennas for the 900 MHz to 930 MHz range

Antenna	Gain
Laird YA9-9	9 dBi
Altelix AU09G5	5 dBi
e-zealot 900 MHz to 2100 MHz	3 dBi
Superbat 2624	5 dBi
Laird YA9-11	11 dBi

From the few examples given in Table 13.2, it is clear that the gain range for dipole omnidirectional antennas is between 3 dBi to 11 dBi.

13.2.5. Closed link

To conclude the approach, the closed link should be defined. A closed link, means that the communication between the transmitter and the receiver can be achieved flawlessly. To avoid confusion, this is translated to a minimum SNR required for different data coding methods. This is represented by Figure 13.5, where the bit error rate of the data coding methods is plotted against the SNR.

Table 13.3: Allowed variable range

Variable	Range	Unit
Antenna type	2 - 3	Number of lobes
SNR	0 - 15	dB
Gains	3 - 11	dBi
Number of antennas	1 - 4	-

From Figure 13.5 can be seen that with a SNR of 13 dB to 14 dB all coding methods can be used at their minimum bit error rate.

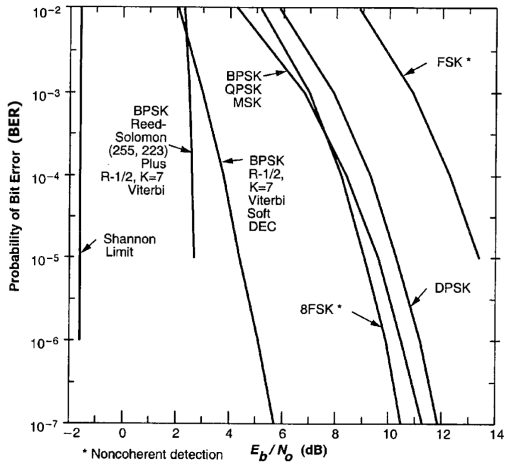

Figure 13.5: Resultant bit error rate of each data coding method for a given SNR

13.3. Sizing

Once the theoretical approach is understood, the sizing can be performed. For both the downlink and the uplink the power required is found. Sizing was done by trial and error. The values that could be changed to close the link are shown in Table 13.3.

In the case of this UAS, the parabolic and horn antennas were not opted for, because of their high directivity (seeFigure 13.6). Due to the versatile missions the system may encounter, it is preferable to chose an antenna type that can be reached from most directions. Therefore, omnidirectional antennas were chosen and more in particular the dipole antennas.

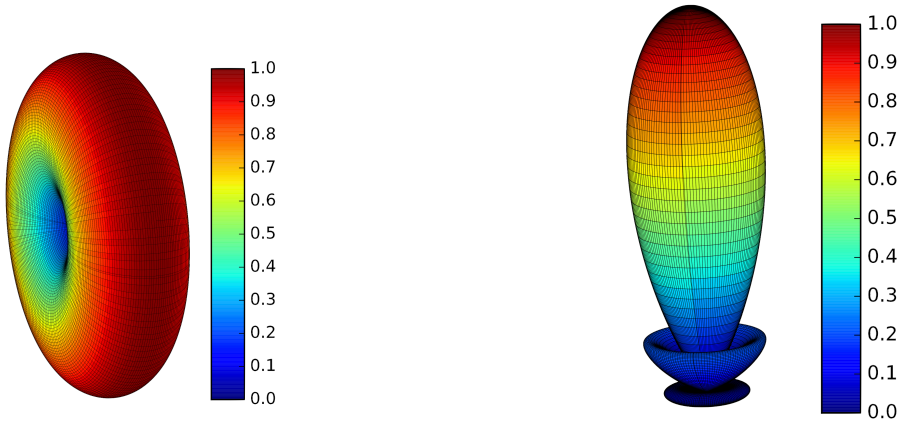

(a) Power distribution of omnidirectional antenna (dipole)

(b) Power distribution of unidirectional antenna (parabola or horn)

Figure 13.6: Atmospheric interference with the signal

13.3.1. Downlink

To start with a link budget, the first step is to know the data rate required. In the case of the downlink, a live feedback to the ground station, or even to the base, is needed. Therefore the complete data gathered by the payload, combined with status data of the UAV should be transmitted.

In collaboration with the payload department, the most critical payload data rate was found to come from the camera in combination with one of the other possible senors. For any other sensors, the data rate was assumed to be of the order of 1 Mbit s^{-1}, as no data was available. Finally the status data was estimated to be in the order of 1 Mbit s^{-1}.

$$\begin{aligned} R &= (R_{\text{camera}} + R_{\text{extra senors}}) + R_{\text{UAV status}} \\ &= N_{\text{pixels}}\text{bit}_{\text{pixel}} \cdot FPS + R_{\text{extra senors}} + R_{\text{UAV status}} \end{aligned} \tag{13.7}$$

In the case of the camera proposed in Section 7.1.1 the total camera data rate at 35 Frames Per Second (FPS) and 14 bit px^{-1} for colored pictures give an outcome of 387 Mbit s^{-1}. Consequently, using the estimated values for the UAV status and the additional payload information, the total data rate to be transmitted is 389 Mbit s^{-1}.

The final step is to fit the power required to the power available with the onboard electronics (see Chapter 14). The pin has a voltage of 5 V, and the maximal available current on such a pin is 16 mA. Therefore the power required for a closed link was limited to 80 mW.

With all the inputs and boundary conditions given above, a trial and error process was performed and resulted in a 65.5 mW to close the downlink. All the important parameters used are shown in Table 13.4.

Table 13.4: Important parameters of the downlink linkbudget

Variable	Value	Unit	Variable	Value	Unit
Num. of lobes type	2	-	SNR	13	dB
G_{UAV}	5	dBi	$G_{\mathrm{G.S.}}$	6	dBi
T_{system}	221	K	$\alpha_{1/2}$	70.8	deg
$e_{t_{\mathrm{UAV}}}$	90	deg	$e_{t_{\mathrm{G.S.}}}$	22.5	deg
Num. antennas UAV	1	-	Num. antennas UAV	4	-
Space loss	81	dB			

With the values presented in Table 13.4, some contingencies are taken into account. For example, the distance between the UAV and the ground station was changed to 30 km. These overdesigned features are there to compensate the eventual losses that were not taken into account and for possible estimation errors.

13.3.2. Uplink

For the uplink the data rate needed is significantly less, since only the control data has to be uploaded to the UAV. This was estimated to be 30 Mbit s^{-1}. Other than that, the same values as in Table 13.4 were used, as well as the same overdesigned features. The uplink needs only 6 mW and receives a minimum of 80 mW from the motherboard.

13.3.3. Antenna recommendation

Antennas were looked up for which the values found in Section 13.3 were within the boundaries of their specs. In Table 13.5 the recommended antennas are shown.

Table 13.5: Recommended anetenna models for UAV and ground station

Device	Antenna	Number
UAV	Superbat 2624	1
Ground Station	VFM ANT0906	4

13.3.4. Recommendations and Suggestions

From the analysis in this chapter, it is clear that most of the possibilities of an open link are dealt with. However, if certain circumstances occur making some assumptions invalid, communication loss might happen. In order to avoid such problems, the specific antenna patterns of the the chose antennas will need to be taken to estimate the final link budget. Also the actual system characteristics will need to be applied into the program, instead of estimations.

II-14

Avionics

The avionics subsystem is a crucial part of the Unmanned Aerial System (UAS). Its purpose is regulating everything that the system should do. Ranging from the control of the attitude, by means of ailerons to the data handling and coding for the communication between the Unmanned Aerial Vehicle (UAV) and the ground station.

14.1. Incorporation of Requirements

For the design of the avionics, requirements are needed. These requirements were taken from Chapter 6 and are discussed in this section.

14.1.1. Operation in a room

SPARTA-UAV-9 specifies that the UAV should be operable in a 2 m × 2 m × 2 m box. Since external positioning systems, such as Global Positioning System (GPS), will be compromised inside buildings, the UAV will have to switch over to a built-in Attitude Determination and Control System (ADCS) system. Due to an absence or malfunction of external position verification (e.g. GPS), the ADCS should be as reliable as possible. Therefore, redundancies should be taken into consideration.

14.1.2. Remote controlled

The system is remote controlled and should therefore be able to communicate. A closed link, needs antennas on the transmitter and the receiver.

Additionally, when connection loss occurs, the UAV should be able to sustain an autonomous flight, without crashing. The decision was made in collaboration with the control department to incorporate an autopilot in the system.

14.1.3. Attitude control

The main goal of any mission performed by this system is to observe and identify possible targets. This can be done with the multiple available payload modules presented in Chapter 7. In order to get accurate measurements, the UAV should be as stable as possible. Consequently the ADCS should be as accurate as possible.

Besides the accurate sampling, the mission also requires position awareness. It was therefore opted for the GPS option.

14.2. Data Transfer Analysis

In order to be able to choose a motherboard for the system, the data transfer needs to be analyzed. The analysis has to be performed on the UAV as well as the ground station. In each of these cases, the data rate of the different components will be researched. After which the number of bits per module will be explained and the signal type will be described.

14.2.1. UAV

First of all, a diagram was made showing what the different components were to be analyzed. In Figure 14.1 the relation between these components can be seen.

Motherboard connections

From Figure 14.1, one can observe that it has four main inputs, 4 main outputs and a continuous data exchange with the autopilot unit.

In a first step, the antenna was researched. This single component is part of input as well as output. It should be known by the reader that an antenna uses analog signal to radiate energy. Since a SubMiniature version A connector is used, only 2 analog pins are needed on the motherboard. The antenna suggested in Chapter 13 is shown in Figure 14.2a.

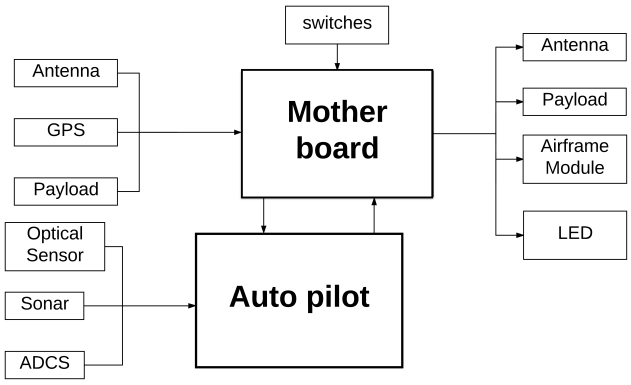

Figure 14.1: Overview of avionics components and their relations

Secondly, the GPS module was looked at. Although, the module could also have been connected to the autopilot, it was chosen to connect it to the motherboard. For the reason that the position coordinates should be transmitted to the ground station as part of the status data described in Section 13.3. The mother board will then communicate the GPS data to the autopilot. The GPS module found was the *PmodGPS GPS Receiver Module*. Because it fulfills the requirements while being light and small.

(a) Recommended antenna with SubMiniature version A connector

(b) PmodGPS GPS Receiver Module

The module shown in Figure 14.2b is using six digital General Purpose Input/Ouput (GPIO) pins to communicate the gathered data, as well as being powered.

Thirdly, there is the payload. The multiple payloads described in Chapter 7 will all have different required data rates, and type. However, it was decided to look at the worst case, which is the camera combined with one or more other sensors and eventually an extra battery. For the chosen camera, 14 bit/pixel are needed for color imaging. Therefore to make the processing of the image go faster, 14 GPIO pins were allotted to the camera part of the payload. For the other sensor two more bits were added. The data rate will first transmit all the pixel data, after which the extra sensor data will be passed on. This process will repeat during the operational time of the payload. Aside from the sensor data, the identification of the payload module needs to be passed on to the mother board. For this ID, four digital GPIO pins were allotted. This enables 15 different payload modules, and that is not counting the eventual inclusion of a battery. For the latter, one extra pin is taken for the payload. This gives a total of 21 pins for the payload, without counting the power and ground pins used for powering the payload.

Furthermore, the airframe module, needs the control signals for the motors and servos. The signal will be a Pulse Modulate Wave (PMW) type of signal, using square waves. With PMW only one pin per engine or actuator is required, which allows for a simple 4 bit system that communicates with the airframe module. For the quadcopter, differential thrust is used, which is perfect with a PMW signal. On the other hand there is the fixed-wing module. This one will have two aileron actuators and two elevator actuator, since the motor will be mounted at the back of the fuselage. For the servo, the PMW signal is perfectly fitting as well. To conclude the airframe module architecture, their identification needs to be addressed. The simplest way to do so is with a mechanical switch that can manually be set to the right mode.

Finally the switches and Light Emitting Diode (LED) lights are usually incorporated in the motherboards. These have their own predefined signal in the board and should not be taken care of during the analysis. The function of the switches is mainly for the maintenance modes. For example the *software upgrade* mode, or the *manual input* mode and also the *operational mode*. The LED lights on the other hand give feedback on the field or during maintenance, depending on the mode selected by the switches.

Autopilot connections

For the autopilot four inputs are taken into account and one output is generated. The output will be the motors' Revolutions Per Minute (RPM) status in case the quadcopter module is in use. If not, the output will be the angle at which the servos will have to be positioned.

Most autopilot hardware have an ADCS built in. These are then consisting of a 3-axis accelerometer, and a 3-axis (or 2-axis) gyroscope unit. These can be used in case the GPS signal is lost, or as redundancy to have a better estimation of the position.

In the case of hovering in a room or flying in a dense urban area, a 360 deg by 360 deg situational awareness is wanted. This is where the visual and sonar sensors come play a big role. The set-up shown in Section 14.2.1 was chosen for the best awareness in dense environments.

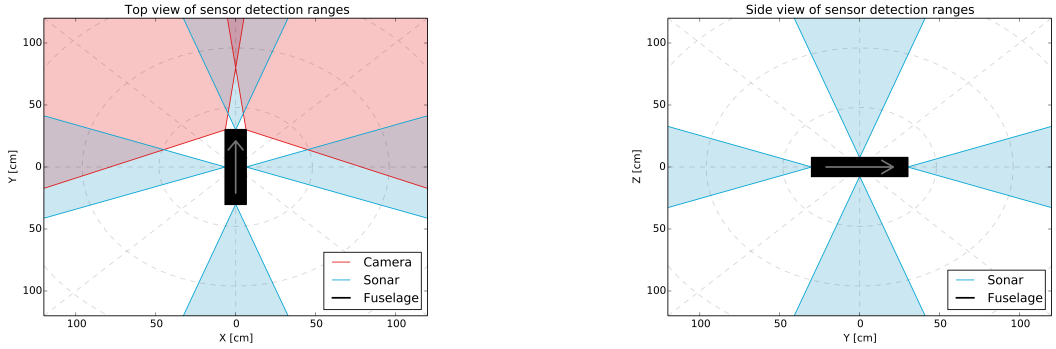

(a) Top view of sensor coverage

(b) Side view of sensor coverage

Figure 14.3: Sensor coverage

It is clear that there are two dead angles in Figure 14.3a. However, most of the mission, the UAV will advance forwards (direction of the arrow) and not backwards. Additionally, when the fixed-wing is installed, the rear sonar would be removed due to the engine of that mode being placed at the rear. The sonar will have to be taken off, making the fuselage a little bit lighter. Additionally, the fixed-wing will not fly backwards in any nominal scenario. It is therefore not a problem that the sensor is removed.

The sonar angle of detection and the camera field of view are taken from their recommended models. These being the *LV-MaxSonar-EZ series* for the sonar and the *Lumenier SM600 Wide angle camera* for the visual sensor.

For the sonar a deeper analysis was made on how to connect the six of them in series. The model presented comes with a feature to do this. When positioned in series, the first sonar is activated. When this one has a measurement, it activates the next sonar while sending its own results to the autopilot.

For the visual sensors, a multiplexer will be required. This device changes the input it takes at a certain frequency. These sensors have a field of view of 120 deg, which gives it a convenient view on the front sides, as well as a good front view.

14.2.2. Ground station

Little information was given on how the ground station should interact with the infantry men, and eventually with a military base. Therefore it was assumed that the ground station will back up all the data gathered in a local hard drive. In addition to this, a live feed should be available to the infantry.

The general idea of the components needed as well as the interaction between these is displayed in Figure 14.4.

Starting with the antennas. There are four antennas connected on the ground station, as explained in Chapter 13. These have a combined power distribution that forms a dome around the ground station. Consequently that means that if the UAV is in this dome, the link budget is closed. It also means that more than one UAV can be communicated with when they are in the dome. The ground station should be able to back up the data of two fully operating drones and control these without connection loss.

Secondly the mother board of the ground station should be able to interpret the data of both UAVs besides other tasks. Remembering that the data rate needed for a single UAV when using the worst case payload, was 460 Mbit s^{-1}. Combining two aircraft to the ground station, means that the motherboard should be able to read a total of 960 Mbit s^{-1} of data. If this is converted from bits to bytes, the data to be stored per second becomes 120 MB s^{-1}. Taking the worst case scenario, where both drones fly for 2 hs each, the total data to be stored is 828 GB. Under these circumstances the motherboard needs at least a 300 MHz processor clock speed to handle this data rate next to the other tasks it will have to perform.

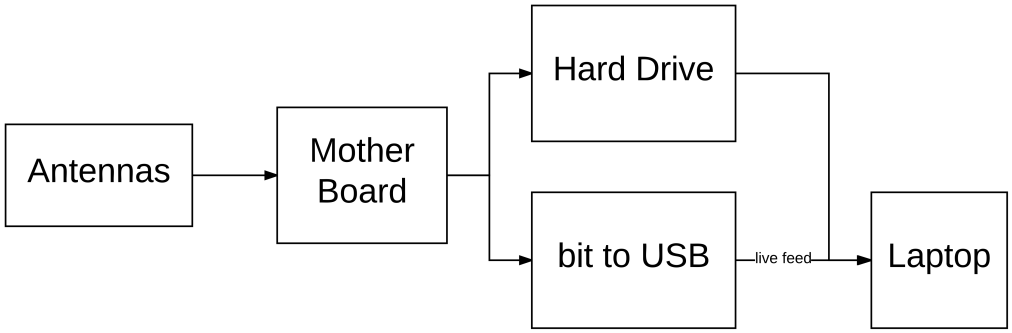

Figure 14.4: Overview of the ground station subsystems

The result of the search was the big brother of the *De0-Nano*, namely the *DE1-SoC* board [1]. The main characteristics of this Field Programmable Gate Array (FPGA) are the 80 GPIO pins and more importantly, its ability to handle image content. It also has multiple output ports, including a VGA port for video transmission. In addition to this it also has an 8 pin array for analog signal inputs, which are perfect for the four antennas required.

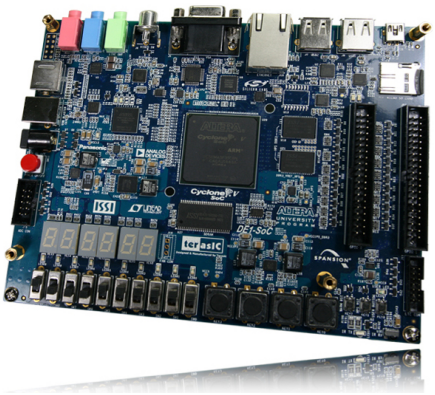

(a) Motherboard De1 SoC (Cyclone V)

(b) Samsung T3 Portable SSD (1 TB)

Figure 14.5: Most important components of the ground station (motherboard and hard drive)

Finally the Hard Drive needs a minimal capacity of at least 828 GB, which rounded up becomes 1 TB. This hard drive would then be able to back up data from two missions (in the worst case scenario). The hard drive world is made out of the mechanical and the solid-state families. For the sake of durability and resistance to hard environments the solid-state family was preferred because there are no moving parts in this type of drive. More specifically the model *Samsung T3* (1 TB) is recommended. With a writing speed of 450 MB, the drive will be able to store the 120 MB s^{-1} generated data from both drones.

14.3. Mother Board Selection

With the information described in Section 14.2 a motherboard was searched that could handle all the inputs and outputs with a small size, cost and power draw. In general an FPGA is a great, off the shelf, solution. These are boards that can mostly be programmed in hardware description language. Another advantage of such a system is the multiplicity of applications and system modularity. Finally these boards are reliable and limited in cost.

14.3.1. UAV

For the UAV the *De0-Nano* board with a *Cyclone IV* FPGA is chosen. This board fits all the needs of the data transmission. With its 106 GPIO pins from which 8 are analog, it can handle all the inputs and outputs, with a contingency. In Figure 14.7a the hardware pin connections are shown. From the same diagram the empty pins and thus the possibility of adding modules can be observed.

[1] `ftp.altera.com/up/pub/Altera_Material/Boards/DE1-SoC/DE1_SoC_User_Manual.pdf`, last accessed: 2017-06-24

Also the *De0-Nano* offers four switches, from which one could be taken for the mode of flight (quadcopter or fixed-wing). That leaves three other switches for the a total of eight different modes. One of which is the *Mission Mode*, leaving seven modes for maintenance. Moreover, the eight LED lights can give the status when maintaining, as well as during operations. To mention a couple of examples, the link status or the battery charge. Last but not least, there are two buttons which could be transformed into *reset* buttons, or to switch between mission modes.

Although, more research was done on the FPGA, it is beyond the scope of this report. If more information is required about the technical capabilities as well as the total specifications of the central processing unit, the reader is advised to consult [2] and [3].

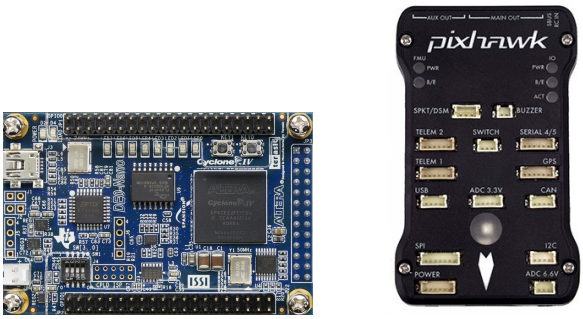

(a) Motherboard De0 Nano (Cyclone IV)

(b) Autopilot board Pixhawk

Figure 14.6: Main printed circuit board components in the UAV

14.4. Autopilot

The autopilot unit is required to have the ability to handle the control algorithm made by the control department. As explained in Section 11.3, the open source algorithm *Ardupilot* will be recommended for the UAS. Since this code is running in `C`, the printed circuit board handling the code, should understand this language. The *Pixhawk* matched this requirement. Although the development of this board stopped two years ago, it could be a good base for an updated version. The advantage, with this board is that it is completely compatible with the sensors recommended in Section 14.2 and can communicate with the motherboard with 48 pins.

14.5. Hardware and Software Diagrams

The diagrams presented in Section 14.5 are there to give a better overview of the systems described in this chapter. First the hardware diagrams of avionics on board of the UAV will be presented, after which the same will be done for the ground station. To end this section, the expected software architecture will be presented in the form of software diagrams.

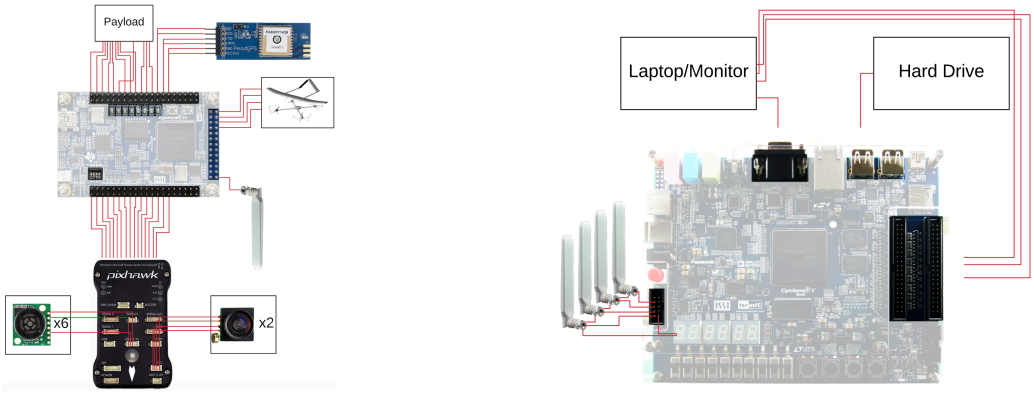

(a) Hardware diagram of the UAV

(b) Hardware diagram of the ground station

Figure 14.7: Hardware diagrams of UAV and ground station

[2] `www.altera.com/en_US/pdfs/literature/hb/cyclone-iv/cyiv-51001.pdf`, last accessed: 2017-06-19

[3] `www.ti.com/lit/ug/tidu737/tidu737.pdf`, last accessed: 2017-06-10

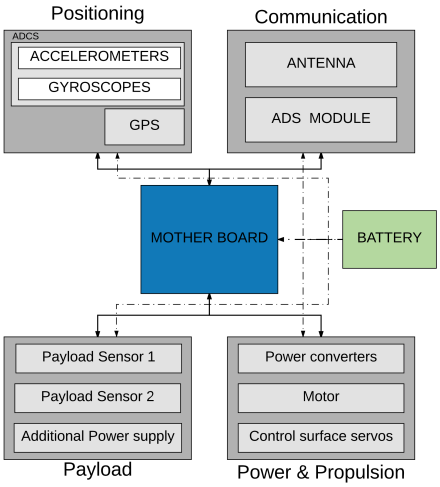

Figure 14.8: Electric block diagram of the UAV

It is clear that the hardware diagram of the UAV is more elaborate than the one of the ground station. The main reason is the fact that little was known about the army laptops. A possible way to connect the ground station to such a laptop could be with the standard dock-station connector. Besides the hardware diagrams, the software diagrams of each system were made accordingly. These are shown and described in Section 11.3. Finally the Electrical block diagram is presented in Figure 14.8.

14.6. Control Surface Actuators

With all the electronics described, the last components left to define are the actuators of the the ailerons and elevators. These were sized in Section 11.3, and a hinge moment was the result.The actuators will be servo motors, consequently these are characterized by the exerted torque. With 3.9 kg cm hinge moment for the ailerons and a hinge moment of 3.27 kg cm at the elevator hinge, the *Power HD 1810MG* servo motor is recommended. The specifics are shown in Table 14.1.

Table 14.1: Technical specifications of the control surface actuators

Variable	Value	Unit
$\text{Torque}_{4.6V}$	3.10	kg cm
$\text{Torque}_{6.0V}$	3.90	kg cm
$\text{Speed}_{4.6V}$	0.16	s/(60 deg)
$\text{Speed}_{6.0V}$	0.13	s/(60 deg)
Mass	15.8	g
Dimensions	$22.8 \times 12.0 \times 29.4$	mm

14.7. Power and Cost

The systems recommended in this chapter should also be described in terms of costs and power draw. These are shown in Chapter 19. The total costs for the avionics is €1463, which is the sum of the UAV cost of €808 and the cost of the ground station being €656. The total avionics cost stay within affordable boundaries, although the system is made of several components. Making the final system look complex. The total power required, is described in Chapter 19 and stays within the acceptable boundaries as well.

II-15

Sensitivity Analysis

This chapter details the analysis of the design sensitivity. Because of the integration of the different subsystems, the initial estimates performed in Chapter 4 will turn out to have deviations. These deviations are to be resolved in an iterative process. In order to aid this process and to determine the impact of deviations, the individual relations will be discussed. Also, the structure of iterations within the design will be discussed.

To aid in the analysis of the iterations, several N2 charts were constructed, these symbolize the breakdown of the individual connections between the subsystems. From Table 15.1, it can be seen that the subsystems were arranged into several groups: structures, materials and production (*S, M & P*); control, avionics and stability (*C, A & S*); and propulsion, aerodynamics and noise (*P, A & N*). This distinction was made because the elements of these groups have a lot of interconnectedness.

To simplify and streamline the iteration process and mitigate a lot of problems (e.g. a highly sensitive parameter not being recalculated, leading to a large design error), two systems were used: Firstly, a central *GitHub* project was created to share all programs created. This ensured all team members could check the results of their design decisions at all times. Secondly, a central database was made which stored all relevant design parameters. Thus, all designers had access to all current data at all times when an internet connection was available.

Table 15.1: Top level N2 chart of the iterative process

S, M & P	COG, MOI	Mass, shape constraints
Control surface locations	**C, A & S**	Control power, control surface shapes, stability parameters
Loads, dimensions, shape	Velocity, forces and moments, aerodynamic center	**P, A & N**

15.1. Structures, Materials and Production

The N2 chart of the structures, materials and production group is shown in Table 15.2. This group mainly performed their iterations based on limitations. An example of this is the the limitation in minimum required skin thickness. Due to the low loading imposed by the hand-launchability (as described in Chapter 9), the required thickness for the structure is lower than the minimum skin thickness. For the quadcopter mode, this process is less restrictive and inherently simplifies to an analytical process. This is also the reason that no simulations are required for it within the scope of this report. The input functions this group is most sensitive to were the required shape and wing area generated by the aerodynamics department. The most important outputs are the mass, inertia and Center of gravity (COG).

Table 15.2: Structures, materials and production N2 chart

Structures	Required yield stress	Geometry
Skin thickness	**Materials**	Material
Method limitations	Method limitations	**Production**

15.2. Control, Avionics and Stability

The control, avionics and stability group is connected through the N2 chart shown in Table 15.3. This group is largely responsive in its iterations: for example, a change in COG set forth by the structures, materials and production group, will prompt the stability department to recalculate the static and dynamic stability modes. From the results obtained, the control department might need to change the active control. One of the main internal trade-offs is the decision between active and passive stability, especially in the fixed-wing mode. The highly sensitive inputs to this group are the inertia and flight conditions. The prime outputs are the requirements on extra systems and the sizing of the empennage.

Table 15.3: Control, avionics and stability N2 chart

Control	Hardware requirements	Active control
Software requirements	**Avionics**	Hardware specifications
Active control requirements	Hardware requirements	**Stability**

15.3. Propulsion, Aerodynamics and Noise

The propulsion, aerodynamics and noise group, whose N2 chart is shown in Table 15.4, took an approach based more on commercially available off-the-shelf products and known airfoils. For example after the determination of the required hover power, a database was referenced to find an engine capable of fitting the power needs. From this engine, a propeller is sized, which is then also obtained from a database. The function of the noise department is largely restrictive. It verifies all propulsion and aerodynamic decisions with respect to the inaudibility requirement, as these are the groups that produce the most noise. The most important outputs of this group are the forces, moments, aerodynamic shapes and power draw of the engine. The most sensitive inputs are the shape constrains and the mass.

Table 15.4: Propulsion, aerodynamics and noise N2 chart

Propulsion	Rotor data, velocity, thrust	RPM, Engine noise, Thrust, Rotor data
Required thrust, Airfoil data	**Aerodynamics**	Vorticity, Pressure differences
Noise constraints	Noise constraints	**Noise**

III

Product Integration Analysis

III-16

Sustainability Analysis

With global warming due to greenhouse gas emissions and depletion of resources being two major threats to humanity's prosperity, the adherance to the sustainability mandate that was set forth by the team is imperative. This chapter discusses the decisions taken to, and the influence of decisions on, the environmental impact of the Unmanned Aerial Vehicle (UAV).

Sustainability Mandate
We believe that protecting the biosphere is of utmost importance and our product shall not adversely affect the environment by unnecessarily contributing to climate change. Our scope of sustainability includes negating the depletion of natural resources, reducing green-house gas emissions, elimination of hazardous waste, and ensuring economic well being. These issues will be dealt with at each step of the design process to ensure that our product takes part in the global movement for future generations to inherit a prosperous biosphere.

16.1. Advantages of Modularity

One of the very pleasant *side-effects* of the modular design is the benefits with regards to sustainability. One of the major causes of sustainability degradation in products is the obsoletion and breaking of components. In a modular design, the relevant components are easily exchangeable. This means that if, for example, a major increase in motor technology occurs, the new engines can be easily implemented to increase the lifetime of the rest of the product. The same goes for repairs: a broken component is always easily replaceable, obviating the premature end-of-life of the system.

16.2. Execution of Sustainability Plan

During the discussion in the project plan [7], the decision was made for a sustainability control department to oversee the integration of sustainable design strategies into the final design. The predominant idea behind fulfilling the sustainability requirements is the implementation of a largely cradle-to-cradle lifecycle: A lifecycle where the product begins and ends as recyclable goods. Two elements in particular are very important to consider: The structural material and the power source. For both these factors, a life-cycle assesment was carried out. The stages of the life-cycle assesment are presented in Figure 16.1, which are subsequently grouped into Materials and Manufacturing (1-3), Product Operation (4-6) and Phase-out (7-∞) [20]. As sustainability is not the main design driver, the options for these categories will also be analysed in terms of feasibility.

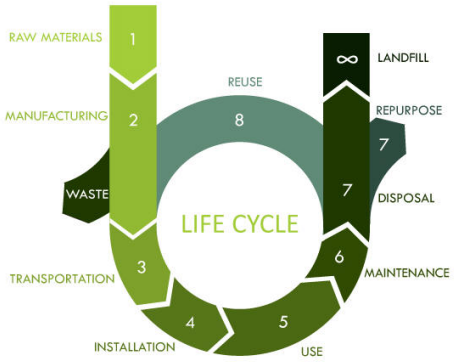

Figure 16.1: Stages of the life cycle assessment [1]

[1] www.southwest-environmental.co.uk/further%20info/life_cycle_assessment/life_cycle_assessment_consultants.html, last accessed: 2017-04-28

16.3. Power Source

For the power source, three main options exist: internal combustion engines, that use fossil fuels; battery powered electromotors; and fuel cells, which use hydrogen redox to make electricity. Both Internal Combustion Engine Vehicle (ICEV) and Battery Electric Vehicle (BEV) are seen as feasible. They provide high amounts of power and have decent capacity and high reliability. Fuel cells, however, have a very low power generation, making them unfeasible for high-power applications such as flight [1]. Thus, they will not be considered with regards to sustainability. ICEV use large amounts of relatively basic metals to produce, reducing the energy investment needed to produce and recycle these powerplants. This is in contrast with the production and recycling of lithium-ion batteries. This is because BEV use relatively complex materials that are hard to work with (e.g. metallic lithium may not contact oxygen or it will oxidize).

During operation, however, the BEV has a better performance due to the complete lack of greenhouse gas exhausts. Internal combustion engines producing greenhouse gas are a major source of global warming [16]. On the contrary, batteries can be charged exclusively using renewable energy sources such as solar power, eliminating their greenhouse gas exhaust during operation.

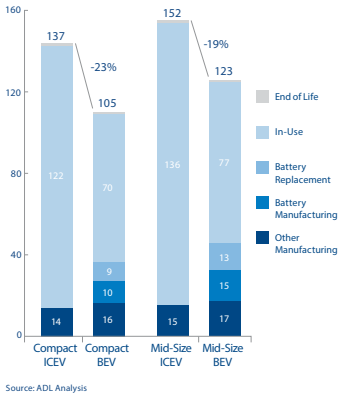

Figure 16.2: Internal Combustion Equipped (ICEV) vs. Battery Equipped Vehicle (BEV) emissions over a 20-year lifetime

Figure 16.2 shows the proportions of greenhouse gas emissions for a 20-year lifetime. As can be seen, the decreased production and disposal energy of the combustion engine does not outweigh its usage of fossil fuels and the associated emissions. One factor that is, however, not considered is the possible expulsion of harmful substances (e.g. 1,3-propanesultone, a known carcinogen) during incorrect disposal, as this violates Registration, Evaluation and Authorization of Chemicals [EU Reg 1907/2006] (REACH) requirements. The batteries are to be recycled, one of the major downsides of lithium-ion batteries, however, is the fact that their recycling is not commercially viable right now. This introduces an extra source of costs that can not be estimated reliably at this point.

16.4. Construction Material

For the structural components of the UAV, a lot of different materials were considered. The three main categories in this are polymers, composites and metals. Firstly, the production of carbon fiber composites is quite energy intensive, inluding 10 MJ kg^{-1} for transfer molding. However, on top of this comes the enormous energy cost of up to 500 MJ kg^{-1} of producing the carbon fiber itself, due to it requiring a lot of heating. Assuming a 50/50 fiber matrix division (the matrix having an energy requirement of approximately 160 MJ kg^{-1}, the total production energy of the raw material comes to 330 MJ kg^{-1}. The lowest energy method for the small production size is hand lay-up, at 20 MJ kg^{-1}. This brings the total to 350 MJ kg^{-1}. Other fiber materials such as amarid (Kevlar) or glassfiber have lower energy requirements, as they require significantly less energy to produce. However, these still amount to approximately 220 MJ kg^{-1} for their production[31]. Lower is the energy requirement for polymers, coming to 60 MJ kg^{-1} for most polymers, which also require fossil oils for their production. As the most common aerospace metal, 200 MJ kg^{-1} is needed for the production of Aluminum (Al). This high number comes from the difficulty of extracting it from the ore. The operational costs for the structural material are negligible, however as composite structures tend to be lighter, the overall energy usage of the UAV during operation will be lower. At end of life the possibility for recycling exists for all materials. However, for the plastics and composites, the recycling usually takes the form of down cycling into lower performance materials, denying a complete cradle-to-cradle approach. For metals, recycling can also significantly decrease the energy requirement for production of the raw material

16.5. Results and Recommendations

The data from the initial research were combined into two trade-off tables. The first one, Table 16.1, concerns the power source of the UAV and the second one, Table 16.2, tabulates the material options. From the power source trade-off and Section 9.6.4, it becomes evident that, if the Royal Netherlands Air Force or any other client is willing to fund the recycling, lithium-ion batteries are superior to internal combustion engines. Another important factor are the possible impracticalities caused by using combustion engines instead of smaller battery based systems, such as the cooling needed for combustion engines. However, in the case of a battery-based system, care should be taken to produce the neccessary energy using sustainable power sources. This will ensure (mostly) CO_2 neutral operation.

For the material selection, the performance will probably be a more driving factor than the sustainability. This is because the feasibility of the design requires a high performance. A very important factor to consider from a sustainability standpoint however, is the logistics of recycling. This begins at the design stage, where materials should be easily seperable at end-of-life, allowing extraction of the different resources from the airframe.

Table 16.1: Preliminary trade-off of the environmental impact of battery powered electric vs. internal combustion engines

Power plant	**Materials & manufacturing (1-3)**	**Operations (4-6)**	**Phase-out (7-∞)**
Battery electric	High energy expenditure to produce	No direct emissions	Difficult to recycle
Internal combustion	Lower production energy	Direct GHG emission	Good recyclability

Table 16.2: Preliminary trade-off of the environmental impact of plastics vs. composites vs. metals

Material	**Materials & manufacturing (1-3)**	**Operations (4-6)**	**Phase-out (7-∞)**
Polymers	Medium energy expenditure but uses oil	Unchanged	Downcycle
Composites	High production energy	Lower operational energy use	Downcycle
Metals	High production energy that can be decreased through recycling	Unchanged	Good recyclability

III-17

Operations and Logistics

This chapter presents the operation and logistics of the Unmanned Aerial System (UAS). In Section 17.1 the operation activities are described for both configurations including pre-and post-operational activities. In Section 17.2 the assembly of both configurations is described while Section 17.3 and Section 17.4 describe the logistics, transport and handling of the Unmanned Aerial Vehicle (UAV).

17.1. Operations

Figure 17.1 depicts the entire operational phase of the UAS. Firstly, the UAS is deployed on the operation site by two soldiers, as per [6]. The UAS is mounted and launched in 10 min, which is further elaborated in Section 17.1.1. Afterwards the UAV performs the mission, which will not be further elaborated upon, as it depends on the mission plan of the military. Finally, the post-operation activities are performed, described in Section 17.1.2. The rest of the operational activities are not elaborated upon further, as they are mission dependent.

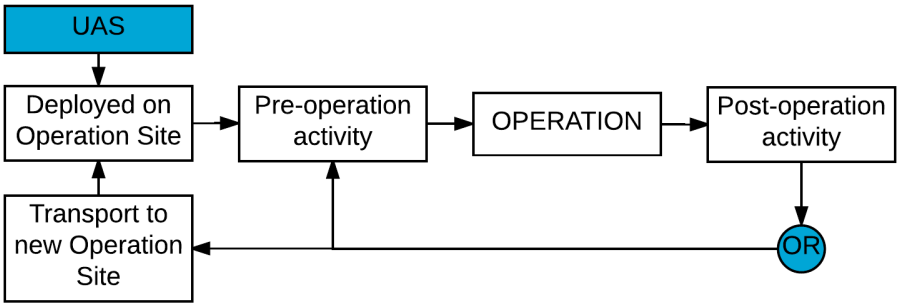

Figure 17.1: Mission characteristics

17.1.1. Pre-operation activity

The UAV should be deployed in less than 10 min as per the requirements. To see if this requirement is being fulfilled, a preliminary deployment set-up is made. This can be seen in Figure 17.2, taken and modified from [8]. In this mounting time line, all the different functions that need to be performed by the maintainer and the UAV operator are present. The functions are mainly subsequent, except for the communication link set-up and performing the take-off checks, check-out for short in Figure 17.2.

17.1.2. Post-operation activity

After the landing the UAV needs to be dismounted and packed together with the ground station if no further mission will be performed. If the military wants to perform a new mission, with a different payload module, the old one will need to be replaced, and the chosen propellant (either batteries, fuel cells or fuel) will need to be changed.

17.2. Assembly

When the UAS is brought to the location, it will be assembled by the infantrymen carrying the complete system in under 10 min (**SPARTA-SYS-6**). The UAV configuration depends on the mission type and has been designed in such a way that either the fixed-wing or the quadcopter configuration can be easily connected onto the fuselage.

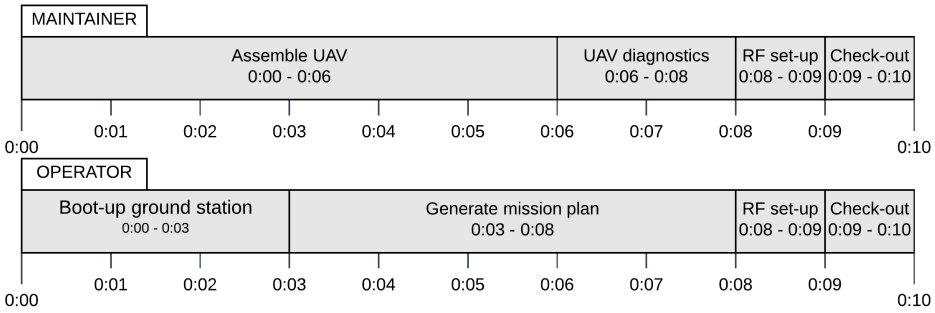

Figure 17.2: Estimate of deployment time line

17.2.1. Fixed-wing configuration

The winged configuration consists of the main wing, two rods that are attached to the wing and connect it with the tail. Since the wing is too large, it is folded such that it fits into the backpack. Also, the rods disconnect from the wing and the tail such that the whole configuration can be (dis)assembled.

During the assembly, the middle part of the wing is fixed to the engine first, as can be seen in Figure 17.3a. After this the two outer wing parts are connected to the middle one through a rod. Then, the modular electrical engine with rotors is attached to the rear of the fuselage. The first two pieces of the rod are fixed to the fuselage by using a ball locking pin and then the other two pieces are attached to the already fixed rods. This all can be seen in Figures 17.3b to 17.3f. Finally, the tail is assembled while it is still easy to flip it upside down and then it is attached to the rods, as shown in Figures 17.3g and 17.3h.

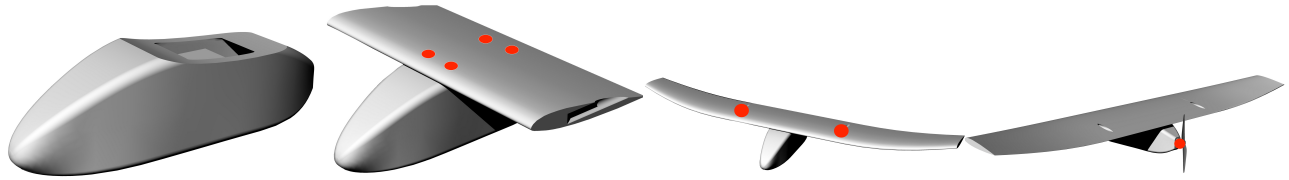

(a) Place fuselage on ground (b) Fix middle wing part to fuselage (c) Assemble outer two wing parts on the middle one (d) Attach the propeller and motor

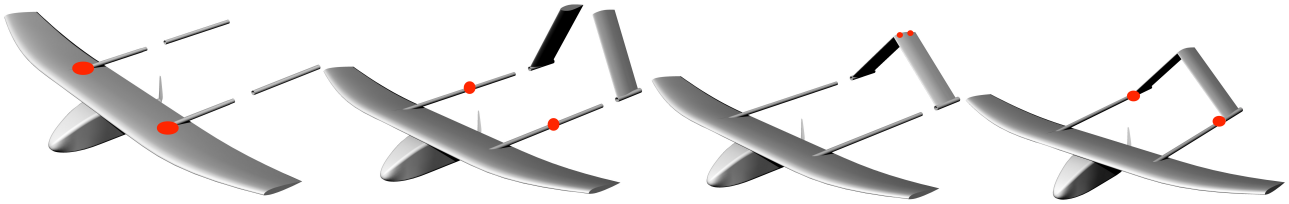

(e) Place rods in fixed-wing (f) other part of the rod the already assembled one. (g) Assemble the tail (h) Attach the tail to the rods

Figure 17.3: Recommended assembly of the fixed-wing configuration

Taking into account the allotted time to assemble the UAV, it would mean that if each action would take the same amount of time, each step would take around 30 seconds to fulfill. If the maintainer of the infantrymen responsible for the assembly is acquainted with the configuration, then it can certainly be performed within the given time margin.

17.2.2. Quadcopter configuration

This section describes the assembly of the quadcopter configuration. In general, this configuration should take less time to assemble than the wing configuration since there are less attachment points (15 for the wing and 12 for the quadcopter). Figure 17.4 shows the assembly of the quadcopter in intermediate steps. Since the quadcopter is too large to fit in the backpack, the rods can be detached in order to fit in the backpack (**SPARTA-UAV-15.1**). The assembly of the quadcopter starts with attaching the four simple ducts around the rotors which already are attached to the quadcopter rods (Figure 17.4a). When these are secured, the next step is to attach each rod with the connected ducts to the fuselage attachment, which is displayed in Figure 17.4b. Lastly, the fuselage attachment is assembled onto the body so that the quadcopter assembly is completed (Figure 17.4c).

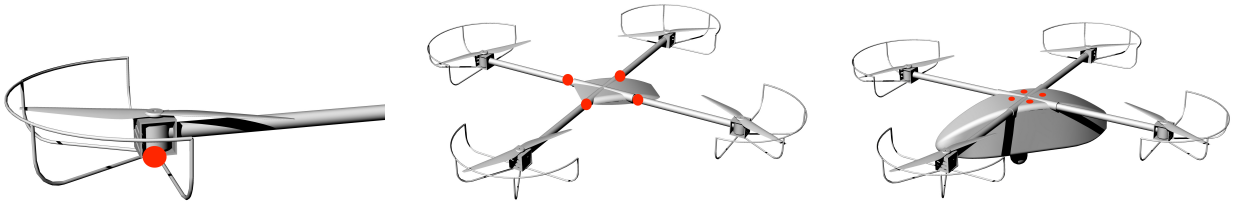

(a) Place rotor protector around each rotor

(b) Attach the four rods with rotors to the fuselage-attachment element

(c) Attach the assembled piece to the fuselage

Figure 17.4: Assembly of the quadcopter configuration

As discussed, the fixed-wing configuration consists of a larger amount of steps than the quadcopter configuration. Furthermore, considering that the assembly of the quadcopter does not contain any that are more difficult than the ones in the fixed-wing configuration, the assembly of the quadcopter will take less time than the fixed-wing and will therefore be completed within 10 min (**SPARTA-SYS-6**).

17.3. Logistics

Proper logistics are required for the UAS to perform its mission properly. To decrease the logistical footprint, and thus the operational cost of the UAS, the logistics is done according to North Atlantic Treaty Organization (NATO) policies [2]. Particularly, by developing a plan for integrated logistics support in which specific attention should be paid to transport, supply handling, and maintenance which includes the facilities, tools and spare parts needed. When these elements of the integrated logistics support are properly planned, the system will have an operational readiness as required by the customer. However, due to the fact that it is a small hand-launched system it can be classified in *Class I* category, which means that less logistic support is required. Furthermore, at this design stage, the logistics support system of the UAV is extremely preliminary and will need to be refined in later design stages. The UAV support system depends on the UAV configuration, and its operational requirements and environment. An overview of the different support system elements and what they are dependent on can be found in Figure 17.5 [61].

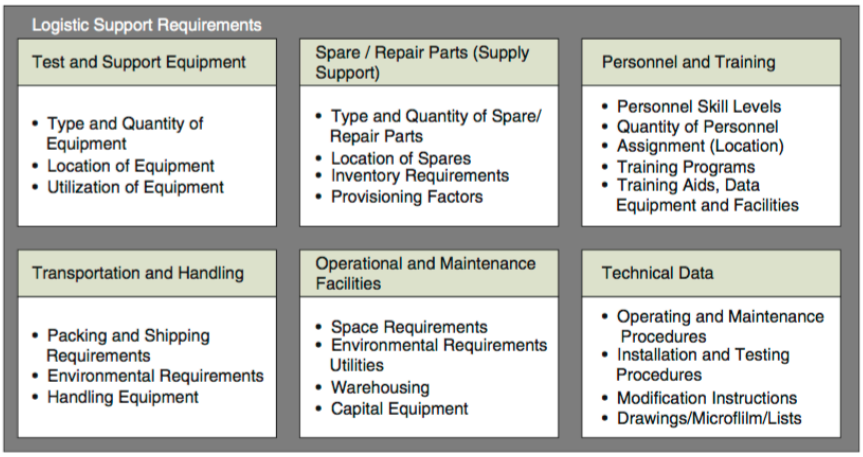

Figure 17.5: Logistics support system

The first part is the test and support equipment for the UAS. As seen in the figure, this includes all the relevant information about the equipment necessary to perform maintenance and operations. It includes of course maintenance equipment, but also other tools such as generators, calibration equipment, and manual and automatic test equipment. When designing the logistical support and thus choosing the necessary equipment one needs to take into account the tools that are already present at the military base the UAS will be stationed.

The second element is the spare parts present at the military base and in the backpack. This mainly depends on the Reliability, Availability, Maintenance, and Safety (RAMS) of the UAS. The amount of spares decreases if RAMS increases, so one should aim for an optimal RAMS characteristics of the UAS.

The third part is the Personnel and training. To operate and maintain the UAS technical background and training is needed. One thus needs to find the adequate military and civilian personnel with those skills required to operate and support the UAV during its lifetime. It also includes all the necessary training and other aids the personnel might need. This can be in the form of technical publications or real lessons and training.

Next is the transportation and handling phase of the support system. As the UAS is already man-portable and will come in a case, this element will not be as elaborate as for other UASs. Some of the transportation characteristics are described in Section 17.3.1.

Afterwards, the operational and maintenance facilities are described. This is one of the most important support elements as it provides a location for storage, maintenance, and training to maximize the effectiveness of the logistic support system. This minimizes the overall cost of the logistics and also decreases the maintenance time necessary per revision [61].

Finally, the technical data necessary for UAV maintenance ins elaborated upon. The first thing that the UAV needs is technical information about the UAS and its tools. This includes technical drawings, and necessary documentation about the soft- and hardware specifications that are used for maintenance. It also requires to provide the necessary information to manufacture and support the system after deployment. All this so that manufacturing and support of the UAS can be done by the customer [61].

17.3.1. Transport and handling

The transportation of the UAS needs to be accounted for during the design of the concepts, as it influences the design of the casing. This casing needs to ensure safe transportation as cargo, where careful handling cannot be guaranteed. Each concept should be designed to be transportable, not only during regular operations, but also during shipment between facilities. Transportation of the UAV during regular operations will be done by two man-carried backpacks, as per the requirements [5, 27].

During operational life the deployment of the UAS will occur at many different location. This impacts the location of the maintenance depending on the duration of its deployment. Another consideration is that compatibility with the transport system at each location has to be assured, so that the UAS can be transported safely.

As the UAV is small with a short range, it is more favorable to store the UAV, then transport it to the new location, instead of the UAV taking flight there itself [61].

17.4. Transport Casing

The UAS will be carried to its deployment zone by two soldiers who will carry it in their backpack. Through contact with the Royal Netherlands Air Force (RNLAF) the backpack model and size have been communicated which is the *Lowe Alpine Saracen* backpack with dimensions of 79x38x26 cm, resulting a 78 L volume. Therefore two boxes with these outer dimensions are supplied with the UAS. Figure 17.6 shows how these boxes can be loaded so that the whole system fits in there.

1. The boxes shown in Figure 17.6a are made from a plastic skin with 2cm of foam on the outer side. This is used in music instrument cases as well and it is assumed to be strong enough to protect this UAS as well.
2. In one of the boxes, the ground station, payload and enough batteries for 5 missions can be loaded on the floor of the box. This box will from now on be called box (A). In the other box (B), the body can be stored in one corner, next to it there is space for the two parts of the fixed-wing A-tail on the other side of the box, the four simple ducts for the quadcopter rotor protection can be stacked up on the other side of the box.
3. After an internal layer of foam to prevent the parts touching each other and to prevent them from moving when the box is held at a different angle, in box A one of the wingtips can be stored upside down. In box B, also after a layer of foam, three of the four quadcopter rods with their motors and rotors attached can be stored together with the fixed-wing motor and rotor above the tail parts.
4. After a next layer of foam in both cases, the remaining quadcopter rod and the fixed-wing tail rods can be stored in box A. There is also room for the main connection part of the quadcopter in this box. In box B first the other wing tip can be stored with the tip down and the middle part of the wing can be stored on top of that.
5. After that, all parts are stored safely in the boxes and they can be put into the backpacks so that the soldiers can take the system to its deployment zone.

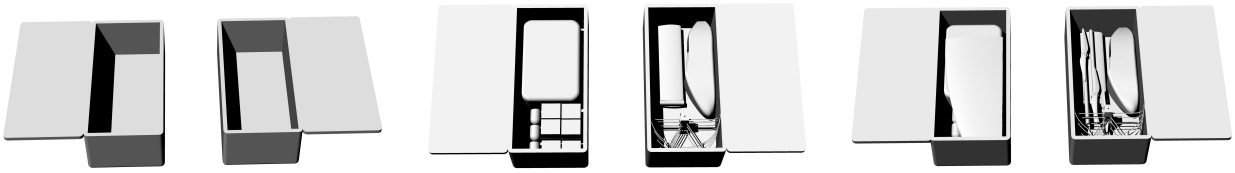

(a) Transport boxes

(b) Loading step 1: *Box A: Ground station, 5 pairs of batteries, 3 payload modules and a layer of foam. Box B: Fuselage, quad copter rotor protection, tail parts and a layer of foam.*

(c) Loading step 2: *Box A: Right wing tip and a layer of foam. Box B: 3 rotors with their rods from the quadcopter module; the motor and rotor from the fixed-wing module and a layer of foam.*

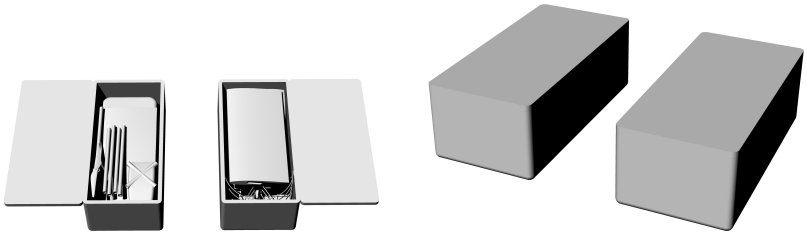

(d) Loading step 3: *Box A: Final rotor, rod, and the central piece of the quadcopter module plus the rods of the fixed-wing module. Box B: the central and left wing piece.*

(e) Loading step 4: Finished loading

Figure 17.6: Loading of the UAV into the transport box. Between each step is a layer of 1 cm of foam that is not shown in the model

III-18

Risk Management and RAMS

In this chapter the risk management together with the Reliability, Availability, Maintenance, and Safety (RAMS) will be discussed. Firstly the risks are addressed, followed by the RAMS evaluation of the design.

18.1. Risk Management

This section describes the risk management procedures of the product. The structure of the risk management will be similar with [6, 8]. They will classified and identified per department and later assessed based on their probability of occurrence and the impact they will have on the mission. Once this procedure is completed mitigation strategies will be investigated to minimize the overall risk.

18.1.1. Risk identification

This section identifies the most important risks per department. The risk manager, in cooperation with the responsible departments, the possible risks their field could have on the vehicle. From this, the full set of risks was identified. The identified risks are described together with the risk assessment in Section 18.1.2.

18.1.2. Risk assessment

In this section the risks will be assessed. The assessment will be done in the same way as in previous reports concerning the criteria of probability of occurrence and impact [6, 8].

Structures

These risks are associated with any kind of possible failure due to structural damage or destruction.

- **STR-1 Joint snap:** This risk is about the failure between the different connection points. Its probability of happening is **unlikely** as during the detailed design phase the structures department has given a lot of attention in design of the connection points. The impact is **catastrophic** because if such failure occurs it will lead to mission failure as the structure breaks apart.
- **STR-2 Collision:** This risk is associated with the structural failure of the Unmanned Aerial Vehicle (UAV) due to external influences such as birds and collision with walls. Its probability is **unlikely** for both configurations because of the integrated avoidance system. The impact would be **critical** as it can cause major mission degradation, however the vehicle would probably still be able to land at some point.
- **STR-3 Weather:** This risk is associated with the structural failure of the UAV due to unpredicted weather conditions such as gusts and lighting storms. This risk strictly depends on the environment and the region in which the vehicle is operating. The worst case scenario is taken into account and thus it's considered **possible**. Concerning the impact, depends on the severity of the weather it can vary from moderate to catastrophic. The worst case scenario is taken for this risk and it's considered **catastrophic** as it can cause total destruction of the UAV.
- **STR-4 Downwards gust:** This risk is associated with the structural damage of the UAV while performing a landing and a downward gust causes the drone to face a hard landing. The probability that this occurs, depends on the landing area and the region that it is performing. The worst case scenario is considered and is taken as **possible**. This can impact the structural integrity of the drone, and it depends on how strong the gust is. The impact can be from negligible to critical. Since the worst case scenario is taken into account is considered **critical**.

Avionics and control

These risks are associated with failures in electronics and avionics of the UAV.

A&C-1 Overheating: This risk is associated with overheating of the avionics and control systems due to high temperatures, malfunction of the system, or a possible hack. The probability of this happening is **unlikely** because of the careful design that is taken into consideration with regard to the cooling of important subsystems. Furthermore, its impact is critical to catastrophic depending on the subsystem that is overheated as it can damage the UAV and terminate the mission. Since the worst case is taken into account its considered **catastrophic**.

A&C-2 Corrosion: This risk is associated with corrosion of electronic boards when then drone is performing in salty, humid, and rainy environments. Since the UAV is going to be protected from the aforementioned factors, its probability is considered **very unlikely**. Its impact depends on the corroded electronic board, but since backup systems are implemented, the impact is considered **critical** as opposed to catastrophic.

A&C-3 Communication: Loss of communication is a crucial factor for the successful mission performance. The probability of this occurring is **possible** considering the fact that in conflict areas, signal interference happens often. A possible jam could be **catastrophic** for the mission as the drone would lose contact with the soldiers, voiding their way of control.

A&C-4 Sensor reliability: This risk is associated with the reliability of sensors at unusual environments and conditions. The probability that sensors fail is **unlikely** because of their usage in previous military projects. The impact of sensor failure can be moderate to critical as it can affect the mission greatly, though still be able to accomplish it with reduced performance. The worst case scenario is taken into account and thus the impact is considered to be **critical**.

A&C-5 Actuator jamming: This risk is only applicable for the fixed-wing while actuators fail to work due to a malfunction of the system. This risk is **possible** to happen due to weather condition (salty, dusty environment), lack of maintenance, or possible hacks. In any case the impact is **critical** as the vehicle would still be able to perform part of the mission and land safely to the nearest checkpoint.

A&C-6 Short circuits: This risk is associated with malfunction of electronics inside the vehicle due to unexpected behavior or conductive debris. The probability of this happening strictly depends on the reliability of the systems and for this vehicle is considered **unlikely**. Short circuit damage can affect the system in a very negative way with overload and can destroy the electronics of the system and thus is considered **catastrophic**.

A&C-7 Hacker attack: Since the vehicle will perform at enemy lines there is a risk that the drone will be hacked to lose communication or control with its user. The probability of this happening is **likely** since it will normally perform at low altitudes and it will be visible. Depending on the nature of the hack it can be moderate to catastrophic, not only for the mission but also for gathering of information. Worst case scenario is taken and its considered **catastrophic**.

A&C-8 EM attack: This risk is associated with a possible electromagnetic attack towards the drone. This risk has a very low chance of happening since in countries like Afghanistan and Mali such weapon technologies are extremely hard to find and thus it is **very unlikely** to occur. Its impact is **catastrophic** since electromagnetic attacks are severe for electronic systems.

A&C-9 Autopilot failure: This risk is associated with the malfunction of the autopilot system or a possible shut down of the system. The probability of this risk occurring is considered **unlikely** due to the safety factors taken while designing the autopilot system. Its impact would be **critical** as it would need manual assistance to perform and complete the mission.

Payload

These are the risks associated with payload failure within the vehicle while performing its mission.

PL-1 Connector failure: This risk is associated with any type of connector failure including communication and power loss due to environmental conditions such as dust and salt. The probability of this happening is **unlikely** due to the sealing material such as O-rings surrounding the connection points of the vehicle. The impact will be **critical** as it can cause operational degradation, though the UAV would still be able to accomplish part of the mission with reduced performance.

PL-2 Overheating: This risk is similar to the overheating of control and avionics presented previously, however it concerns overheating of the payload due to very high temperatures or a malfunction of the power unit. The probability of this risk occurring is **unlikely** due to the careful design and integrated cooling systems. The impact is **catastrophic** due to the possibility of catching fire, structurally damaging the drone and causing a complete mission failure.

Performance, Propulsion, and Stability

These are the risks associated with most important functions of the vehicle with respect to performance, propulsion and stability.

P&P-1 **Provide lift:** This risk is about both fixed-wing and quadcopter providing enough lift for the vehicle to perform both missions. Both are flight proven and flight used concepts and therefore have a high reliability. The probability of a wing failure or any other subsystem providing lift is **possible** as the vehicle will perform at relative low altitudes with the possibility of being shot down. Its impact is **catastrophic** as it would cause a complete failure of the mission.

P&P-2 **Provide thrust:** Similarly with providing lift, this risk is associated with a possible malfunction or destruction of a blade. The possibility of this occurring is **unlikely** due to the shielding and the careful blade design. The impact is **catastrophic** as a significant thrust loss would terminate the mission and would possibly cause the vehicle to crash.

P&P-3 **Power to subsystems:** This risk is associated with the power delivery to different subsystems. A possible error while assembling the drone, a malfunction of the power module (batteries), or its overheating can affect the integrity of the vehicle. The probability of occurrence is fairly low considering the reliability of power modules. Human errors are possible, however simple instructions will be given to the soldiers and thus this risk will be considered **unlikely**. The impact can be moderate to catastrophic depending on the subsystem that is affected. If it's a minor payload module the impact would be moderate; however, if it's the propulsion unit affected then the impact would be catastrophic. The worst case is considered in this report and thus considered **catastrophic**.

P&P-4 **Provide stability:** Another important aspect of the vehicle is to provide stability in order to capture better images. A possible gust can affect the stability of the drone and have blurry images when it comes to important targets. The chance of this happening is considered as **possible** due to the environments and the places in which the vehicle will operate. The impact is **critical** as it affects mission performance, however the vehicle would still be able to follow the target and identify the target.

Once the risks have been identified per department and assessed a risk map is created to understand the areas where mitigation strategies should be emphasized. The risk map is portrayed in Table 18.1 and it follows the same format as in the previous reports as well.

Table 18.1: Risk map constructed from risk assessment

Probability / Impact	Negligible	Moderate	Critical	Catastrophic
Very likely				
Likely				A&C7
Possible			STR3, A&C5, P&P4	STR3, A&C3, P&P1
Unlikely			STR2, A&C4, A&C9, PL1	STR1,A&C1, A&C6, PL2, P&P2, P&P3
Very unlikely			A&C2	A&C8

18.1.3. Risk mitigation

In this section the above mentioned risks are going to be mitigated. Looking at the risk map, it is clear to observe that some risks are necessary to mitigate for the smooth and safe completion of the mission. The mitigation strategies is going to follow the same format as the risk assessment. The risks that require alleviation will be mitigated to reduce their probability of occurrence and intrinsically their impact on the mission.

Structures

These are the necessary actions to mitigate structural risks.

STR-1 **Joint snap:** To reduce the **probability** use simple connections and use Finite Element Method (FEM) for exact force distribution and behavior of the system when it comes to structural analysis. **Impact** cannot be reduced.

STR-2 **Collision:** Unnecessary to mitigate

STR-3 **Weather:** To reduce the **probability** of occurrence, weather forecasts can be used to see whether or not it's possible to fly the drone. Depending on importance of target, take the necessary actions/risk to fly the drone. **Impact** cannot be mitigated.

STR-4 **Downwards gust:** The probability can only be reduced by carefully inspecting the landing area, looking at the weather for gusts, and landing at areas where gust is minimal. The impact can be reduced, by simulating several landing scenarios, registering the points where highest damage occurs, and reinforce them structurally as necessary.

Avionics and Control
These are the necessary actions to mitigate risks concerning avionics and control.

- **A&C-1 Overheating:** To reduce the probability of occurring different strategies can be integrated in the system. However, they might have a snowball effect on the weight and thus the performance of the vehicle. A trade-off is essential to see whether or not it's necessary to overcome overheating. Ways of reducing it include cooling systems and shading.
- **A&C-2 Corrosion:** Unnecessary to mitigate.
- **A&C-3 Communication:** Decrease the likelihood by the using multiple channels, larger bandwidth, larger mission power, and multiple receiving antennas. The more autonomous the drone is the less communication is necessary.
- **A&C-4 Sensor reliability:** Unnecessary to mitigate.
- **A&C-5 Actuator Jamming:** Increase amount of checks and maintenance to every <tbd> flights. The actuator design should have an appropriate material choice which is easy to replace in case of emergency. Impact is reduced by adding redundant actuators however this will also cause a snowball effect with extra weight and so on.
- **A&C-6 Short circuits:** Damage from short circuits can be reduced by fuses, circuit breakers, and overload protection.
- **A&C-7 Hacker attack:** One of the most important risks to be mitigated. In terms of reducing the probability of occurrence, producing encrypted, secure links, as well as salted credentials can be used. Communication is done via classified keywords at the highest level of protocol.
- **A&C-8 EM attack:** Unnecessary to be mitigated.
- **A&C-9 Autopilot link:** Similarly with the communication system, use of better communication links, safer protocols, and secure systems. Use of tested and advanced technology is essential such as LOS and BLOS M2M datalink.

Payload
These are the necessary actions to mitigate risks concerning payload modules.

- **PL-1 Connector failure:** Use shielding and protective layers in order to avoid connector failures between the main power sources and payload. In addition, create a simple and safe connection system.
- **PL-2 Overheating:** Similarly with control and avionics, use cooling systems for the payload. However, since it has a fairly lower chance of occurring this risk might not have to be mitigated.

Performance, propulsion, and stability
These are the necessary actions to mitigate risks concerning Performance, Propulsion and Stability of the drone.

- **P&P-1 Provide lift:** In order to mitigate this risk, the wing structure should be strong enough to support the loads acting on it and provide the necessary lift. Use of extensive software, verification and validation techniques.
- **P&P-2 Provide thrust:** Choice of materials for blades and extensive analysis, while analyzing different scenarios that could lead to the blade disconnecting or breaking.
- **P&P-3 Power to subsystems:** Unnecessary to mitigate
- **P&P-4 Provide stability:** Use systems ensuring the stable operation of the camera for image capturing tasks even when the drone is unstable due to a possible gust.

All of the above mentioned risks have been mitigated in terms of their probability of occurring and impact on the mission. With that taken into account, Table 18.1 is updated and presented by Table 18.2 where it shows that most risks are under control so that the mission can run without any issues.

18.2. Reliability, Availability, Maintainability, and Safety

This part of the chapter will discuss the RAMS of the product and how they can be predicted. They will be presented in the same order as described in the title. Basic equations will be covered in this section, which will determine an initial guess for the RAMS of the system.

Reliability
According to systems engineering reliability relates the probability of the system that it will perform in a satisfactory manner for a given time period when it is being used under specified operating conditions. A study that was conducted from the United States Office of the Secretary of Defense [46] gives a good indication concerning reliability of military UAVs. The main equation to calculate the reliability of the vehicle is given by Equation (18.1)

Table 18.2: Updated risk map obtained from mitigation strategies

Probability / Impact	Negligible	Moderate	Critical	Catastrophic
Very likely				
Likely				
Possible		STR3		
Unlikely		A&C6, A&C7, PL1	STR2, A&C1, A&C4, A&C5, P&P4	STR3, P&P1, P&P3
Very unlikely			A&C2, A&C3, A&C9	STR1, A&C8, PL2, P&P2

$$R(t) = \exp^{-\lambda t} \tag{18.1}$$

In the above equation, t represents the period of interest given in hours and λ is the failure rate which is the inverse of Mean Time Between Failure (MTBF). This corresponds to the failure rate of a specific subsystem. In order to determine the failure rate of the entire system Equation (18.2) is used.

$$\lambda_{\text{system}} = \frac{1}{MTBF_{\text{AV}}} + \frac{1}{MTBF_{\text{GCS}}} + \frac{1}{MTBF_{\text{MMP}}} + \frac{1}{MTBF_{\text{LRE}}} + \frac{1}{MTBF_{\text{GDT}}} + \frac{1}{MTBF_{\text{MPS}}} \tag{18.2}$$

From the above equation the MTBF are not known, since it is based on statistics and tests of the product. The MTBF on average of military UAVs is about 25 h [46]. It was decided to find the reliability using reference military UAVs from the report with similar mission characteristics. Based on different UAVs the method of averaging out was used as shown in Equation (18.3).

$$R(t)_{\text{avg}} = \frac{\sum R(t)_{\text{UAV}}}{\text{number of UAVs}} \tag{18.3}$$

Using Equation (18.3) it was estimated than the reliability of the UAV is 81.7 %. This value is expected to increase since the drone is a less complex system compared to several referenced UAVs.

Availability

On the other hand, availability shows the degree of readiness to use the product. Research suggests that there are various ways of calculating availability based on the available data. Since this project is still at its design phase, prototypes and products are not built and thus calculating the availability of the UAV will not be precise. A general equation used to calculate the availability is portrayed in Equation (18.4) [49].

$$A_0 = \frac{t_{\text{uptime}}}{t_{\text{total}}} \tag{18.4}$$

In this equation, uptime is the time the vehicle is being used to perform the mission in its entire lifetime, while t_{total} is the summation of uptime and downtime. Where the downtime is the time that the vehicle is being repaired, transported, and assembled [49]. Similarly as with reliability, the availability was calculated based on reference UAVs and their availability data. It was estimated that the operational availability is 90 % [46].

Maintainability

Maintainability according to system engineering is the ease, accuracy and safety of the system while performing maintenance actions. Maintenance is the most critical and time-consuming part of the logistic activities during the life cycle of all kind of systems [61]. Therefore, to reduce the overall cost of the UAV operation, the maintenance should already be planned as much as possible. It can be divided into two main activities: corrective and preventive maintenance. Corrective maintenance includes repair or replacements of parts with wear or damage by for example a hard landing. Preventive maintenance is performed before a problem occurs, by for example lubricating and inspecting moving parts, as these are prone to damage. Also, the propellers need to be regularly checked for damages, as these ensure the fly-ability of the UAV. After asking for advice from experts at Logistiek Centrum Woensdrecht (LCW) the following conclusions were drawn for the safest, most efficient and cheapest maintenance of the vehicle.

- Parts that require frequent inspections or replacement should be easily found within the vehicle.
- The modularity of the UAV in terms of components have both advantages and disadvantages. An important advantage is that in case of maintenance, several parts can be easily replaced without the need of replacing the entire drone. However, a drawback is that this reduces the reliability and availability.

- Kevlar is the main material used in the structure and can be maintained by adding more material. However, this can be done up to a certain extent since it may exceed the operational weight of the UAV. Therefore, at a certain point, it might be more efficient to replace the part in consideration rather than adding more layers of Kevlar.

Another issue that should be discussed in this section is where the maintenance will take place. This will happen at several locations with three different levels. The first level is about organizational maintenance, which is performed at the operational military base or at the mission location. The second level known as intermediate level maintenance, is done at line-replaceable unit facilities. It consists of repairs, removals and replacement of critical components. The final level is for the depot-level maintenance. It will be performed at LCW. It consists of the replacement of parts, disposal of the UAV and other maintaining activities which cannot be performed in the area of operations. Using this information the UAV should be designed in a way that makes parts easily accessible and consists of parts that can be easily stransported to and stored in army bases. Another aspect concerning maintainability is the realization of whether or not the vehicle is worth being repaired. If the maintenance cost is >5 % of the overall aircraft cost (**SPARTA-SYS-4**), it should be replaced and recycled where its useful parts could be used as replacement parts.

Furthermore, personnel needs to be able to sustain operations and cover maintenance. The modularity of the system increases the speed of repair as changing subcomponents is faster and more cost effective than replacing the entire subsystem. This has an increased availability as a result, which has a positive impact on the operational costs. Modules should be interchangeable so they can be replaced or updated over the lifetime of the vehicle. Even though there is a possibility that the vehicle will be fully operational during its entire lifetime, taking into account the fact that it will perform missions in hostile environments and for the education of the users, it is unlikely that this will be the case [61].

The implementation of these strategies is an effective way of optimizing maintainability in terms of time and cost.

Safety

Safety is one of the most important aspects for the UAV as it should not cause any harm to the surrounding environment, its users and potentially civilians. There are two kinds of regulations concerning the regulations and safety of UAVs. These regulations are described below: [1]

- ”Process standards describe the development processes to be followed to ensure that the finished product is written in a safe manner (DO-178) or a secure manner (ISO 14508).”
- ”Coding standards describe a high-level programming language subset that ensures the software is written as safely (MISRA C) and securely (CERT C) as possible.”

In order to guarantee the safety of the UAV and its users it has to be uncontrollable by hostile forces. More particularly ISO 14508 has different requirements which have to be met. EAL-7 is the most secure system and can be found in Table 18.3.[2]

Table 18.3: ISO 14508

Evaluation Assurance Level (EAL)	Process required
EAL 1	Functionality testing
EAL 2	Structurally testing
EAL 3	Methododically tested and checked
EAL 4	Methododically designed tested and reviewed
EAL 5	Semi-formally designed and tested
EAL 6	Semi-formally verified designed and tested
EAL 7	Formally designed and tested

The most secure system include a lot of functions which are stated below:

- Audit
- Communication cryptography
- Data protection
- Authentication
- Protection of possible targets
- Protection of information

[1] mil-embedded.com/articles/whats-needed-ensure-safety-security-uav-software/, last accessed: 2017-06-22

[2] www.ecnmag.com/article/2014/10/ensuring-safe-and-secure-uav-systems, last accessed: 2017-06-22

Another important aspect concerning the safety of the UAV is the environment at which it will be performing its missions. A critical requirement is that it needs to perform at very low and very high temperatures. However this can be dangerous for the several components of the UAV as explained in the Section 18.1. This mainly concerns overheating and corrosion of major subsystems. Special attention needs to be paid to the assembly of the UAV. A manual is needed to be distributed to the soldiers for the safe attachment of the modules for a successful mission completion. If one of the components is not attached properly it can cause a malfunction of the system, causing a failure in the mission or even an injury of the users. This is the reason why the Surveillance Platform for Aerial Reconnaissance and Target Acquisition (SPARTA) UAV has simple attachment points for efficiently fast and safe assembly.

Another aspect concerning safety is a possible puncture caused by bullets or fatigue of the materials. In that scenario the users need to be trained to land the UAV safely so there are no casualties caused. In the worst case scenario, it should erase the stored data and communication protocols so that the enemy doesn't obtain any information about possible future targets or communication links.

Furthermore, there are several parameters which will increase the UAV security and thus safety. According to Humphrey, military UAVs should implement jamming sensors which detect and ignore false transmission data which could have been sent from unwanted sources [15]. Humphrey also suggests a solution towards the problem of video data link and common data link interference which can either happen naturally due to the Earth's and Sun's electromagnetic emissions or be caused by unwanted sources. The common data link connections can be made safer by filtering, attenuating and grounding. Safety is also associated with the vehicle's ability to remain undetected so that it can perform the complete missions and obtain valid and reliable information. This was done successfully in the Los Angeles Police Department (LAPD) when they did a joint police and military operation in order to track down drug dealers and look at crime scenes [15].

In conclusion, safety is a major factor concerning the successful completion and the obtain of reliable information for UAVs. In hostile environments its necessary to guarantee the security of systems in terms of software, hardware and stealth. All of the above mentioned safety issues, need to be addressed in a sustainable way in order to be harmless to the environment and the surrounding civilians.

III-19

Cost Analysis

This section presents the current cost breakdown and allocation for the Unmanned Aerial System (UAS). The costs include mass, power, link, and funds. The analysis of costs is important for the feasibility of the design and limits must be posed on them. This section firstly presents all breakdowns and concludes with an analysis and future suggestions. The breakdown structures have been carried out based on the current detailed design. Note must be given that these may change profoundly as detailed design in the future may give a new insight.

19.1. Mass Allocation Budget

The breakdown of mass is important for feasibility of any flying design. The Unmanned Aerial Vehicle (UAV) has been designed for minimum weight, so that it may achieve hand-launch functionality described in Chapter 9. The overall mass breakdown can be found in Table 19.1. Here it can be seen that the quadcopter configuration is overall lighter than the fixed-wing configuration. The detailed breakdown of the quadcopter and fixed-wing configuration is presented in Tables 19.2 and 19.3, respectively.

Table 19.1: Final mass breakdown of the UAV

		Quadcopter	Fixed-wing
OEW	[g]	1151	2431
PAYLOAD	[g]	750	750
BATTERY	[g]	1699	1500
MTOW	[g]	3600	4681

Table 19.2: Mass breakdown of the quadcopter

Flying module			Fuselage module		
Type	**Amount**	**Weight [g]**	**Type**	**Amount**	**Weight [g]**
Engines	4	71	**Avionics**	1	187
Propellers	4	25	**Fuselage**	1	300
Rod	4	11	**Attachments**	1	40
Motor attachment	4	3	**Slide snap-fit**	4	120
Body attachment	4	4			
Wire	4	12			
Total		504	**Total**		647
Allowed		500	**Allowed**		650
Extra		−4	**Extra**		3

Table 19.3: Mass breakdown of the fixed-wing configuration

Flying module			Fuselage module		
Type	**Amount**	**Weight [g]**	**Type**	**Amount**	**Weight [g]**
Wing	1	1106	**Avionics**	1	187
Tail	1	350	**Fuselage**	1	300
Boom	2	69	**Slide snap-fit**	4	120
Engines	1	71	**Motor**	1	90
Propellers	1	18			
Wing attachment	4	1			
Wire	4	12			
Boom attachment	6	3			
Total		1753	**Total**		678
Allowed		720	**Allowed**		650
Extra		−1033	**Extra**		−28

19.2. Power Allocation Budget

The power consumption has a profound effect on mass due to the battery mass, thus its allocation needs to be optimized. Even a small increase in power usage may snowball to large changes. Both configurations are using RimFire .10 engine that uses 325 W of power.[1] The electronics is further split into D0Nano board which uses 2.5 W, PixHawk board with 2.5 W, GPS sensor [2] peeking at 8.25×10^{-2} W power usage, sonar sensors at each 15×10^{-3} W and Visual cameras 2.5×10^{-1} W. The power allocation is presented below in Table 19.4.

Table 19.4: Power breakdown

	Quadcopter module		Fixed-wing module	
Type	**Amount**	**Power per [W]**	**Amount**	**Power per [W]**
RimFire .10 Engine	4	325	1	325
D0Nano	1	2.5	1	2.5
PixHawk	1	2.5	1	2.5
HRLV-MaxSonar-EZ sonar	6	0.015	6	0.015
Lumenier SM600	2	0.25	2	0.25
PmodGPS GPS Receiver	1	0.083	1	0.083
SuperBat 2624	1	0.013		
Servos			1	0.083
Payload	1	11.6		
Total		1300		330
Contingency	5 %	70	5 %	16
Final		1370		346

[1] `www.electrifly.com/motors/gpmg4505.html`, last accessed: 2017-06-22

[2] `reference.digilentinc.com/_media/reference/pmod/pmodgps/globaltop-fgpmmopa6h-datasheet-v0a.pdf`, last accessed: 2017-06-22

Table 19.5: Power breakdown ground station

Ground station		
Type	**Amount**	**Power [W]**
De1-SOC	1	6
Samsung T3	1	4.5
Generalized PC	1	80
Total		90.5

19.3. Cost Allocation Budget

The total cost of the drone was estimated based on preliminary design and re-iterated for detailed design. Still it should be noted that the current allocation of money is still preliminary due to lacking information on various producers. Better estimates could be achieved given more detailed design. It has been assumed that the labour cost is 20 [€]/h (Section 12.4).

Table 19.6: Total cost breakdown for the UAS

Total costs		
Type	**Amount**	**Cost [€]**
Motors		
RimFire .10 Engine	5	55
Batteries		
UAV Battery 5xpacks	8.1 kg	2710
Ground Station Battery	5 kg	1700
Electronics		
D0Nano	1	125
PixHawk	1	280
HRLV-MaxSonar-EZ sonar	6	27
Lumenier SM600	2	29
PmodGPS GPS Receiver	1	38
SuperBat 2624	1	7
Power HD 1810MG	4	16
Ground Station		
De1-SOC	1	250
Samsung T3	1	340
Raw Materials		
Kevlar	1.8 kg	160
Others	-	500
Maintenance and Retire Costs		
Maintenance	-	1000
Retire Costs	-	1000
Production Hours		
Work Hours	880 h	17 600
Total		26 660

IV

Future Development

IV-20

Future Activities

In this chapter the project design and development logic will be discussed. Section 20.1 includes the description of how the overall design process was assessed and what further post-Design Synthesis Exercise (DSE) activities would be performed. Next in Section 20.2, the Gantt chart is presented which shows the timeline of these planned post-DSE activities.

20.1. Project Design and Development Logic

At first the steps that were followed for the design process for the Unmanned Aerial Vehicle (UAV) will be discussed. This can be visualized by the Work Flow Diagrams (WFDs) for each subsystem, because it shows the relevant steps that were taken to come up with results. These WFDs have been placed at the beginning of each chapter of the technical analysis for it to be easier for the reader to understand the process. These WFDs can be found in Chapters 9 to 14 where each WFD displays the input values of different departments, what output is desired, what happens if the output does not meet the requirement and what happens when the process is finished. Every subsystem, has used different techniques to come up with results. Several occasions, the different departments had to share their values and communicate with each other (e.g. structures with aerodynamics).

Concerning the post-DSE activities, these are explained in the project Gantt chart (Section 20.2) where the estimated time for the product to be delivered in the army is also given. At first, the group needs to be re-organized and get in contact with the Royal Netherlands Air Force (RNLAF) for the necessary funding of the project. This includes a new phase where each subsystem is designed in further detail. Analysis will be performed in greater detail and prototype models will be built in order to check the analytical results by means of testing. Each department will have different types of testing. For instance, in aerodynamics, the model will be placed in a wind tunnel. A prototype model will be tested for the noise emissions with microphones. Concerning structures, the prototype model will be tested for all the failure modes, including the drop requirement (**SPARTA-UAV-11.1**) since this has not been analyzed yet. For performance, the model will need to perform flying tests with sensors on board to validate the results. Once the main model is completed, it should be optimized when necessary. Once the government grants permission to start production, at least 50 % will be manufactured in the Netherlands. Once manufactured, the product will undergo its final tests. Finally, the product will be delivered to RNLAF for its first operational use. In Chapter 18 it was estimated that the Mean Time Between Failure (MTBF) is about 25 h of flying time which corresponds to 12 missions before a subsystem does not act according to the design. If this is case, the product needs to be maintained as explained in Section 18.2. If the costs of the maintenance are higher than 5 % of the product cost, it should be taken into consideration whether or not the UAV replaced and recycled or actually maintained in terms of cost. Once it reaches 5000 flight cycles with maintenance it should be recycled where some parts could be used in future drones.

20.2. Gantt Chart

All the necessary activities are shown in the Gantt chart which can be found in Figures 20.1 to 20.4. It portrays all the post-DSE necessary steps to push the product for further development, manufacture and delivery to the RNLAF by the end of this year. All the times are estimated based on experience gained from the DSE while performing tasks and literature study. The Gantt chart should be updated every now and then, to see whether or not it is on schedule. One of the main reasons why milestones were registered is to ensure the smooth completion of the project. It must be taken into account that there is a contingency of at least six months that the plan might be delayed, as it is difficult to predict the exact time for every activity. This is the reason why task hours are very generic.

ID	Task Name	Duration
1	**Post DSE group organization**	**12 days**
2	WBS for post DSE	10 days
3	WFD for post DSE	7 days
4	Gantt Chart for post DSE	5 days
5	Task distribution within team	2 days
6	Finished project re-organization	0 days
7	**Contact with Customers**	**33 days**
8	Contact with Airforce & Fokker	13 days
9	Funding for manufacturing and design improvement	20 days
10	**Extensive research and analysis**	**210 days**
11	**Aerodynamic analysis**	**195 days**
12	Extensive design analysis begins	0 days
13	Extensive CFD analysis	60 days
14	Complete noise model	50 days
15	Reduce noise based on current noise model	20 days
16	Improved aerodynamic model	45 days
17	Design own airfoil and optimization	90 days
18	**Performance analysis**	**181 days**
19	Performance optimization	1 day
20	Extensive research and application of blade element and momentum theory	60 days
21	Design own blade and optimization	120 days
22	Look at improving performance parameters	60 days

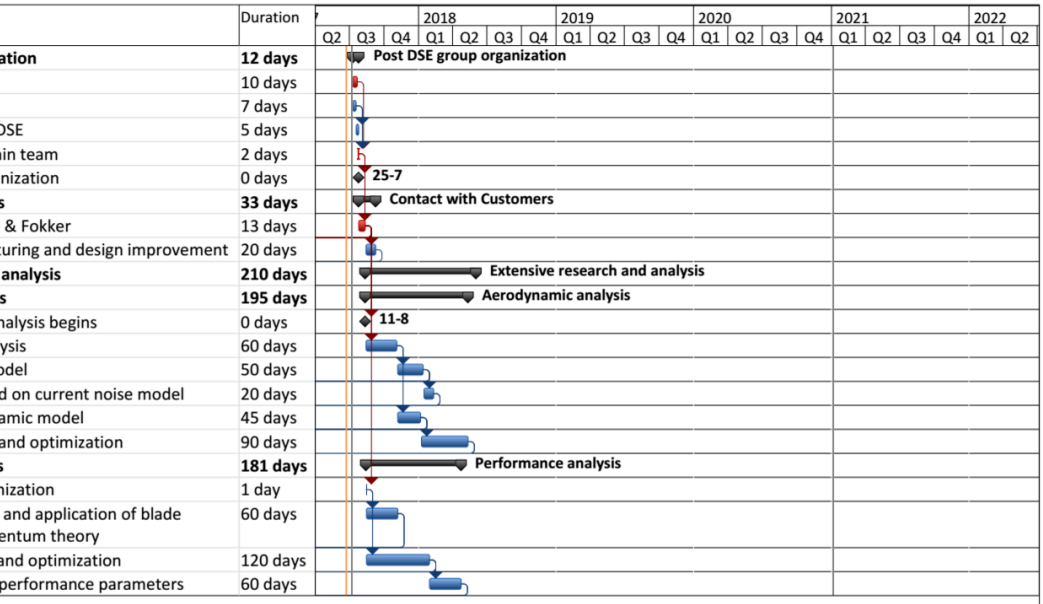

Figure 20.1: Post-DSE Gantt chart part 1

ID	Task Name	Duration
23	**Structural Analysis**	**210 days**
24	Material research	60 days
25	Material testing	30 days
26	Structural analysis on wing platform	60 days
27	Structural Analysis on fuselage & quadcopter structure	45 days
28	Optimize wing structure	60 days
29	Optimize fuselage & quadcopter structure	55 days
30	**Stability Analysis**	**125 days**
31	Advanced stability and control models	60 days
32	Investigate critical and non critical condition	55 days
33	Create dynamic models and simulations for drone behavior	65 days
34	**Payload Analysis**	**115 days**
35	Optimize payload capabilities	45 days
36	Create numerical models for space optimization	70 days
37	Improve avionics and add army safe systems	60 days
38	**Avionics and Control Analysis**	**210 days**
39	Build software	50 days
40	Unit test software	15 days
41	Test software/hardware	60 days
42	Simulation configurations	45 days
43	Control systems prototypes	40 days
44	Build in secure communication systems	35 days

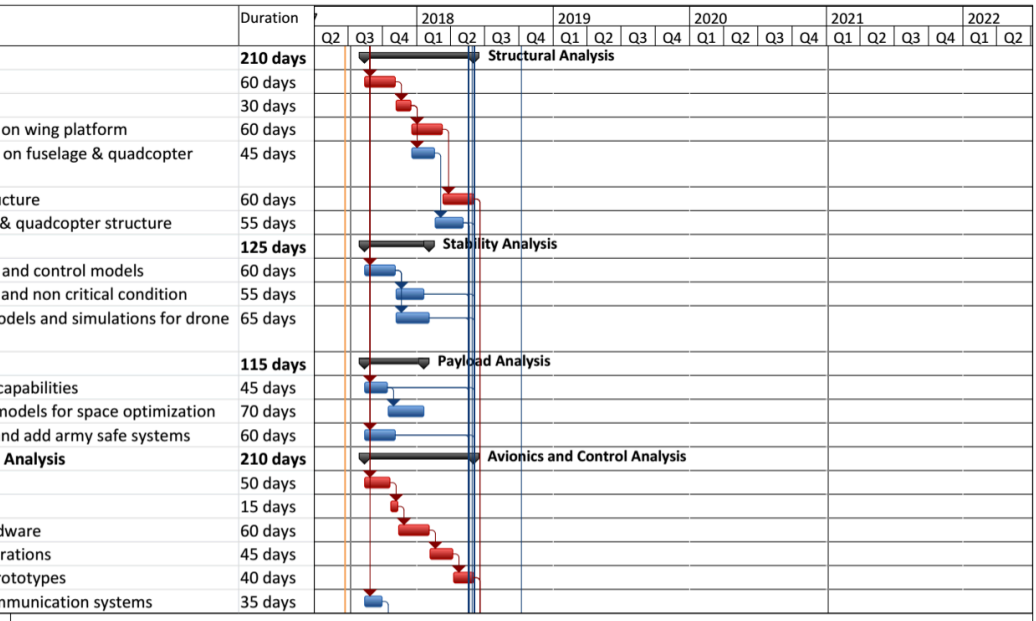

Figure 20.2: Post-DSE Gantt chart part 2

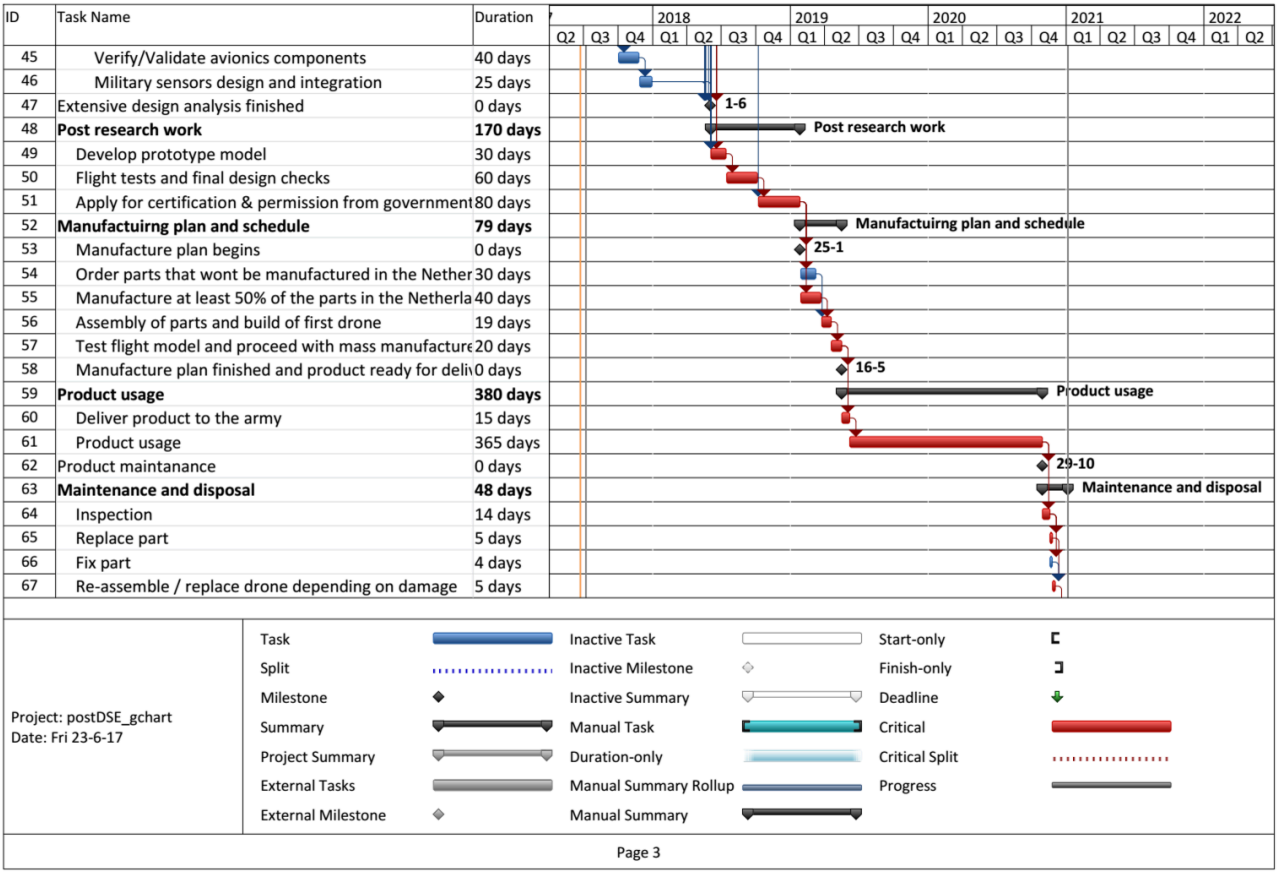

ID	Task Name	Duration
45	Verify/Validate avionics components	40 days
46	Military sensors design and integration	25 days
47	Extensive design analysis finished	0 days
48	**Post research work**	**170 days**
49	Develop prototype model	30 days
50	Flight tests and final design checks	60 days
51	Apply for certification & permission from government	80 days
52	**Manufactuirng plan and schedule**	**79 days**
53	Manufacture plan begins	0 days
54	Order parts that wont be manufactured in the Nether	30 days
55	Manufacture at least 50% of the parts in the Netherla	40 days
56	Assembly of parts and build of first drone	19 days
57	Test flight model and proceed with mass manufacture	20 days
58	Manufacture plan finished and product ready for deli	0 days
59	**Product usage**	**380 days**
60	Deliver product to the army	15 days
61	Product usage	365 days
62	Product maintanance	0 days
63	**Maintenance and disposal**	**48 days**
64	Inspection	14 days
65	Replace part	5 days
66	Fix part	4 days
67	Re-assemble / replace drone depending on damage	5 days

Figure 20.3: Post-DSE Gantt chart part 3

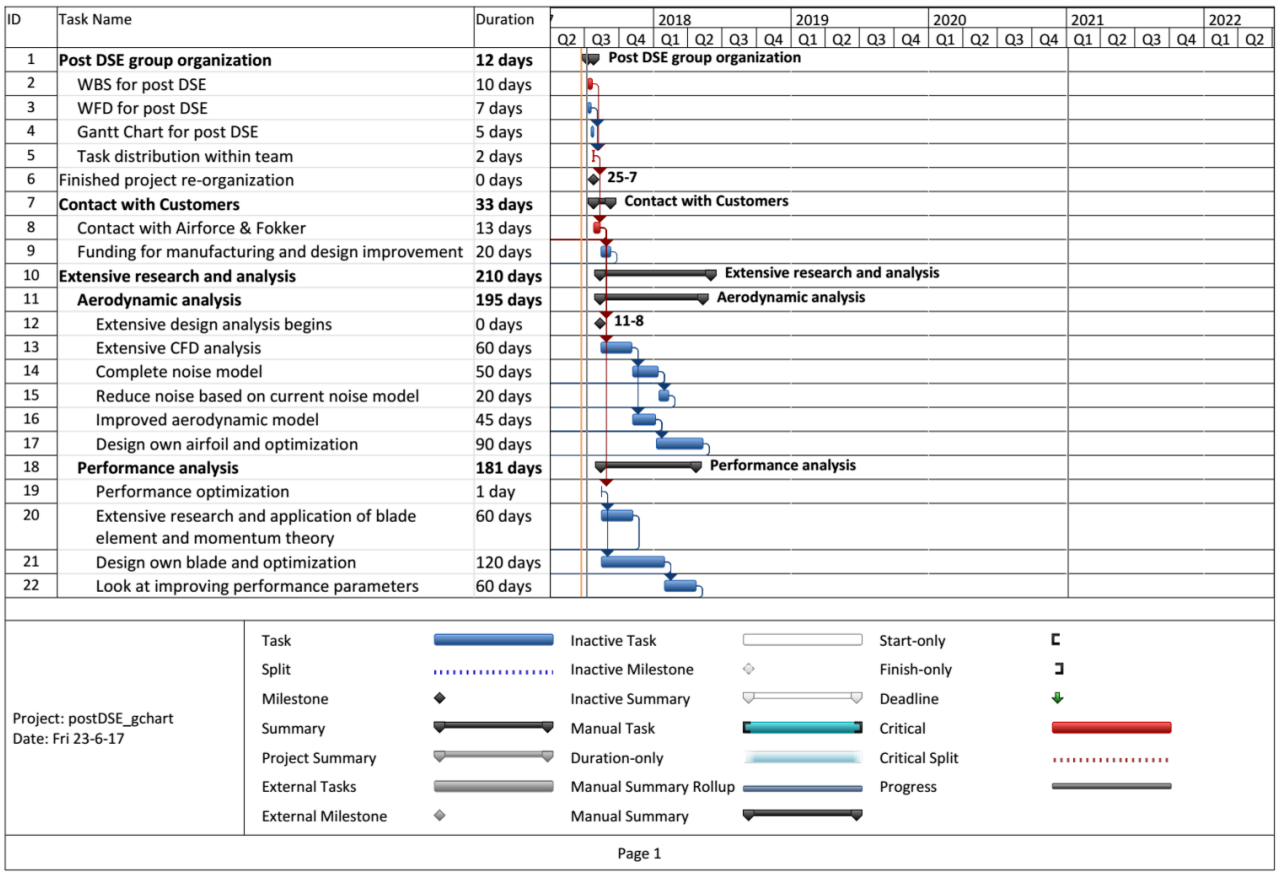

ID	Task Name	Duration
1	**Post DSE group organization**	**12 days**
2	WBS for post DSE	10 days
3	WFD for post DSE	7 days
4	Gantt Chart for post DSE	5 days
5	Task distribution within team	2 days
6	Finished project re-organization	0 days
7	**Contact with Customers**	**33 days**
8	Contact with Airforce & Fokker	13 days
9	Funding for manufacturing and design improvement	20 days
10	**Extensive research and analysis**	**210 days**
11	**Aerodynamic analysis**	**195 days**
12	Extensive design analysis begins	0 days
13	Extensive CFD analysis	60 days
14	Complete noise model	50 days
15	Reduce noise based on current noise model	20 days
16	Improved aerodynamic model	45 days
17	Design own airfoil and optimization	90 days
18	**Performance analysis**	**181 days**
19	Performance optimization	1 day
20	Extensive research and application of blade element and momentum theory	60 days
21	Design own blade and optimization	120 days
22	Look at improving performance parameters	60 days

Figure 20.4: Post-DSE Gantt chart part 4

IV-21

Conclusion

The goal of this report was to present the current work done on the detailed design phase of the Surveillance Platform for Aerial Reconnaissance and Target Acquisition (SPARTA) UAV. SPARTA is a multipurpose UAV capable of carrying multiple payload modules on one hand and interchanging its flying configuration between a quadcopter and fixed-wing configuration, depending on the mission needs on the other hand.

From the conceptual design phase to the preliminary design phase and finally culminating in the detailed design, the work of 10 weeks of DSE group 15 was presented. In the conceptual design the project planning and design choices were evaluated. Out of those designs, a preliminary design was chosen based on extensive trade study, inter-design comparison and stakeholders' input. The design was tested for feasibility and performance in various environments and found to accomplish the needs of the mission.

The detailed design elaborated further on the preliminary choices, sizing the components individually and estimation of their characteristics. The final design has been shown to fulfill a great amount of stakeholder requirements and most importantly their core mission needs. The quadcopter module has an loiter of 1.7 h and a range of 24.7 km, which, compared to any other quadcopter in the same weight class, is significantly higher. For the fixed-wing module an endurance was found of 2.4 h and a range of 99.9 km. The cost of Unmanned Aerial System (UAS) is €26 660, which includes one fuselage, a quadcopter module, a fixed-wing module, and the ground station. In conclusion, the report has shown the sheer complexity of the problem that SPARTA had to solve. A UAV that is both modular and can push the boundaries of performance. The compromise was found by splitting the concerns and thus two configurations were created; a fixed-wing and a quadcopter configuration.

Even though the current design is still in the start of the detailed phase, it showed a lot of potential. It fulfills both the loiter and hover requirements while being light and easy to assemble. Furthermore, its untapped potential is demonstrated in further possible improvements for future design. Moreover, the team believes that more detailed design and further optimization of the subsystems could additionally increase the current performance and system characteristics, thus making the UAS competitive on the market.

In conclusion, the SPARTA UAV is highly modular and an autonomous, for various environments and conflict zones. Its minute sound footprint makes the UAV capable of flying into the target area, gathering the important information and leaving without being detected. It is capable of self-maneuvering and has extensive detect and avoid systems making it extremely easy to control the UAV. All of this results in a system that can see but remains unseen, can hear but remains unheard and that gathers proof, while leaving none behind. But most importantly, it saves human lives. This is SPARTA.

Bibliography

[1] E-Lighter® Lightweight diesel-fueled power source for the modern soldier.

[2] *NATO Logistics Handbook*. North Atlantic Treaty Organization, Brussels, 2012.

[3] John D. Jr. Anderson. *Fundamentals of Aerodynamics*. McGraw-Hill, Maryland, 2nd edition, 1991. ISBN 0-07-001679-8. doi: 10.2514/1.52157.

[4] Mario Asselin. Gliding Flight.

[5] Reg Austin. *Unmanned Aircraft Systems*. 2010. ISBN 9780123745187. doi: 10.1016/B978-0-12-374518-7.00016-X.

[6] Urban Avsec, Diego De Buysscher, Bart Herremans, Dana de Leeuw, Erine de Leeuw, San Kilkis, Kostadinos Nikolakopoulos, Roderick Tam, Thijs van Veen, and Arjan Vermeulen. Baseline Report. Technical report, Delft University of Technology, Delft, the Netherlands, 2017.

[7] Urban Avsec, Diego De Buysscher, Bart Herremans, Dana de Leeuw, Erine de Leeuw, San Kilkis, Kostadinos Nikolakopoulos, Roderick Tam, Thijs van Veen, and Arjan Vermeulen. Project Plan. Technical report, Delft University of Technology, Delft, the Netherlands, 2017.

[8] Urban Avsec, Diego De Buysscher, Bart Herremans, Dana de Leeuw, Erine de Leeuw, San Kilkis, Kostadinos Nikolakopoulos, Roderick Tam, Thijs van Veen, and Arjan Vermeulen. Technical Design Report. Technical report, Delft University of Technology, Delft, the Netherlands, 2017.

[9] Moses Bangura, Marco Melega, Roberto Naldi, and Robert Mahony. Aerodynamics of Rotor Blades for Quadrotors. 2016.

[10] BASF Corporation. Snap-Fit Design Manual, 2007.

[11] Bayer. Snap-fit joints for plastics A design guide. Technical report, Pittsburgh, 2000.

[12] Dmitry Bershadsky, Steven Haviland, and Eric N Johnson. Electric Multirotor UAV Propulsion System Sizing for Performance Prediction and Design Optimization. *57th AIAA/ASCE/AHS/ASC Structures, Structural Dynamics, and Materials Conference*, (January):1–20, 2016. doi: 10.2514/6.2016-0581.

[13] Randolph Cabell, Robert Mcswain, and Ferdinand Grosveld. Measured Noise from Small Unmanned Aerial Vehicles. 2016.

[14] William D. Callister and David G. Rethwisch. *Fundamentals of Materials Science and Engineering: An Integrated Approach*. 2012. ISBN 978-1-118-06160-2.

[15] Evan Baldwin Carr. Unmanned Aerial Vehicles: Examining the Safety, Security, Privacy and Regulatory Issues of Integration into U.S. Airspace. Technical report.

[16] Lee Chapman. Transport and climate change: a review. *Journal of Transport Geography*, 15(5):354–367, 2007. ISSN 09666923. doi: 10.1016/j.jtrangeo.2006.11.008.

[17] Curran Crawford. Blade Element Momentum Theory. (June):457–478, 2006. doi: 10.1002/we.

[18] Filipe Szolnoky Cunha. Blade Element Theory. .

[19] Filipe Szolnoky Cunha. Helicopters Performance, .

[20] Isa Diana de Sousa Baptista Morais Carvalho. *Low Reynolds Propellers for Increased Quadcopters Endurance*. PhD thesis, Universidade de Beira Interior, 2013.

[21] EASA. Policy Statement Airworthiness Certification of Unmanned Aircraft Systems (UAS) E . Y013 01, 2009.

[22] EASA. Certification Specifications for Large Aeroplanes CS-VLA, 2009.

[23] EASA. Notice of Proposed Amendment 2017-05 (A) Introduction of a Regulatory Framework for the Operation of Drones, 2018.

[24] Bernard. Etkin. *Dynamics of flight : stability and control*. Wiley, 1982. ISBN 0471089362.

[25] European Aviation Safety Agency. Certification Specifications for Normal-Category Aeroplanes CS-23, 2017.

[26] George Gerard and Herbert Becker. Part III - Buckling of curved plates and shells. In *Handbook of structural stability*. New York University, Washington, 1957.

[27] Jay Gundlach. *Designing Unmanned Aircraft Systems: A Comprehensive Approach*. American Institute of Aeronautics and Astronautics, Inc., Blacksburg, 2011. ISBN 9781600868436. doi: 10.2514/4.868443.

[28] Menno Hochstenbach, Cyriel Notteboom, Bart Theys, and Joris De Schutter. Design and control of an unmanned aerial vehicle for autonomous parcel delivery with transition from vertical take-off to forward flight - VertiKUL, a quadcopter tailsitter. *International Journal of Micro Air Vehicles*, 7(4):395–405, 2015. ISSN 17568293.

[29] H. Harvey Hubbard. Aero acoustics of flight vehicles. *NASA*, 1:11–23, 1991.

[30] Grant Ingram. Wind Turbine Blade Analysis using the Blade Element Momentum Method. Version 1.1. *October*, (c):1–21, 2011.

[31] S.V Joshi, L.T Drzal, A.K Mohanty, and S Arora. Are natural fiber composites environmentally superior to glass fiber reinforced composites? *Composites Part A: Applied Science and Manufacturing*, 35(3): 371–376, 3 2004. ISSN 1359835X. doi: 10.1016/j.compositesa.2003.09.016.

[32] Bertan Karahoda, Xhemajl Mehmeti, and Uran Cabra. Noise Reduction in Quadcopter Accelerometer and Gyroscope measurements based on Kalman Filtering. doi: 10.13140/RG.2.1.4300.2486.

[33] Christos Kassapoglou, Peter Belobaba, Jonathan Cooper, Roy Langton, and Allan Seabridge. Design and Analysis of Composite Structures Second Edition Aerospace Series.

[34] Eva Saadé Latorre. *Propulsion system optimization for an unmanned lightweight quadrotor*. PhD thesis, Universitat Politècnica de Catalunya, 2011.

[35] D.Sc.(Eng.) Ph.D. F.R.Ae.S. J. Gordon Leishman. Principles of Helicopter Aerodynamics, 2006. ISSN 14337851.

[36] Alfred C Loos and George S Springer. Curing of Epoxy Matrix Composites. Technical Report March, Department of Mechanical Engineering and Applied Mechanics, The University of Michigan, 1983.

[37] John Love. The Truth About Range Data: How to Assess Thermal Camera Range Capability for Site Design Purposes. Technical report, DRS Technologies, 13532 N. Central Expwy, Dallas, TX, 2014.

[38] Jack E Made and Donald W Kurtz. A Review of Aerodynamic Noise From Propellers, Rofors, and Liff Fans. 1970.

[39] Pier Marzocca. AE429 - Aircraft Performance and Flight Mechanics.

[40] Kevin Massey and Richard Gaeta. Noise Measurements of Tactical UAVs. In *16th AIAA/CEAS Aeroacoustics Conference*, 2010. ISBN 978-1-60086-955-6. doi: 10.2514/6.2010-3911.

[41] T H G Megson. An Introduction to Aircraft Structural Analysis.

[42] J.A. Mulder, W.H.J.J. van Staveren, J.C. van der Vaart, E. de Weerdt, C.C. de Visser, A.C. in 't Veld, and E. Mooij. *Flight Dynamics*. TU Delft, Delft, 2013.

[43] Fusanobu Nakamura, Takehiko Noguchi, and Katsutoshi Katoh. Battery attaching mechanism for portable computers, 1998.

[44] Nederlands Normalisatie-instituut. *Standards for mechanical engineering drawings*. 1 edition, 1993.

[45] Martin Neubauer, Georg Günther, and Konrad Füllhas. Structural Design Aspects and Criteria for Military UAV. Florence, 2007. European Aeronautic Defence and Space, Munich.

[46] Office of the Secretary of Defense. OSD UAV Reliability Study. Technical report, Washington DC, 2003.

[47] Jason L Pereira. *Hover and wind-tunnel testing of shrouded rotors for improved micro air vehicle design*. PhD thesis, University of Maryland, 2008.

[48] R. W. Prouty. Helicopter Performance, Stability, and Control, 2002.

[49] Reliability Analysis Center. Introduction to Operational Availability.

[50] Beibei Ren, Shuzhi Sam Ge, Chang Chen, Cheng Heng Fua, and Tong Heng Lee. *Modeling, control and coordination of helicopter systems*. Springer, 2012. ISBN 9781461415633. doi: 10.1007/978-1-4614-1563-3.

[51] Jan Roskam. *Airplane flight dynamics and automatic flight controls*. DARcorporation, 1995. ISBN 9781884885174.

[52] Sascha Schneider, Rainer Heger, and Peter Konstanzer. BLUECOPTER™ DEMONSTRATOR: THE STATE-OF-THE-ART IN LOW NOISE DESIGN MTOW Maximum TakeOff Weight EPNL Effective Perceived Noise Level HOGE Hover Out of Ground Effect FLM Flight Manual BETA Side Slip Angle.

[53] Michaels Selig, James J Guglielmo, Andy P Broeren, and Philippe Giguere Volume. Summary of Low-Speed Airfoil Data. Technical report, Univerisity of Illinois at Urbana-Champaign, 1995.

[54] KP Shabeer and M A Murtaza. Optimization of Aircraft Wing with Composite Material. *International Journal of Innovative Research in Science, Engineering and Technology*, 2(6), 2013.

[55] Jos Sinke. Production of Aerospace Systems.

[56] Tim Spahr. Snap-fits for Assembly and Disassembly. 1991.

[57] David Stienstra. Introduction to Design for (Cost Effective) Assembly and Manufacturing. pages 1–81.

[58] William Joseph Stuart. Composite Materials Layup Lab. pages 1–9, 2010.

[59] George P. Succi. *Design of Quiet Efficient Propellers*. PhD thesis, Stanford California, 2012.

[60] H H B M Thomas. Estimation of Stability Derivatives (State of the Art).

[61] Kimon P. Valavanis and George J. Vachtsevanos. *Handbook of Unmanned Aerial Vehicles*. Springer, 2015.

[62] H.C.M. Veerman. *Preliminary multi-mission UAS design*. PhD thesis, Delft University of Technology, 2012.

[63] N. Wagner, S. Boland, B. Taylor, D. Keen, J. Nelson, and T. Bradley. Powertrain Design for Hand-Launchable Long Endurance Unmanned Aerial Vehicles. *47th AIAA/ASME/SAE/ASEE Joint Propulsion Conference & Exhibit*, pages 1–16, 2011. doi: 10.2514/6.2011-6047.

[64] XFLR5. Analysis of Foils and Wings Operating at Low Reynolds Numbers. Technical Report September, 2010.